UNIVERZITA PALACKÉHO V OLOMOUCI
PŘÍRODOVĚDECKÁ FAKULTA

Katedra optiky

Kvantově optické experimenty zaměřené na kvantové zpracování informace

Martina Miková

Disertační práce

Studijní program: Fyzika, P1701
Studijní obor: Optika a optoelektronika, 1701V029

Školitel: prof. RNDr. Miloslav Dušek, Dr.
Konzultant: RNDr. Miroslav Ježek, Ph.D.

Olomouc 2017

PALACKY UNIVERSITY OLOMOUC
FACULTY OF SCIENCE

Department of Optics

Quantum optical experiments focused on quantum information processing

Martina Miková

Ph.D. thesis

Study program: Physics, P1701
Branch of study: Optics a optoelectronics, 1701V029

Supervisor: prof. RNDr. Miloslav Dušek, Dr.
Co-Supervisor: RNDr. Miroslav Ježek, Ph.D.

Olomouc 2017

Abstrakt

Tato disertační práce je založena na pěti originálních publikacích [1–5] a shrnuje hlavní experimentální výsledky, které vznikly během mého doktorského studia.

První realizovaný experiment testoval využití elektro-optické dopředné vazby pro zvýšení pravděpodobnosti úspěchu lineárně optických hradel [1]. Experimentální výsledky ukázaly, že dopředná vazba zdvojnásobila pravděpodobnost úspěchu lineárně-optického programovatelného kvantového fázového hradla aniž by ovlivnila kvalitu dosažených výsledků. Koncept zavedení podmíněné operace pomocí dopředné vazby byl úspěšně aplikován i v dalších realizovaných experimentech.

Následující experimenty se zabývaly přenosem kvantového stavu a rozlišovacími strategiemi. Bylo sestrojeno experimentální zařízení pro bezchybné rozlišení dvou optických paměťových záznamů reprezentovaných dvěma děliči svazku s navzájem různými odrazivostmi [3]. Realizované zařízení využívalo nejmenší možné energie, v průběhu měření byl paměťový záznam vystaven v průměru pouze zlomku energie jednoho fotonu. Následným projektem byla experimentální realizace optimálního rozlišení dvou známých projektivních kvantových měření pomocí kvantově provázaného stavu [4]. Výsledná experimentální data jasně demonstrovala výhodu rozlišovací strategie využívající dvě kvantově provázané částice v porovnání se strategií využívající pouze jeden kvantový bit.

Dále byl realizován experiment pro přenos stavu kvantového bitu. Experiment byl využit k ověření nově navržené, přímo měřitelné míry efektivní nerozlišitelnosti částic, která určuje reálnou hranici kvality přenosu kvantového stavu [2]. Zároveň jsme tuto míru porovnali s běžně užívaným překryvem stavů, i když překryv stavů lze použít pouze tehdy, jsou-li tyto částice ve faktorizovaném stavu. Výsledky experimentu potvrdily, že částice mohou sloužit pro přenos kvantové informace, i když jsou jejich další stupně volnosti provázané. Posledním realizovaným experimentem byl přenos neznámého kvantového stavu mezi dvěma vzájemně slabě interagujícími částicemi [5]. Přenosu kvantového stavu bylo dosaženo vhodným měřením fotonu, který nesl neznámý kvantový stav, v kombinaci s aplikací filtrace na stav cílového fotonu. Optimální filtrace závisí na vzájemné interakci částic, na výsledku měření a na původním stavu částice, na niž je neznámý stav přenášen.

Výsledky těchto experimentů přispěly k rozvoji základního výzkumu v oblasti experimentální lineární kvantové optiky a kvantového zpracování informace.

Klíčová slova

Experimentální kvantová optika, lineární optika, vláknová optika, kvantové zpracování informace, elektro-optická dopředná vazba, integrovaný elektro-optický fázový modulátor, fotony, Machův-Zehnderův interferometr, sekvenční aktivní fázová stabilizace.

Abstract

This Thesis is based on five original publications [1–5] and concludes my main experimental results reached during the years of my Ph.D. studies.

Firstly, we experimentally verify the possibility of increasing success probability of linear optical quantum gates utilizing an electro-optical feed-forward loop [1]. We find out that the loop doubles the success probability of linear-optical programmable quantum phase gate. Moreover, any gate parameters like a fidelity, purity etc. are not influenced. The concept of a conditionally applied operation via the feed-forward loop is successfully implemented into other experiments.

Further publications deal with quantum state transfer and discrimination tasks. We experimentally implement a device for perfect discrimination of two optical memory records which are represented by two beam splitters with different splitting ratios [3]. For discrimination, this device utilizes in average less than fraction of a single photon energy. Further, we experimentally implement the device for optimal discrimination of two known projective single-qubit quantum measurements [4]. The experimental results clearly confirm the advantage of the proposed more demanding entanglement-assisted discrimination scheme compared to a single-qubit probe scheme.

A quantum state transfer is experimentally realized to examine particle properties. A new measure of particles' effective indistinguishability directly determines the fidelity of the transferred state [2]. We compare it with commonly used overlap of quantum states of particles, which is defined only for factorable states. The experimental results confirm that even if some noninformational degrees of freedom of two particles are entangled, the particles can still serve as good carriers of qubits. Finally, we experimentally realize a faithful unidirectional qubit state transfer between two weakly interacting photonic qubits [5]. The qubit state transfer is achieved by a combination of a suitable measurement on the unknown qubit and a quantum filtering on the target qubit. The filtering depends on the initial target-qubit state and on the outcome of the measurement applied on the unknown qubit.

The results of these proof-of-principle experiments support scientific research in the area of experimental linear-optical quantum information processing and quantum optics.

Key words

Quantum optics experiments, linear optics, fibre optics, quantum information processing, electro-optical feed-forward loop, integrated electro-optical phase modulator, photons, Mach-Zehnder interferometer, sequential active phase stabilization.

Acknowledgement

Firstly, I want to express my gratitude to my supervisor Miloslav Dušek for his support, guidance, patience, help, and scientific discussions. I would like to extend my thanks to my co-supervisor Miroslav Ježek for his indispensable help in the laboratory and overall support. I am also grateful to Jaromír Fiurášek and Radim Filip for many fruitful scientific discussions, which greatly improves my the theoretical background. My special thanks belong to Ivo Straka for his unconditional support and irreplaceable help. I would express my thanks to other colleagues who shared their experimental know-how with me during my studies, particularly to Michal Mičuda and Lucie Čelechovská (Bartůšková) for a launching of the feed-forward experiments. My thanks go also to my schoolmate Helena Fikerová for the collaboration in 2009-2012 and to Vojtěch Krčmarský for the collaboration in 2015.

Furthermore, I would like to express my great thanks to all the co-authors of the presented publications, lab-team, officemates, my students, and colleagues. I appreciate their friendly attitude and creative environment where know-how, coffee, and waffles are shared. I am really glad, that I could spend my Ph.D. studies in such a nice collective.

At the same time, I would like to thank all my colleagues, that I met during my research stays at Austrian Institute of Technology (Safety and Security Department, unit of Optical Quantum Technologies) in Vienna and Technical University of Denmark (Department of Physics, a group of Quantum Physics and Information Technology) in Lyngby for the possibility to learn from them.

I would like to thank funding agencies and organizations for the financial support: Czech Grant Agency (202/09/0747, GA13-20319S, 17-26143S), Czech Ministry of Education, Youth and Sports (LC06007, MSM6198959213), and Palacký University (PrF-2011-015, PrF-2012-019, PrF-2013-008, IGA_PrF_2014008, IGA-PrF-2015-005, IGA-PrF-2016-009, and IGA-PrF-2017-008.) Also, I would like to thank the principal investigators of the mentioned projects for the opportunity to participate in the research and fruitful collaboration.

I would express my gratitude to my other friends who have been cheering me up during my studies, especially to Michaela and Michal, Petra and Jarka, Petra, Ester, Monika, and Lucie.

Finally, my warmest thanks belong to my family and my boyfriend Petr for their continuous support, love, and care.

Thank you

Martina

Declaration

This Thesis is based on five original publications [1–5]. My contribution to these publications consists mainly in the experimental implementations of recently suggested quantum information protocols. The main goals of this effort were to validate theoretical predictions of the protocols and experimentally verify their feasibility and robustness. Theoretical concepts and methods used in the publications were developed by the co-authors or, alternatively, their sources are properly cited.

Here I shall declare the contribution of other Ph.D. students working on the experimental part of the publications [1–5]: I have cooperated with Ivo Straka since my Master's studies. His main contribution lies in the realization of the source of correlated photon pairs, its development and maintenance. The source was utilized in all the publications presented in this Thesis.

I declare that I wrote this Ph.D. Thesis "Quantum optical experiments focused on quantum information processing" on my own under the guidance of my supervisor prof. RNDr. Miloslav Dušek, Dr. and my co-supervisor RNDr. Miroslav Ježek, Ph.D. using the resources which are cited in the Bibliography.

I agree with the further usage of this Thesis according to the requirements of Palacký University and the Department of Optics.

In Olomouc, ... 2017

.....
Martina Miková

List of Abbreviations

ADC	Analogue to Digital Converter
APD	Avalanche Photo Diode
BD	Beam Displacer
BNC	Bayonet Neill–Concelman, radio-frequency connector for coaxial cables
BS	Beam Splitter
$C_{i,j}$	Coincidence rate between two detectors no. i, j
CW	Continuous Wave
D, D_i, DI, Det	Detector no. i, I
DAC	Digital to Analogue Converter
DC	Direct Current
η	efficiency, transparency
F	Flip
FBS	Fibre Beam Splitter, Fibre Coupler
FC	Fibre Coupler (the same as FBS), or Fibre Connector
FC/PC	Fibre Connector / Physical Contact
FWHM	Full Width at Half Maximum
HOM	Hong-Ou-Mandel
HWP	Half-Wave Plate
M	Mirror
MZI	Mach-Zehnder Interferometer
N, N_i	*usually denotes* count rate of detector no. i
NIM	specifications of electronics modules Nuclear Instrumentation Module, negative electric pulse
PBS	Polarizing Beam Splitter
PC	Polarization Controller
PM	integrated electro-optical Phase Modulator
PMF	Polarization Maintaining optical Fibre (for example PM780-HP)
POVM	Positive-Operator Valued Measure
PPBS	Partially Polarizing Beam Splitter
QWP	Quarter-Wave Plate
SMF	Single Mode optical Fibre (for example 780-HP)
SNR	Signal to Noise Ratio
SPAD	Single-Photon Avalanche Diode
SPCM	Single Photon Counting Modules
SPDC	Spontaneous Parametric Down Conversion
TTL	Transistor-Transistor Logic, positive electric pulse
U_π	half-wave voltage of a phase modulator (PM)
VRC	Variable Ratio Coupler – a FBS with adjustable splitting ratio

Contents

Abstrakt a Klíčová slova (CZ) vi

Abstract and Key words vi

Acknowledgement vii

Declaration viii

List of Abbreviations ix

Contents xi

1 Goals of the Thesis and a brief introduction 1

2 Contemporary state of research 5

3 Methods and Tools 11

3.1 Relevant formalism of quantum optics . . . 11

3.1.1 Qubit . . . 11

3.1.2 Focks state representation . . . 12

3.1.3 Qubit encoding . . . 13

3.2 Components used in the experiments . . . 13

3.2.1 Collimating lens (C) . . . 13

3.2.2 Mirrors (M) . . . 14

3.2.3 Kinematic mounts and holders . . . 14

3.2.4 Wave plates (HWP), (QWP) . . . 14

3.2.5 Optical fibres . . . 15

3.2.6 Polarization controller (PC) . . . 16

3.2.7 Automatic beam stop, flip (F) . . . 16

3.2.8 Detectors . . . 17

3.2.9 Integrated electro-optical phase modulator (PM) . . . 18

3.3 Beam splitters . . . 21

3.3.1 Beam splitter (BS) – polarization insensitive . . . 21

3.3.2 Fibre beam splitters (FBS) with fixed splitting ratio . . . 26

3.3.3 Variable ratio couplers (VRC) . . . 27

3.3.4 Measurement of BS splitting ratio $R:T$ . . . 28
3.3.5 Polarization sensitive beam splitters . . . 28
3.4 Mach-Zehnder interferometer (MZI) . . . 31
3.5 Electronic signal processing . . . 35
3.6 Air gap (AG) . . . 37
3.7 Light sources . . . 39
3.7.1 Laser diodes (LD) – probe beam . . . 39
3.7.2 Source of correlated photon pairs . . . 39
3.8 Stabilization of experimental setup . . . 41
3.8.1 Passive stabilization . . . 43
3.8.2 Active sequential stabilization of fibre-based MZI operating at single photon level . . . 43
3.9 Real-time electro-optical feed-forward loop . . . 46
3.10 Toolbox for experiment characterization . . . 50
3.10.1 Quantum state tomography . . . 50
3.10.2 How to implement the quantum state tomography measurement and the data acquisition . . . 52
3.10.3 Brief introduction to quantum process tomography . . . 54
3.10.4 How to implement the data acquisition for the quantum process tomography . . . 54

4 Increasing efficiency of a linear-optical quantum gate using electronic feed-forward loop 57
4.1 Basic idea . . . 57
4.2 Theory . . . 58
4.3 Experiment . . . 59
4.4 Measurement . . . 61
4.5 Results . . . 61

5 Carrying qubits with particles whose noninformational degrees of freedom are nonfactorable 67
5.1 Basic idea . . . 67
5.2 Theory . . . 68
5.3 Experiment . . . 70
5.4 Measurements . . . 71
5.5 Results . . . 72

6 Experimental implementation of perfect quantum reading of beam splitters 75
6.1 Basic idea . . . 75
6.2 Theory related to the experimental setup . . . 76
6.3 Experiment & Measurement . . . 77
6.4 Results . . . 79

7 Optimal entanglement-assisted discrimination of quantum measurements 81
7.1 Basic idea . . . 81
7.2 Theory . . . 82
7.3 Experiment . . . 84
7.4 Measurement . . . 92
7.5 Results . . . 93
7.5.1 Tables & Additional material . . . 95

8 Faithful conditional quantum state transfer between weakly coupled qubits 97
8.1 Basic idea . . . 97
8.2 Theory . . . 98
8.3 Experiment . . . 100
8.4 Measurement . . . 107
8.5 Results & Discussion . . . 108
8.5.1 Additional material . . . 112

9 Conclusions 115

Stručné shrnutí v češtině (CZ) 117

Publications of the author and a list of citations 119

Bibliography 125

Chapter 1

Goals of the Thesis and a brief introduction

The aim of this Thesis is to comprehensively present experiments which were realized during my Ph.D. studies. The goal of these proof-of-principle linear-optics quantum information processing experiments is to implement the suggested theoretical protocols, verify their feasibility, robustness, and sensitivity to real conditions.

The goal of this chapter is to overview the content of this Thesis and introduce five presented experiments, based on five publications [1–5] described bellow. The *Chapter 2* contains brief contemporary state of research related to the presented experiments. In the *Chapter 3*, called Methods and Tools, there is described used formalism of quantum optics, the individual experimental components, entire function blocks, and procedures common for most experiments. Beside basic experimental components of linear optics like mirrors, beam splitters, wave plates, etc. there are also described typical electronics signal processing, the source of photon pairs, Mach-Zehnder interferometer, sequential active phase stabilization procedure of the Mach-Zehnder interferometer operating at single photon level, real-time feed-forward loop, etc. Then the following *Chapters 4-8* describe the individual experiments. At the beginning of each of these chapters, there is introduced part of the theory necessary for understanding of the experiment. It is followed by a description of the experiment itself, data accumulation, data processing and results. Subsequently, *Chapter 9* includes a conclusion of achieved results. Final chapters are a summary in the Czech language, a list of author's publications, a list of citations, and bibliography.

Furthermore the chapters describing the individual experiments are briefly introduced:

Chapter 4 describes the increase of success probability of a linear optical programmable phase gate via successful implementation of the fast electro-optical feed-forward loop. The probabilistic programmable phase gate itself was proposed by *Vidal, Masanes, and Cirac in 2002* [6]. For the first time, the gate was experimentally implemented using only bulk linear-optical elements and reached only 25 % success probability [7]. We reached the theoretical limit of 50 % in the fibre-optics gate implementation via the fast electro-optical feed-forward loop. We verified the increase of the success probability and characterized

the gate operation by means of quantum process tomography. We demonstrated that the use of feed-forward loop affects neither the process fidelity nor the output state fidelities. The *Chapter 4* is based on a publication [1]: Martina Miková, Helena Fikerová, Ivo Straka, Michal Mičuda, Jaromír Fiurášek, Miroslav Ježek, and Miloslav Dušek. *Increasing efficiency of a linear-optical quantum gate using electronic feed-forward.* Physical Review A **85**, 012305 (2012).

In *Chapter 5*, we have experimentally tested and verified the relevance of *effective indistinguishability* of particles carrying qubits to quantum information transfer and processing. In contrast to commonly used overlap of quantum states of particles, defined only for factorable states, this measure can be generally applied to any joint state of the particles. We test the new measure of *effective indistinguishability* on photons produced by parametric down-conversion employed in a simple linear-optical quantum state transfer protocol. There the measure directly determines the fidelity of the transferred state. The experimental results confirmed that even if other degrees of freedom of two particles are entangled, the particles can still serve as good carriers of qubits. *Chapter 5* is based on publication [2]: Martina Miková, Helena Fikerová, Ivo Straka, Michal Mičuda, Miroslav Ježek, Miloslav Dušek, and Radim Filip. *Carrying qubits with particles whose noninformational degrees of freedom are nonfactorable.* Physical Review A **87**, 042327 (2013).

In *Chapter 6*, there is described the experimental implementation of perfect quantum reading of optical memory records utilizing the smallest possible energy amount. We built the suggested device for perfect and unambiguous distinguishing between two different memory records represented by two mutually different beam-splitters. During the measurement, a superposition of a single photon and vacuum state entered into the beam-splitter. The experimental results of the quantum reading showed that the memory records can be perfectly distinguished even if they are in average exposed to a fraction of photon energy and confirmed the theoretical predictions. *Chapter 6* is based on publication [3]: Michele Dall'Arno, Alessandro Bisio, Giacomo Mauro D'Ariano, Martina Miková, Miroslav Ježek, and Miloslav Dušek. *Experimental implementation of unambiguous quantum reading.* Physical Review A **85**, 012308 (2012).

In *Chapter 7*, we experimentally investigated optimal discrimination between two projective single-qubit measurements on polarization states of a single photon in a scenario where the measurement can be performed only once. We investigated the discrimination strategy in dependence on the amount of inconclusive outcomes. The experimental results demonstrate the advantage of discrimination strategy utilizing entanglement probe state in comparison with unentangled single-qubit probes, for any nonzero rate of inconclusive outcomes. *Chapter 7* is based on publication [4]: Martina Miková, Michal Sedlák, Ivo Straka, Michal Mičuda, Mário Ziman, Miroslav Ježek, Miloslav Dušek, and Jaromír Fiurášek. *Optimal entanglement-assisted discrimination of quantum measurements.* Physical Review A **90**, 022317 (2014).

In *Chapter 8*, there is described the experimental demonstration of a procedure for faithful quantum state transfer between two weakly interacting qubits. The scheme enables a probabilistic yet perfect unidirectional transfer of an arbitrary unknown state of a source qubit onto a target qubit prepared initially in a known state. The transfer is achieved by a combination of a suitable measurement on the source qubit and a quantum filtering on the target qubit. The filtering depends on the outcome of the measurement on the source qubit, initial state of the target qubit, and qubits' mutual interaction. We experimentally verify feasibility and robustness of the transfer using a linear optical setup with qubits encoded into polarization states of single photons. However, the theoretical suggestion of the transfer itself is not restricted to a particular experimental platform. *Chapter 8* is based on publication [5]: Martina Miková, Ivo Straka, Michal Mičuda, Vojtěch Krčmarský, Miloslav Dušek, Miroslav Ježek, Jaromír Fiurášek, and Radim Filip. *Faithful conditional quantum state transfer between weakly coupled qubits.* Scientific Reports **6**, 32125 (2016).

Chapter 2

Contemporary state of research

Linear optics

In recent decades, quantum information processing has been a dynamically growing area. It seems that the **linear-optical platform** belongs to one of the most prominent platforms. It was shown by *Knill, Laflamme, and Milburn in 2001* [8] (which generalized the paper *Gottesman and Chuang in 1999* [9] and later extended by *Kok et al in 2007* [10]) that the linear optics platform is suitable for universal quantum computing. It is an experimentally accessible platform where proof-of-principle protocols' realizations are feasible directly with single photons, linear optical elements, and projective measurements. The essential linear-optical components are mainly beam splitters and phase shifters. Single photons are good carriers of quantum information [11]. A quantum bit (qubit) is the quantum analogy of a classical bit. While a classical bit can be in one of the two well defined states (0 and 1, it is a two level system), the quantum bit can be in an arbitrary linear superposition of these two states. These states are the basis states of two-dimensional Hilbert space. Photons do not interact easily with the environment. Nnon-linearity is required to manage the interaction between the photonics qubits. It is achieved by the means of the non-linearity of quantum measurement. The quantum measurement process collapses the qubit state into one of the basis states of the operator corresponding to the measurement. Unfortunately, quantum measurement has a probabilistic character. It is a random process and by performing a one-shot measurement we cannot obtain complete information.

The linear-optical implementations of quantum information protocols are mostly probabilistic, because of the probabilistic character of the quantum measurement. It means that the measurement and consequently the operation sometimes fails. This fundamental limitation restricts the maximal achievable success probability of the linear-optical implementations of quantum information protocols. It can be in many cases improved by application of a conditional operation applied via a feed-forward loop. *Knill in 2003* [12] demonstrated the increase of the success probability via the feed-forward mechanism on the example of a single-mode non-linear sign shift gate. He reached the bound of the success probability 1/2, compared to 1/4 without the feed-forward loop [8].

Nielsen and Chuang in 2000 generalized in their seminal paper [13] the concept of quantum computing [11], where a gate operation does not have to be determined

only by hardware but it can be determined by software. They proved that an n-qubit quantum register can perfectly encode at most 2^n different quantum operations. They show that it is impossible to build a deterministic universal quantum gate array. However, it is still feasible to realize approximate or probabilistic programmable quantum gates. They can be optimized for a given length of the program register, despite obtained restrictions for perfect universally-programmable quantum gates [6, 14–16]. A probabilistic programmable phase gate, proposed by *Vidal, Masanes, and Cirac in 2002* [6], was for the first time experimentally implemented by *Mičuda et al in 2008* [7]. Its linear-optical implementation utilizing single-qubit program register had the success probability 1/4. *Miková et al in 2012* [1] reached its quantum mechanical limit of 1/2 success probability in experimental implementation employing the feed-forward loop.

Feed-forward loop

Conditional application of an operation via the **feed-forward loop** plays a crucial role in quantum information experiments. Many experiments employing this feed-forward technique are proposed and some of them are realized using various physical platforms.

For the first time, the feed-forward loop concept appeared in *Björk et al in 1988* [17], almost 30 years ago. It was used for a non-classical state of a light generation with sub-Poissonian statistic [17–20]. Then the promising technique was generalized for quantum computation protocols.

A well-known protocol, in which a feed-forward loop can be implemented, is quantum state teleportation *Bennett et al in 1993* [21]. The feed-forward loop is here usually called the classical channel. Such quantum teleportation protocols are experimentally realized for example with continuous variables in an unconditional version [22], with nitrogen-vacancy centre electronic spins [23], or its full deterministic protocol is realized with a chip-based superconducting circuit [24], or with atomic ions $^{40}Ca^+$ [25] and $^{9}Ba^+$ [26] which allow a fully deterministic Bell-state measurement. The teleportation is also implemented over inter-atomic distances using liquid state nuclear magnetic resonance [27]. The teleportation protocol employing the feed-forward loop is also standardly implemented in discrete variables [28–30]. The feed-forward technique for efficient quantum computation with linear optics is described in [8]. It is generalized from papers [9, 31].

Other proposals of quantum communication protocols where the feed-forward loop plays a crucial role have been suggested [32–38]. A lot of experimental results are published which can not be reached without the feed-forward technique. Their implementations include discrete optical systems [39–45], hybrid system [46], and continuous variables optical systems [47–50]. More information about feed-forward control of light in continuous variables is provided in [51, 52].

Let us focus on discrete variables. A conditional unitary operation is applied via an electro-optical modulator. It is one of the most crucial parts of the feed-forward loop. The modulators are typically based on a linear electro-optical effect, known as Pockels effect, where the material birefringence is proportional to applied electric field [53]. Such bulk

high-voltage electro-optical modulators are used in free-space experiments. The maximal speed of the loop is restricted by the modulator capacity together with time-consuming electronic processing for increasing the signal voltage level. This is typical mainly for the bulk feed-forward loop implementations.

We compare the speed of the feed-forward loop implementations in optical systems in relevant papers. The papers usually refer to the optical delay line length which is necessary to be added into the optical system. The delay line ensures the proper timing of the Pockels cell conditional action and the presence of the photon in the cell. The time delay can slightly differ due to the individual experimental implementations. Hereinafter comparison is tentative not absolute. In general the implementations try to be as fast as possible, but there are some exceptions.

All the mentioned papers refer to feed-forward loop implementations employing a bulk modulator. Our implementation of the loop utilizes the integrated electro-optical phase modulator with significantly lower half-wave voltage [54–56]. It is included in a fibre-based setup which has specific experimental difficulties, for example interferometers low phase-stability. However, to the best of my knowledge, there is no such fibre-based implementation in the literature. Thus, just a bulk implementations are listed in the subsequent comparison of loop speeds.

Bulk feed-forward loop implementations utilize high voltage bulk Pockels cells usually made of $LiNbO_3$ (lithium niobate), KDP (potassium dideuterium phosphate), or RTP (rubidium titanyl phosphate). The half-wave voltage of such electro-optical modulators (U_π) is usually in the order of kilo-volts. The operating wavelengths are within range 700-810 nm and the FWHMs of used interference filters are within range 3-10 nm. Some of the papers specify the trigger detector of feed-forward action. They use single photon detector [57] from PerkinElmer where the generated electric pulse after the photon detection has amplitude of several volts. Subsequently, it has to be amplified to the kilo-volt level. Thus the minimal length of the optical delay line depends on the response time of the detector, rising time of the cell, and the response of the electronics amplifier. Another important parameter of the loop is repeatability, it means the maximal operating frequency. Unfortunately, this parameter is not frequently discussed in the papers. It mainly depends on the electronics and Pockels cell parameters.

The feed-forward loop described in *Giacomini et al in 2002* [30] seems to be the fastest bulk implementation. It utilize just an 8-m-long free-space delay line corresponding to a delay of 26,6 ns, U_π=1.4 kV. The loop utilized in *Pittman et al in 2002* [39] has a 20-m-long optical fibre delay line corresponding to 100 ns. However, the modulator's half-wave voltage is only U_π=115 V. *Brida et al in 2004* [40] employs a 50 m long optical fibre delay line from polarization maintaining fibre corresponding to a 248 ns delay, U_π=5.2 kV. The paper *Ursin et al in 2004* [29] reports on teleportation across the Danube. There is not stated any exact delay time because of the feed-forward loop. However, it mentions that the classical signal arrives 1.5 μs before the photon, U_π=3.7 kV. One can assume that this is the case when the nano-seconds do not play any significant role. The paper *Pittmam et al in 2005* [41] points out a similar loop like *in 2002* [39]. However, an optical fibre delay line is 30 m long corresponding to 150 ns. *Sciarrino et al in 2006* [42] utilize the same

piloting electronic circuit as [30] in the loop implementation. However, their delay line is 30 m long, it corresponds to 150 ns. *Prevedel et al in 2007* [43] reports in detail about the feed-forward loop implementation in a separate paper *Böhi et al in 2007* [58] and in his Thesis [59]. The utilized fibre optical delay line is 30 m (35 m) long, it corresponds to a 150 ns (175 ns) delay. They also find out experimentally the average duration of feed-forward step, it is 145±3 ns, U_π=6.3 kV. *Vallone et al in 2008* [44] utilizes a 35-m-long optical fibre delay line corresponding to a 175 ns delay, U_π=1 kV. *Ma et al in 2011* [60] employs a 100 m optical fibre delay line, corresponding to 0.5 μs. *Ma et al 2012* [28] utilizes the same feed-forward loop as *Ursin et al in 2004* [29]. However, [28] mentions the employment of a 100-m-long optical fibre delay line corresponding to 0.5 μs, U_π=3.7 kV. *Zhao et al in 2014* [45] entangles different-colour photons via a time-resolved measurement and the active feed-forward loop. The loop uses a high voltage [kV] modulator and a 150 m long optical fibre delay line corresponding to a 0.75 μs delay.

Interferometer's phase stability

The Mach-Zehnder interferometer [61, 62] is an essential experimental tool for many applications as well as for fundamental research [63]. Various active or passive techniques are developed to **stabilize the relative phase** between the interferometer's arms. Some bulk configurations of the interferometer are inherently stable as shown in [64]. There, the displaced Sagnac configuration of the Mach-Zehnder interferometer exhibits a phase drift below 3 deg per 1.5 hours without any active stabilization or heavy isolation. This Thesis is focused on single-photon level sequential phase-stabilization of fibre-based Mach-Zehnder interferometers. The interferometers are crucial for our feed-forward loop implementation. Their phase drifts are usually slightly smaller than 1 deg per second, even if they are well isolated from the environment. Thus the sequential active phase-stabilization loop usually operates at a lower frequency 2 Hz [1, 65–68].

Discrimination tasks

The qubit state is represented by a linear superposition of basis states. The basis states are mutually orthogonal and it is possible to unambiguously discriminate between them. One can be interested in a task of discrimination between two linearly dependent states with non-zero overlap. The impossibility of perfect **discrimination between two non-orthogonal quantum states** is one of the typical characteristics of quantum mechanics. Many cryptographic schemes [69] are based on this fact. This feature provides security of quantum key distribution protocols. Additionally, this fact prohibits cloning of quantum states [70]. However, it triggers the question what is the optimal discrimination strategy for discrimination between two non-orthogonal quantum states? A suitable state discrimination strategy could be used for example as a cryptographic attack [71].

The projective quantum measurement (Von Neumann measurement [72]) is usually not the optimal one, thus the generalized measurement positive-operator valued measure (POVM) has to be used. A lot of discrimination strategies have been studied in detail both theoretically and experimentally.

In general, there exist two fundamental discrimination strategies. Since the 70s, *Holevo* [73] and *Helstrom* [74,75] have studied the ambiguous quantum state discrimination, where they tried to reach the minimum-error probability. In the 80s, *Ivanovic* [76], *Dieks* [77], and *Peres* [78] started to study the unambiguous state discrimination which is error free but it allows inconclusive results. It is known as IDP scheme.

Later, generalized strategies have been studied that interpolate the two fundamental discrimination schemes. Such theoretical suggestions of discrimination strategies [71, 79–87] are followed by their experimental implementations [88–94]. You can see [95–98] for more overview information. Recently, the discrimination concepts have been extended to discrimination of quantum operations and devices [3,99–111] and measurements [112–115]. Although it has a lot of similarities with the quantum state discrimination, it admits intriguing novel strategies.

Another task is the **discrimination of optical devices** with respect to the minimal energy flux. It can lead to quantum reading of optical memories when one exploits the quantum properties of light. The problem of quantum reading of optical devices is discussed in [116–120]. For the first time, it was introduced by *Pirandola in 2011* [116]. He assumed that the memory cell may behave like a beam splitter with two possible reflectivities. There are applied two fundamental discrimination scenarios. As described above, one of them solves the problem of minimum energy ambiguous discrimination of optical devices [99, 121, 122]. The task is to minimize the error probability while one guesses the unknown optical device. The second scenario deals with unambiguous discrimination of optical devices [123]. It allows the inconclusive outcome while the error probability is zero. There are only a few experimental implementations of the quantum devices discrimination. The paper *Zhang et al in 2008* [109] reports on perfect discrimination between single-bit unitary operations using a sequential scheme and the paper *Laing et al in 2009* [110] shows the result of unambiguous quantum process discrimination employing entanglement.

Indistinguishability

It is impossible to determine a quantum state using a single measurement. However, there are some methods for estimation of the quantum state or its properties [124, 125]. One can be interested in parameters describing how two quantum states or two particles are similar or indistinguishable.

Direct measurements of the states' **overlap** and fidelity, without complete quantum-state reconstruction, are already suggested [126, 127]. Such measurements are performed for a two-photon case utilizing Hong-Ou-Mandel interferometry [128]. One can notice, that the states overlap is proportional to the amount of inconclusive results in the task of non-orthogonal states discrimination.

However, the coherence and indistinguishability of particles are crucial for many quantum protocols ans processes [129–136]. The overlap is defined only for factorable states. A lot of mentioned experiments use the photon pairs from the parametric down conversion and encode the information into their polarization or spatial degrees of freedom. But the

photons, qubit carriers, are entangled in frequencies. One has to admit that the photons are not in a factorable state. This is solved in [2]. There is introduced a measure of effective indistinguishability which can be applied to any joint state. There is shown that even if some noninformational degrees of freedom of two particles are entangled, the particles can still serve as good carriers of qubits.

Qubit-qubit interaction

In quantum communication and information theory [11, 137], the qubits are not related to any particular physical representation. And there is no known theoretical limitation which prohibits full swap of quantum states between various physical platforms by their mutual interaction. It is limited by the real-world imperfections.

Some physical systems are easier controlled than the others and some systems are more suitable for specific tasks. For instance, in quantum communication the photonic qubits serve as ideal carriers of quantum information [138]. While in quantum information the atomic and solid state or superconducting stationary qubits are utilized for local storage and processing of the information [139–142]. Thus, it is crucial to interconnect various physical platforms [143–153] into hybrid architectures [154–161], despite their imperfect real mutual qubit-qubit interaction.

In general, the qubits interact usually weakly. Alternatively, decoherence [133] affects the qubit-qubit strong interaction and the interaction time has to be limited. The resulting effect is a weak interaction. We would like to find out how to overcome **weak interaction** and its limitations. Or even better, we need to find out how to build quantum gates utilizing such weak interaction. This is crucial, because a potential of quantum communication and a information theory [11,137] and its full exploitation requires hybrid quantum information processing.

Weak coupling prevents the perfect implementation of a bidirectional swap of quantum states between two qubits, as shown in [162]. Nevertheless, the high-quality unidirectional quantum states transfer between two physical platforms is sufficient for many applications.

We propose and experimentally verify such unidirectional conditional quantum states transfer, which works with an arbitrary weak purity-preserving coupling between the qubits [5]. The approach combines a suitable projective measurement on the source qubit in an unknown quantum state with the optimal quantum filter [163] on the target qubit. The optimal quantum filtration also requires an exchange of classical information via the feed-forward loop [1, 23–25, 30, 43]. The protocol can be used also for transfer of parts of entangled states. In this way, a hybrid entangled state can be created, however, only in a probabilistic manner. It can be utilized in hybrid quantum communication networks [140].

Chapter 3

Methods and Tools

In this chapter, we give a brief overview of important components, concepts, and principles of experimental quantum information processing that are relevant to this Thesis.

First, the formalism of quantum optics is defined. Subsequently, the linear-optical components of bulk and fibre optics are introduced as well as other optical devices. Further, we describe the typical parts of the experiments such as: a Mach-Zehnder interferometer, a source of correlated photon pairs, a real-time feed-forward loop, electronics for signal processing, qubit state preparation etc. Then the procedures necessary for preparation and execution of experiments are described such as active phase stabilization of a fibre-based interferometer. Finally, the toolbox for experiments characterization is listed. If it is not trivial, we discuss the experimental difficulties of individual topics. We hope, that this chapter would be also useful for future lab students.

3.1 Relevant formalism of quantum optics

In this section, we briefly introduce important parts of quantum optics formalism relevant to this work. If one is more interested in this topics, please see [11, 164, 165].

3.1.1 Qubit

In classical physics and informatics, the elementary unit of information is a bit. The classical bit can exist in one of two well-defined states usually denoted as 0 or 1. However, in quantum physics and informatics, the elementary unit is a quantum bit (qubit). The qubit can exist in an arbitrary linear superposition of two states denoted as $|0\rangle$ and $|1\rangle$, here we use "bra-ket" notation developed by P. Dirac [164]. Mathematically, a qubit state is represented by a vector in two-dimensional Hilbert space in which the vectors $|0\rangle$ and $|1\rangle$ form a basis. The computational basis states $|0\rangle$ and $|1\rangle$ are typically chosen to be orthogonal, $\langle 1|0\rangle = 0$, and normalized, $\langle 0|0\rangle = \langle 1|1\rangle = 1$. General pure qubit state $|\psi\rangle$ is represented by an arbitrary linear superposition of basis states:

$$|\psi\rangle = \alpha|0\rangle + \beta|1\rangle, \tag{3.1}$$

where α and β are complex amplitudes. For normalized state they fulfil $\langle\psi|\psi\rangle = |\alpha|^2 + |\beta|^2 = 1$. A quantum measurement is probabilistic. The squares of the absolute values $|\alpha|^2, |\beta|^2$ determine the probability of finding the state $|\psi\rangle$ in one of its basis states $|0\rangle$,$|1\rangle$, respectively. When $P_i = |i\rangle\langle i|$ is a projection operator onto the basis states, $i = 0, 1$. Then the probability of measurement of the i-th result is given as $p_i = \langle i|P_i|i\rangle = \left|\langle i|\psi\rangle\right|^2$, $0 \leq p_i \leq 1$ and $\sum_i p_i = 1$. Any pure state of a qubit can be also represented as a point on the Bloch sphere. Then the state can be advantageously parametrized by two angles $\varphi,\ \theta$:

$$|\psi\rangle = \cos(\theta/2)\,|0\rangle + e^{i\varphi}\,\sin(\theta/2)\,|1\rangle, \tag{3.2}$$

where $\theta \in [0, \pi]$ and $\varphi \in [0, 2\pi]$. The angle θ determines the absolute value of the complex amplitude. The normalization condition is still fulfilled $\cos^2(\theta/2) + \sin^2(\theta/2) = 1$. The angle φ defines the resulting phase between basis states.

Just a pure state can be expressed as vector $|\psi\rangle$. When a quantum state composes of a statistical mixture of pure states or it is a sub-part of higher dimensional pure state it can be expressed only by a density matrix ρ. The density matrix for pure states is defined as:

$$\rho = |\psi\rangle\langle\psi|. \tag{3.3}$$

Note: In further text, we use shorter notation for the tensor product of two states $|1\rangle_1 \otimes |0\rangle_2 = |1\rangle_1|0\rangle_2 = |1, 0\rangle_{1,2}$, where the indices denote different modes.

3.1.2 Focks state representation

Here, we briefly introduce formalism of creation and annihilation operators and the bosonic commutation relations.

The creation operator $\hat{a}^\dagger$ increases the number of photons in the given mode by one, while the annihilation operator $\hat{a}$ decreases the number of photons in the given mode by one:

$$\begin{aligned} \hat{a}^\dagger|n\rangle &= \sqrt{n+1}|n+1\rangle, \\ \hat{a}|n\rangle &= \sqrt{n}|n-1\rangle, \end{aligned} \tag{3.4}$$

where n is the number of photons in a given mode. The state with $n = 0$ is called the vacuum state $|0\rangle$ and vacuum stability condition is given as $\hat{a}|0\rangle = 0$. When one applies both operators $\hat{a}^\dagger\hat{a}|n\rangle = n|n\rangle$, we obtain the number of photons in given mode. Operator $\hat{n} = \hat{a}^\dagger\hat{a}$ is called the photon number operator. Photon number states, Fock states, create the orthonormal basis $\langle n_i|m_j\rangle = \delta_{i,j}\delta_{n,m}$, where $\delta_{x,y}$ is the Kronecker delta[1].

Here we show the commutation relations in a bosonic system for the creation and annihilation operators. The general commutator is defined as $[A, B] = AB - BA$. It is equal to zero if and only if A and B commute, then $AB = BA$. When A and B represent two operations which commute, it does not depend which operation is applied as the first. The creation and annihilation operators in a bosonic system obey commutation relations:

$$\left[\hat{a}_i, \hat{a}_j^\dagger\right] = \delta_{i,j}, \qquad \left[\hat{a}_i, \hat{a}_j\right] = \left[\hat{a}_i^\dagger, \hat{a}_j^\dagger\right] = 0. \tag{3.5}$$

[1]Kronecker delta $\delta_{x,y} = 1$ if and only if $x = y$, for $x \neq y$ $\delta_{x,y} = 0$

3.1.3 Qubit encoding

In this Thesis, we employ photons as carriers of qubits. We encode the qubit into photon polarization degrees of freedom or spatial degrees of freedom.

Polarization encoding utilizes as basis states $|0\rangle, |1\rangle$ horizontal and vertical linear polarization states $|H\rangle, |V\rangle$, respectively. The basis state $|H\rangle$ is represented by the photon in horizontal linear polarization mode $|1,0\rangle_{H,V} = \hat{a}_H^\dagger |0,0\rangle_{H,V}$, analogically $|V\rangle = |0,1\rangle_{H,V} = \hat{a}_V^\dagger |0,0\rangle_{H,V}$. The states fulfil $\langle H|V\rangle = 0$.

While in spatial encoding[2], basis states are represented by a photon propagating through spatially separated paths. The basis state $|0\rangle$ is represented by a spatial state $|1,0\rangle_{1,2}$ where the photon is in the first path (mode 1), $\hat{a}_1^\dagger |0,0\rangle_{1,2}$, analogically $|1\rangle = |0,1\rangle_{1,2} = \hat{a}_2^\dagger |0,0\rangle_{1,2}$.

In this Thesis, we mainly work with the following six states, utilizing the polarization or spatial encoding:

$$\{|H\rangle, |V\rangle, |D\rangle, |A\rangle, |R\rangle, |L\rangle\}_{polarization\ \ enc.} \approx \{|0\rangle, |1\rangle, |+\rangle, |-\rangle, |+i\rangle, |-i\rangle\}_{spatial\ \ enc.}$$

as mentioned $|H\rangle, |V\rangle$ and $|0\rangle, |1\rangle$ are the basis state of polarization and spatial encoding, respectively. Then $|D\rangle$, $|A\rangle$ are diagonal and antidiagonal linear polarization states, defined as $|D\rangle = (|H\rangle + |V\rangle)/\sqrt{2}$, $|A\rangle = (|H\rangle - |V\rangle)/\sqrt{2}$. $|R\rangle$, $|L\rangle$ are right and left hand circular polarization states, defined as $|R\rangle = (|H\rangle + i|V\rangle)/\sqrt{2}$, $|L\rangle = (|H\rangle - i|V\rangle)/\sqrt{2}$. Analogically in spatial encoding the states $|\pm\rangle$, $|\pm i\rangle$ are defined as follow $|\pm\rangle = (|0\rangle \pm |1\rangle)/\sqrt{2}$, and $|\pm i\rangle = (|0\rangle \pm i|1\rangle)/\sqrt{2}$. For some experiments it is convenient to change the qubit encoding from spatial to polarization, $|0\rangle \approx |H\rangle$, $|1\rangle \approx |V\rangle$, or vice versa.

How to experimentally prepare such qubit states is shown further in the section *Qubit state preparation*.

3.2 Components used in the experiments

In this section and section 3.3, the optical components used in the presented experiments are briefly described.

3.2.1 Collimating lens (C)

Collimating lenses are used in all our experimental setups. They are used for outcoupling of the diverging light beam from the optical fibre and its subsequent collimation, as well as for the opposite task of coupling light beam into the optical fibre. Two such collimation lenses are part of an air gap which is described later. The lens parameters are: focus length f = 11.00 mm, numerical aperture NA = 0.25, anti-reflex coating for 600-1050 nm.

- 60FC-0-A11-02 (Schäfter+Kirchhoff) fibre collimator
- C220TME-B (Thorlabs) aspheric lens

[2] also known as which-way encoding, or path encoding

The first mentioned collimating lens has integrated holder for a fibre optic connector FC/PC or FC/UPC thus for a 0°-polished fibre. The holder also contains an adjustable mechanism for fine tuning of the distance between the lens and a ferrule of the optical fibre connector. The second mentioned lens was used mainly in the earlier experiments. It has to be mount into additional holders to tune the final distance. Their typical mounts are shown in Fig. 3.1(b,a), respectively.

3.2.2 Mirrors (M)

All mirrors used in the experiments are broadband dielectrics mirrors BB1-E03 (Thorlabs) for an angle of incidence 45°. These mirrors have the average reflectivity higher than 99% (750 – 1100 nm). Around 810 nm the reflectivity for S, P polarized and unpolarized light is better than 99.6%. The typical mounted mirrors are shown in Fig. 3.1(c, d).

3.2.3 Kinematic mounts and holders

Many optical components have to be mounted in some holders. Because of the alignment purposes, it is convenient to have this holders kinematic with an adjustable tip and tilt or rotatable. We use mechanical mounts from Thorlabs, Newport, Radiant Dyes or home-made. Some typical kinematic mounts are shown in Fig. 3.1.

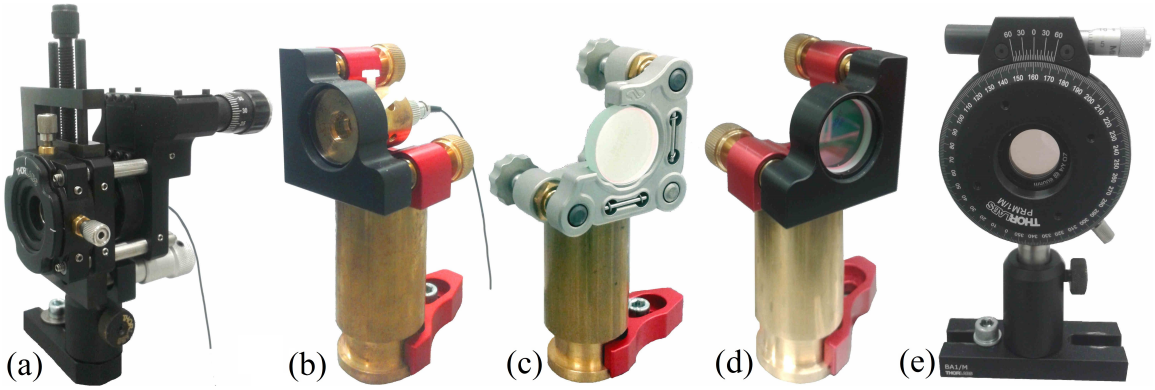

Figure 3.1: Typical kinematic mounts and holders of the collimating lenses, mirrors and wave plates. (a) lens and post from Thorlabs, kinematic mount from; (b) fibre collimator from Schäfter+Kirchhoff, kinematic mount from Radiant Dyes, and home-made post and collimator holder; (c, d) mirrors from Thorlabs and home-made posts, kinematic mount from Newport (c) and Radiant Dyes (d); (e) wave plate in mechanical rotation mount and post from Thorlabs.

3.2.4 Wave plates (HWP), (QWP)

A wave plate is a bulk optical component, which serves for manipulation with a polarization state of light. It is usually made of uniaxial birefringent optical material, for example crystalline quartz. The polarization state of incident light is decomposed into two orthogonal eigen-modes with different indices of refraction (two optical axes). The eigen-states are two orthogonal linearly polarized light waves. They are mutually phase retarded at the wave plate output. According to the phase retardation Γ we recognize two basic wave plates, a half-wave plate (HWP) and a quarter-wave plate (QWP). HWP has the phase

retardation of half-wave $\Gamma = \pi$ $[rad]$ and QWP has the phase retardation of quarter-wave $\Gamma = \pi/2$ $[rad]$. Each of these wave plates can be made as a zero-order or multi-order wave plate. For instance, the phase retardation of HWP is $\Gamma = \pi + n \cdot 2\pi$. When $n \neq 0$ it is the multi-order HWP and when $n = 0$ the resulting phase retardation is $\Gamma = \pi$, it is zero order HWP. The zero order wave plate is usually produced as combination of two mutually rotated multi-order wave plates. The zero-order wave plates are less spectrally sensitive.

At the wave plate output, the two waves propagating in its eigen-modes are put coherently together and create the resulting polarization states. This can be mathematically described with help of Jones calculus and matrix representation of optical devices [166,167]:

$$J_{\mathrm{OUT}} = R(\xi) \cdot W(\Gamma) \cdot R(-\xi) \cdot J_{\mathrm{IN}}. \tag{3.6}$$

J_{IN} and J_{OUT} denote the input and output Jones vectors describing the polarization states of light, respectively. $W(\Gamma)$ is the general wave plate with phase retardation Γ and $R(\xi)$ matrix describe rotation of coordinates by an angle ξ,

$$W(\Gamma) = \begin{pmatrix} 1 & 0 \\ 0 & e^{-i\Gamma} \end{pmatrix}, \qquad R(\xi) = \begin{pmatrix} \cos\xi & \sin\xi \\ -\sin\xi & \cos\xi \end{pmatrix}, \tag{3.7}$$

$$HWP = W(\pi) = \begin{pmatrix} 1 & 0 \\ 0 & -1 \end{pmatrix}, \qquad QWP = W(\pi/2) = \begin{pmatrix} 1 & 0 \\ 0 & -i \end{pmatrix}. \tag{3.8}$$

In further text, there is used notation HWP(ξ) which means $R(\xi) \cdot HWP \cdot R(\xi)$, similarly for QWP. We also say the wave plate is aligned to 0° (HWP(0°), QWP(0°)), when one of the its optical axes is identified with the horizontal linear polarization state. This state remains unchanged by the wave plate. The wave plate is typically mounted in a manually driven rotation mount, as shown in Fig. 3.1(e). Some wave plates are placed in computer controllable motorized mounts from Newport, because of the experiments automation.

3.2.5 Optical fibres

In our experiments, we use a single mode optical fibres for wavelength 810 nm. In the first experiments [1–3], there are used single mode fibres 780-HP from Nufern. Used patchcords and pigtails of optical components are also fabricated from the same fibre type, except integrated electro-optical fibre phase modulators. Its pigtails are made of polarization maintaining fibres (the resulting issues are mentioned in the further subsection *Integrated electro-optical phase modulator*).

The recent experiments [4, 5] combine the advantages of bulk and fibre setups. All used fibres are polarization maintaining fibres PM780-HP panda type from Nufern, as well as patchcords and pigtails of optical components.

The last type of used optical fibre is the polarizing optical fibre HB830Z(5/80) from Fibrecore Zing^{TM}. It has the bow-tie geometry. This fibre is employed as a fibre polarizer.

All the fibre optics patchcords and pigtails are terminated by FC/PC (Fibre Connector / Physical Contact) fibre connector with a key. The key is aligned to its slow optical axis. Two fibre connectors are connected together by a fibre optics adapter FC-FC.

3.2.6 Polarization controller (PC)

In bulk optics, birefringent phase retarders (wave plates) are used for changing polarization state of light. In all-fibre technology, fibre polarization controllers (PC) are used as the birefringent elements. The experiments [1–3], described in *Chapters 4–6* utilize the single mode fibre (780-HP). Three-paddle polarization controllers FPC030 from Thorlabs are employed for polarization state modification. They have a spool diameter approximately 2.7 cm.

The birefringence in the optical fibre is induced by mechanical stress. Each rotatable PC paddle contains a spool where the fibre is coiled. The incoming light is split into two stress-induced perpendicular modes – slow and fast optical axis of the fibre. They are named according to their higher and lower refractive index. The fast axis lies in the plane of the spool (paddle). The position of these two axes in relation to the incoming polarization state is adjustable by the rotation of the PC's paddle. For certain fibre and wavelength, the spool diameter is indirectly proportioned to the resulting phase retardation between the slow and fast axis [168]. The fibre is usually coiled to the three-paddle PC in order one, two and one loops[3]. In this way, a sequence of fibre phase retarders is created which roughly corresponds to QWP, HWP and QWP.

3.2.7 Automatic beam stop, flip (F)

A beam stop is a device which blocks the beam. The automatic beam stop, let us call it a flip, is under computer control and blocks or unblocks the beam on demand. In our experiments the flips are used for switching between two beams or for interrupting an interferometer arm, as described later. These operations are part of stabilization procedure and should be fast. Because of it, we need to switch as fast as possible between a passing beam and a blocked beam. Below we review three flip devices used in our lab during the time.

• Motorized filter flip mount MFF001/M (Thorlabs) with black aluminium foil instead of the filter, Fig. 3.2(a). This switch between two perpendicular positions. When the beam is aligned close to the edge, the flip time is significantly faster in one direction. The unblocking flip time is at least 0.1 s and the blocking flip time is more than 0.4 s.

• Home-made optical chopper disk mounted to a step motor. Its typical flip time is roughly 0.2 s. Unfortunately, the step motor temperature is too high and it heats the setup, Fig. 3.2(b).

These two types of flips are driven by TTL pulses 5 V high and they are in detail described in thesis [169]. These flips are employed in the earlier experiments. However, they are already overcame by a new home-made flip.

• Home-made optical flip using RC servo developed by M. Ježek. In detail, it is described in [170] and it is shown in Fig. 3.2(c). The RC servo is controlled by a pulse-width modulation (PWM) signal. Thus when the beam is aligned to the beam stop edge, it just moves around 5° and its flip time is shorter than 0.03 s.

[3]Sometimes one, two and three loops.

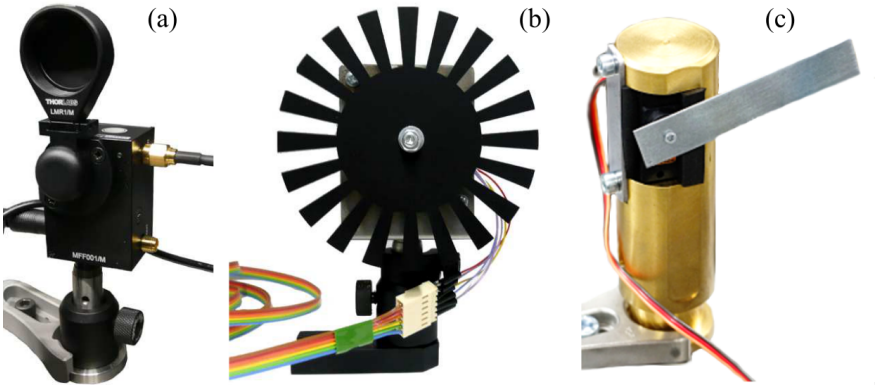

Figure 3.2: Automatic beam stops. (a) Motorized flip mount MFF001 from Thorlabs, (b) Home-made optical chopper disk mounted to a step motor, (c) Home-made flip using RC servo. Photos (a,b) are adopted from [169]. Photo (c) is adopted from [170] and modified.

3.2.8 Detectors

The optical signal, which has to be detected, is at near infra-red region of electro-magnetic spectra centred at 810 nm. We use two types of silicon detectors, which can be used in a region 350–1100 nm.

• PIN photo diodes [167] are used for alignment purposes. The PIN diode detects the strong optical signal produced by a unattenuated probe laser diode. In our laboratory, we use silicon amplified detectors with switchable gain PDA36A-EC or silicon biased detectors DET10A/M, DET36A, DET100A, etc. from Thorlabs. The signal from the detector 0–10 V is post-processed and displayed by an oscilloscope or by a computer via an analogue-to-digital converter (ADC).

• Single photon counting modules (SPCM) [57], later referred as single photon detectors, are used for detection of a weak signals. By the weak signal we mean a signal at a single photon level from the spontaneous parametric down conversion or the probe laser diode attenuated to a level which does not saturate these detectors.

The SPCM is based on a single photon avalanche diode (SPAD). It is high gain avalanche photo diode (APD) operating in Geiger mode. It means that its bias voltage is above the breakdown voltage. The incoming single photon triggers the avalanche of electrons which is big enough to be detected as an electronic pulse. The time duration from the photon incidence to the electronics pulse production is called the response time of the detector.

In our experiments, we employ the single photon detectors from Excelitas (formerly PerkinElmer) [171]. Their single-modules or the quad-modules are adapted to fibre connectors by FC fibre-optic receptacle and a fibre optical lens. Individual detectors differ from each other in parameters, for example: photon detection efficiency, dark count rate, maximum count rate, dead time, linearity, response time of the detector, and output electric pulse – its height, shape, and full width at half maximum (FWHM).

It is useful to choose detectors for the experiment carefully. Ideally, we would like to have detectors with the same detection efficiency. We measure their relative detection efficiencies η_i, where i is the number of the detector. Their average dark count rates are

dc_i per the same time unit. Then raw count rates N_i are normalized $(N_i - dc_i)/\eta_i$, using dark counts and efficiencies. In the case of coincidence rate $C_{i,j}$ between two detectors D_i & D_j the detectors dark counts play a negligible role and the normalization is given as $C_{i,j}/(\eta_i\eta_j)$. The detectors differ in their response times. For general applications it is not crucial and they are compensated by electronics delay lines or by coaxial cables. Although, the detector with the shortest response time is chosen for the feed-forward loop, because the response significantly influences the overall loop time. This has to be compensated by fibre optical delay lines inside the fibre-based interferometer. Each 5 ns adds roughly 1 m of the optical fibre.

The typical parameters of used detectors from PerkinElmer and Excelitas are: dark counts 150-1200 s^{-1}, total efficiencies about 50-70 %, response time 15-45 s.

3.2.9 Integrated electro-optical phase modulator (PM)

A phase modulator is an optical device which modulates the phase of the passing light beam. An electro-optical phase modulator (PM) is based on a linear electro-optical effect (Pockels effect) in optical crystals. We utilize transverse integrated electro-optical phase modulators from EOSPACE, made of lithium-niobate $LiNbO_3$ uniaxial crystal. Applied voltage proportionally changes only the index of refraction, not the directions of the optic axes, as described in [53, 172]. Each PM axis has a different index of refraction and different electro-optical coefficient. The overall crystal birefringence is given by the natural and electrically induced birefringence. The voltage applied to PM induces different phase shifts in each axis. Thus, working with general polarization states would be too complicated or impossible. However, by using only one PM axis, the change of refractive index results in phase changes of the output state of light, while its polarization state remains unchanged. This is the reason, why in all the experiments only the PM slow axis is used. The PM itself is pigtailed by polarization maintaining fibres. Thus a proper coupling of a light into fibre slow axis should correspond to correct coupling into PM slow axis. In the first generation of experiments, which do not use the polarization maintaining fibres, the additional linear polarizer is placed into the PM output port or the PM with integrated polarizer is used. The polarizer transmits only light which pass the slow axis and it is correctly phase shifted. In front of the PM, there is placed a fibre polarization controller (PC). Via the PC we maximize the intensity of transmitted light through the polarizer. It corresponds to proper coupling of light into the slow axis.

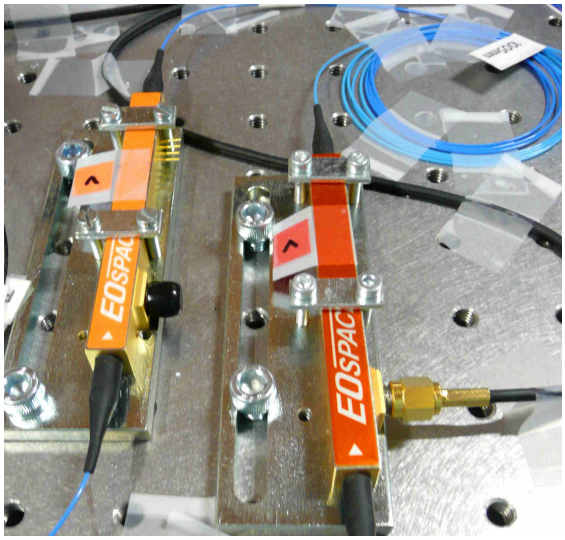

Figure 3.3: Photo of phase modulators.

The PM can be characterized by several typical parameters:

- Insertion losses IL [dB], typically 2 dB $\leq IL \leq$ 5 dB, $IL = 10 \cdot \log(P_{\text{IN}}/\max(P_{\text{OUT}}))$.
- Extinction ratio or polarization crosstalk E [dB], typically 18 dB $\leq E \leq$ 36 dB, $E = 10 \cdot \log(P_{\text{SLOW}}/P_{\text{FAST}})$ (for light correctly coupled into its slow optic axis).
- Operational wavelength $\lambda = 810$ nm.
- RF port termination – with termination (the fast PM) $R = 50\ \Omega$ or without termination $R = 1$ MΩ.
- Bandwidth B [Hz], typically $DC \leq B \leq 500$ MHz (for the fast PM $B < 30$ GHz).
- S21 [dB] - Electro-optical modulation response, frequency response.
- S11 [dB] - Electrical return loss.
- Maximal applicable voltage $U_{\max} = \pm 10$ V.
- Half-wave voltage U_π [V], specified for slow axis $U_\pi < 3$ V, typically U_π for slow optic axis $1.4 - 1.9$ V and for fast optic axis roughly 5.5 V.
- Maximal optical input power at operational wavelength $P_{\text{IN}} < 30$ mW.

The PM is placed in each arm of fibre-based interferometer. One PM serves for the interferometer active phase stabilization. The second one is a part of the feed-forward loop or it just serves as a passive component for dispersion compensation. The knowledge of the exact value of a half-wave voltage U_π is crucial for the mentioned applications. The application of the half-wave voltage U_π to PM changes the phase of its output light by half-wave, π rad, compare to the situation without applied voltage. In all our experiments, we use only the slow axis of the PMs. The U_π of slow axis is typically within the range $1.4 - 1.9$ V. With respect to the maximally applicable voltage ± 10 V, the dynamical range of the PM is approximately $\pm 6\pi$ rad. It corresponds to ± 3 interference fringes. For the wavelength of 810 nm, it is roughly ± 2.5 μm of optical path difference. However, we want to keep the applied voltage close to 0 V. To minimize the negative influence of possible inaccuracies of measured U_π and to protect the PM against heating, which may negatively influence the value of U_π. Thus during the stabilization routine dynamical range is maximally ± 1 interference fringe.

The exact value of the half-wave voltage U_π is crucial for our applications. It is better to measure it under our laboratory conditions and with the used light source, because the half-wave voltage depends on a wavelength, $U_\pi(\lambda)$.

Measurements of PM's half-wave voltage U_π: Here, we briefly describe two methods of half-wave voltage measurement: Method (A) is based on interference fringe scan [172]. Method (B) is based on a fact that phases shift of 2π applied between the interferometer's arms should not change the output intensity [173,174]. Both these methods are applicable with (a) a strong signal and PIN diodes or with (b) a weak signal and single photon detectors. However, some combinations are not suitable as discussed below. Both these variants employ an experimental setup, where the PM is inserted into the well balanced fibre-based Mach-Zehnder interferometer with good visibility and with high signal-to-noise ratio (SNR) of an output signal.

(a) the measurement using a **strong signal** requires the laser diode with a power detectable by a PIN diode. The signal from the PIN diode is displayed or stored by an oscilloscope or an analogue-to-digital converter (ADC) which is under computer control.

(b) the measurement using a **weak signal** requires the attenuated laser diode with a power which does not saturate a single photon detector. The electric signal from the detectors is processed by counting electronics and the count rate is stored.

The measurement of U_π should be as fast as possible. Because the phase inside interferometer drifts spontaneously[4].

(A) the measurement of U_π based on interference fringe scan: The goal is to obtain the interference pattern in dependence on the voltage applied to the PM. Thus, we need to drive the PM and observe the interferometer output. Both these action have to be synchronized and under control.

During the measurement, a bipolar triangle electric signal is applied to the PM. When it is not enabled by the signal generator, the PM is driven just by a positive triangle signal. Both with respect to the maximal applicable voltage. The electric signal is generated by a function generator or a digital-to-analogue converter (DAC) which is under computer control.

For subsequent data processing, we restrict to one edge of a driving signal, where the voltage is linearly increasing. The obtained interference patterns is fitted by sinusoidal function $a \cdot \sin(b \cdot U_{\text{app}} + c) + d$, where U_{app} denotes the applied voltage and a, b, c, d are the fit parameters. From parameter b we obtain the half-wave voltage as $U_\pi = \pi/b$.

There are several possibilities how to measure the interference fringe with a **(a) strong signal**. One of them is by employing DAC and ADC (data-logger controlled by computer), but the sampling frequency and all communication protocols take some time. We can repeat the measurement several times to decrease the uncertainty. However, the phase drift accumulated during the measurement time substantially influence our result as a systematic error. The measurement employing a function generator and an oscilloscope is the fastest solution, however, it is not the best for our purposes. We can measure the exact value of the U_π, in this way. Unfortunately, during the main experiment measurement all the procedures are implemented via the DAC,[5] not via the function generator. Obtained half-wave voltages by these two methods may slightly differ. Nevertheless, the measured U_π value with a strong signal is for us approximative, but useful for other usage.

The task of the interference fringe measurement with a help of the **(b) weak signal** is also a part of active stabilization procedure, described later. This measurement takes several seconds and a phase drift accumulated during the measurement significantly influences the resulting U_π. However, the measured fringe visibility is not significantly influenced.

[4]This fact is discussed mainly in following section *Stabilization of experimental setup*

[5]The stabilization procedure is implemented via the DAC and utilize weak signal. It is the reason, why we prefer the value of U_π measured via the DAC. Thus, under the same conditions.

(B) the measurement of U_π based on idea that phases shift of 2π between interferometer's arms remains the output intensity unchanged: This measurement is more robust with respect to a time phase drift. It consists of many short and independent measurements. However, the overall measurement time can reach a few hours. First, we define a measurement range, where the approximative value of the U_π is in the middle, and a step. Then two fast measurements are performed for applied voltage $+U$ and $-U$ and two intensities or count rates x_+ and x_- are obtained, respectively. This is repeated several hundred times, for each value of U from the range to accumulate enough data. When $U = U_\pi$ the difference between x_+ and x_- should be zero. However, we have to take into account phase fluctuations. We can say that the absolute value of the count rate difference $|x_+ - x_-|$ does not need to be zero for $U = U_\pi$, however, the difference should be minimal. This method is applicable for both signals **(a) strong** and **(b) weak**.

In general, we prefer measurement of the U_π using DAC and a weak signal from the single-photon source (Spontaneous parametric down conversion) because of their wavelength. Because the U_π measurement is performed in the same configuration as the main measurement.

3.3 Beam splitters

3.3.1 Beam splitter (BS) – polarization insensitive

A beam splitter is an optical device which splits an incoming light beam. We use only beam splitters 2x2, which have two input ports and two output ports. The light entering the beam splitter by one input port 1(2) is divided into two spatially separated parts, outcoming by ports 3 and 4 as shown in Fig. 3.4. The beam is transmitted by BS with transmissivity T and reflected with reflectivity R. Here $T, R \,\epsilon [0, 1]$ for lossless BS fulfil:

$$T + R = 1. \tag{3.9}$$

$T : R$ is called a splitting ratio of BS. T and R, the intensity variables, are directly experimentally measurable parameters. However, amplitude variables transmittance t and reflectance r are more convenient for calculations. Their absolute values read:

$$|t| = \sqrt{T}, \qquad |r| = \sqrt{R} \tag{3.10}$$

Figure 3.4: left – scheme of a beam splitter (BS) with clarified mode notation, 1,2 – input modes, 3,4,– output modes; right – Photo of a typical cube BS.

Let us consider the lossless BS, where t_x and r_x denote the amplitude transmittance and reflectance according to input ports, $x = 1, 2$. Their absolute values are $|r_1| = |r_2|$, $|t_1| = |t_2|$ thus the Eq. (3.9) is still fulfilled $|r_1|^2 + |t_1|^2 = |r_2|^2 + |t_2|^2 = 1$ and $r_1 t_1^* + r_2^* t_2 = 0$, where the asterisk denote complex conjugate value. Their phase shifts have to fulfil a condition $\arg(r_1) + \arg(r_2) - \arg(t_1) - \arg(t_2) = (1 - 2k)\pi$, where $k = 0, 1, ...$ It is deduced from conservation law of energy [130, 175]. Without loss of generality, we can restrict the BS parameters to $t_1 = t_2 = t$ and $r_1 = r \wedge r_2 = -r$ or $r_1 = r_2 = ir$.

The quantum mechanical description of BS utilizes the formalism of creation operators, $a^\dagger$, in the Heisenberg picture. The BS transforms the modes in a following way [165, 176]:

$$\begin{aligned} a_1^\dagger &= r a_3^\dagger + t a_4^\dagger, & a_3^\dagger &= r a_1^\dagger + t a_2^\dagger, \\ a_2^\dagger &= t a_3^\dagger - r a_4^\dagger, & a_4^\dagger &= t a_1^\dagger - r a_2^\dagger. \end{aligned} \tag{3.11}$$

The BS transformation (3.11) can be also written using matrix formalism:

$$\begin{pmatrix} a_1^\dagger \\ a_2^\dagger \end{pmatrix} = \begin{pmatrix} t & r \\ -r & t \end{pmatrix} \begin{pmatrix} a_4^\dagger \\ a_3^\dagger \end{pmatrix}, \qquad \begin{pmatrix} a_3^\dagger \\ a_4^\dagger \end{pmatrix} = \begin{pmatrix} r & t \\ t & -r \end{pmatrix} \begin{pmatrix} a_1^\dagger \\ a_2^\dagger \end{pmatrix}. \tag{3.12}$$

In further text, we investigate the single photon and two photons behaviour at the BS.

A **single photon enters the BS** by port 1, the output state is given as:[6]

$$|\psi\rangle_{\text{IN}} = |1,0\rangle_{1,2} = a_1^\dagger |0,0\rangle_{1,2} \xrightarrow{\text{BS Eq.(3.11)}} (r a_3^\dagger + t a_4^\dagger)|0,0\rangle_{3,4} = r|1,0\rangle_{3,4} + t|0,1\rangle_{3,4} = |\psi\rangle_{\text{OUT}}. \tag{3.13}$$

The result is superposition of photons being in outputs port 3 and 4. *Note: We can see, that by replacing* $|1,0\rangle_{3,4}$ *and* $|0,1\rangle_{3,4}$ *for logical quantum states*[7] $|0\rangle$ *and* $|1\rangle$*, respectively, the quantum mechanical states* $|\psi\rangle = \alpha|0\rangle + \beta|1\rangle$ *in spatial encoding (which way encoding) can be easily prepared.*

Two photons enter the BS each of them by own port, the output state is given:

$$\begin{aligned} |\psi\rangle_{\text{IN}} = |1,1\rangle_{1,2} = a_1^\dagger a_2^\dagger |0,0\rangle_{1,2} \xrightarrow{\text{BS Eq.(3.11)}} (r a_3^\dagger + t a_4^\dagger)(t a_3^\dagger - r a_4^\dagger)|0,0\rangle_{3,4} = \\ = (rt a_3^\dagger a_3^\dagger - rt a_4^\dagger a_4^\dagger + T a_4^\dagger a_3^\dagger - R a_3^\dagger a_4^\dagger)|0,0\rangle_{3,4} = \\ = \sqrt{2} rt |2,0\rangle_{3,4} - \sqrt{2} rt |0,2\rangle_{3,4} + T|1,1\rangle_{3,4} - R|1,1\rangle_{3,4} = |\psi\rangle_{\text{OUT}}. \end{aligned} \tag{3.14}$$

The resulting state consists of four contributions, it is also graphically shown in Fig. 3.5.

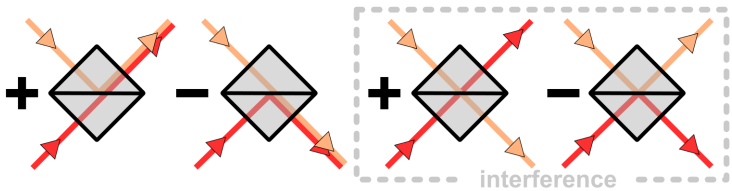

Figure 3.5: The Hong-Ou-Mandel effect.

[6] Here we would like to remind the notation: $|1\rangle_1 \otimes |0\rangle_2 = |1\rangle_1 |0\rangle_2 = |1,0\rangle_{1,2}$.

[7] Here 0 and 1 denote the logical states, not the photon numbers.

When one of the photons is reflected and the second one transmitted or vice versa it gives both photons in one output port $|2,0\rangle_{3,4}$ and $|0,2\rangle_{3,4}$.

When both photons are transmitted or reflected it gives one photon at each output port $|1,1\rangle_{3,4}$. However, these two contributions have a different sign. For indistinguishable photons, it means an incident at the balance beam splitter (R=T). Then these two contributions are subtracted to each other and completely disappear. Or let us say, these two cases destructively interfere, as shown in Fig. 3.5. It is known as the Hong-Ou-Mandel effect [129]. When two indistinguishable photons enter a balanced beam splitter ($r = t = 1/\sqrt{2}$) each of them by own input port and interfere, the resulting output state is known as the two-photon NOON state:

$$|\psi\rangle_{\mathrm{NOON}} = (|2,0\rangle_{3,4} - |0,2\rangle_{3,4})/\sqrt{2}. \tag{3.15}$$

Let us go back to the contribution given by a single photon in each output port $|1,1\rangle_{3,4}$. Such contributions are crucial for our applications. In our experiments, we detect photons by single photon detectors. The detectors are not photon number resolving. Thus the detector placed for instance in mode 3 gives a single click regardless if there is the state $|1\rangle_3$ or $|2\rangle_3$ (the efficiency of a detector is not discussed here). Therefore, we use the coincidence measurement. It means the final click is given if and only if the detectors in modes 3 and 4 click simultaneously.

The resulting output state of Eq. (3.14) contributing to the coincidence rate is:

$$|\psi\rangle_{\mathrm{OUT}} = (T - R)|1,1\rangle_{3,4}. \tag{3.16}$$

Thus, when the two totally indistinguishable photons interfere at the balanced BS ($r = t = 1/\sqrt{2}$) the output coincidence rate is equal to zero, $|\psi\rangle_{\mathrm{OUT}} = 0$.

However we should ask, what happens when the **photons are distinguishable**. Further we discuss two cases. The first case (a) describes what happens when the two photons do not interact together at the BS because one photon enters earlier then the second one. The second case (b) describes what happens when the two photons enter to BS at the same time, however, their polarization states are orthogonal.

(a) The first case describes, what happens when the time delay Δt between the photons incoming the BS is bigger than their coherence time. The photons do not interfere and behave as classical distinguishable particles. Via a newly obtained mode, a temporal degree of freedom, we can recognize the photons from each other. Let us call the modes F and S, according to the First and the Second (or Fast and Slow), respectively. Then we can modify Eq. (3.14) to:

$$\begin{aligned}
|\psi\rangle_{\mathrm{IN}} = |1\rangle_{1F}|0\rangle_{1S}|0\rangle_{2F}|1\rangle_{1S} = a^\dagger_{1F}a^\dagger_{2S}|0,0,0,0\rangle_{1F,1S,2F,2S} \xrightarrow{\text{BS Eq.(3.11)}} \\
\xrightarrow{\text{BS Eq.(3.11)}} (ra^\dagger_{3F} + ta^\dagger_{4F})(ta^\dagger_{3S} - ra^\dagger_{4S})|0,0,0,0\rangle_{3F,3S,4F,4S} = \\
= (rta^\dagger_{3F}a^\dagger_{3S} - rta^\dagger_{4F}a^\dagger_{4S} + Ta^\dagger_{4F}a^\dagger_{3S} - Ra^\dagger_{3F}a^\dagger_{4S})|0,0,0,0\rangle_{3F,3S,4F,4S} = \\
= rt|1,1,0,0\rangle - rt|0,0,1,1\rangle + T|0,1,1,0\rangle - R|1,0,0,1\rangle = |\psi\rangle_{\mathrm{OUT}}.
\end{aligned} \tag{3.17}$$

When we restrict the output state to coincidence rate contributions[8] then it reads:

$$|\psi\rangle_{\mathrm{OUT}} = T|0,1,1,0\rangle_{3F,3S,4F,4S} - R|1,0,0,1\rangle_{3F,3S,4F,4S}. \tag{3.18}$$

As visible, the interference does not occur. Even for $R = T$ the two terms do not cancel each other.

We have discussed just two extremal cases of a perfectly indistinguishable and a totally distinguishable particle. In general, we can change the time delay Δt between the photons from 0 till they are completely distinguishable. The observed coincidence rate increases from its minimum, given by Eq. (3.16) for indistinguishable photons, to the maximum, given by Eq. (3.18) for distinguishable photons. This is called the **Hong-Ou-Mandel (HOM) dip**, it was for a first time experimentally measured in *1987* [129]. The HOM dip measurement is shown in Fig. 3.6.

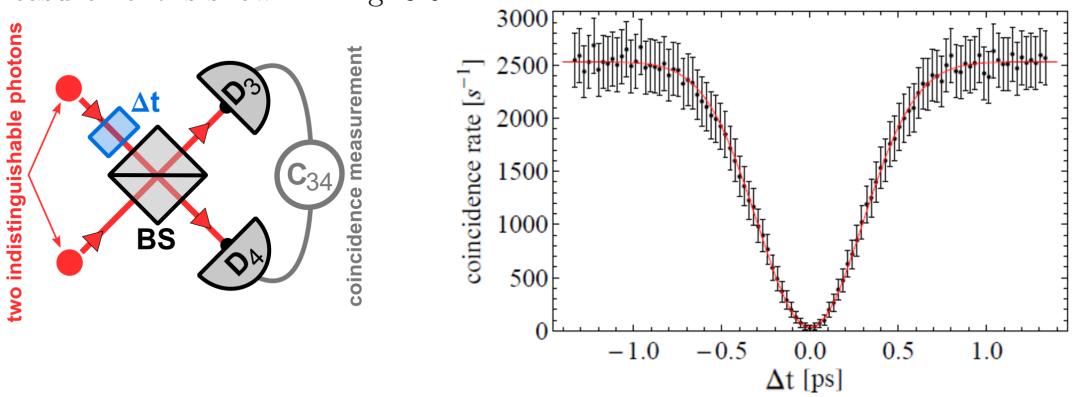

Figure 3.6: left – scheme of HOM dip measurement, D – single photon detector, BS – beam splitter, Δt – time delay, C – coincidence measurement; right – measured HOM dip for filter with FWHM=2 nm, measured data is adopted from [177]

We use the HOM dip as an effective tool: to align the optical path lengths, to measure the photons indistinguishability, or to measure how much the photons become distinguishable by passing through the experiment. HOM dip is characterize by its visibility V (the visibility is in detail described in *Section Mach-Zehnder interferometer* also in relation to experimentally measured values),

$$V = \frac{M - m}{M + m}. \tag{3.19}$$

m denotes HOM dip minimum given as ${}_{\mathrm{OUT}}\langle\psi|\psi\rangle_{\mathrm{OUT}}$ from Eq. (3.16). Thus, the two photons are perfectly indistinguishable and do not interfere at the BS. The coincidence count rate is obtained for $\Delta t = 0$. It corresponds to measurement "in the dip". M denotes HOM dip maximum given as ${}_{\mathrm{OUT}}\langle\psi|\psi\rangle_{\mathrm{OUT}}$ from Eq. (3.18). Thus, the two photons are completely distinguishable and do not interfere at the BS. The coincidence count rate is obtained for $\Delta t \gg$ photons coherence time. It corresponds to measurement "out of the dip". However, the reachable values of m and M depend on the BS parameters:

$$\begin{aligned} m &= (T - R)^2 = (2R - 1)^2, \\ M &= T^2 + R^2 = 2R^2 - 2R + 1. \end{aligned} \tag{3.20}$$

[8] The case when one photon is in mode 3 and one photon in mode 4.

The best minimum of HOM dip, $m = 0$, can be reached with a balanced beam splitter. Then the dip visibility is maximal, $V = 1$.

To visualize, how the maximal reachable visibility depends on the BS splitting ratio, one can express the visibility as a function of R by substituting from the Eq. (3.20) to Eq. (3.19):

$$V = \frac{R(1-R)}{1-3R(1-R)}, \tag{3.21}$$

the result is plotted on the left part of Fig. 3.7.

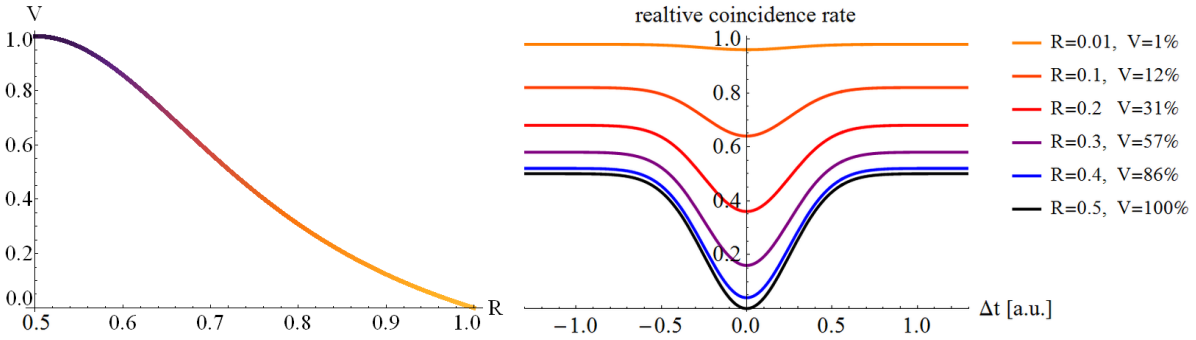

Figure 3.7: left – dependence of the HOM dip visibility V on the BS splitting ratio R; right – several examples of HOM dips for different splitting ratios of BS and Gaussian shaped spectral profile of interfering photons.

The dip shape is related to a frequency spectrum of the interfering single photons [129]. The HOM dip shown in the right part of Fig. 3.7 has a Gaussian shape, because the frequency spectrum of the photons is also Gaussian. When the frequency spectrum of the photons has a squared shape spectral profile, the HOM dip shape is given as $1 - \mathrm{sinc}(\Delta t)$, [2,178], as shown in Fig. 3.8. However, the single photon source used in our experiments employs a band-pass interference filter, its spectral profile shape is given by a convolution of Gaussian shape and square shape.

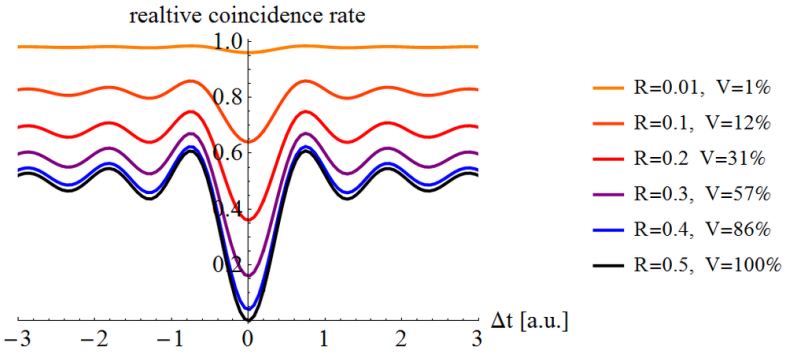

Figure 3.8: Several examples of HOM dips for different splitting ratios of BS and square shaped spectral profile of interfering photons. The dip shape is given as $1 - \mathrm{sinc}(\Delta t)$.

(b) The second case describes what happens when the two photons enter the BS at the same time $\Delta t = 0$, however, their polarization states are orthogonal. Let us denote the polarization degrees of freedom H and V according to horizontal and vertical linear polarization states, respective. We use a shorter notation:

$$a^\dagger_{1H}|0,0\rangle_{1H,1V} = |1,0\rangle_{1H,1V} = |H\rangle_1, \qquad a^\dagger_{1V}|0,0\rangle_{1H,1V} = |0,1\rangle_{1H,1V} = |V\rangle_1. \tag{3.22}$$

We assume $R_H = R_V = R, T_H = T_V = T$. Then we can modify Eq.(3.14) in following way:

$$\begin{aligned}|\psi\rangle_{\text{IN}} = |H,V\rangle_{1,2} = a^\dagger_{1H}a^\dagger_{2V}|0,0\rangle_{1,2} \xrightarrow{\text{BS Eq.(3.11)}} (ra^\dagger_{3H} + ta^\dagger_{4H})(ta^\dagger_{3V} - ra^\dagger_{4V})|0,0\rangle_{3,4} = \\ = (rta^\dagger_{3H}a^\dagger_{3V} - rta^\dagger_{4H}a^\dagger_{4V} + Ta^\dagger_{3H}a^\dagger_{4V} - Ra^\dagger_{4H}a^\dagger_{3V})|0,0\rangle_{3,4} = \\ = rt|H,V\rangle_{3,3} - rt|H,V\rangle_{4,4} + T|H,V\rangle_{3,4} - R|V,H\rangle_{3,4} = |\psi\rangle_{\text{OUT}}.\end{aligned} \tag{3.23}$$

The part of the resulting state contributing to coincidence rate reads:

$$|\psi\rangle_{\text{OUT}} = T|H,V\rangle_{3,4} - R|V,H\rangle_{3,4}. \tag{3.24}$$

The post-selected maximally entangled Bell state $|\Psi^-\rangle = (|H,V\rangle_{3,4} - |V,H\rangle_{3,4})/\sqrt{2}$ can be prepared in this way, by using the balanced BS ($R = T = 1/2$)[9] . The experimental implementation of the post-selected maximally entangled Bell state $|\Psi^-\rangle$ is shown in *Chapter 7, Optimal entanglement-assisted discrimination of quantum measurements.*

3.3.2 Fibre beam splitters (FBS) with fixed splitting ratio

A fibre base analogy of the bulk BS is called a fibre beam splitter 2x2 (FBS) or a fibre coupler 2x2 (FC). It is schematically depicted in Fig. 3.9. Earlier, we use polarization insensitive FBSs, fused or chip-based, made of single-mode optical fibres (780-HP) [179]. Their coupling ratio $R:T$ depends on the coupling length L and the coupling coefficient C of the two optical fibres. C depends on indices of refraction of used fibres, wavelength of the light source, the distance of the fibre cores, and other technical parameters. The power at its outputs P_{out} are given as:

$$\begin{aligned}P_{\text{out3}} &= P_{\text{in1}} \cdot \cos^2(CL), \\ P_{\text{out4}} &= P_{\text{in1}} \cdot \sin^2(CL),\end{aligned} \tag{3.25}$$

where, $R = \cos^2(CL)$, $T = \sin^2(CL)$, and R, T are reflectivity and transmissivity of the FBS, respectively.

Figure 3.9: left – general scheme of fibre beam splitter (FBS), 1,2 – input ports, 3,4,– output ports. right – photo of the typical FBS [adopted from Thorlabs.com].

There is one important difference compared to the cube BS. The polarization state of light coupled into a FBS changes during the propagation through optical fibre. When the FBS is used just for splitting one optical part into two, we do not have to take care about the polarization state. However, an interference of FBS input signals is required, we need to set a polarization mode overlap at the FBS. Hence a polarization controller (PC) has to be placed at least in one input port. However, it is not so practical to use just one

[9]The state $|\psi\rangle_{\text{OUT}}$ is not normalized hence for $R = T = 1/2$ the $|\psi\rangle_{\text{OUT}} = (|H,V\rangle_{3,4} - |V,H\rangle_{3,4})/2$.

PC to adjust the maximal polarization overlap according to interference fringe visibility. Because of practical reasons, we placed PC in each input port and polarizers at the FBS outputs. The PCs are used for step-by-step maximizing of detected light intensity behind the polarizer. The polarizer selects just one polarization mode, where lights interfere. In this way, the polarization overlap at the FBS is automatically provided.

Such troubles with polarization mode overlap can be overcame by using FBS made of single mode polarization maintaining optical fibres (PM780-HP), by chip-based technology. When the light is propagated just in one optical axis, the polarization mode overlap is automatically provided. In general, the splitting ratio for slow and fast axis is different. Because of the used spectral width of light, the light becomes incoherent after passing several tens of centimetres in slow and fast axis. It is called polarization mode dispersion. Such components made of polarization maintaining fibre work properly, when light is coupled just into one of its axis, typically a slow one. In our experiments, we employ FBSs from Sifam, Gooch & Housego, OZoptics, SQS, Lightel Technologie, and Optokon companies.

3.3.3 Variable ratio couplers (VRC)

The variable ratio coupler (VRC) is fibre beam splitters with a settable splitting ratio. A splitting ratio is tunable from 0:100 to 100:0 and vice versa. In our laboratory, we use VRCs from Evanescent Optics (formerly Canadian Instrumentation and Research), in both fibre variants[10]. The VRC splitting ratio can be tuned mechanically by a micrometer screw or a piezo controller for some models. Unfortunately, during the time it stopped working properly. Hence, a required splitting ratio is set manually. VRC exhibits hysteresis behaviour during tuning the splitting ratio by the screw. Thus one screw position set in clockwise or counter-clockwise direction does not correspond to the same splitting ratio, as shown in a left part of Fig. 3.10.

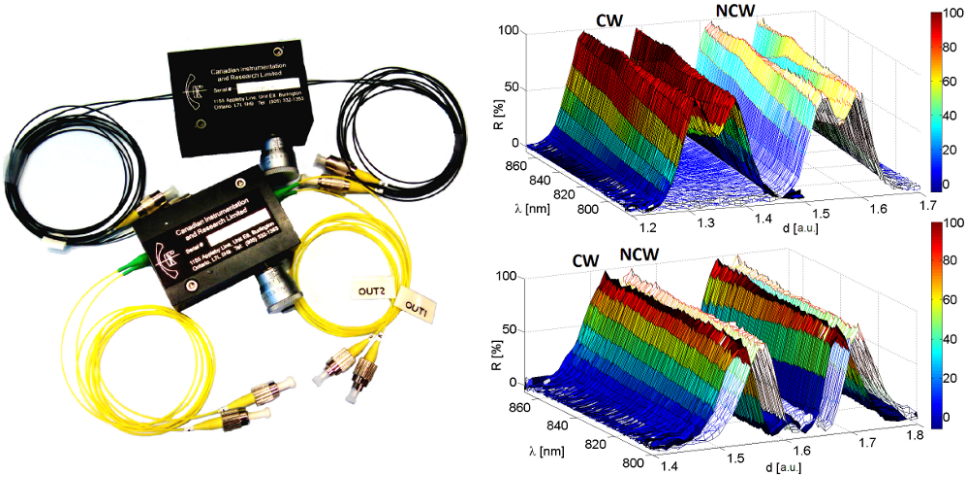

Figure 3.10: left – photo of variable ratio couplers (VRC). right – typical dependence of VRC reflectivity R on screw position d exhibits the typical "M" shaped dependence. However, the dependence on wavelength λ is linear [180]. The two plots in one graph are given by hysteresis. The screw was turned clockwise (CW) and counter-clockwise(NCW).

[10]polarization maintaining fibre (PM780-HP) and single mode fibre (780-HP)

3.3.4 Measurement of BS splitting ratio $R:T$

For many applications, it is preferable a splitting ratio $R:T$ as close as possible to 50:50. Let us denote FBS ports according to the Fig. 3.11, input ports are no. 1, 2 and output ports are no. 3, 4. η_x is efficiency or transmittance of the corresponding port $x = 1, 2, 3, 4$. A power of an input signal coming through the input port 1, 2 is P_A, P_B, respectively. The output powers P_{A3}, P_{A4}, P_{B3}, P_{B4} (labelled according to the input signal and the output port) are given by relations:

$$\begin{aligned} P_{A3} &= P_A \cdot \eta_1 \cdot R \cdot \eta_3 \\ P_{A4} &= P_A \cdot \eta_1 \cdot T \cdot \eta_4 \\ P_{B3} &= P_B \cdot \eta_2 \cdot T \cdot \eta_3 \\ P_{B4} &= P_B \cdot \eta_2 \cdot R \cdot \eta_4. \end{aligned} \tag{3.26}$$

We cannot calculate a correct splitting ratio of the FBS by measuring output powers just for one input port. Indeed, the result is influenced by the path transparencies η_3 and η_4:

$$\frac{T}{R} \not\equiv \frac{P_{B3}}{P_{B4}} = \frac{T \cdot \eta_3}{R \cdot \eta_4}. \tag{3.27}$$

We can calculate the correct splitting ratio, which is not influenced by port transparencies, when we employ all output powers, [181]:

$$X = \frac{P_{A4} \cdot P_{B3}}{P_{A3} \cdot P_{B4}} = \frac{T^2}{R^2} = \frac{(1-R)^2}{R^2}. \tag{3.28}$$

Then we solve a quadratic equation for R. Only the result with the minus sign has physical significance, because $0 \leq R \leq 1$:

$$(1-X) \cdot R^2 + 2 \cdot R + 1 = 0 \qquad \longrightarrow \qquad R_{1,2} = \frac{1 \pm \sqrt{X}}{1-X}. \tag{3.29}$$

Figure 3.11: Measurement of fibre beam splitter splitting ratio $R:T$, 1,2 – input ports, 3,4,– output ports, η – efficiency / transparency of the port.

3.3.5 Polarization sensitive beam splitters

In the previous section, we have described the polarization insensitive beam splitters. In further text, we describe a general polarization sensitive beam splitter which has a different splitting ratio for horizontally (H) and vertically (V) linearly polarized light[11]. Thus, we assume $T_H \neq T_V$. We extend the Eq. (3.11) by polarization degrees of freedom H and V.

[11] H (V) polarized light corresponds to p-polarization (s-polarization). Notation p and s is related to the plane of incidence. p denotes the electric field component parallel to the plane, while s denotes the perpendicular one. Notation s is derived from German word senkrecht.

Polarizing beam splitter (PBS)

The polarizing beam splitter (PBS) is a well known special type of a general polarization sensitive beam splitter. The ideal PBS usually fully transmits the H polarized light, while fully reflects the V polarized light. We use the same mode notation as in Fig. 3.4. Parameters of the ideal PBS are $t_{1H} = t_{2H} = 1$, $t_{1V} = t_{2V} = r_{1H} = r_{2H} = 0$ and $r_{1V} = 1, r_{2V} = -1$, and the description using creation operators reads:

$$\begin{aligned} a_{1H}^\dagger &= a_{4H}^\dagger, \\ a_{1V}^\dagger &= a_{3V}^\dagger, \\ a_{2H}^\dagger &= a_{3H}^\dagger, \\ a_{2V}^\dagger &= -a_{4V}^\dagger. \end{aligned} \tag{3.30}$$

In our experiments, PBSs are mainly employed for a polarization state analysis to split the perpendicular polarization modes. They are also used as horizontal linear polarizers for transmitted light.

Partially polarizing beam splitter (PPBS)

The partially polarizing beam splitter (PPBS) is another well known special type of general polarization sensitive beam splitter. The ideal PPBS usually behaves like PBS for H polarized light and like general BS for V polarized light. Thus H polarized light is fully transmitted $T_H = 1$ and V polarized light is split in a ratio $R_V : T_V$. We use the same mode notation as in Fig. 3.4. Parameters of ideal PPBS are $t_{1H} = t_{2H} = 1$, $r_{1H} = r_{2H} = 0$, $t_{1V} = t_{2V}$ and $r_{1V} = -r_{2V}$. The description using creation operators reads:

$$\begin{aligned} a_{1H}^\dagger &= a_{4H}^\dagger, \\ a_{1V}^\dagger &= r_V a_{3V}^\dagger + t_V a_{4V}^\dagger, \\ a_{2H}^\dagger &= a_{3H}^\dagger, \\ a_{2V}^\dagger &= t_V a_{3V}^\dagger - r_V a_{4V}^\dagger. \end{aligned} \tag{3.31}$$

General polarization sensitive beam splitter

The general polarization sensitive beam splitter has $T_H \neq T_V$, $0 < T_x < 1$ and $T_x + R_x = 1$, where $x = H, V$. We can extend the Eq. (3.11), describing the BS, by polarization degrees of freedom H and V:

$$\begin{aligned} a_{1H}^\dagger &= r_H a_{3H}^\dagger + t_H a_{4H}^\dagger, & a_{4H}^\dagger &= t_H a_{1H}^\dagger - r_H a_{2H}^\dagger, \\ a_{1V}^\dagger &= r_V a_{3V}^\dagger + t_V a_{4V}^\dagger, & a_{4V}^\dagger &= t_V a_{1V}^\dagger - r_V a_{2V}^\dagger, \\ a_{2H}^\dagger &= t_H a_{3H}^\dagger - r_H a_{4H}^\dagger, & a_{3H}^\dagger &= r_H a_{1H}^\dagger + t_H a_{2H}^\dagger, \\ a_{2V}^\dagger &= t_V a_{3V}^\dagger - r_V a_{4V}^\dagger, & a_{3V}^\dagger &= r_V a_{1V}^\dagger + t_V a_{2V}^\dagger. \end{aligned} \tag{3.32}$$

It can be also express using matrix formalism:

$$\begin{pmatrix} a_{1H}^\dagger \\ a_{1V}^\dagger \\ a_{2H}^\dagger \\ a_{2V}^\dagger \end{pmatrix} = \begin{pmatrix} t_H & 0 & r_H & 0 \\ 0 & t_V & 0 & r_V \\ -r_H & 0 & t_H & 0 \\ 0 & -r_V & 0 & t_V \end{pmatrix} \begin{pmatrix} a_{4H}^\dagger \\ a_{4V}^\dagger \\ a_{3H}^\dagger \\ a_{3V}^\dagger \end{pmatrix}, \quad \begin{pmatrix} a_{4H}^\dagger \\ a_{4V}^\dagger \\ a_{3H}^\dagger \\ a_{3V}^\dagger, \end{pmatrix} = \begin{pmatrix} t_H & 0 & -r_H & 0 \\ 0 & t_V & 0 & -r_V \\ r_H & 0 & t_H & 0 \\ 0 & r_V & 0 & t_V \end{pmatrix} \begin{pmatrix} a_{1H}^\dagger \\ a_{1V}^\dagger \\ a_{2H}^\dagger \\ a_{2V}^\dagger \end{pmatrix}. \tag{3.33}$$

Here, we consider the case, when two photons enter the polarization sensitive beam splitter, each of them by own input port. We assume that the photons are distinguishable only in their polarization degrees of freedom. Photons normalized polarization states are: $|\psi\rangle_1 = \alpha|H\rangle_1 + \beta|V\rangle_1$ and $|\varphi\rangle_2 = \gamma|H\rangle_2 + \delta|V\rangle_2$, where $|\alpha|^2 + |\beta|^2 = |\gamma|^2 + |\delta|^2 = 1$. The overall input state reads:

$$|\psi\rangle_{\mathrm{IN}} = |\psi\rangle_1 \otimes |\varphi\rangle_2 = \alpha\gamma|H,H\rangle_{1,2} + \alpha\delta|H,V\rangle_{1,2} + \beta\gamma|V,H\rangle_{1,2} + \beta\delta|V,V\rangle_{1,2} \tag{3.34}$$

The state transformed by the polarization sensitive beam splitter reads:

$$\begin{aligned}|\psi\rangle_{\mathrm{OUT}} = \alpha\gamma\,(\,&T_H|H,H\rangle_{3,4} - R_H|H,H\rangle_{3,4} - t_H r_H|H,H\rangle_{4,4} + t_H r_H|H,H\rangle_{3,3}) + \\ +\alpha\delta\,(\,&t_H t_V|V,H\rangle_{3,4} - r_H r_V|H,V\rangle_{3,4} - t_H r_V|H,V\rangle_{4,4} + t_V r_H|H,V\rangle_{3,3}) + \\ +\beta\gamma\,(\,&t_H t_V|H,V\rangle_{3,4} - r_H r_V|V,H\rangle_{3,4} - t_V r_H|V,H\rangle_{4,4} + t_H r_V|V,H\rangle_{3,3}) + \\ +\beta\delta\,(\,&T_V|V,V\rangle_{3,4} - R_V|V,V\rangle_{3,4} - t_V r_V|V,V\rangle_{4,4} + t_V r_V|V,V\rangle_{3,3}).\end{aligned} \tag{3.35}$$

We restrict the output state $|\psi\rangle_{\mathrm{OUT}}$ to coincidence rate contributions:

$$\begin{aligned}|\psi_{\mathrm{coinc}}\rangle_{\mathrm{OUT}} = \alpha\gamma\,(\,&T_H|H,H\rangle_{3,4} - R_H|H,H\rangle_{3,4}) + \alpha\delta\,(\,t_H t_V|V,H\rangle_{3,4} - r_H r_V|H,V\rangle_{3,4}) + \\ +\beta\gamma\,(\,&t_H t_V|H,V\rangle_{3,4} - r_H r_V|V,H\rangle_{3,4}) + \beta\delta\,(\,T_V|V,V\rangle_{3,4} - R_V|V,V\rangle_{3,4}).\end{aligned} \tag{3.36}$$

The transformation matrix of Eq. (3.36) can be written as:

$$\begin{pmatrix}\alpha_{H,H}\\ \alpha_{H,V}\\ \alpha_{V,H}\\ \alpha_{V,V}\end{pmatrix} = \begin{pmatrix}T_H - R_H & 0 & 0 & 0\\ 0 & r_H r_V & t_H t_V & 0\\ 0 & t_H t_V & r_H r_V & 0\\ 0 & 0 & 0 & T_V - R_V\end{pmatrix}\begin{pmatrix}\alpha\gamma\\ \alpha\delta\\ \beta\gamma\\ \beta\delta\end{pmatrix}. \tag{3.37}$$

This general description of polarization sensitive beam splitter can be advantageously used for models of imperfect PBS or PPBS. For example when r_H should be equal to zero, but is not. This approach is used in *Chapter 8, Faithful conditional quantum state transfer between weakly coupled qubits*, to explain steep decrease of process fidelity.

Beam displacer (BD)

A beam displacer has a similar function as PBS. It splits the light into two spatially separated modes of ordinary and extraordinary polarized light. However, the geometry is different. It is schematically shown in Fig. 3.12. The BD is made of birefringent calcite crystal (uniaxial optical crystal). The BD output beams are orthogonally polarized and parallel to each other. Their mutual separation is given by the calcite cut, length, and the wavelength used. In our experiment, we design the BD positions that V polarized light is directly transmitted, while the H polarized light is displaced. It is schematically shown in the upper part of Fig. 3.12. The bottom part of Fig. 3.12 schematically shows, how a BD can combine two parallel orthogonally polarized beams into single spatial mode. Later, we describe, how two BDs can be used for a realization of inherently stable Mach-Zehnder interferometer, which can serve as polarization sensitive filter. Via such filter, a polarization dependent losses can be induced.

Such filter is utilized in the experiment, described in *Chapter 8*. It uses BDs BD40 from Thorlabs, with 4.2 mm beam separation for wavelength 810 nm.

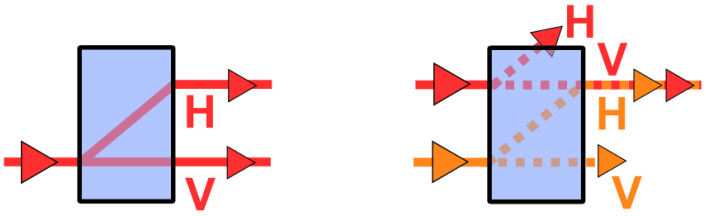

Figure 3.12: Scheme of calcite beam displacer (BD); left – BD spatially separates H and V polarized light; right – two parallel beams are combined into one spatial mode.

3.4 Mach-Zehnder interferometer (MZI)

The Mach-Zehnder interferometer (MZI) is one of the basic interferometric devices. The first beam-splitter (BS1) divides the beam into two spatially separated paths with splitting ratio $R_1 : T_1$ as shown in the Fig. 3.13. Each of the optical paths 1, 2 has some efficiency η due to its insertion losses. At the second beam-splitter (BS2) with splitting ratio $R_2 : T_2$, the two beams interfere. Subsequently, the interference is observed by detectors at the output ports 3, 4. Let us denote I_{13} the intensity of the beam reflected by BS1, transmitted by path 1, and again reflected by BS2 into the output port 3. Analogically I_{14}, I_{23}, I_{24}.

$$\begin{aligned} I_{13} &= \eta_3 \cdot R_2 \cdot \eta_1 \cdot R_1 \cdot I_{\mathrm{IN}}, & I_{14} &= \eta_4 \cdot T_2 \cdot \eta_1 \cdot R_1 \cdot I_{\mathrm{IN}}, \\ I_{23} &= \eta_3 \cdot T_2 \cdot \eta_2 \cdot T_1 \cdot I_{\mathrm{IN}}, & I_{24} &= \eta_4 \cdot R_2 \cdot \eta_2 \cdot T_1 \cdot I_{\mathrm{IN}}. \end{aligned} \tag{3.38}$$

When both arms are opened, the beams interfere and the intensities at the output ports are given as:

$$\begin{aligned} I_3 &= I_{13} + I_{23} + 2 \cdot \sqrt{I_{13} \cdot I_{23}} \cdot \cos\varphi \cdot \left|\gamma_{12}(\tau)\right|, \\ I_4 &= I_{14} + I_{24} + 2 \cdot \sqrt{I_{14} \cdot I_{24}} \cdot \sin\varphi \cdot \left|\gamma_{12}(\tau)\right|, \end{aligned} \tag{3.39}$$

where φ denotes phase difference between MZI arms.

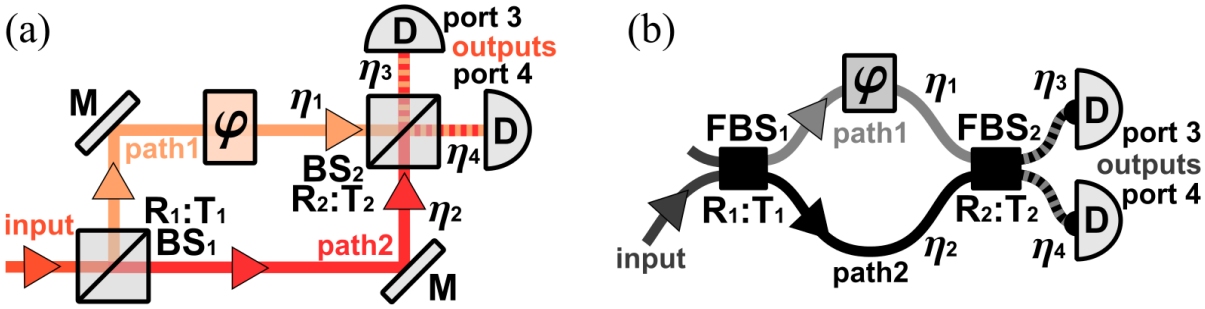

Figure 3.13: Scheme of Mach-Zehnder interferometer (MZI) in bulk (a) and fibre (b) optical implementation. (F)BS – (fibre) beam splitter; R:T – splitting ratio; M – mirror, D – detector; η – optical path efficiency; φ – phase difference between MZI arms.

Let us show a model situation. We assume balanced paths lengths and an absolute value of the complex degree of time coherence equal to one, $\left|\gamma_{12}(\tau)\right| = 1$ [167, 182]. We also assume indistinguishable particles in all degrees of freedom. From the knowledge of range of functions sine and cosine, we can easily calculate the maximal and minimal intensities of the interference fringe, which can be detected at the MZI outputs:

$$m_3 = \min(I_3) = I_{13} + I_{23} - 2 \cdot \sqrt{I_{13} \cdot I_{23}}, \qquad m_4 = \min(I_4) = I_{14} + I_{24} - 2 \cdot \sqrt{I_{14} \cdot I_{24}},$$
$$M_3 = \max(I_3) = I_{13} + I_{23} + 2 \cdot \sqrt{I_{13} \cdot I_{23}}, \qquad M_4 = \max(I_4) = I_{14} + I_{24} + 2 \cdot \sqrt{I_{14} \cdot I_{24}}. \tag{3.40}$$

To quantify the interference fringes, we calculate their visibilities from Eq. (3.19):

$$V_3 = (M_3 - m_3)/(M_3 + m_3), \qquad V_4 = (M_4 - m_4)/(M_4 + m_4). \tag{3.41}$$

We find out that visibility is independent on output port efficiencies η_3 resp. η_4 and input beam intensity I_{IN}, by substituting into Eq. (3.41) from Eqs. (3.40) and (3.38). In a case, when the light enters the MZI just by one input port, we can include the path efficiencies η_1 and η_2 into an effective splitting ratio of input beam-splitter BS1 $R'_1 : T'^{12}_1$. Than the MZI visibility can be expressed as a function of the splitting ratios R'_1 and R_2, as described in [183] and shown in Fig. 3.14:

$$V_3 = \frac{2\sqrt{I_{13} \cdot I_{23}}}{(I_{13} + I_{23})} = \frac{2\sqrt{R'_1 \cdot R_2 \cdot T'_1 \cdot T_2}}{R'_1 \cdot R_2 + T'_1 \cdot T_2}, \qquad V_4 = \frac{2\sqrt{I_{14} \cdot I_{24}}}{(I_{14} + I_{24})} = \frac{2\sqrt{R'_1 \cdot R_2 \cdot T'_1 \cdot T_2}}{R'_1 \cdot T_2 + T'_1 \cdot R_2}. \tag{3.42}$$

The 100% visibility at both output ports is reachable if and only if $R'_1 = R_2 = 0.5$. Otherwise, when only one of these splitting ratios R'_1, R_2 is equal 0.5, the output port visibilities are lower than one, but equal to each other, $V_3 = V_4 < 1$. On the other hand, the effective splitting ratio R'_1 is tunable by path efficiencies. Thus, it is possible to reach 100% visibility at least at one MZI output port for any splitting ratio of BS2. This gives us a strategy, how to reach the MZI with high visibility at both output ports. BS2 should be a BS with splitting ratio closest to 50:50%. Paths transmittances η_1 and η_1 should be as high as possible and should balance the BS1. In this way, we can easily estimate the maximal expected MZI visibility.

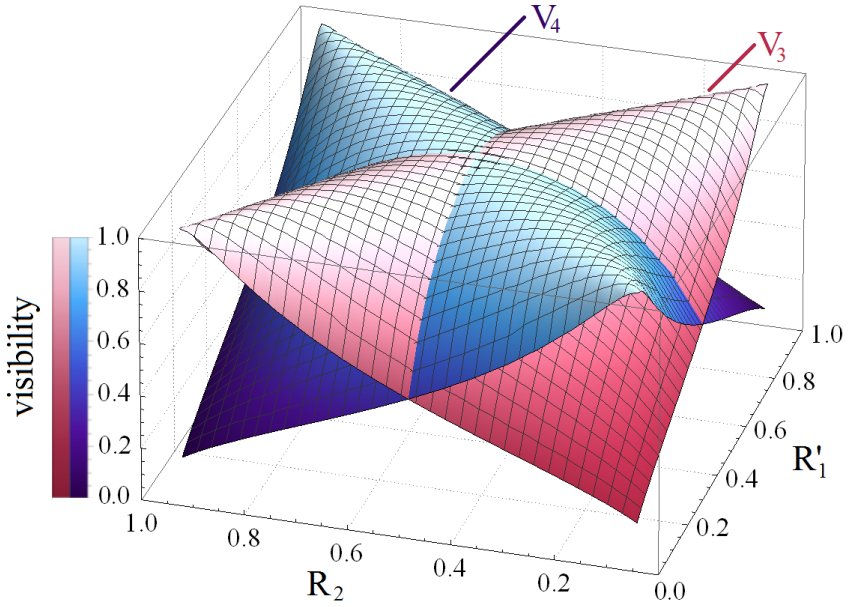

Figure 3.14: Mach-Zehnder interferometer visibilities, given by Eq. (3.42), are shown as a function of the effective splitting ratio R'_1 of BS1, and splitting ratio R_2 of BS2, where interference occurs. The graph is plotted for R'_1 and R_2 within range $[0.06, 0.94]$.

[12] $R'_1 = R_1 * \eta_1/y$ and $T'_1 = T_1 * \eta_2/y$, where $y = R_1 * \eta_1 + T_1 * \eta_2$ and $R'_1 + T'_1 = 1$.

In our experiments, we use MZIs operating at a single photon level. As a light source, attenuated laser diode (coherent state) is utilized, further we call it a probe beam. The signal is detected by a single photon detector. Instead of beam intensity, we detect a number of counts per time unit – count rate. By tuning the phase difference φ between MZI arms, the count rate is changed. Thus for certain φ, N counts per the time unit is detected. The uncertainty of the count rate is given as $\Delta N = \sqrt{N}$ (in the case of coherent state the probability of photon detection obeys Poissonian statistic).

Here we focus on **interference fringe measurement and evaluation**. The interference fringe visibility gives us information, about quality of interaction provided by the MZI. As described in next section *Stabilization of experimental setup*, the phase drift inside MZI, caused by environmental fluctuations, has to be actively stabilized (specially inside fibre-based MZI). The developed method for its active stabilization utilizes the interference fringe scan.

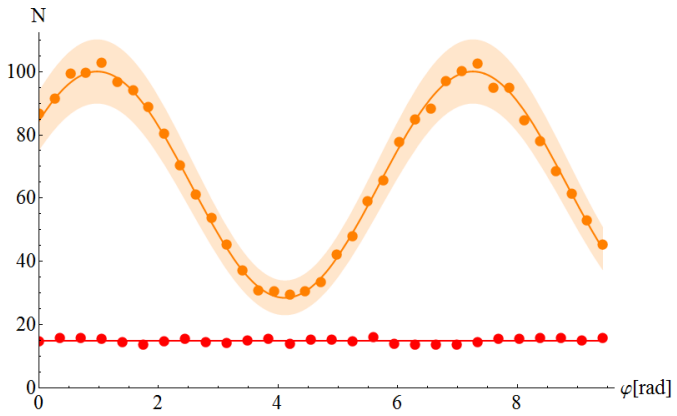

Figure 3.15: Illustration of interference fringe (orange) and offset (red). The count rate N is plotted as function of phase difference between MZI arms. Line – model of average value; light area – confidence interval; points – simulation of measured data. In this case, fringe visibility is 0.7 ± 0.1, according to Eqs.(3.43),(3.44).

In Fig. 3.15, there is shown an illustrative interference fringe by orange colour. By red colour is depicted the offset, which consists of background and detectors dark counts. The offset is measured separately, when all beams are switched off. The offset should be constant. Subsequently, the data are corrected for the offset in following way: measured fringe data minus average offset (o). Then the visibility $V \pm \Delta V$ is calculated as:

$$V = \frac{M - m}{M + m - 2 \cdot o}, \tag{3.43}$$

$$\begin{aligned} \Delta V &= \sqrt{\left(\frac{\partial V}{\partial M} \cdot \Delta M\right)^2 + \left(\frac{\partial V}{\partial m} \cdot \Delta m\right)^2 + \left(\frac{\partial V}{\partial o} \cdot \Delta o\right)^2} = \\ &= \frac{2 \cdot \left((m-o)^2 \Delta M^2 + (M-o)^2 \Delta m^2 + (M-m)^2 \Delta o^2\right)^{1/2}}{(M + m - 2 \cdot o)^2}, \end{aligned} \tag{3.44}$$

where M, m denote maximum, minimum of the measured fringe with uncertainties $\Delta M = \sqrt{M}$, $\Delta m = \sqrt{m}$, respectively. o denotes an average value the offset with uncertainties Δo. Because the offset is a constant value, it is possible to measure it for a longer time with resulting lower uncertainty, thus $\Delta o \ll \Delta m$. Finally, it is rescaled to the same measurement time as is used for the interference fringe measurement, to value $o \pm \Delta o$.

Our illustrative example of interference fringe is visible in Fig. 3.15. Its fringe visibility is relatively low[13] 0.7 ± 0.1 even with applied correction to the offset. However, low visibility is not crucial for the active stabilization function. Low count rate is the weak point, because it causes relatively wide interval of uncertainty which makes the stabilization procedure less sensitive.

During the stabilization procedure, the counting time is set to 0.1 s to keep it as fast as possible. On the other side, we need adequate count rate, ideally as high as possible, to keep the count rate uncertainty as low as possible. Unfortunately, it is limited by saturation of single photon detectors. Thus to be on "safe side", the attenuation of the probe beam is chosen as follows: We redirect maximal amount of photons by the active components (under computer control) into each single photon detector. Each detector should be still far from saturation regime, although the maximum of interference occurs. By this setting of the probe beam, we usually reach count rate roughly 300.000 c/s (counts per second) in the interference maximum at the end of the setup. The typical interference fringe scan, with interference maximum 30 kc/0.1s, is shown in Fig. 3.16. The typical level of dark counts depends on used single photon detector. It is between 10–100 c/0.1s. It is almost negligible in comparison with typical count rate. Note: The dark counts create incoherent offset signal which is also present during the main measurement with photon pairs. However, it is substantially reduced by coincidence measurements.

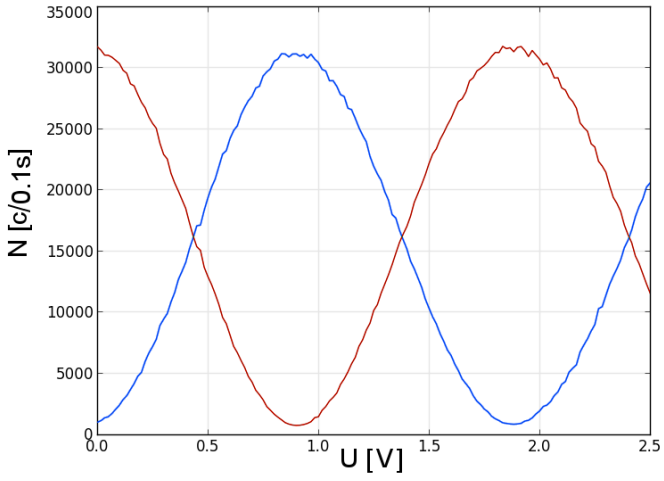

Figure 3.16: Typical interference fringe scans at both output ports of MZI. Count rates N are plotted in dependence on applied voltage to a PM, causing the phase shift φ between MZI arms. Fringe visibilities are $V_3 = 0.950 \pm 0.002$ and $V_4 = 0.958 \pm 0.002$.

[13]Lower fringe visibility can be caused for instance by: used imbalanced BSs in MZI, different length of MZI optical paths ($\Delta t \neq 0$), partially distinguishable photons in other degrees of freedom than temporal, etc.

3.5 Electronic signal processing

As already mentioned, a single-photon detector produces a positive electric pulse as a result of photon detection. However, the pulse properties as height and FWHM differ from detector to detector. Such electric signal has to be processed to evaluate single-photon count rates or coincidence rates between detectors.

First, we convert positive electric pulses into negative electric pulses, because counting and coincidence electronics work with negative NIM logic levels. It is done by passive inverter *Inverting transformer model* ***#460***, from Phillips Scientific. In earlier experiments, it was done by home-made TTL to NIM converter (developed by R. Čelechovský). Pulses incoming into a coincidence logic have to be synchronized. Thus, electric signals go through passive delay lines *Dual nanosecond delay module* ***#792***, from Phillips Scientific. The delay line has a range 0.0 – 63.5 ns per section with step of 0.5 ns and additional constant offset 1.7 ns. Then signals are propagated through coaxial cables into a discrimination module *Octal 300MHz discriminator* ***#708***, from Phillips Scientific. There, a required voltage level is set. When the level is exceeded by a signal the discriminator produces NIM electric pulse with required FWHM and height. The narrowest possible pulse has FWHM approximately 2.6 ns. Then signals are fed into a fan-out *Octal bipolar linear fan-out* ***#748***, from Phillips Scientific. The fan-out replicates each electric pulse up to four copies. Such processed electric signal is fed directly into a counter to obtain a single-photon count rate or into a coincidence logic module. The coincidence logic module *Quad 300MHz four-fold majority logic unit* ***#754***, from Phillips Scientific can evaluate 2-fold, 3-fold or 4-fold coincidences. However, all described experiments in this Thesis utilize just two-photon coincidences. Thus this module provides the logical operation AND between signals from two single-photon detectors. When a two-pulse overlap is bigger than 50 % the coincidence logic evaluates it as a coincidence event and output electric pulse is produced. A coincidence window is tuned by a FWHM of incoming pulses. An electric signal from a coincidence logic is fed directly into a counter to obtain a coincidence rate. We employ counters *Quad Counter/Timer* ***#974A***, 100 MHz from Ortec (QUAD), *Dual Counter and Timer* ***#994***, 100 MHz from Ortec (DUAL) and home-made counters which are part of Universal Box (UBOX, 8 channels, 40 MHz)[14]. Counters QUAD and DUAL operate in NIM logic, while UBOX counts the positive TTL pulses with FWHM > 12 ns. Because of it, processed electric signals from a fan-out directed to the UBOX have to go through another discriminator which increases pulses FWHM. Subsequently, widespread pulses have to go through a *16 channel logic level translator* ***#726***, from Phillips Scientific. It converts NIM pulses into TTL pulses and preserves their FWHM.

All modules from Phillips Scientific and Ortec are powered through NIM-Bins 4001A from Ortec or by NIM/CAMAC from Wiener.

[14]The UBOX is developed in our laboratory by M.Dušek and it is available for last two mentioned experiments. The UBOX counter has 8 counting channels and utilizes the Python libraries.

The basic concept of signal processing remains the same for all the performed experiments. A main difference in electric signals processing lies in number of employed detectors. Most of the realized experiments employ 4 detectors. However, one of the experiments uses 5 detectors. Subsequently, electric signals from detectors have to be processed and counted. The single-photon count rates and coincidence rates from all channels have to be stored. Counters are controlled by a computer via serial ports (RS-232) using Python or MATLAB environment. UBOX is controlled via USB port or via virtual serial port.

QUAD counter has 3 counting channels, when it is used independently. However, when QUAD counter has an external time base, it is possible to use all 4 counting channels. DUAL has 2 counting channels. Standard connection of counting modules used in earlier experiments is 2x QUAD triggered by external time base from DUAL. In total, we have 10 counting channels available. It is enough for experiments with maximally 4 detectors. Since UBOX is available, we modify the connection of counting modules to 2x QUAD and 1x UBOX. One QUAD counter and UBOX are externally triggered by a time base from a master QUAD counter. In total, we have available 15 counting channels. Typical electronic signal processing is schematically shown in Fig. 3.17. Single-photon count rates are counted by UBOX, while coincidence rates by QUAD counters. It is because the sequential phase stabilization procedure of an interferometer is based on counting of single-photons and it utilizes UBOX[15].

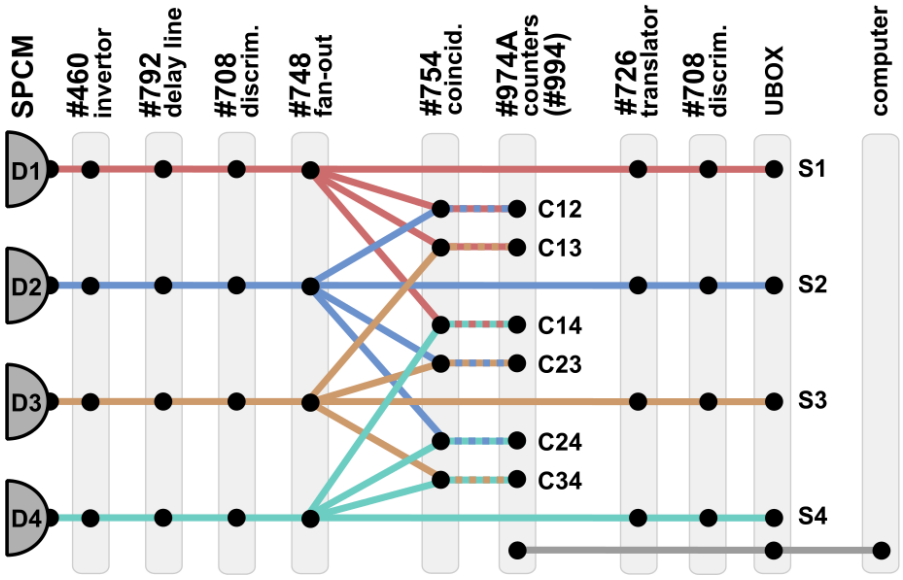

Figure 3.17: Simplified scheme of typical electronic signal processing from 4 single-photon detectors (D) to single-photon rates (S) and coincidence rates (C), for details see text. Photos of signals processing are shown in Fig. 3.18.

[15]The stabilization procedure is described later. Its Python implementation is done by M.Dušek and it advantageously uses UBOX counters and digital-to-analogue converters.

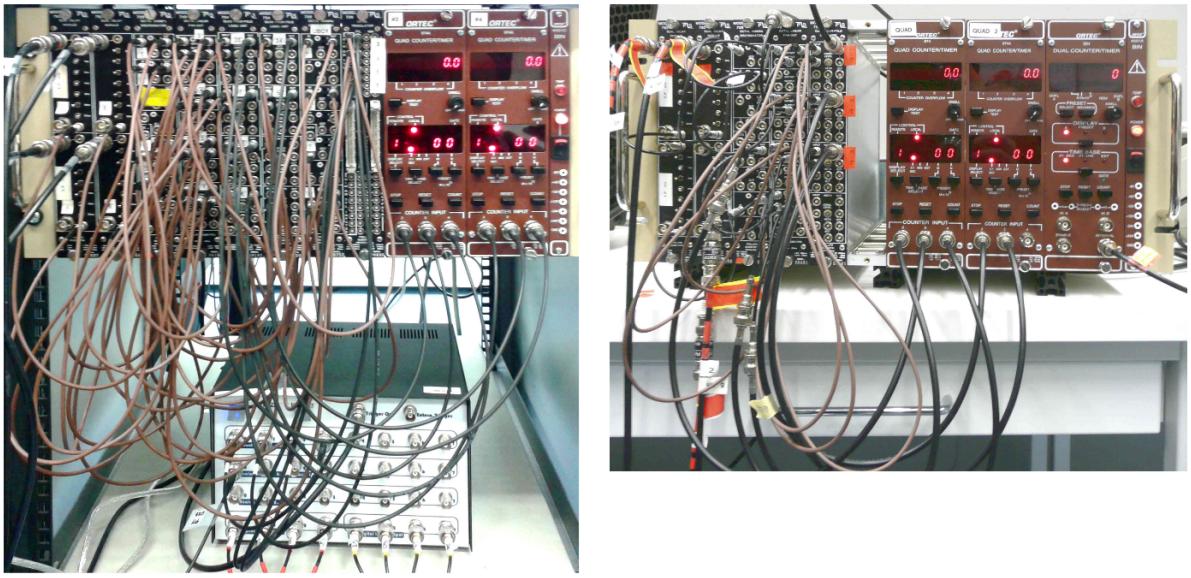

Figure 3.18: Photos of the electronics signal processing employing: left – two QUADs and UBOX together with logic level translator **#726**; right – two QUADs and DUAL.

3.6 Air gap (AG)

An air gap (AG) is placed in each arm of the fibre-based interferometer. It is not usually shown in the simplified schemes of experimental setups. There are several reasons for placing AG into interferometer arm.

Basic AG consists of two collimating lenses and two mirrors placed in kinematic mounts. One collimating lens serves for outcoupling of light from an optical fibre into a free space as a collimated beam. The second one serves for coupling of light from free space into an optical fibre. Two adjustable mirrors give us sufficient number of degrees of freedom to redirect the collimated beam to be optimally coupled into an optical fibre again. AG design is usually "Z" shaped or "triangle" shaped, as shown in Fig. 3.19.

An outcoupling lens is usually placed at fixed post. While an incoupling lens is placed at linearly translating stage which enables us to decrease or increase the distance between optical fibres. Thus, it enables us to change the AG length. In one interferometer arm, there is usually AG with a mechanical movable stage. In the second arm, there is AG with a motorized stage. It is necessary to make the beam direction coaxial with the axis of the stage translation. If it is not coaxial, a change of AG length causes a change of light incoupling efficiency. Thus insertion losses in interferometer arm would be a function of a stage position.

AGs are used for balancing of interferometer arm lengths. All fibre-based components and patchcords have fixed lengths. We try to combine the components to balance the overall length as much as possible. But, there are usually still few centimetres missing. This length discrepancy is compensated by a length of AG. Unfortunately, we do not know precise optical lengths of optical components. Thus, precise arm lengths tuning is done by the stage scanning and finding the maximum of an autocorrelation function of a probe beam. The final arm lengths balancing is usually done by the motorized stage scan with photon pairs. Path lengths are aligned according to the minimum of HOM dip.

Inside AG, there is easier to tune insertion losses of interferometer arms. It is done by a partial beam-blocking or neutral density filters. Advantage of bulk attenuators are that their maximum transparency is 100%. Fibre attenuators, available in our laboratory, have maximal transparency roughly 70%.

AGs are also suitable places for polarization state control of light or for improving light degree of polarization (DOP). Thus inside AGs, there are usually placed PBSs that transmit H polarized light.

In earlier experiments which used single mode optical fibres, the polarization state of light is set by polarization controller (PC) according to maximal detected intensity behind polarizer. It is schematically shown in the left part of Fig. 3.19. Experiments, where the polarization maintaining optical fibres are employed, use half-wave plates (HWP) to modify the polarization state of light. Linearly polarized light outcoupled from a slow axis of a fibre is via HWP identified with H-polarized light transmitted by a PBS. It is followed by proper incoupling of H-polarized light into a slow axis of a fibre. It is schematically shown in the right part of Fig. 3.19.

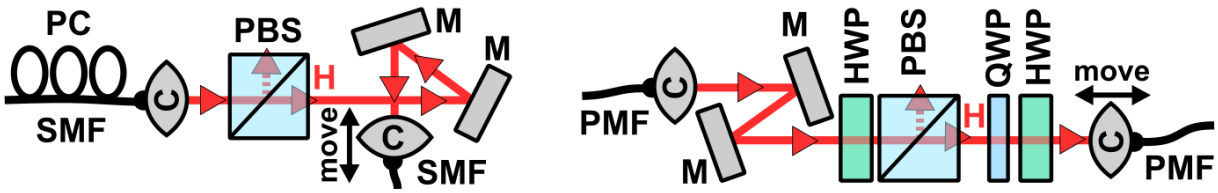

Figure 3.19: Schemes of air gaps (AGs) in different configurations: left – "triangle" shape using single-mode optical fibres, right – "Z" shape using polarization maintaining optical fibres. SMF – single mode optical fibre (type 780-HP), PMF – polarization maintaining optical fibre (type PM780-HP), C – collimating lens, PC — polarization controller, M – mirror, PBS – polarizing beam splitter used as polarizer, move – linearly translating stage for AG length alignment, HWP – half-wave plate, QWP – quarter-wave plate, H – horizontally linearly polarized state of light.

A proper coupling of a linearly polarized light into a slow axis of a polarization maintaining fibre consist of QWP and HWP placed in front of the coupling lens. It enables us to change the polarization state of light and eventually compensate a birefringence induced for example by an imperfect coupling lens [184]. First, QWP and HWP have to be calibrated to zero[16]. Then we rotate a HWP approximately according to a direction of a fibre connector key, to avoid the coupling into a fast axis. The key denotes the slow axis. The second end of the optical fibre is connected into a simple DOP meter realized using rotating linear sheet polarizer followed by a PIN diode. Such DOP meter is not able to measure all Stokes parameter only two of them. However, we expect linear polarization state, thus it is sufficient for our alignment purpose. A signal from the PIN diode is displayed on an oscilloscope and one can observe a sinusoidal behaviour of the detected light. By HWP rotation (close to the pre-set position, no more than $\pm 22.5°$) we try to maximize the pattern visibility and consequently DOP of the light. When we

[16]Position of their optic axes are identified with a direction of H polarization, determined by the PBS.

reach maximum then we can try to improve the visibility by QWP rotating by several degrees. We perform walk-in, iterative alignment, by HWP and QWP, till we reach the global maximum. Obviously, the exact value of the pattern visibility is not important for this alignment method. We align wave plates positions towards the maximum pattern visibility.

To clarify how the coupling into a polarization maintaining fibre works: one should know that used light has a relatively short coherence length. When such light with DOP=1 is equally coupled into slow and fast axis of the optical fibre, one can observe polarization mode dispersion. Thus, at the end of the fibre, the light has DOP$\ll$1. However, when the light is coupled just into the one optical axis, the DOP at the end of the fibre is still $\approx$1.

3.7 Light sources

In this section, we briefly describe a source of correlated photon pairs and other light sources necessary for a proper alignment and operation of experiments.

3.7.1 Laser diodes (LD) – probe beam

To make the construction and alignment of experimental setups practical, a strong probe beam is used. The strong probe beam is a light from a laser diode (LD) with a power level detectable by PIN-diode detectors. The LD has ideally the same central wavelength as the photon pairs, $\lambda_c = 810$ nm. LD FWHM should be similar or narrower compared to the photons pairs, FWHM$\lesssim 2.7$ nm. When setup is aligned, the LD is attenuated to a single photon level. It is used as a weak probe beam (coherent state) detectable by single-photon detectors. The level of LD attenuation, safe for the single-photon detectors, was already discussed[17]. A weak probe beam serves mainly for active stabilization procedure.

How the probe beam is usually fed into an experiment is shown in Fig. 3.20. The probe beam goes through the same interference filter (IF) as the photon pairs.

Our recent experiments utilized a LD QFLD-810-10S from QPhotonics (S/N:12.12.08), $\lambda_c = 810$ nm. The LD is single mode fibre pigtailed. The light is re-coupled into a polarization maintaining fibre via AG. There, the strong signal is also attenuated to a weak signal level by neutral density filters and bulk beam attenuator. This LD is chosen because of its long-term stability of output power and frequency spectra.

3.7.2 Source of correlated photon pairs

The source of correlated photon pairs was built by I. Straka and M. Ježek, for more details see Ivo's Master thesis [177] ev. [185]. Photon pairs generation is based on degenerated collinear spontaneous parametric down conversion (SPDC) [186, 187], type-II in 2 mm thick crystal BBO (beta-barium borate, β-BaB_2O_4). The source utilizes another BBO crystal 1 mm thick to compensate the transversal walk-off and group velocity dispersion.

[17] It was discussed in the section *Mach-Zehnder interferometer*, its part *interference fringe measurement and evaluation*.

The non-linear crystal BBO is pumped by CW laser diode (iBeam Smart from Toptica set to 115 mW) with a central wavelength $\lambda_c = 405$ nm. With certain probability, a pump source photon is split into two photons, called signal and idler. They obey conservation laws of energy and momentum, which are expressed as follows:

$$\omega_P = \omega_S + \omega_I, \qquad \mathbf{k}_P = \mathbf{k}_S + \mathbf{k}_I, \tag{3.45}$$

where ω_x is angular frequency, $\mathbf{k}_x$ is wave vector and $x = P, S, I$. It denotes a pump (P), signal (S), and idler (I) photons. In reality, the Eq. (3.45) reads:

$$\Delta\omega = \omega_P - \omega_S - \omega_I, \qquad \Delta\mathbf{k} = \mathbf{k}_P - \mathbf{k}_S - \mathbf{k}_I, \tag{3.46}$$

however, SPDC process is most efficient, when the $\Delta\omega$ and $\Delta\mathbf{k}$ is equal to zero.

SPDC type-II means, that obtained signal and idler photons are orthogonally polarized. The pump beam enters the non-linear anisotropic crystal as extraordinary polarized light and the signal and idler photons appear as extraordinary and ordinary polarized photons, respectively. It is commonly schematically denoted as $e \rightarrow eo$.

Collinear SPDC means, that signal and idler photons have the same direction of wave vectors. This direction is also collinear with the direction of a pump photon wave vector.

Degenerated SPDC means, that signal and idler photons have the same central frequency. From the Eq. (3.45) we obtain:

$$\omega_S = \omega_I = \omega_P/2. \tag{3.47}$$

Our signal and idler photons have the same central wavelengths $\lambda_c = 810$ nm. They go through the same IF (Semrock, Laser-line customized, labelled MITC #4, $\lambda_c = 810$ nm, FWHM = 2.7 nm, its spectral profile is convolution of Gaussian shape and square shape), while a pump beam is blocked by a cut-off filter. They are spatially separated according their polarizations by a PBS. It is shown in Fig. 3.20. Subsequently, the photons are coupled into slow axes of polarization maintaining optical fibres connected to an experiment.

Inside the idler arm, there is a linear motorized stage. It serves for tuning of time delay between signal and idler photons. When the source of photon pairs is characterized, the signal and idler photons are fed into a balanced FBS from polarization maintaining fibre and by this stage, HOM dip is scanned. HOM dip shape, visibility, and count rate are mainly determined by the IF used [129, 177].

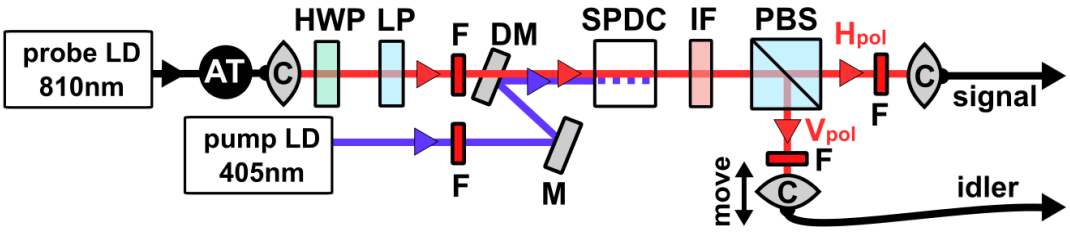

Figure 3.20: Scheme of the source of photon pairs and its interconnection with the probe beam . HWP – half-wave plate, LP – linear sheet polarizer in rotation mount, F – flip, automatic beam stop, (D)M – (dichroic) mirror, IF – interference filter, PBS – polarizing beam splitter, C – coupling lens, move – motorized stage, AT – attenuation in AG, SPCD – spontaneous parametric down conversion, this block include non-linear crystals BBO, cut-off filters, lenses etc., for details see [177].

3.8 Stabilization of experimental setup

First, we explain why an overall experimental setup stability is so important for its performances. We demonstrate it at examples of instability consequences. Finally, we describe how we reach sufficient experiment stability by passive and active methods.

Our laboratory conditions: For first experiments, temperature changes at the setup place were $\Delta T_{pp} = 7°\mathrm{C}$ with peak-to-peak changes several times per day. Now it is $\Delta T_{pp} < 3°\mathrm{C}$, but the temperature oscillations have a higher frequency. Overall temperature gradient inside our laboratory used to be $\sim 5°\mathrm{C}$, now it is $\sim 3°\mathrm{C}$, and the air flux is decreased. The air ventilation and air condition are under our manual control, however, they are not automatically correlated. The relative humidity is not under our control and varies from $\sim 7\%$ to $\sim 80\%$ RH.

Consequences of experimental setup instability: Mechanical vibrations, air fluctuations, temperature changes and gradients cause the experimental setup instability. For example, the mechanical part of the experiment consists of posts, mounts, holders, clamps, screws, an optical table, and so on. These parts are made of different materials with different coefficient of thermal expansion. During the time, the mechanical post and mounts misalign and the whole experimental setup decohere under the imperfect laboratory conditions. For example the air gaps coupling efficiencies decrease which negatively influence insertion losses and balancing of optical path efficiencies are changed.

Optical components under different temperatures exhibit slightly different optical properties. It may negatively influence retardations of wave plates, or a half-wave voltage of phase modulator. However, the optical fibres are the most sensitive part of the experimental setup, because of their length.

In standard single mode optical fibre, fluctuations are translated into phase and polarization changes of an optical signal. Due to the last mentioned, we place into an experimental setup several polarizers with polarization controllers, at the places where it is possible to control a polarization state of light. Polarization changes are translated by a polariser to intensity changes. Thus the insertion losses of the optical paths are slightly changing. As a consequence, the interferometer is imbalanced. It causes a lower

interferometer visibility. Thus before each final measurement, it is necessary to verify the polarization states of light. They are set by polarization controllers according to maximal transmitted intensity by polarizers.

If we do not translate polarization changes into intensity changes, particles passing through individual paths start to be distinguishable in polarization modes.

It is not a case of polarization maintaining fibres. By employing polarization maintaining fibres we restrict number of degrees of freedom which are necessary to keep under control. We use only a slow axis of the polarization maintaining fibres. When a signal is properly coupled into the axis, it is not necessary to re-align it after some time again. Then, changes of refractive index cause only misalignment of optical path lengths. The other effect, which appears with the use of polarization maintaining fibres is a decrease of signal degree of polarization. It is because of connection more patchcords together by FC-FC fibre connectors or because of used polarization maintaining fibre components. However, this problem is solved during the experiment alignment. It is solved by placing polarisers or polarizing fibres (HB830Z(5/80)) at crucial setup places to increase the degree of polarization. It is important to note, that the signal coupled into the fast axis of a polarization maintaining fibre becomes incoherent with a signal in the slow axis. It is due to a polarization mode dispersion and short coherent length of used light. If such incoherent signal from fast axis is partially coupled back to a slow axis at a fibre connectors, it is impossible to remove such a parasitic signal from the correct one. These two signals in one optical axis do not interfere together. It creates an incoherent noise which decreases the signal degree of polarization.

A phase signal instability is common for both fibre types. It causes imbalance of optical paths. We can divide the phase changes into two categories. Let us call them slight and serious phase misalignments. Some of the processes which serve as a standard tool of linear quantum optics are sensitive to small phase misalignment and some of them not, like single photon interference and two-photon interference, respectively. Two-photon HOM interference is not so sensitive to slight relative photons phase changes. However, both these interference types are sensitive to serious phase changes.

By a **slight phase misalignment** between optical paths we mean such phase change which can be repaired by active phase stabilization procedure. Such phase change is within a dynamical range of employed PM.

Fibre interferometric devices serving for single-photon interference has to be actively stabilized as described below. A dynamical range of used PM is up to ± 3 interference fringes. It corresponds to a phase of $\pm 6\pi$ rad or a path difference approximately $\pm 2.5\mu$m. But, we automatically tune the relative phase of paths just within a range ± 0.5 of the interference fringe, to keep the voltage at a PM close to zero.

By a **serious phase misalignment** we mean such massive phase difference between optical paths which causes their temporal distinguishability. Compensation of such phase change is out of PM range. A resulting effect is that we are out of the HOM dip minimum or far from the autocorrelation function maximum. The serious phase misalignment is repairable by a linear motorized stage placed in an air gap of MZI arm.

3.8.1 Passive stabilization

All experiments are built on an optical table with pneumatic vibration isolators. The table (Newport RS 4000) sandwich structure itself damps vibrations. However, table legs, isolators, are the most important parts. Their automatic vibration control system (Newport Stabilizer I-2000) supported by air compressor, produces something like air pillow and the table floats. Thus the table is well isolated from a floor. Such table has a relatively high heat capacity which helps us to protect experiments against a short time temperature fluctuations.

To improve a passive stability of a whole experiment, we cover it by a two-layer box to decrease an influence of air convection, air fluctuations, temperature changes, and mechanical vibrations. The first layer is created by black hardboard (Thorlabs - TB4). The second layer is made of extruded polystyrene. Longer fibre optical delay lines of MZI are coiled to an aluminium holder fixed to the table, to be less sensitive to short time temperature fluctuations. Other fibre components are clamped to the optical table, eventually they are covered by bubble-foil.

A resulting passive phase stability of a fibre-based interferometer is typically better than 1° per second. The correct phase inside a fibre interferometer is kept by active stabilization procedure, described below. The passive phase stability of a calcite interferometer is better by several orders of magnitude when compared with fibre-based MZI. Such device exhibits phase drift approximately 1° per hour. Interferometer phase stability was discussed in *Chapter 2, Contemporary state of research* and in paper [64].

3.8.2 Active sequential stabilization of fibre-based MZI operating at single photon level

Sequential phase stabilization procedure periodically changes short periods of stabilization procedure and main measurement. The duration of data acquisition is short, to minimize the phase drift, because during the main measurement the stabilization does not work. Here, we explain firstly continuous stabilization procedure which runs in parallel with the main measurement.

First steps are the same for both methods. We balance optical paths according to HOM dip minimum or autocorrelation function maximum. Subsequently, we scan an interference fringe by a PM. The fringe shows a dependence of a relative phase between MZI arms on applied voltage to the PM. According to this scan, we choose wanted position inside the interference fringe and we set corresponding voltage to the PM. Then these two stabilization methods start to differ.

A continuous stabilization procedure requires a phase modulator with sufficient dynamical range which systematically compensates phase differences and keeps both relative and absolute phases unchanged. It is running parallel with the main measurement. A sequential phase stabilization procedure just checks a relative phase between optical paths when the main measurement is interrupted. Thus it sets the proper relative phase before the main measurement. A sufficient dynamical range of a PM is a half of interference fringe. It is enough to compensate slight misalignments. However, during the main measurement, several settings of an experiment are performed. It takes some time to change

a setting. During this process a stabilization procedure is switched off and a setup instability (phase drifts) may be increased. After this process stabilization procedure sets a properly relative phase, whereas the absolute phase is not under control. Its phase change may be larger than a fringe. It results in a serious misalignment.

A hardware implementation of continuous phase stabilization of interferometric device operating at single-photon level is complicated, however, it is in the progress [188] in our lab. Below, we describe a procedure of sequence phase stabilization of interferometric device operating at single photon. It utilizes probe beam operating at a single-photon level and with the same central wavelength. This sequence procedure is also used for stabilization of more complicated interferometric setups with two interconnected MZIs or serially chained MZIs.

The sequential active phase stabilization procedure of fibre-based MZI: A CW LD attenuated to single photon level is employed as a weak probe beam. This beam serves for phase stabilization purposes. The central wavelength of a probe beam is set to 810 nm, to be similar to a central wavelength of the photon pairs. This beam goes through the same interference filter as photon pairs from SPDC[18]. We choose LD with coherence length comparable to a coherence length of photons from SPDC. Its polarization state is set according to setup specifics. In what follows, a description of the stabilization procedure is restricted to a stabilization of a single MZI. Details of phase stabilization of complicated experimental setups are discussed directly in chapters describing the particular experiments.

A PM is contained in each MZI arm. One of them is used for a stabilization, the second one is used as a part of the feed-forward loop or as passive components due to the dispersion compensation between MZI arms. The PM half-wave voltage (U_π) is precisely measured to have a clear correspondence between applied voltage to the PM and the phase shift between MZI arms ($U_\pi \approx 1.5$ V). Half-wave voltage measurement technique is described in previous section *Integrated electro-optical phase modulator*. Pairs from SPDC and probe beam are switched by motorized flip mounts (controllable beam stops). Both these signals are detected by the same single-photon detectors.

The stabilization routine, where the phase drift is actively compensated by means of PM is described in protocol [189] and theses [181, 190]. For our experiments, this procedure is implemented to Matlab code by H. Fikerová within her Bachelor's Thesis [174]. Further, it is extended and utilized for measurements in papers [1–3] and theses [169, 178]. Subsequently, the stabilization procedure is generalized and implemented to Python code by M. Dušek and employed in papers [4, 5].

The stabilization routine of each MZI is based on count rate measurements at the end of the interferometer. The routine requires the knowledge of the interference fringe visibility and maximal count rate at one detector. For optimal operation, it needs also the sum of counts from both detectors and their dark counts. Then, the routine is insensitive to long-term fluctuations of probe beam intensity.

[18] It was detail described in section *Source of correlated photon pairs.*

Before the stabilization routine starts, the interference fringe is scanned by applying voltage to the PM inside MZI (from 0 V to at least wave voltage). Subsequently, from the scan the centre of the first fringe is chosen which corresponds to phase shift $\pi/2$ (It is a position in the middle between the minimum and maximum of the fringe. In this place the fringe has the highest positive derivation. Because of it, we reach highest phase sensitivity.). This information is stored: visibility (V), voltage (U_{mid}), count rate in the middle of the fringe (I_{mid}). If it is available, sum of the count rates from both detectors corrected for dark counts and relative detectors efficiencies are also stored.

Then, corresponding voltage U_{mid} is applied onto the PM and the count rate is verified. In general, several typical situations can occur.

(i) If the measured value is in the confidence interval of the stored value I_{mid}, the beams are swapped, required phase inside MZI and the main measurement can starts. The required phase inside MZI is set with respect to the already applied phase correction from the stabilization routine. After some time, 1–3 s, the data accumulation is interrupted by the stabilization procedure. The beams are swapped, onto the PM is applied voltage U_{mid} which should correspond to the phase shift $\pi/2$ inside MZI and the count rate is verified again. If the measured value is in the confidence interval of the stored value I_{mid}, the data accumulation continues.

(ii) If the measured value is out of the confidence interval of the stored value I_{mid}, it means that the applied voltage U_{mid}, which should correspond to the phase shift $\pi/2$ inside MZI, does not correspond to this phase anymore. Calculated voltage correction is applied to the PM and count rate is checked again (let us call it a correction of the first order). If the measured value is in the confidence interval of the stored value I_{mid}, the new voltage $U_{\mathrm{mid}} = U_{\mathrm{mid}} + U_{\mathrm{correction}}$ is stored. Just note that the first order correction is within the range $\pm\pi/2$.

(iii) If the first order correction does not help, another measurement is performed shifted by $\pi/2$. From these two measurements, the true position inside the fringe is determined. Calculated voltage correction is applied onto the PM (let us call it second order correction) and the count rate is checked again. If the measured value is in the confidence interval of the stored value I_{mid}, the main measurement continues. The second order correction is not used too often, only when the phase drift is bigger than $\pi/2$.

When the stabilization operates with two detectors, the routine also verifies the sum of the count rates, which should be constant. If the sum is not in the confidence interval of stored value, the routine rescales the intensity I_{mid}, so it still corresponds to the intensity in the middle of the fringe. It is how the typical adaptive setpoint works.

(iv) If also the second order correction does not help several times (N times), the stored visibility V is reduced. Then, the second order correction is applied again, but maximally N times. If the MZI is not stabilized anymore, the interference fringe is scanned again.

This happens only rarely. Usually, the first order correction is sufficient. However, when the fringe visibility is significantly lower, it points out to the serious setup misalignment. Thus the setup should be re-aligned. Firstly, balancing of optical path lengths according to the HOM dip minimum should be verified.

3.9 Real-time electro-optical feed-forward loop

Here, we describe an experimental realization of a real-time electro-optical feed-forward loop operating at single photon level and its utilization in linear optical quantum information processing. Introduction to feed-forward loop utilization is in *Chapter 2 Contemporary state of research*.

Basic idea: A feed-forward loop is used to conditionally influence one part of the experimental setup in real-time. This change is triggered by a measurement result obtained from the other part of the setup. This measurement result is as classical information fed-forward to the experiment. There, it triggers an appropriate operation.

In our experiments, we encode quantum information into states of single photons. Subsequently, qubits carried by photons are processed. It leads to a complex, generally entangled, two-qubit state consisting of qubit I and qubit II. Then a projective von Neumann measurement is applied onto the ancillary qubit I. The result determines if the unitary operation is applied onto the target qubit II, or not.

Thus the conditional application of an unitary operation onto the qubit II according to the measurement result of the qubit I is called the feed-forward loop. It is schematically depicted by the yellow box in Fig 3.21.

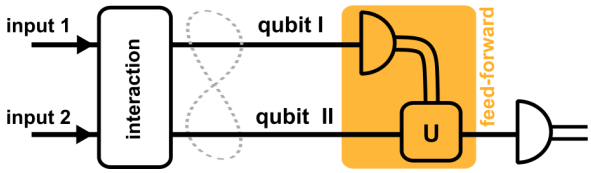

Figure 3.21: Schema of a feed-forward loop, shown by the yellow box. The measurement result of the auxiliary qubit I triggers the application of unitary operation (U) onto the target qubit II.

Our feed-forward loop is based on a single photon detector, a fast integrated electro-optical phase modulator (PM), and a single photon interference in a fibre-based Mach-Zehnder interferometer (MZI). We implemented both passive and active version[19] of the feed-forward loop.

In our experiments, we utilize the feed-forward loop for different tasks: to increase a success probability of liner optical quantum gates [1]; to fully harness benefits of entanglement state in discrimination strategy of quantum measurements [4]; as a part of qubit state transfer protocol investigating states of particles carrying quantum information [2]; and as a part of quantum filter in quantum state transfer protocol between weakly coupled qubits [5]. Simultaneously, we experimentally verify its feasibility and robustness in linear optical setups operating at a single photon level.

In further text, we describe a typical experimental setup, where the feed-forward loop is implemented. We explain difference between passive and active loop implementation and other important terms like half-wave voltage and timing. Finally, we discus how to make it even faster than 25 ns.

[19]We call them passive and active according to electric pulse processing. Passive version utilizes a potentiometer as a voltage divider, while the active version employs a level translator.

Experimental setup description: An experimental setup, shown in Fig 3.22, is realized as follows: the qubit I goes to a polarization state analysis consisting of a half-wave plate, a quarter-wave plate (WPs1) and a polarizing beam-splitter (PBS1). Then, it is detected by a single-photon detector D1 or D2. Thus, the bipartite state of qubit I and II is reduced to a *single-photon state*.

Subsequently, the quantum state of the qubit II is re-encoded from polarization degrees of freedom to spatial ones (which way encoding). It is done by proper settings of a half-wave plate and a quarter-wave plate (WPs2) in front of a PBS2. The PBS2 spatially separates its eigenstates, horizontal (H) and vertical (V) linear polarizations, into spatial paths 0 and 1, respectively. Simultaneously, the PBS2 creates an input beam-splitter of MZI. The signal in each MZI arm is coupled into single mode optical fibres. Subsequently, the signal goes through a phase modulator (PM). PM0 serves for active phase stabilization of the MZI and PM1 is a part of the feed-forward loop. Then the signal interferes at the output fibre beam-splitter (FBS). Finally, it is detected by the single-photon detector D3 or D4. Electric signals from all 4 detectors are led to electronic coincidence logic. There, just simultaneous click-events of two detectors, detecting the qubit I and II, are taken into account (coincidences $C_{1,3}$, $C_{1,4}$, $C_{2,3}$, and $C_{2,4}$).

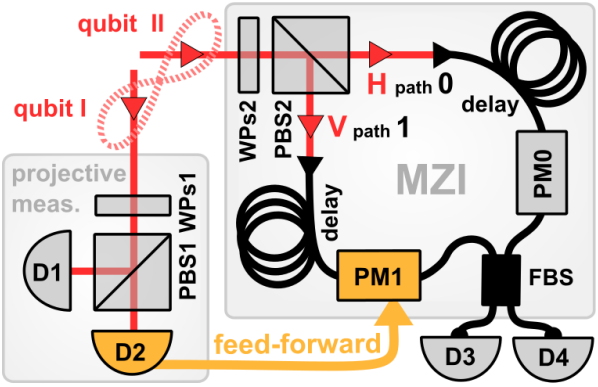

Figure 3.22: An example of a feed-forward loop implementation. WPs – set of HWP and QWP; PBS – polarizing beam-splitter; feed-forward – electro-optical feed-forward loop, for details see Fig 3.23; PM – phase modulator; H (V) – horizontal (vertical) linear polarization state of light; FBS – balanced fibre beam-splitter; D – single-photon detector.

Illustrative example: If the qubit I is detected by the detector D1, the quantum state of qubit II can be written as $\alpha|0\rangle + \beta|1\rangle$. By passage through the MZI, the state remains unchanged. When the qubit I is detected by the detector D2, the quantum state of qubit II is different $\alpha|0\rangle - \beta|1\rangle$. However, it differs only in the sign. To obtain $\alpha|0\rangle + \beta|1\rangle$, the state has to be influenced by a feed-forward loop.

Implementation of the feed-forward loop: After photon detection, the single-photon detector D2 produces a positive electric pulse of defined height, FWHM and with a certain time delay known as a response time of the detector. The height of the electric pulse is modified to precisely correspond to the half-wave voltage of PM1[20]. Then the

[20]The pulse modification is done by passive [1, 2, 4] or active [5] components. Exact implementations of pulse height modification are described later.

electric pulse of the proper height is directly led by a coaxial cable to the PM1. It is necessary to keep the timing of electric pulse application onto the PM1 and presence of the photon in the PM1. Therefore, the photon has to be delayed in several meters long optical fibre delay line. Such fibre delay line is placed in both MZI arms.

Subsequently, the phase inside the MZI is shifted by π rad via PM1. It corresponds to application of required unitary operation operation to the qubit state. Thus the quantum state of qubit II is rotated around z-axis of a Bloch sphere:

$$\alpha|0\rangle - \beta|1\rangle \xrightarrow{\text{feed-forward}} \alpha|0\rangle - e^{i\pi}\beta|1\rangle = \alpha|0\rangle + \beta|1\rangle, \tag{3.48}$$

where $|\alpha|^2+|\beta|^2 = 1$. In other words, information about the measurement result of qubit I is successfully fed-forward into the experiment. Consequently, the output quantum state of qubit II is the same as in the previous case, when the qubit I is detected by D1.

As mentioned above, an electro-optical feed-forward loop is utilized in both variants (a) passive and (b) active. They differ to each other in processing of electric pulses from a single-photon detector.

(a) a passive implementation of the electro-optical feed-forward loop is shown in Fig 3.23(a). It consists of a single photon detector, coaxial cables, a BNC Tee, a potentiometer (acting as a voltage divider), an integrated electro-optical phase modulator implemented in a fibre-based MZI.

The single photon detector, used in this passive implementation, has the response time roughly 17 ns. The produced positive electric pulse has FWHM=30 ns and its height is 2.5 V. The pulse is split by the BNC Tee. One output port is connected by coaxial cable to counting electronics modules terminated by 50 Ω impedance. The second output port is connected through the potentiometer into the PM1 terminated by roughly 43 Ω impedance (at DC). The length of coaxial cables is kept as short as possible, totally 1.2 m. The precise pulse height, corresponding to the half-wave voltage U_π of the PM1, is set by the potentiometer[21].

PM half-wave voltage U_π: Such voltage applied onto a PM changes a phase of transmitted light by π rad, half-wave. In the previous section, we have explained how to measure this PM parameter. However, we do not know, how to precisely set the potentiometer to modify an electric pulse height to the U_π-level. Moreover, when we take into account the imperfect electric pulse shape, the jitter of the detector (0.5 ns) and the coherence length of photon ($\gtrsim$2 ps), we can pre-set approximately the height of the pulse using an oscilloscope. Therefore, the proper potentiometer setting is determined experimentally in the following way.

The precise value of the PM1 U_π is set by observing single photon interference at outputs of the phase stabilized MZI, as shown in Fig. 3.22. First measurement is performed with a disconnected feed-forward loop. Then the constructive and destructive

[21] In each loop implementation, we employ the 10-turn potentiometer as a voltage divider. Its input resistance is 100 Ω, while the output one is tunable in rage 0–100 Ω.

interference should correspond to coincidence rates $C_{2,3}$ and $C_{2,4}$, respectively. After the feed-forward loop connection and potentiometer tuning, the constructive and destructive interference should be perfectly swapped to correspond to coincidences $C_{2,4}$ and $C_{2,3}$, respectively. There should be no difference between normalized coincidence rates with detectors D1 and D2 ($C_{1,3} \approx C_{2,3}$ and $C_{2,4} \approx C_{2,4}$).

To verify the potentiometer setting, we check the coincidence rates again when the phase inside stabilized MZI is shifted by $\pi/2$. It is a position in the middle of the interference fringe. The coincidence rates $C_{2,3}$ and $C_{2,4}$ should be the same, $C_{2,3} \approx C_{2,4}$, even with connected or disconnected feed-forward loop. If they are not equal to each other, the potentiometer should be slightly tuned to set the correct U_π value.

Timing: It is necessary to synchronize the electric pulse application onto the PM1 and the presence of the photon in the PM1. The coherence time of the photon from the photon pair is $\gtrsim$2 ps. The detector jitter is 0.5 ns. We try to choose the electric pulse plateau, far from the leading edge, in the first half of the pulse (roughly 10-th ns of the pulse with the overall FWHM of 30 ns). Because of the response time of the detector (17 ns), chosen position in electric pulse (10 ns) and overall delay in coaxial cables (6 ns), therefore, the photon is delayed roughly **33 ns** in **6.6-m**-long optical fibre delay line, placed in each MZI arm.

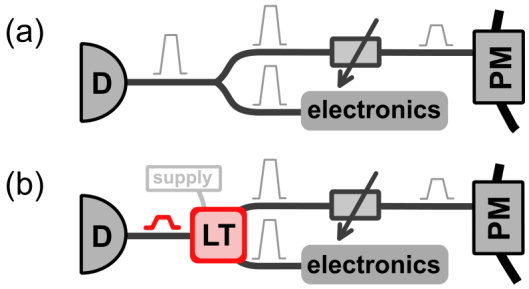

Figure 3.23: Illustration of a feed-forward loop implementation (a) passive variant, (b) active variant. It is depicted by yellow colour in Fig 3.21 and 3.22. D – single photon detector; PM – integrated electro-optical phase modulator (10 GHz, EOSPACE); electronics – electronics for a signal processing; LT – level translator (74LVC4245A).

(b) an active implementation of the feed-forward loop is shown in Fig 3.23(b). Here we describe mainly the differences between passive and active versions of the loop. In an active implementation, the height of an electric pulse from the detector could not be only decreased as in the passive version, however, it can be amplified. This version is developed, because of a newer and faster single photon detector with response time roughly 14 ns and jitter 0.5 ns. This detector produces electric pulses with FWHM=7 ns and pulse height only 1.4 V. Unfortunately, the electric pulse height is not high enough, to be directly used as the half-wave voltage of the PM1. This problem is solved by an active element, level translator 74LVC4245A, placed instead of the passive T BNC connector (details of the level translator are listed at the end of this section). At the output of the level translator the electric pulses are amplified and delayed by approximately 3 ns. The precise pulse height corresponding to U_π of the PM1 is set by the potentiometer. The other wiring and electric elements are roughly the same. The coaxial cables are kept as

short as possible, totally 1 m. Just the **timing** is re-adjusted. The photon passes through the PM1 when the central part of the short electric pulse is applied onto the PM1. Thus the photon is delayed by roughly **25 ns**, it corresponds to **5-m**-long optical fibre delay line inside MZI.

Discussion. Feed-forward action requires approximately 25 ns. However, the loop could be even faster by optimizing the experimental implementation: by using a single-photon detector with shorter response time; improving of the timing, it could be shifted closer to the leading edge of electric pulse; re-designing of the experimental setup at the optical table, it could help shorten the coaxial cables; usage of faster electronics.

Here should be also stressed that the feed-forward loop it not restricted only to phase changes and it is definitely not restricted to phase change by π. It can perform also amplitude changes by replacing a PM by an amplitude modulator (AM). Both the PM and AM devices and their adjustable functions can also be suitable combined or multiplied [60].

Pinout of the active level translator: type 74LVC4245A: Octal dual supply translating transceiver (3-state, from NXP Semiconductors). Pins 21, 20 are used for data input. Pins 3, 4 are used for data output. The active level translator is powered by laboratory source through pins 23, 24 (1). We found out the optimal supply voltages for our application and set them: input to U_{IN}=4.0 V and output to U_{OUT}=4.8 V. The common ground is connected between pins 2, 11, 12, 13, 22.

3.10 Toolbox for experiment characterization

In this section, we briefly introduce the typical toolbox for experiment characterization which serves for comparison between experiment and theory. Moreover, we explain how the data utilized for the experiment characterization are measured.

First, let us remind that in experiments described in this Thesis we employ photon pairs and one qubit is encoded into each of these photons . A projective measurement is applied onto the idler qubit I. The measurement result is used as a part of the feed-forward loop. Alternatively the photon I is used as a trigger.

According to a nature of an experiment, we choose the most suitable method for the experimental result characterization. In general, we can compare normalized coincidence rates between detectors applying the projective measurement on qubits I and II. We can fully characterize an output state of a qubit II and calculate a state fidelity and a purity. Or we can fully characterize a whole process, i.e. reconstruct a quantums process matrix and calculate a process fidelity and a purity [11].

3.10.1 Quantum state tomography

To reconstruct a quantum state, the quantum state tomography has to be used. It consists of several suitably chosen projective measurements applied to the quantum state. The measured data are processed by the iterative reconstruction algorithm [125, 191] from which we obtain the reconstructed density matrix ρ. For a two-level system it is 2×2 matrix.

We utilize measurements, which are similar to measurement of Stokes parameters, when a polarization state of light and its degree of polarization are determined. However, we do not measure classical light intensities, but photon count rates. Thus we have to repeat the state preparation and measurements till we accumulate an adequate amount of data. It enables us to reconstruct the quantum state with required statistical uncertainty.

When the qubit is encoded into polarization degree of freedom, the tomography measurement is realized as projections onto set of polarization states. We use six-state analysis and the particular set of states used is: $\{|H\rangle, |V\rangle, |D\rangle, |A\rangle, |R\rangle, |L\rangle\}$. $|H\rangle$ and $|V\rangle$ denote horizontal and vertical linear polarization states, respectively. These states are used as computational basis states in our experiments. $|D\rangle$ and $|A\rangle$ denote diagonal and antidiagonal linear polarization states, respectively. They are defined as $|D\rangle = (|H\rangle + |V\rangle)/\sqrt{2}$, $|D\rangle = (|H\rangle - |V\rangle)/\sqrt{2}$. $|R\rangle$ and $|L\rangle$ denote right and left hand circular polarization state, respectively, defined as $|R\rangle = (|H\rangle + i|V\rangle)/\sqrt{2}$, $|L\rangle = (|H\rangle - i|V\rangle)/\sqrt{2}$.

Analogically, the tomography measurement can be expressed in a spatial encoding with basis states $|0\rangle$ and $|1\rangle$. When $|0\rangle \approx |H\rangle$ and $|1\rangle \approx |V\rangle$, then the projection set is defined as $\{|0\rangle, |1\rangle, |+\rangle, |-\rangle, |+i\rangle, |-i\rangle\}$. The states $|\pm\rangle$ and $|\pm i\rangle$ are defined as follows $|\pm\rangle = (|0\rangle \pm |1\rangle)/\sqrt{2}$, and $|\pm i\rangle = (|0\rangle \pm i|1\rangle)/\sqrt{2}$.

The reconstructed density matrix ρ of analyzed quantum state can be compared with the expected results. We can calculate characteristics like a quantum state fidelity or purity.

• The quantum **state fidelity** measures how two quantum states ρ, ρ_{id} are "similar". It is calculated as [192]:

$$\mathcal{F} = \mathcal{F}(\rho_{\mathrm{id}}, \rho) = \left[\mathrm{Tr}\sqrt{\sqrt{\rho_{\mathrm{id}}}\ \rho\ \sqrt{\rho_{\mathrm{id}}}}\right]^2 \tag{3.49}$$

where the density matrix ρ describes the reconstructed state and ρ_{id} denotes the desired ideal state. In general, pure and normalized state fulfils $\sqrt{\rho} = \rho = |\psi\rangle\langle\psi|$ and $\mathrm{Tr}[\rho] = 1$. Thus, when at least the ideal state is pure, the fidelity can be rewritten as $\mathcal{F} = \left[\mathrm{Tr}\sqrt{|\phi_{\mathrm{id}}\rangle\langle\phi_{\mathrm{id}}|\rho|\phi_{\mathrm{id}}\rangle\langle\phi_{\mathrm{id}}|}\right]^2 = \langle\phi_{\mathrm{id}}|\rho|\phi_{\mathrm{id}}\rangle\ \ \mathrm{Tr}\left[\sqrt{|\phi_{\mathrm{id}}\rangle\langle\phi_{\mathrm{id}}|}\right]^2$,

$$\mathcal{F} = \mathcal{F}(\rho_{\mathrm{id}}, \rho) = \langle\phi_{\mathrm{id}}|\rho|\phi_{\mathrm{id}}\rangle. \tag{3.50}$$

When both these states are pure the quantum state fidelity is given as an overlap of the ideal state $|\phi_{\mathrm{id}}\rangle$ with the reconstructed state $|\psi\rangle$. $\mathcal{F} = \left[\mathrm{Tr}\sqrt{|\phi_{\mathrm{id}}\rangle\langle\phi_{\mathrm{id}}|\psi\rangle\langle\psi|\phi_{\mathrm{id}}\rangle\langle\phi_{\mathrm{id}}|}\right]^2 = \langle\phi_{\mathrm{id}}|\psi\rangle\langle\psi|\phi_{\mathrm{id}}\rangle\ \ \left[\mathrm{Tr}\sqrt{|\phi_{\mathrm{id}}\rangle\langle\phi_{\mathrm{id}}|}\right]^2$,

$$\mathcal{F} = \mathcal{F}(\rho_{\mathrm{id}}, \rho) = \left|\langle\phi_{\mathrm{id}}|\psi\rangle\right|^2. \tag{3.51}$$

One should also note, that the fidelity is bounded $0 \leq \mathcal{F} \leq 1$. $\mathcal{F} = 1$ if and only if $\rho_{\mathrm{id}} = \rho$ and $\mathcal{F} = 0$ when these two states are orthogonal.

• The quantum **state purity** is defined as:

$$\mathcal{P} = \mathcal{P}(\rho) = \mathrm{Tr}\left[\rho^2\right], \tag{3.52}$$

where ρ is the density matrix of the normalized quantum state. The purity gives us information how much the quantum state is mixed or pure. It is bounded $1/d \leq \mathcal{P} \leq 1$, where d is a dimension of the state Hilbert space. For a pure state the purity is $\mathcal{P} = \mathrm{Tr}\left[\rho^2\right] = \mathrm{Tr}\left[\rho\right] = 1$. However, for maximally mixed state is $\mathcal{P} = 1/d$.

3.10.2 How to implement the quantum state tomography measurement and the data acquisition

Here, we explain how to experimentally realize the quantum state tomography measurement via bulk or fibre-based components.

The polarization state analysis consists of HWP, QWP, and linear polarizer realized by a PBS. The state of light is transformed by the wave plates in such way that the polarizer realizes a projection onto required polarization state. In another word, the polarization state from the set $\{|H\rangle, |V\rangle, |D\rangle, |A\rangle, |R\rangle, |L\rangle\}$ is transferred to $|H\rangle$ state. $|H\rangle$ state is transmitted by the PBS and further detected. It is schematically described in the diagram bellow and shown in Fig. 3.24(a).

$$
\begin{array}{lcllcll}
|H\rangle & \rightarrow & \mathrm{HWP}(0°) & \rightarrow & \mathrm{QWP}(0°) & \rightarrow & |H\rangle \\
|V\rangle & \rightarrow & \mathrm{HWP}(45°) & \rightarrow & \mathrm{QWP}(0°) & \rightarrow & |H\rangle \\
|D\rangle & \rightarrow & \mathrm{HWP}(22.5°) & \rightarrow & \mathrm{QWP}(0°) & \rightarrow & |H\rangle \\
|A\rangle & \rightarrow & \mathrm{HWP}(\text{-}22.5°) & \rightarrow & \mathrm{QWP}(0°) & \rightarrow & |H\rangle \\
|R\rangle & \rightarrow & \mathrm{HWP}(22.5°) & \rightarrow & \mathrm{QWP}(45°) & \rightarrow & |H\rangle \\
|L\rangle & \rightarrow & \mathrm{HWP}(22.5°) & \rightarrow & \mathrm{QWP}(\text{-}45°) & \rightarrow & |H\rangle
\end{array}
$$

Polarization state analysis utilizing just one detector requires to perform six independent measurement runs. However, such analysis can be also performed in three measurement runs using two detectors. The measurement is realized in orthogonal measurement basis $\{\{|H\rangle, |V\rangle\}, \{|D\rangle, |A\rangle\}, \{|R\rangle, |L\rangle\}\}$. The PBS transmits and reflects $|H\rangle$ and $|V\rangle$ states, respectively. Thus the measurement basis is fully determined by the HWP and QWP rotation in front of the PBS. Further, the photon can be detected by one of the two detectors. The detectors relative detection efficiencies have to be calibrated. The analysis is schematically described in the diagram bellow and shown in Fig. 3.24(b).

$$
\begin{array}{lcllcll}
|H\rangle\ (|V\rangle) & \rightarrow & \mathrm{HWP}(0°) & \rightarrow & \mathrm{QWP}(0°) & \rightarrow & |H\rangle\ (|V\rangle) \\
|D\rangle\ (|A\rangle) & \rightarrow & \mathrm{HWP}(22.5°) & \rightarrow & \mathrm{QWP}(0°) & \rightarrow & |H\rangle\ (|V\rangle) \\
|R\rangle\ (|L\rangle) & \rightarrow & \mathrm{HWP}(22.5°) & \rightarrow & \mathrm{QWP}(45°) & \rightarrow & |H\rangle\ (|V\rangle)
\end{array}
$$

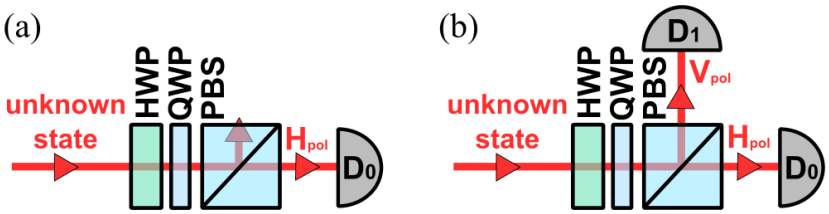

Figure 3.24: Scheme of polarization state analysis (a) measurement of individual projections, utilized one detector (b) measurement in orthogonal basis, utilized two detectors. HWP – half-wave plate, QWP – quarter-wave plate, PBS – polarizing beam splitter, D – single-photon detector, $\mathrm{H_{pol}}$ ($\mathrm{V_{pol}}$) – horizontal (vertical) linear polarization.

Moreover, we can perform the quantum state tomography measurement via fibre-based MZI. The measurement basis is determined by the relative phase between MZI arms and by the splitting ratio of output fibre beam splitter. When the output beam splitter has a variable splitting ratio, R:T, the state analysis can be performed in three measurement runs using two detectors $\{\{|0\rangle, |1\rangle\}, \{|+\rangle, |-\rangle\}, \{|+i\rangle, |-i\rangle\}\}$. It is schematically described in the table bellow and shown in Fig. 3.25(a).

phase [rad]	R:T [%]	→	projection onto states	
no int.*	100:0	→	$\|0\rangle, \|1\rangle$	clicks of D_0, D_1, respectively
0	50:50	→	$\|+\rangle$, $\|-\rangle$	clicks of D_0, D_1, respectively
$\pi/2$	50:50	→	$\|+i\rangle$, $\|-i\rangle$	clicks of D_0, D_1, respectively

* "no int." means, there is no interferometer, because of the $R:T = 100:0$. The phase can be arbitrary.

However, when the output beam splitter with fixed splitting ratio 50:50 is employed instead of the variable ratio coupler, the state analysis can be performed in four measurement runs using two detectors $\{\{|0\rangle\}, \{|1\rangle\}, \{|+\rangle, |-\rangle\}, \{|+i\rangle, |-i\rangle\}\}$. It is schematically described in the table bellow and shown in Fig. 3.25(b).

phase [rad]	R:T [%]	→	projection on to states	
blocked arm 1, no int.*	50:50	→	$\|0\rangle$	sum of the clicks $D_0 + D_1$
blocked arm 0, no int.*	50:50	→	$\|1\rangle$	sum of the clicks $D_0 + D_1$
0	50:50	→	$\|+\rangle$, $\|-\rangle$	clicks of D_0, D_1, respectively
$\pi/2$	50:50	→	$\|+i\rangle$, $\|-i\rangle$	clicks of D_0, D_1, respectively

* "no int." means, there is no interferometer because one of the MZI arms is interrupted.

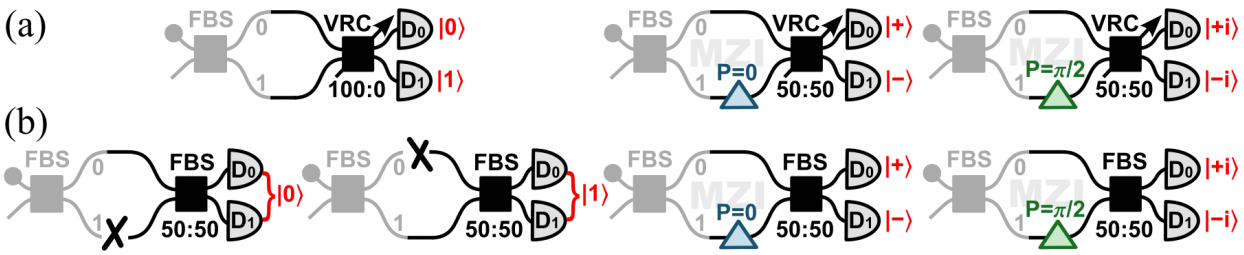

Figure 3.25: Scheme of the state analysis using fibre-based MZI (a) in three measurement runs utilizing VRC and two detectors, (b) in four measurement runs utilizing FBS and two detectors. VRC – variable ratio coupler, FBS – fixed balanced fibre beam splitter (50:50), P – phase between the MZI arms, D – single photon detector.

3.10.3 Brief introduction to quantum process tomography

Any quantum operation can be fully described by a completely positive (CP) map. According to the Choi-Jamiolkowski isomorphism, any CP map can be represented by a positive-semidefinite operator χ acting on the tensor product of input and output Hilbert spaces $\mathcal{H}_{\text{in}}$ and $\mathcal{H}_{\text{out}}$, respectively [193, 194]. The input state ρ_{in} is transformed to output state as: $\rho_{\text{out}} = Tr_{\text{in}}[\chi(\rho_{\text{in}}^T \otimes I_{\text{out}})]$ [22]. Combinations of different input states with measurements on the output quantum system represent effective measurements performed on $\mathcal{H}_{\text{in}} \otimes \mathcal{H}_{\text{out}}$. A proper selection of input states and final measurements makes possible to reconstruct the Choi matrix χ from the measured data. For the reconstruction, we use maximum-likelihood (ML) estimation technique [125, 191].

When we fully characterize the process by a quantum process tomography, we calculate the Choi matrix χ. Then we can determine the density matrix of the output state ρ_{out} for any input state ρ_{in}. In our case both Hilbert spaces are two-dimensional, thus the process matrix χ is 4×4.

The Choi matrix of the ideal process χ_{id} is obtained from the maximally entangled Bell state $|\Phi^+\rangle = (|HH\rangle + |VV\rangle)/\sqrt{2}$, when one of its parts is propagated through the ideal transformation corresponding to the experimental setup. The ideal process is usually represented by unitary operation U. Then the ideal process matrix can be written as: $\chi_{\text{id}} = |I\rangle \otimes U|\Phi^+\rangle\langle\Phi^+|U^\dagger \otimes \langle I|$ [23].

• The **process fidelity** compares two quantum processes, real process described by the reconstructed process matrix χ and the ideal desired process described by χ_{id}. The process fidelity tells us how much these two processes are "similar". It is given as:

$$\mathcal{F}_\chi = \mathcal{F}(\chi_{\text{id}}, \chi) = \frac{\text{Tr}\left[\chi\chi_{\text{id}}\right]}{\text{Tr}\left[\chi\right]\text{Tr}\left[\chi_{\text{id}}\right]}. \tag{3.53}$$

When χ_{id} is not a "pure state" but both χ and χ_{id} are normalized, it is given as:

$$\mathcal{F}_\chi = \mathcal{F}(\chi_{\text{id}}, \chi) = \left[\text{Tr}\sqrt{\sqrt{\chi_{\text{id}}}\ \chi\ \sqrt{\chi_{\text{id}}}}\right]^2. \tag{3.54}$$

3.10.4 How to implement the data acquisition for the quantum process tomography

For a process acting on a single qubit, we explain how the quantum process tomography measurement can be realized experimentally. We experimentally prepare a set of six input quantum states, typically $\{|H\rangle, |V\rangle, |D\rangle, |A\rangle, |R\rangle, |L\rangle\}$ or $\{|0\rangle, |1\rangle, |+\rangle, |-\rangle, |+i\rangle, |-i\rangle\}$ depending on the qubit encoding. For each of these input states, we perform the same set of measurements as we used in quantum state tomography described above. In total, we perform 36 (6 input states $*$ 6 output measurements) projective of measurements. Further, we show how to prepare the input quantum state. We show how to encode the qubit state into the carrier photon using polarization or spatial mode encoding.

[22] We trace over input Hilbert space. T denotes transposition and I denotes identity operation.
[23] $\dagger$ denotes Hermitian conjugation.

Qubit encoding into the polarization degree of freedom – first, we need a photon in defined polarization state. Therefore, the photon passes a linear polarizer (PBS), and it is horizontally linearly polarized. Subsequently, an arbitrary state is encoded via QWP and HWP. It is schematically described in the table bellow and shown in Fig. 3.26.

$\|H\rangle$	$\rightarrow$	QWP(0°)	$\rightarrow$	HWP(0°)	$\rightarrow$	$\|H\rangle$
$\|H\rangle$	$\rightarrow$	QWP(0°)	$\rightarrow$	HWP(45°)	$\rightarrow$	$\|V\rangle$
$\|H\rangle$	$\rightarrow$	QWP(0°)	$\rightarrow$	HWP(22.5°)	$\rightarrow$	$\|D\rangle$
$\|H\rangle$	$\rightarrow$	QWP(0°)	$\rightarrow$	HWP(-22.5°)	$\rightarrow$	$\|A\rangle$
$\|H\rangle$	$\rightarrow$	QWP(45°)	$\rightarrow$	HWP(22.5°)	$\rightarrow$	$\|R\rangle$
$\|H\rangle$	$\rightarrow$	QWP(-45°)	$\rightarrow$	HWP(22.5°)	$\rightarrow$	$\|L\rangle$

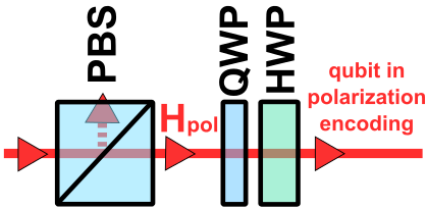

Figure 3.26: Scheme of a qubit state preparation in polarization encoding. PBS – polarizing beam splitter, QWP – quarter-wave plate, HWP – half-wave plate, H_{pol} – horizontal linear polarization state of light.

Qubit encoding into the spatial degrees of freedom using fibre-based components can be realized via a balanced fibre beam splitter with fixed splitting ratio (FBS) and phase modulator (PM) or via fibre beam splitter with variable splitting ratio (VRC) and PM. The option utilizing VRC+PM enables us to prepare arbitrary state $t|0\rangle + e^{i\varphi}r|1\rangle$, where $\varphi \in [0, 2\pi]$ and r, t denote set VRC amplitude reflectance and transmittance.

While the simpler option employing balanced FBS+PM enables us to prepare only the equatorial states $(|0\rangle + e^{i\varphi}|1\rangle)/\sqrt{2}$, where $r = t = 1/\sqrt{2}$. However, if we add an attenuator with intensity transmittance $\mathcal{A}$ into appropriate port, we can prepare any state $(\sqrt{\mathcal{A}}|0\rangle + e^{i\varphi}|1\rangle)/\sqrt{\mathcal{A}+1}$. But non-equatorial states $(0 \leq \mathcal{A} < 1)$ have lower success probability. It is schematically described in the table bellow and shown in Fig. 3.27.

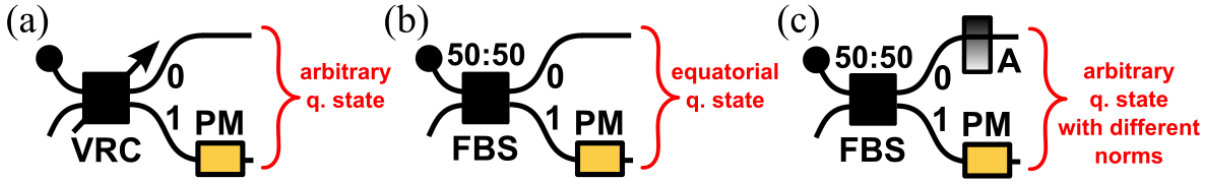

Figure 3.27: Scheme of a qubit state preparation in spatial encoding. Preparation of: (a) arbitrary quantum state via VRC+PM, (b) equatorial state via FBS+PM, (c) arbitrary quantum state via FBS+PM+A. VRC – fibre variable ratio coupler, FBS – fixed balanced fibre beam splitter (50:50), PM – phase modulator, A – attenuation of the basis state.

R:T [%]	phase* [rad]	→	prepared states
50:50	0	→	$\|+\rangle$
50:50	$-\pi$	→	$\|-\rangle$
50:50	$\pi/2$	→	$\|+i\rangle$
50:50	$-\pi/2$	→	$\|-i\rangle$
100:0	0	→	$\|0\rangle$
0:100	0	→	$\|1\rangle$

R:T [%]	phase* [rad]	$\mathcal{A}$**	→	prepared states
50:50	0	$0 \cdot \|1\rangle$	→	$\|0\rangle/\sqrt{2}$
50:50	0	$0 \cdot \|0\rangle$	→	$\|1\rangle/\sqrt{2}$

* Denotes phase encoded by PM placed at the port corresponding the basis state $|1\rangle$.

** Denotes the basis state attenuation. For example, $0 \cdot |1\rangle$ means the basis state $|1\rangle$ is completely blocked.

During the experiment, it is sometimes convenient to change the form of qubit encoding. Here, we show how to **re-encode the quantum state of photonic qubit** from polarization degree of freedom into spatial one, or vice versa.

In our experiments, it is done by a PBS which is appropriately sets to separate the polarization basis states. When the basis states are $|H\rangle$ and $|V\rangle$, then the PBS spatially separates horizontally and vertically polarized light into spatial modes $|0\rangle$ and $|1\rangle$, respectively. It is schematically shown in Fig. 3.28. However, when the basis states are $|D\rangle, |A\rangle$, then the PBS has to be rotated into their basis, or the basis states have to be transformed by HWP(22.5°) into the basis of the PBS, $|D\rangle \rightarrow |H\rangle$ and $|A\rangle \rightarrow |V\rangle$. Then the PBS again spatially separates horizontally and vertically polarized light into spatial modes $|0\rangle$ and $|1\rangle$, respectively. Subsequently, the linearly polarized light in the spatially separated modes is usually coupled into the slow axis of polarization maintaining optical fibres. Next, it can be led for instance to a fibre beam splitter (FBS) to interfere. Then the quantum state tomography can be applied onto the state via the FBS as described above.

The qubit re-encoding from polarization into spatial degrees of freedom is shown in Fig. 3.28. It works also in opposite direction and the spatially encoded qubit can be transformed by this scheme into the polarization encoded one.

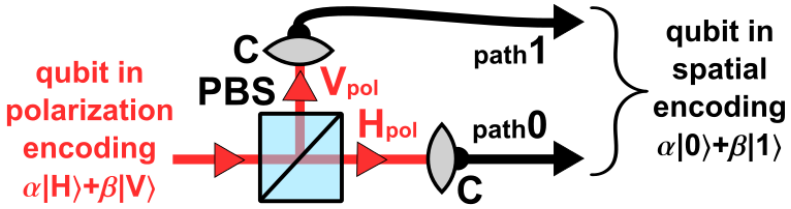

Figure 3.28: Scheme of a qubit re-encoding from polarization degree of freedom into the spatial one. PBS – polarizing beam splitter, C –coupling lens, black line – polarization maintaining optical fibre, red line – free space light, see text for details.

Chapter 4

Increasing efficiency of a linear-optical quantum gate using electronic feed-forward loop

This chapter is based on the following publication:

[1] Martina Miková, Helena Fikerová, Ivo Straka, Michal Mičuda, Jaromír Fiurášek, Miroslav Ježek, and Miloslav Dušek. *Increasing efficiency of a linear-optical quantum gate using electronic feed-forward.* Physical Review A **85**, 012305 (2012).

4.1 Basic idea

As already mentioned, the probabilistic programmable phase gate is proposed by Vidal, Masanes, and Cirac [6]. The gate rotates a single-qubit state along the z-axis of the Bloch sphere. In other words, the arbitrary input state $\alpha|0\rangle + \beta|1\rangle$ is at the output of the gate rotated in following way $\alpha|0\rangle + e^{i\varphi}\beta|1\rangle$. In the simplest case, the angle of rotation, the phase shift φ, is programmed into the state of a single qubit. Thus according to [6] the overall gate success probability is limited by 50 %. Let us stress, that this programmable quantum phase gate has no classical analogy. An exact specification of the angle of rotation φ would require infinitely many classical bits.

For the first time, the gate was experimentally implemented in 2008 [7]. It was based on linear optics using bulk elements. Its success probability reached only 25 %. Later in 2012, we showed how to increase the success probability of the gate to its quantum mechanical limit of 50 %[24] by means of electronic feed forward loop [1].

I started to work on this experiment during my Master's studies. I have finished it at the beginning of my Ph.D. studies. Therefore particular details about the experimental layout are described in my Master's thesis [169]. Here we focus mainly on the full characterization of the gate by means of quantum process tomography.

[24] The success probabilities discussed here do not include signal attenuation due to technological losses.

4.2 Theory

Here I would like to stress, that the theoretical part of [1] is not my work. A part of the theory directly related to the experiment is described below. For more details see also [6].

The programmable phase gate is a two-qubit gate, consisting of a data and a program qubit. The gate can be experimentally implemented by the linear optical setup shown in Fig. 4.1. The qubits are encoded into the states of single photons using spatial encoding. It means, each qubit is represented by a single photon which may propagate into two optical fibres. Basis states $|0\rangle$ and $|1\rangle$ correspond to the presence of the photon in the first or the second fibre, respectively.

The gate performs a unitary evolution of the data qubit (D) which depends on the state of the program qubit (P).

$$U(\varphi) = |0\rangle_D\langle 0| + e^{i\varphi}|1\rangle_D\langle 1|. \tag{4.1}$$

The program qubit contains information about the phase shift φ encoded in following way $|\psi\rangle_P = (|0\rangle_P + e^{i\varphi}|1\rangle_P)/\sqrt{2}$.

Without loss of generality, we can consider only pure input states of the data qubit $|\psi_{\text{in}}\rangle_D = \alpha|0\rangle_D + \beta|1\rangle_D$, where $|\alpha|^2 + |\beta|^2 = 1$. Then the initial state of the gate is:

$$|\psi\rangle_P \otimes |\psi_{\text{in}}\rangle_D = (\alpha|0\rangle_P \otimes |0\rangle_D + \beta|0\rangle_P \otimes |1\rangle_D + \alpha e^{i\varphi}|1\rangle_P \otimes |0\rangle_D + \beta e^{i\varphi}|1\rangle_P \otimes |1\rangle_D)/\sqrt{2}. \tag{4.2}$$

The gate operation can be described as follows[25] $|0\rangle_P \to |0\rangle_P, |1\rangle_P \to |1\rangle_D, |1\rangle_D \to |1\rangle_P$, $|0\rangle_D \to |0\rangle_D$, modes corresponding to $|1\rangle_D$ and $|1\rangle_P$ are swapped. After passing though the gate the overall state reads:

$$(\alpha|0\rangle_P \otimes |0\rangle_D + \beta|0\rangle_P \otimes |1\rangle_P + \alpha e^{i\varphi}|1\rangle_D \otimes |0\rangle_D + \beta e^{i\varphi}|1\rangle_D \otimes |1\rangle_P)/\sqrt{2}. \tag{4.3}$$

If we consider only cases when a single photon emerges in each output port of the gate (it corresponds to the coincidence measurement), the conditional two-photon output state is:

$$(\alpha|0\rangle_D \otimes |0\rangle_P + \beta e^{i\phi}|1\rangle_D \otimes |1\rangle_P)/\sqrt{2}, \tag{4.4}$$

(the normalization reflects the fact that the probability of this situation is 1/2). We can rewrite this state as:

$$\left[(\alpha|0\rangle_D + \beta e^{i\varphi}|1\rangle_D)\otimes|+\rangle_P + (\alpha|0\rangle_D - \beta e^{i\varphi}|1\rangle_D)\otimes|-\rangle_P\right]/2, \tag{4.5}$$

where $|\pm\rangle_P = (|0\rangle_P \pm |1\rangle_P)/\sqrt{2}$. If we realize a measurement on the program qubit in the basis $\{|\pm\rangle_P\}$, then the output state of the data qubit collapses into one of the two following states according to the result of the measurement:

$$|\psi_{\text{out}\pm}\rangle_D = \alpha|0\rangle_D \pm \beta e^{i\varphi}|1\rangle_D. \tag{4.6}$$

[25] Notice, that each of these kets represents a single photon in one of four modes (fibres).

If the measurement outcome is $|+\rangle_P$, then the unitary transformation $U(\varphi)$ is applied to the data qubit. If the outcome is $|-\rangle_P$, then $U(\varphi + \pi)$ is executed. Than the data-qubit state acquire an extra π phase shift. The corrective phase shift of $-\pi$ is applied via the food-forward loop PM. (However, in practice we apply a phase shift of π which is equivalent.) Subsequently, the final output state of the data qubit reads:

$$|\psi_{\text{out}}\rangle_D = \alpha|0\rangle_D + e^{i\varphi}\beta|1\rangle_D. \tag{4.7}$$

4.3 Experiment

Scheme of the experimental setup is shown in Fig. 4.1.

Photon pair: Pairs of photons are created by type-II collinear frequency-degenerate spontaneous parametric down conversion (SPDC) in a two-millimetre long BBO crystal pumped by a diode laser (Coherent Cube) at 405 nm [177, 185] (it is not shown in the figure, for details see Fig. 3.20 in *Chapter 3, Methods and Tools*). Photons of each pair are separated by a polarizing beam splitter and coupled into single-mode fibres (780-HP). The same polarization states are set on both photons via fibre polarization controllers (PCs).

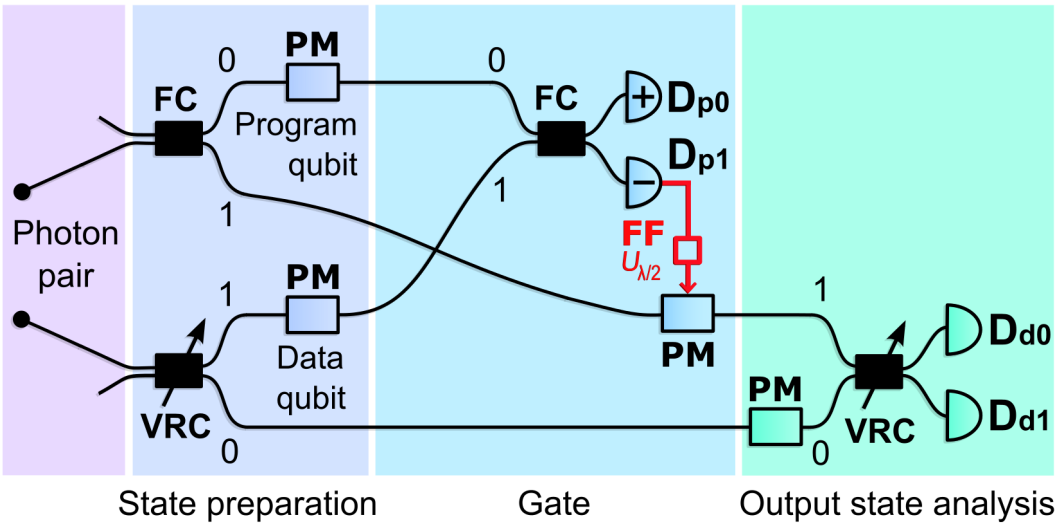

Figure 4.1: Scheme of the experimental implementation of the programmable quantum phase gate. FC – fibre coupler, VRC – variable ratio coupler, PM – phase modulator, FF – electro-optical feed-forward loop, D – detector. Photo of the experimental setup is shown at the end of this chapter in Fig 4.4

State preparation: By means of fibre beam splitters and phase modulators (PMs), required input states of the program and data qubits are prepared. To prepare a program-qubit state $|\psi\rangle_P = (|0\rangle_P + e^{i\varphi}|1\rangle_P)/\sqrt{2}$ the balanced beam splitter with fixed splitting ratio 50:50 (FC) is used. An arbitrary state of the data qubit $|\psi_{\text{in}}\rangle_D = \alpha|0\rangle_D + \beta|1\rangle_D$ is prepared via the variable ratio coupler (VRC). All employed PMs are based on the linear electro-optic effect in lithium niobate. Their half-wave voltages are roughly 1.5 V. These PMs exhibit relatively high dispersion. Therefore, one PM is placed in each interferometer arm in order to compensate dispersion effects. The overall phase of a quantum state is irrelevant. It is equivalent to apply either a phase shift φ to $|1\rangle$ or $-\varphi$ to $|0\rangle$.

Gate: The gate itself consists of exchange of basis states of input qubits $|1\rangle_D$ and $|1\rangle_P$ (swap of two rails) and of the auxiliary measurement on the data qubit (see Fig. 4.1). The measurement in basis $\{|\pm\rangle_P\}$ is accomplished by a fibre coupler with fixed splitting ratio 50:50 and two single-photon detectors. Detectors D_{p0}, D_{d0}, and D_{d1} belong to a quad module SPCM-AQ4C (from PerkinElmer, with total efficiencies 50–60 %, dark counts 370–440 s^{-1}, response time 33–40 ns). A single module SPCM AQR-14FC is used as D_{p1}. It serves for the feed-forward operation, because of its faster response time (from PerkinElmer, total efficiency about 50 %, dark counts 180 s^{-1}, response time 17 ns, the output electric pulse FWHM = 30 ns, height approximately 2.5 V).

To implement the feed forward, the signal from detector D_{p1} is led to a passive voltage divider, in order to change the voltage level to the half-wave voltage level ($\sim$1.5 V). Then it is directly led to the PM to change the phase shift by π. Coaxial cables are as short as possible. The total delay is 33 ns, it includes a response time of the detector and feed-forward loop setting. To compensate this delay, photon wave-packets representing data qubits are retarded by additional fibre delay lines (6,6-m-long fibre in each interferometer arm). The timing of the feed-forward electric pulse and the photon arrivals to the PM are precisely tuned. The coherence time of photons created by our SPDC source is $\gtrsim 2$ ps.

Output state analysis: The right-most block in Fig. 4.1 enables us to measure the data qubit at the output of the gate in an arbitrary basis. These measurements are necessary for the gate performance evaluation.

The experimental setup is formed by two interconnected Mach-Zehnder interferometers (MZI). Total lengths of shorter MZI arms are $\sim$10.5 m (the upper interferometer in Fig. 4.1). The arms lengths of the longer MZI are $\sim$21.5 m (the lower interferometer in Fig. 4.1). To balance the arm lengths we use motorized air gaps with adjustable lengths. In MZI arms equipped with PMs without integrated polarizers we use air gaps also for placing bulk polarizers and wave plates. They select the proper polarization mode of PMs. To obtain high interference visibilities, the polarization states at the end of both interferometer arms must be the same. It is ensured by the PCs.

To reduce the effect of the phase drift caused by fluctuations of temperature and temperature gradients, we apply both passive and active stabilization. The experimental setup is covered by a shield minimizing air flux around components and both fibre delay-lines are coiled on an aluminium cylinder which is thermally isolated. Besides, an active stabilization[26] is performed after each three seconds of measurement. It is based on intensity measurements for phase shifts 0 and $\pi/2$. If necessary it calculates the phase compensation and applies corresponding corrective voltage to the phase modulator. This guarantees a precision of the phase setting during the measurement period better than $\pi/200$. For the stabilization purposes, we use the probe laser diode at 810 nm. To ensure the same spectral range, both the probe beam and SPDC generated photons pass through the same band-pass interference filter (spectral FWHM 2 nm, Andover). During active stabilization, the source is automatically switched from SPDC to the probe beam.

[26]This stabilization procedure is implemented into the MATLAB code by H. Fikerová.

4.4 Measurement

To fully characterize the programmable quantum phase gate, we perform the quantum process tomography as described in *Chapter 3*. To see the influence of the feed-forward loop, we performed the process tomography for both disconnected loop and active loop. We set various combinations of input states and output measurements. From the measured data, we reconstruct the process matrix χ.

For a fixed state of the program qubit, we used six different input states of the data qubit, namely $|0\rangle, |1\rangle, |\pm\rangle = (|0\rangle \pm |1\rangle)/\sqrt{2}$, and $|\pm i\rangle = (|0\rangle \pm i|1\rangle)/\sqrt{2}$. For each of these input states, the output state of the data qubit is measured in three different measurement basis, $\{|0\rangle, |1\rangle\}, \{|\pm\rangle\}$, and $\{|\pm i\rangle\}$. Each time we simultaneously measure two-photon coincidence count rates between detectors D_{p0} & D_{d0}, D_{p0} & D_{d1}, D_{p1} & D_{d0}, D_{p1} & D_{d1} in 12 three-second intervals. Unequal detector efficiencies are compensated by proper rescaling of measured coincidence counts. This procedure is repeated for 7 phase shifts encoded into the program qubit, $\varphi \in \{0, \pi/6, \pi/3, \pi/2, \pi 2/3, \pi 5/6, \pi\} = \{0°, 30°, 60°, 90°, 120°, 150°, 180°\}$. It is schematically shown in Fig 4.2.

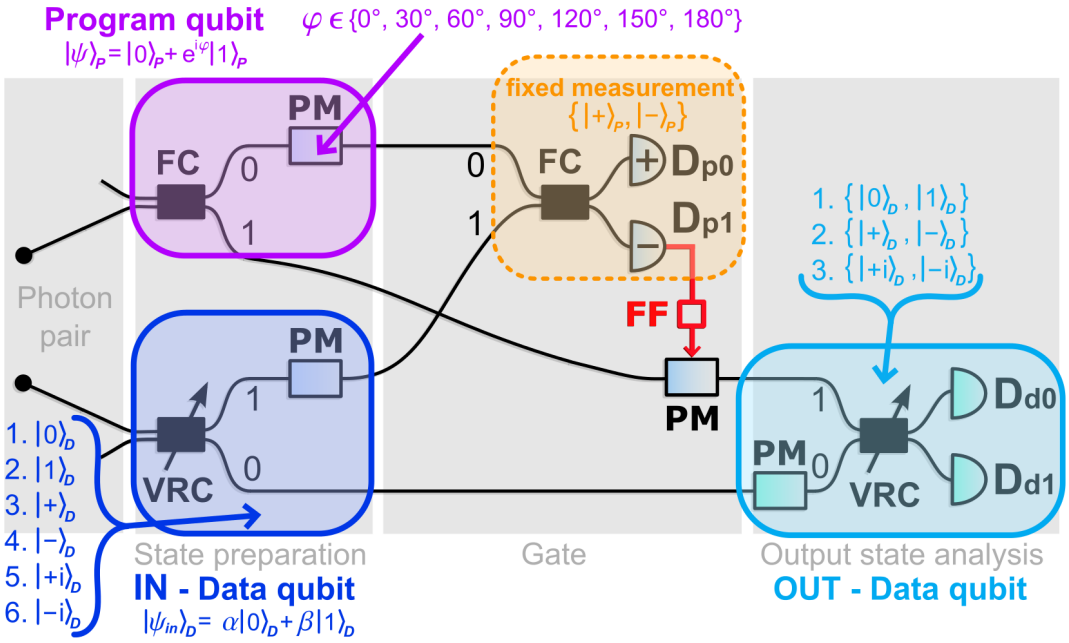

Figure 4.2: Block scheme of the tomographic measurement of the programmable phase gate with the feed-forward loop. FC – fibre coupler, VRC – variable ratio coupler, PM – phase modulator, FF – electro-optical feed-forward loop, D – detector.

4.5 Results

From the measured data, we reconstruct Choi matrices χ describing the function of the gate for several different phase shifts φ. We utilize the maximum likelihood estimation technique [125,191]. In the upper part of Fig. 4.3 there are examples of reconstructed Choi matrices of the programmable phase gate for $\varphi = 0$, $\varphi = \pi/2$ and $\varphi = \pi$, respectively. For comparison, in the lower part of Fig. 4.3, there are examples of ideal Choi matrices of the gate for the same phases φ of the program qubit.

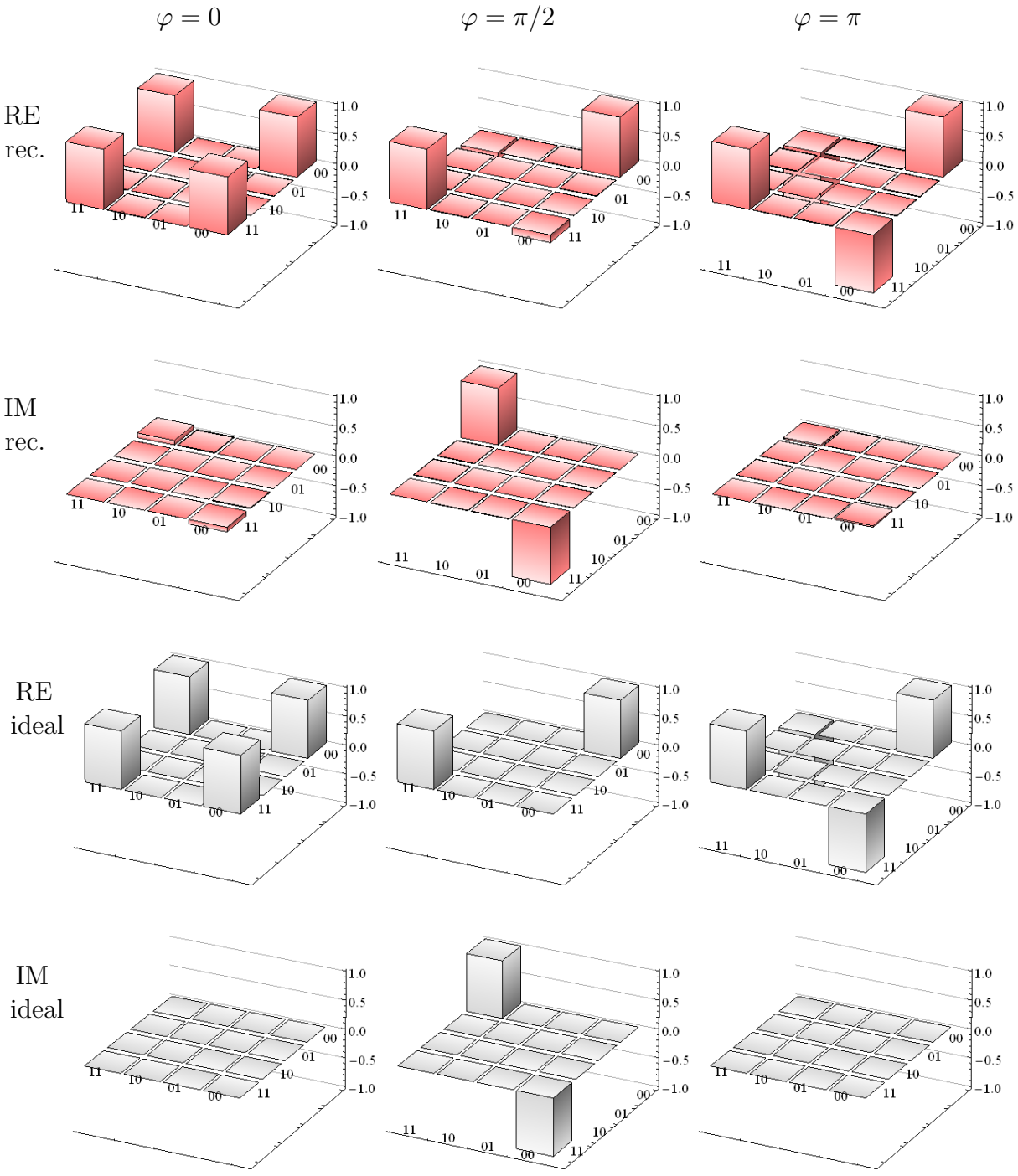

Figure 4.3: Choi matrices of the gate with active feed-forward loop. Upper pink part – reconstructed process matrices, they real (imaginary) parts are displayed in the first (second) row. Lower gray part – ideal process matrices, they real (imaginary) parts are displayed in the third (fourth) row. The left, middle and right columns display process matrices for $\varphi = 0$, $\varphi = \pi/2$ and $\varphi = \pi$ encoded into the program qubit, respectively.

To quantify the quality of gate operation we calculate the process fidelity. If χ_{id} is a one-dimensional projector, then the common definition of the process fidelity is

$$\mathcal{F}_\chi = \mathrm{Tr}[\chi\chi_{\mathrm{id}}]/(\mathrm{Tr}[\chi]\mathrm{Tr}[\chi_{\mathrm{id}}]). \tag{4.8}$$

Here, χ_{id} represents the ideal transformation of our gate. In particular,

$$\chi_{\mathrm{id}} = \sum_{i,j=0,1} |i\rangle\langle j| \otimes U|i\rangle\langle j|U^\dagger, \tag{4.9}$$

where U is the unitary operation (4.1) applied by the gate.

We have also reconstructed density matrices of data qubit output states corresponding to all input states. We calculate their fidelities and purities. The fidelity of output state ρ_{out} is defined as $\mathcal{F} = \langle\psi_{\mathrm{out}}|\rho_{\mathrm{out}}|\psi_{\mathrm{out}}\rangle$, where $|\psi_{\mathrm{out}}\rangle = U|\psi_{\mathrm{in}}\rangle$ with $|\psi_{\mathrm{in}}\rangle$ being the (pure) input state and $\rho_{\mathrm{out}} = \mathrm{Tr}_{\mathrm{in}}[\chi(\rho_{\mathrm{in}}^T \otimes I_{\mathrm{out}})]$ [27]. The purity of the output state is given as $\mathcal{P} = \mathrm{Tr}[\rho_{\mathrm{out}}^2]$. If the input state is pure, the output state is expected to be pure as well.

The left part of the Table 4.1 shows process fidelities for seven different phase shifts with active feed-forward loop. It also shows the average and minimal values of output state fidelities and average and minimal purities of output states. Fidelities and purities are averaged over six output states corresponding to six input states described above. Also minimum values are related to these sets of states. Statistical errors are estimated to be lower than 0.005 for process fidelities and lower than 0.01 for output-state fidelities and purities. Deviations of the experimental values from the ideal ones are mainly due to imperfections in splitting-ratio settings, phase fluctuations, polarization misalignment, and partial distinguishability of the photons in a pair.

To evaluate how the feed-forward affects the performance of the gate, we have also calculated process fidelities, output state fidelities and output state purities for the cases when the feed-forward is not active. It means, that we select only the situations when detector D_{p0} (corresponding to $|+\rangle_P$) clicked and no corrective action is needed (like in Ref. [7]). Coincidences are measured between detectors D_{p0} & D_{d0} and D_{p0} & D_{d1} only. The total coincidence rate (44 coincidences per second in average) is half in comparison with the sum of all conclusive-result rates in the case with active feed-forward (88 coincidences per second in average). Values of fidelities and purities are displayed in the right part of the Table 4.1. One can see that there is no substantial difference between the operation *with* feed-forward (success probability 50 %) and *without* feed-forward (success probability 25 %). In particular, the process fidelity in the case *with* feed forward, averaged over all 7 phases, $\mathcal{F}_\chi^{\mathrm{with}} = 0.976 \pm 0.003$ and the average process fidelity in the case *without* feed-forward $\mathcal{F}_\chi^{\mathrm{without}} = 0.979 \pm 0.005$. The process fidelity remains unchanged and moreover the gate success probability is doubled by the feed-forward loop.

[27] The input state is $\rho_{\mathrm{in}} = |\psi_{\mathrm{in}}\rangle\langle\psi_{\mathrm{in}}|$. $\mathrm{Tr}_{\mathrm{in}}$ is trace over input Hilbert space. T denotes transposition of matrix and I denotes identity operation.

	WITH feed-forward, $p_{\text{succ}} = 50\,\%$					WITHOUT feed-forward, $p_{\text{succ}} = 25\,\%$				
φ	$\mathcal{F}_\chi$	$\mathcal{F}_{\text{av}}$	$\mathcal{F}_{\text{min}}$	$\mathcal{P}_{\text{av}}$	$\mathcal{P}_{\text{min}}$	$\mathcal{F}_\chi$	$\mathcal{F}_{\text{av}}$	$\mathcal{F}_{\text{min}}$	$\mathcal{P}_{\text{av}}$	$\mathcal{P}_{\text{min}}$
0	0.976	0.985	0.970	0.974	0.947	0.977	0.985	0.973	0.975	0.953
$\pi/6$	0.977	0.986	0.972	0.975	0.951	0.975	0.985	0.972	0.973	0.949
$\pi/3$	0.977	0.985	0.970	0.975	0.943	0.988	0.989	0.971	0.980	0.946
$\pi/2$	0.974	0.983	0.973	0.975	0.953	0.979	0.986	0.976	0.976	0.957
$2\pi/3$	0.978	0.987	0.962	0.988	0.961	0.981	0.989	0.966	0.982	0.935
$5\pi/6$	0.972	0.981	0.953	0.974	0.944	0.974	0.984	0.961	0.976	0.947
π	0.980	0.987	0.975	0.977	0.961	0.979	0.986	0.977	0.978	0.960

Table 4.1: Process fidelities ($\mathcal{F}_\chi$), average ($\mathcal{F}_{\text{av}}$) and minimal ($\mathcal{F}_{\text{min}}$) output-state fidelities, average ($\mathcal{P}_{\text{av}}$) and minimal ($\mathcal{P}_{\text{min}}$) output-state purities for different phases (φ). The left part of the table shows the results *with* feed forward ($p_{\text{succ}} = 50\,\%$), while the right part of the table shows the results *without* feed forward ($p_{\text{succ}} = 25\,\%$).

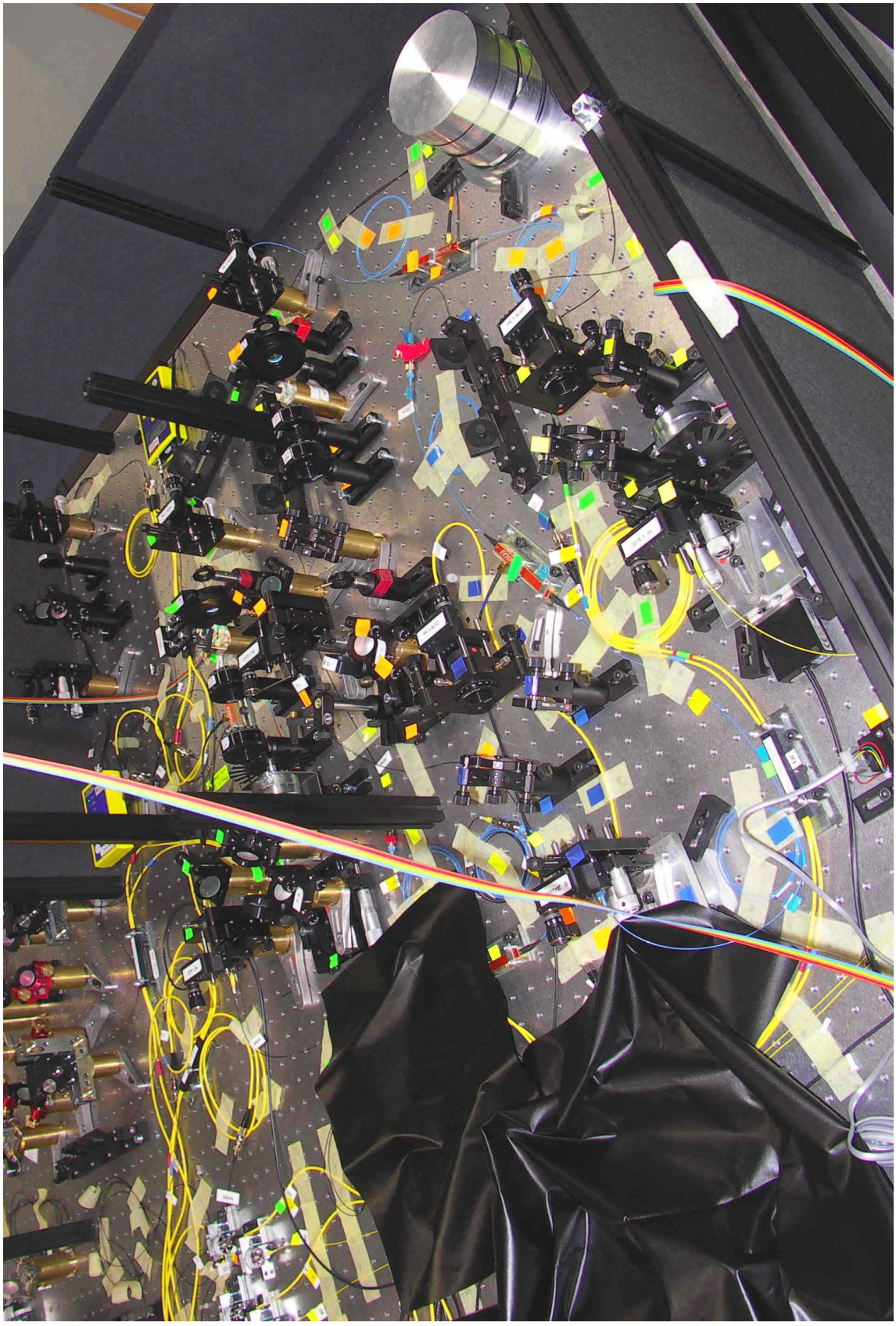

Figure 4.4: Photo of the experimental layout of the programmable quantum phase gate.

Chapter 5

Carrying qubits with particles whose noninformational degrees of freedom are nonfactorable

This chapter is based on the following publication:

[2] Martina Miková, Helena Fikerová, Ivo Straka, Michal Mičuda, Miroslav Ježek, Miloslav Dušek, and Radim Filip. *Carrying qubits with particles whose noninformational degrees of freedom are nonfactorable.* Physical Review A **87**, 042327 (2013).

5.1 Basic idea

Here we experimentally investigate directly measurable parameter, D, quantifying effective indistinguishability of particles. This new measure can be used for an arbitrary quantum state of particles, in contrast to the commonly used overlap of quantum states, which is defined only for factorable states, for details see [2]. To show how distinguishability of particles used as information carriers affects quantum information processing we design a relatively simple linear-optical quantum-state-transfer protocol. It depends only on indistinguishability of particles, so we can exclude influence of other imperfections of resources. We consider the transfer of a state of a source qubit (S) to a target qubit (T). The qubits are represented by single-photons. The transfer is performed by a partial exchange of photons, optimal measurement on S, and conditional feed-forward correction on T. We show that fidelity of the transferred state depends directly on D. The parameter D not only quantifies the effective indistinguishability of particles but also determines an upper bound of quantum state transfer quality. We show that particles can serve as good carriers of qubits even if their internal degrees of freedom are entangled.

The suggested experimental layout follows the setup employed in previous publication [1]. This work [2], focused on the effective indistinguishability of particles quantifying by the measurable parameter, is also summarized by my colleague Helena in her Master's thesis [178].

5.2 Theory

Here we show only a few parts of theoretical results of [2], which are directly related to the experiment. The theory is work of my colleagues.

Let us have two particles, source S and target T, carrying the same qubit states (only certain degrees of freedom are used for encoding qubit states). Subsequently, let $\rho_{E,ST}$ denotes the state, not necessarily separable, of all other (inaccessible) degrees of freedom. Internal *environmental* E degrees of freedom can even be entangled with external environment. Clearly, these environmental degrees of freedom are responsible for distinguishability of particles. The theory of quantum information processing requires all resources to be in the same states which are decoupled from each other, in our notation $\rho_{E,ST} = \rho_{E,S} \otimes \rho_{E,T}$ (their total state must be factorable) and $\rho_{E,S} = \rho_{E,T}$ (environmental states of two spatially separated particles are indistinguishable). But these strict conditions are not always fulfilled in practice.

Let us define a measure $|D|$ quantifying a level of the effective indistinguishability of particles carrying qubits as a mean value of a flip operator:

$$D = \mathrm{Tr}\left[F\,\rho_{E,ST}\right], \tag{5.1}$$

where F is the flip operator acting on the joint environment of both particles, which exchange their basis states. The flip operator has two eigenvalues ± 1, thus $-1 \leq Tr[F\rho] \leq 1$, subsequently $0 \leq |D| \leq 1$.

To demonstrate the relevance of effective indistinguishability $|D|$, we have proposed and experimentally tested the simplest example of a quantum information transfer, where $|D|$ directly determines the quantum fidelity of the transferred state. It manifests a clear operational meaning of the above defined effective indistinguishability.

We consider only equatorial states of the source qubit S

$$|\Psi\rangle_S = (|0\rangle_S + e^{i\varphi}|1\rangle_S)/\sqrt{2}, \tag{5.2}$$

where phase φ may be unknown during the transfer. This state should be transferred to target qubit T represented by another single photon, which is in state

$$|\Phi\rangle_T = (|0\rangle_T + |1\rangle_T)/\sqrt{2} \tag{5.3}$$

at the beginning. In our case, basis states $|0\rangle$ and $|1\rangle$ correspond to the presence of the photon in the first or the second fibre, respectively. All other degrees of freedom, all physical differences between the particles, are described by a density matrix of the environmental state $\rho_{E,ST}$. So the overall initial state reads:

$$\rho_{\mathrm{ini}} = |\Psi\rangle_S\langle\Psi| \otimes |\Phi\rangle_T\langle\Phi| \otimes \rho_{E,ST}. \tag{5.4}$$

To avoid, an imperfect interaction between qubits (which can also limit the quality of the transfer) we consider implementation without any direct interaction. The transfer of the quantum state is performed by a partial exchange of the photons. Thus we swap two rails between S and T see Fig. 5.2 and it swaps some of basis states. Then the optimal measurement on qubit S is performed, in the basis $\{|\pm\rangle_S\}$, where $|\pm\rangle_S = (|0\rangle_S \pm |1\rangle_S)/\sqrt{2}$. It is followed by conditional feed-forward correction on T, which corrects the phase shift of π (similarly like in previous *Chapter 4*). So we obtain the same output states of the target qubit for both outcomes $|+\rangle_S$ or $|-\rangle_S$ of the measurement on the source qubit.

The resulting output state of the target qubit is:

$$\rho_T = \frac{1+D}{2}|\Psi\rangle_S\langle\Psi| + \frac{1-D}{2}|\Psi^\perp\rangle_S\langle\Psi^\perp|, \tag{5.5}$$

where $|\Psi^\perp\rangle_S = (|0\rangle_S - e^{i\varphi}|1\rangle_S)/\sqrt{2}$ is the orthogonal complement to $|\Psi\rangle_S$. The output state ρ_T (5.5) corresponds to the original qubit state, $|\Psi\rangle_S$, disturbed by decoherence, with its off-diagonal elements (in the computation basis) reduced by factor D.

In the case when $|D| = 1$, resources behave in the same way as if they are factorable even if they actually are not. It means, they can be used for encoding of qubits even if some of their degrees of freedom are e.g. entangled. Thus the output target qubit is the same state as the source qubit.

$$|\Theta\rangle_T = (|0\rangle_T + e^{i\varphi}|1\rangle_T)/\sqrt{2} \equiv |\Psi\rangle_S. \tag{5.6}$$

The transfer protocol is schematically shown in Fig. 5.1.

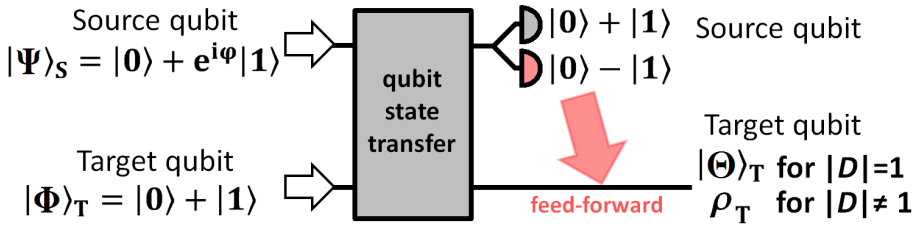

Figure 5.1: Scheme of the qubit state transfer protocol (without states normalizations). It point out to different results in dependence on the parameter D.

Experimental quantum information processing and transfer often use photonic qubits [10, 195] encoded into photons generated by spontaneous parametric down-conversion (SPDC). These photons represent a typical example of qubit carriers with internal degrees of freedom which may exhibit complex behaviour [196, 197]. The information is usually encoded into polarization or spatial degrees of freedom but frequency degrees of freedom are entangled. Thus parameter $|D|$ quantifies effective indistinguishability of resources for quantum information processing.

It can be shown by calculations [2] that the measured coincidence rate is:

$$R(\Delta t) \propto 1 - D \tag{5.7}$$

The parameter D is obtained as:

$$D = 1 - R_{\mathrm{rel}}, \tag{5.8}$$

where R_{rel} is normalized coincidence rate with respect to coincidence rate R_{out} measured far from the HOM dip position, where the particles are completely distinguishable,

$$R_{\mathrm{rel}} = R(\Delta t)/R_{\mathrm{out}}. \tag{5.9}$$

In this experiment qubits are encoded into spatial modes. Thus the role of the "environment" is played by frequency degrees of freedom. Parameter D can be really measured only by means of a beam splitter and coincidence detection. It can be varied by changing delay Δt between the two photons. Its negative values correspond to partially entangled states containing vectors from anti-symmetric subspace.

If generated photons have a frequency spectrum with rectangular shape, with FWHM=v and central frequency $\omega_0/2$ then $D = \mathrm{sinc}(\Delta t\, v)$.

5.3 Experiment

Our setup is depicted in Fig. 5.2. Photon pairs are created by collinear frequency-degenerate type-II SPDC in a BBO crystal pumped at 405 nm. Both photons pass through the same band-pass interference filter of *approximately* rectangular shape with central frequency 810 m and spectral width (FWHM) 2.7 nm. Then they are separated by a polarizing beam splitter and coupled into single-mode fibres. One of the photons is retarded by Δt in a delay line (DL) with adjustable length. By means of polarization controllers both photons are set to have the same polarization states. Qubit states are encoded into spatial modes of individual photons. Each basis state corresponds to a single photon in one, $|0\rangle$, or in another, $|1\rangle$, of two optical fibres. Initial equatorial states of both qubits are prepared using fibre couplers (FC and VRC) with splitting ratio 50:50 and integrated electro-optical phase modulators (PMs). The source qubit is in the "unknown" equatorial state (5.2) and the target qubit is in initial state (5.3).

The key part of our device is the swap of two rails between source qubits and target qubit followed by measurement on the source qubit. This measurement is performed in basis $(|0\rangle \pm |1\rangle)/\sqrt{2}$ using a FC with fixed splitting ratio 50:50 and two single photon detectors. When detector $\mathrm{D_{a1}}$ clicks, phase correction π is applied on the target qubit by means of feed-forward loop. The feed-forward uses a direct electric signal from detector $\mathrm{D_{a1}}$. The electric signal is modified by a passive voltage divider to circa 1.5 V and then it is led to the PM (1.5 V corresponds to the phase shift of π). Output states of target qubit are characterized by quantum tomography. Different measurement bases are set by a PM and VRC, as described in *Chapter 3, Methods and Tools*. Photons are counted by detectors $\mathrm{D_{d0}}$ and $\mathrm{D_{d1}}$. Small differences in detector efficiencies are corrected numerically in data sets.

The whole experimental setup consists of two interconnected Mach-Zehnder interferometers. Lengths of their arms are balanced by motorized air gaps (not shown in the figure). To reduce a phase drift caused by environmental influences, like air convection and temperature fluctuations, the whole setup is covered and actively stabilized. After each 3 s period of measurement the phase drifts are determined and compensated by adding a proper correcting voltage on the PMs. The HOM dip [129], which we use for characterization of input photons properties, is measured at the output VRC.

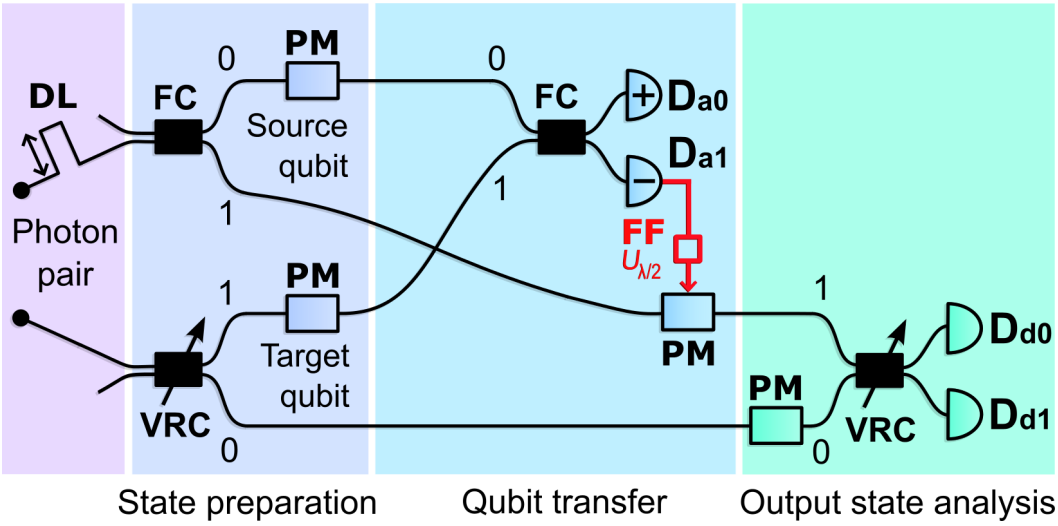

Figure 5.2: Scheme of the experiment implementation of the qubit state transfer protocol. DL – delay line, FC – fibre couplers, VRC – variable ratio couplers, PM – phase modulators, FF – feed-forward loop, D – detectors. The couplers and PMs in the *State preparation* stage enable us to prepare required qubit states (each qubit is represented by a single photon which may propagate in two optical fibres). In *Qubit transfer* stage, the two rails are swapped and the auxiliary measurement on the source qubit is performed. The middle PM applies conditional phase shift depending on the measurement result. The PM is a part of the feed-forward loop and also the part of the protocol. *Output state analysis* stage consists of PM and VRC, which serve for output state tomography.

5.4 Measurements

The target qubit is prepared in state (5.3) and the source qubit is prepared in state (5.2) with phase $\varphi = 0°, 30°, 60°, 90°, 120°, 150°, 180°$, in sequence. On the output we perform measurement on the target qubit in three different bases: $\{|0\rangle, |1\rangle\}$, $\{(|0\rangle \pm |1\rangle)/\sqrt{2}\}$, and $\{(|0\rangle \pm i|1\rangle)/\sqrt{2}\}$, for each setting of input states. Each measurement consists of 15 three-second measurement intervals interlaced by active stabilization. During the measurement, the coincidences between detectors D_{a0} & D_{d0}, D_{a0} & D_{d1}, D_{a1} & D_{d0}, and D_{a1} & D_{d1} are accumulated.

Each such measurement set is repeated 16 times with different delays Δt between the input photons. It corresponds to 16 different positions in HOM dip. The measurement is depicted in block scheme in Fig. 5.3.

To evaluate the parameter D, we measure the coincidence rate $R(\Delta t)$ between detectors D_{d0} & D_{d1}, in each of these 16 positions in the HOM dip. Once, we measure separately this coincidences in position far from the dip to obtain R_{out}.

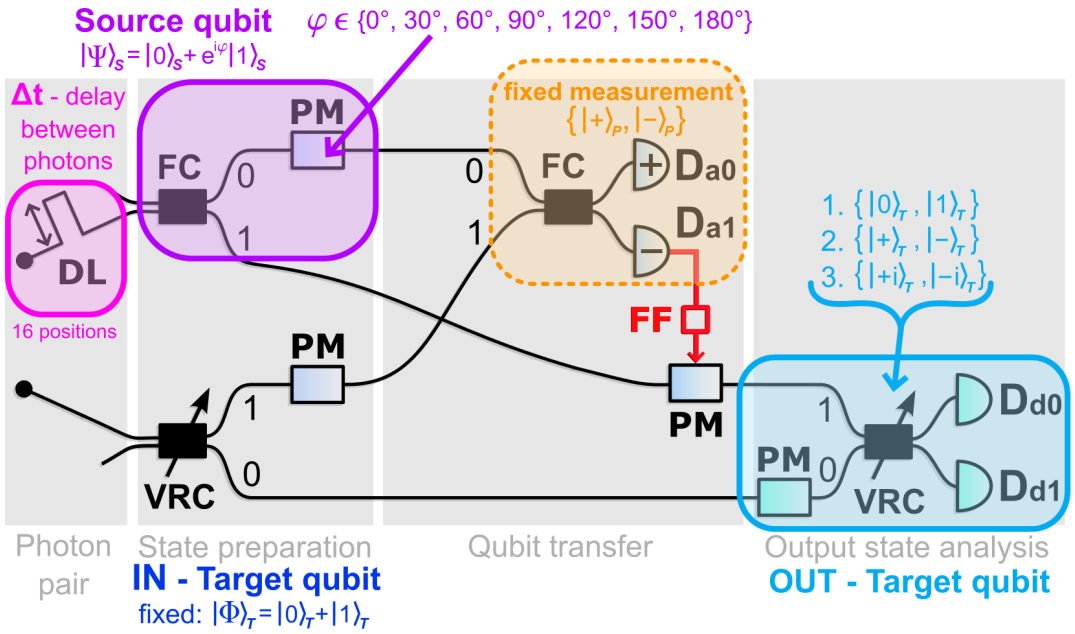

Figure 5.3: Block scheme of the final measurement of the qubit state transfer protocol. FC – fire coupler, VRC – variable ratio coupler, PM – phase modulator, FF – electro-optical feed-forward loop, D – detector, DL – delay line.

5.5 Results

The measured results are used to reconstruct output density matrices, ρ_T^{rec}, by means of maximum-likelihood quantum tomography [124, 125, 191]. Reconstruction of density matrices enable us to calculate various quantities including purity and overlap with corresponding input states.

For each position in HOM dip, corresponding to certain delay Δt, we evaluate parameter $D = 1 - R_{\text{rel}}$. R_{rel} is the normalized coincidence rate $R(\Delta t)$ between detectors D_{d0} & D_{d1} with respect to the coincidence rate measured far from the dip, R_{out} It is obtained as $R_{\text{rel}} = R(\Delta t)/R_{\text{out}}$.

Negative values of D correspond to the positions in the raised "shoulders" of the HOM dip, as it is shown in the inset in the bottom right corner in Fig. 5.4. They reveal that "environments" of our photons are entangled. The values of $\langle\Psi|_S\, \rho_T\, |\Psi\rangle_S$ lower than 0.5 mean that roles of states $|\Psi\rangle_S$ and $|\Psi^{\perp}\rangle_S$ are swapped (see Eq. 5.5).

According to the theory, overlap $\langle\Psi|_S\, \rho_T\, |\Psi\rangle_S = \frac{1+D}{2}$ and eigenvalues of ρ_T are $\frac{1+D}{2}$ and $\frac{1-D}{2}$, see Eq. (5.5). Fig. 5.4 shows the overlap and the maximal eigenvalue as functions of parameter D. Each point represents an average over all seven phases φ. Vertical error bars visualize standard deviations obtained from ensembles of measurements with different

phases. Due to various experimental imperfections (phase fluctuations, drift of splitting ratios, etc.) they are greater than standard deviations calculated purely from Poissonian photo-count distribution. But on the graph they are mostly smaller than the size of symbols. Horizontal error bars reflect (Poissonian) statistical fluctuations of coincidence rates $R(\Delta t)$ and R_{out}. Average output state fidelity, $[\text{Tr}(\sqrt{\sqrt{\rho_T}\rho_T^{\text{rec}}\sqrt{\rho_T}})]^2$, (averaged over all phases and all delays) was 99.2 ± 0.8 %. The measured HOM dip is shown in the lower right inset of Fig. 5.4. Relative measurement error is less than 6 % in its minimum and less than 2 % for maximal values. Dip visibility is 96.4 ± 0.4 %.

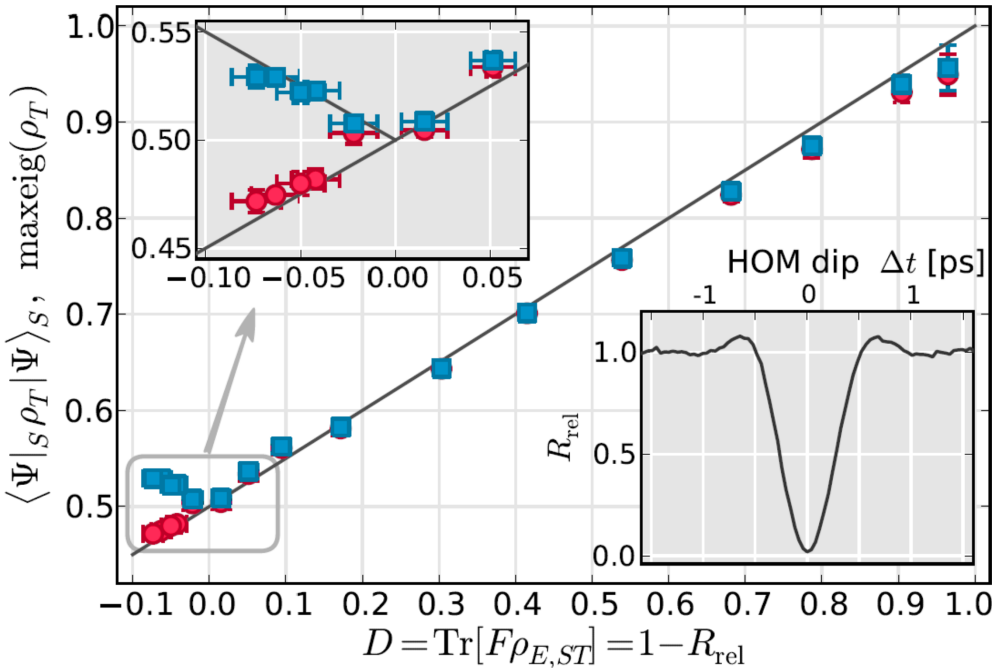

Figure 5.4: Dependence of the quality of qubit-state transfer on the parameter D. Red circles denote the overlap of output and input states, $\langle\Psi|_S \rho_T |\Psi\rangle_S$. Blue squares denote maximal eigenvalues of output states ρ_T. Straight lines are theoretical predictions. The upper left inset magnifies the area where D is close to zero. The lower right inset shows the measured Hong-Ou-Mandel dip, R_{rel} denotes relative (normalized) coincidence rate.[28]

[28]This graph is originally plotted by M. Dušek.

Chapter 6

Experimental implementation of perfect quantum reading of beam splitters

This chapter is based on the following publication:

[3] Michele Dall'Arno, Alessandro Bisio, Giacomo Mauro D'Ariano, Martina Miková, Miroslav Ježek, and Miloslav Dušek. *Experimental implementation of unambiguous quantum reading.* Physical Review A **85**, 012308 (2012).

6.1 Basic idea

The next experiment implements unambiguous reading of optical memories using the smallest possible amount of energy. The information is stored as a reflectivity of the memory cell. The experimentalist challenge is to built theoretically suggested device [3] which can perfectly and unambiguously distinguish two different memory records.

In the experiment, the memory cell is represented by a beam splitter. Two different reflectivities of the beam splitter determine two memory records represented by two devices, I and U. Our aim is to discriminate between these two devices. It corresponds to reading of the memory record.

During the measurement process, a superposition of a single photon and vacuum enters the unknown device (I or U). Thus the unknown device is in average exposed just to the fraction of single-photon energy. The experimental results confirm the feasibility of quantum reading.

6.2 Theory related to the experimental setup

The comprehensive theoretical background of ambiguous, unambiguous, and perfect quantum reading is described in [3]. The theoretical part of this paper is work of our Italian colleagues. Here we show only a part of the theory, directly related to our experiment.

One can be interested in discrimination between two unitary operations described by unitary matrices U_1 and U_2, where $U_1 \neq U_2$. These matrices can be written as $U_1 = W^\dagger I W$ and $U_2 = W^\dagger U W$, where I represents identity operation and W is a unitary matrix. Thus discrimination between two general operations U_1 and U_2 is unitary-equivalent to discrimination between I and U. The special case of such unitary operation U is the action of a beam splitter. Reflectivity of such beam splitter may convincingly represent an optical memory record.

Let us call our two devices I and U according to the performed unitary operations. Our aim is to discriminate between these two devices.

Device U is depicted in scheme (6.1). It is realized by a beam splitter V, with reflectivity R_V, and phase shifters acting on each input and output mode. But, in our experimental realization, two $-\pi/2$ phase shifters on mode 1 are irrelevant and they can be discarded. It is because the input mode 1 acts on a vacuum state and the output mode 1 is immediately followed by a photo-detector. Without loss of generality, we can also apply a cumulative phase shift of π on input mode 2 in front of beam splitter V. So we can redefine device U as follows:

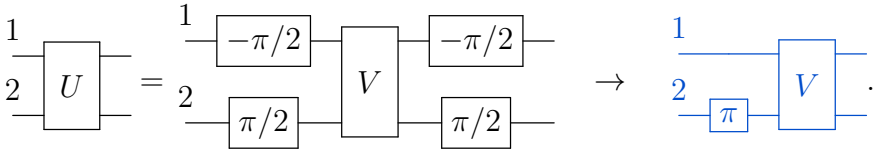

(6.1)

Device I makes the identity operation. It is represented by a beam splitter with unit reflectivity without any additional phase shifts:

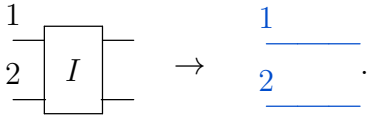

(6.2)

The theoretical scheme for perfect quantum reading is experimentally feasible with present quantum optical technology. The general setup consists of an MZI with beam splitters B and $B^\dagger$, acting on modes 2 and 3, see scheme (6.3). An additional beam splitter, representing the unknown device, is inserted in the MZI arm corresponding to mode 2. During the measurement procedure the unknown device is randomly chosen from the set $\{I, U\}$ with equal prior probabilities. The optimal strategy for quantum reading i.e., the optimal discrimination between these two devices (beam splitters with different reflectivities) is described by the following scheme where $\Pi_U, \Pi_{U'}$ and Π_I denote photo-counters:

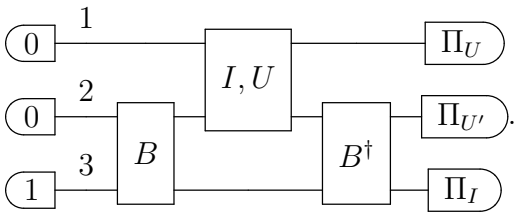

(6.3)

In our experimental setup, the unknown device is realized by a fibre beam splitter with a variable splitting ratio, VRC-mid. The device U is represented by $R_V \neq 1$ plus a cumulative phase of π.

To provide optimal discrimination the reflectivity and transmissivity of beam splitters B must be given as:

$$R_B = \frac{\sqrt{R_V}}{1+\sqrt{R_V}}, \qquad T_B = \frac{1}{1+\sqrt{R_V}}. \tag{6.4}$$

The optimal measurement for perfect discrimination is implemented by three photocounters Π_U, $\Pi_{U'}$, and Π_I. The conditional probabilities $p_{X|Y}$ of photon detection by the detector Π_X $(X = U, U', I)$ given that the unknown device is Y $(Y = U, I)$ read:

$$p_{U|U} = 1 - \sqrt{R_V}, \qquad p_{U'|U} = \sqrt{R_V}, \qquad p_{I|I} = 1, \qquad p_{I|U} = p_{U|I} = p_{U'|I} = 0 \tag{6.5}$$

Detecting a photon by the detector Π_U or $\Pi_{U'}$ implies that the unknown device is U. While a photon detection by the detector Π_I implies that the unknown device is I.

6.3 Experiment & Measurement

To demonstrate experimental feasibility of quantum reading we have built a laboratory setup, shown in Fig. 6.1, for perfect discrimination of two beam splitters according to scheme (6.3). It consists of a Mach-Zehnder interferometer (MZI) with an additional beam splitter VRC-mid in its upper arm. The beam splitter has a variable splitting ratio and it serves as the unknown device which has to be discriminated.

We use a heralded single photon source based on spontaneous parametric down conversion (SPDC). Namely, we employ a collinear frequency-degenerate SPDC process with type-II phase matching in a 2 mm-long BBO crystal pumped by a cw laser diode (Coherent Cube) at 405 nm. In this process pairs of photons at 810 nm are created. Photons from each pair are separated by a polarizing beam splitter and coupled into single-mode optical fibres. One of them is led directly to a trigger single-photon detector D_T (PerkinElmer SPCM AQR-14FC) which heralds the creation of a pair. The second photon enters MZI through a variable ratio coupler VRC-in.

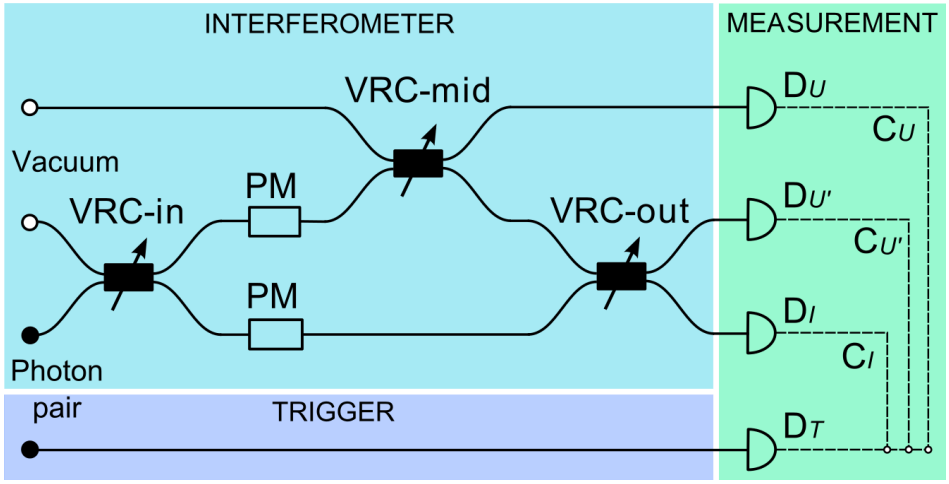

Figure 6.1: Scheme of the experimental implementation of perfect quantum reading. VRC – variable ratio coupler, PM – phase modulator, D – detector, C – coincidence rate.

An additional variable ratio coupler, VRC-mid, represents the unknown device. When its reflectivity equals one, $R_V = 1$, it corresponds to device I. To switch to device U one has to set a required splitting ratio, $R_V \neq 1$, and apply additional phase shift of π, see scheme (6.1). In the experiment phase shifts are introduced by electro-optical phase modulators (PMs). Their half-wave voltages are ∼1.5 V. These phase modulators exhibit relatively high dispersion. Therefore one PM is placed in each interferometer arm in order to compensate dispersion effects. In case of a device U we use the PM in the upper interferometer arm to apply the additional phase shift of π.

Output fibres from the interferometer and from the unknown device are connected to single-photon detectors D_U, $\mathrm{D}_{U'}$, and D_I. These detectors are parts of Perkin-Elmer quad module SPCM-AQ4C.

To reduce the effect of the phase drift caused by air convection, fluctuations of temperature, and temperature gradients, we apply both passive and active stabilization. The experimental setup is covered by a shield minimizing air flux around the components. Besides, after each three seconds of measurement an active phase stabilization of MZI is performed. The stabilization procedure[29] measures intensity for a phase shift of $\pi/2$ and if necessary it calculates phase compensation and applies corrective voltage to the phase modulator in the lower interferometer arm. These results are in the precision of the phase setting during the measurement period better than $\pi/200$.

For each pair of devices U and I the proper splitting ratio of fibre couplers VRC-in and VRC-out must be set to discriminate these devices optimally. Thus the MZI beam splitters B, VRC-in and VRC-out, are set for relevant R_V according to Eq. (6.4). We perform measurement for 11 different devices U with intensity reflectivities $0, 0.1, 0.2, \ldots, 1$. For each pair of devices U and I the counts at detectors D_U, $\mathrm{D}_{U'}$, and D_I are cumulated

[29]The stabilization procedure employed in this experiment is implemented into the MATLAB code by H. Fikerová, within her Bachelor's [174] and Master's [178] thesis.

during 30 three-second measurement intervals interlaced by stabilization procedures. All measurements are done in coincidence with the trigger detector D_T. It means we measure coincidence counts $C_U, C_{U'}, C_I$ between detectors $D_T \,\&\, D_U$, $D_T \,\&\, D_{U'}$, and $D_T \,\&\, D_I$, respectively, using 3 ns coincidence time window. These results are normalized to obtain relative frequencies, $f_j = C_j/(C_U + C_{U'} + C_I)$, where $j = U, U', I$. Because, relative frequencies can be directly compared with theoretical probabilities of photon detection.

6.4 Results

The final experimental results provided for the perfect quantum reading of devices U and I are depicted below. Measured relative frequencies and theoretical probabilities are listed in Table 6.1 and shown in Figure 6.2. The left parts of the table 6.1 and Fig. 6.2 summarize the results for devices U, while the right parts of the table 6.1 and Fig. 6.2 show the results obtained with device I inserted. Each row in the table corresponds to one pair of U and I with R_V being the reflectivity of a device U. It corresponds to different MZI settings and alignments.

One can observe very good agreement between the theory and the experiment. Small discrepancies appear mainly due to imperfections in splitting-ratio settings, phase fluctuations, and polarization misalignment. In coincidence measurements the contribution of detector noise is completely negligible and error bars are smaller than symbols in the figure 6.2.

The advantage of the implemented setup is that in an ideal case there is one photon in the output ports. It makes detection relatively easy. Nevertheless, it is still a superposition of a single photon and vacuum what is entering the unknown device. So the unknown device is exposed just to a fraction of energy of a single photon in average. Even if the overall success probability of the setup is relatively low because of technological losses, we were able to measure precisely the relative probabilities of all outputs and our experiment convincingly validate the theoretical predictions.

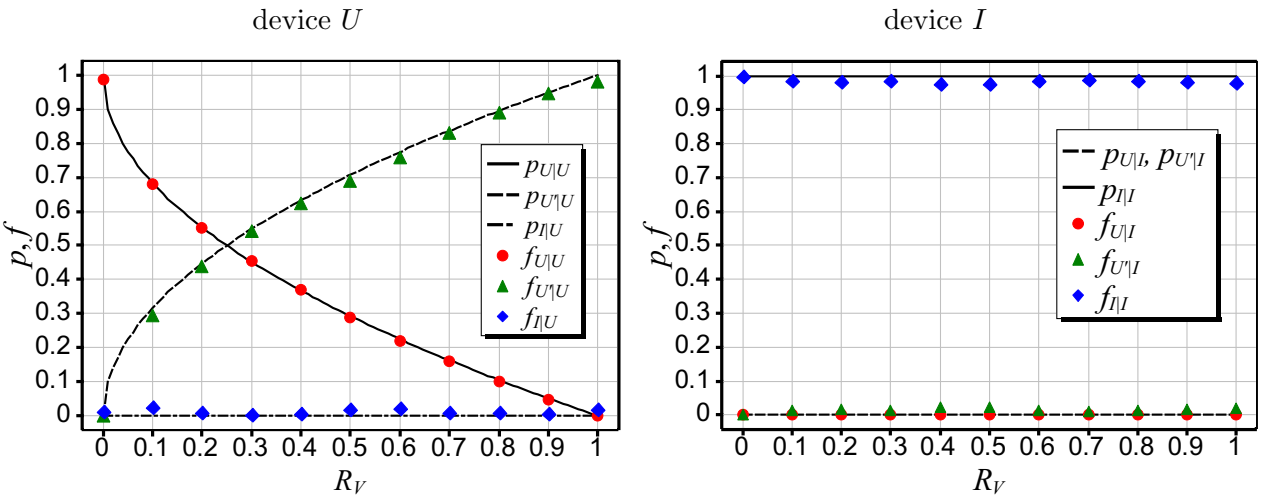

Figure 6.2: Results for devices U and I are shown in left and right graph, respectively. Detection probabilities and measured relative frequencies are plotted as a functions of the reflectivity R_V of VRC-mid. Where different reflectivities R_V of VRC-mid correspond to different devices U and to appropriate settings of MZI. [30]

	device U						device I					
	theory			experiment			theory			experiment		
R_V	$p_{U\|U}$	$p_{U'\|U}$	$p_{I\|U}$	$f_{U\|U}$	$f_{U'\|U}$	$f_{I\|U}$	$p_{U\|I}$	$p_{U'\|I}$	$p_{I\|I}$	$f_{U\|I}$	$f_{U'\|I}$	$f_{I\|I}$
0.0	1.000	0.000	0	0.986	0.000	0.014	0	0	1	0.000	0.002	0.998
0.1	0.684	0.316	0	0.680	0.295	0.025	0	0	1	0.000	0.012	0.988
0.2	0.553	0.447	0	0.551	0.440	0.009	0	0	1	0.000	0.018	0.982
0.3	0.452	0.548	0	0.455	0.542	0.003	0	0	1	0.000	0.012	0.988
0.4	0.368	0.633	0	0.369	0.623	0.008	0	0	1	0.000	0.023	0.977
0.5	0.293	0.707	0	0.288	0.691	0.021	0	0	1	0.000	0.022	0.978
0.6	0.225	0.775	0	0.219	0.758	0.022	0	0	1	0.000	0.014	0.986
0.7	0.163	0.837	0	0.160	0.830	0.010	0	0	1	0.000	0.011	0.989
0.8	0.106	0.894	0	0.100	0.891	0.009	0	0	1	0.000	0.013	0.987
0.9	0.051	0.949	0	0.046	0.946	0.007	0	0	1	0.000	0.018	0.982
1.0	0.000	1.000	0	0.000	0.980	0.020	0	0	1	0.000	0.021	0.979

Table 6.1: Results for devices U and I are summarized in left and right part of the table, respectively. R_V – reflectivity of VRC-mid in device U. **Device** U inserted in the MZI: $p_{U|U}, p_{U'|U}, p_{I|U}$ – theoretical probabilities of photon detection at detectors D_U, $\mathrm{D}_{U'}$, D_I, respectively, $f_{U|U}, f_{U'|U}, f_{I|U}$ – relative frequencies measured at detectors D_U, $\mathrm{D}_{U'}$, D_I, respectively (measured in coincidence with D_T). **Device** I inserted inside the MZI: $p_{U|I}, p_{U'|I}, p_{I|I}$ – theoretical probabilities of photon detection at detectors D_U, $\mathrm{D}_{U'}$, D_I, respectively, $f_{U|I}, f_{U'|I}, f_{I|I}$ – relative frequencies measured at detectors D_U, $\mathrm{D}_{U'}$, D_I, respectively (measured in coincidence with D_T).

[30] These graphs were originally plotted by M. Dušek.

Chapter 7

Optimal entanglement-assisted discrimination of quantum measurements

This chapter is based on the following publication:

[4] Martina Miková, Michal Sedlák, Ivo Straka, Michal Mičuda, Mário Ziman, Miroslav Ježek, Miloslav Dušek, and Jaromír Fiurášek. *Optimal entanglement-assisted discrimination of quantum measurements.* Physical Review A **90**, 022317 (2014).

7.1 Basic idea

In this chapter we experimentally investigate optimal discrimination between two projective single-qubit measurements $\mathcal{M}$ and $\mathcal{N}$ in a scenario where the measurement can be performed only once [4]. We consider general discrimination strategies[31] involving a certain fraction of inconclusive outcomes, P_I. It is shown that the optimal discrimination procedure requires entangled probe state for any nonzero rate of inconclusive outcomes $P_I > 0$. Due to various experimental imperfections, it is necessary to include also additional erroneous conclusive results. Therefore we consider general discrimination scheme where we maximize success probability P_S, hence minimize P_E, for a fixed fraction of P_I; $P_S + P_I + P_E = 1$. We experimentally implement this optimal discrimination strategy for projective measurements on polarization states of single photons. Our setup is based on linear optics, polarization maintaining fibre interferometers, and single-photon detectors. The setup involves the real-time electro-optical feed-forward loop which allows us to fully harness the benefits of entanglement in discrimination of quantum measurements. The experimental data unequivocally confirm the advantage of entanglement-based discrimination strategy as compared to our benchmark, provide by optimal discrimination schemes using single-qubit probes without any entanglement.

[31] Where inconclusive results P_I and conclusive erroneous results P_E are in general nonzero.

7.2 Theory

The theory in [4] is a work of my colleagues. Therefore, below is described only the part of the theory directly related to the experiment. For more details regarding for example the protocol optimality, please see the paper.

Optimal entanglement-assisted discrimination

The measurement bases $\mathcal{M}$ and $\mathcal{N}$ are illustrated in Fig. 7.1(a). Without loss of generality, the projectors specifying the measurements can be parametrized by a single angle θ,

$$\begin{aligned} M_0 &= |\phi\rangle\langle\phi|, & M_1 &= |\phi^\perp\rangle\langle\phi^\perp|, \\ N_0 &= |\psi\rangle\langle\psi|, & N_1 &= |\psi^\perp\rangle\langle\psi^\perp|, \end{aligned} \tag{7.1}$$

where

$$\begin{aligned} |\phi\rangle &= \cos\theta|0\rangle + \sin\theta|1\rangle, & |\phi^\perp\rangle &= \sin\theta|0\rangle - \cos\theta|1\rangle, \\ |\psi\rangle &= \cos\theta|0\rangle - \sin\theta|1\rangle, & |\psi^\perp\rangle &= \sin\theta|0\rangle + \cos\theta|1\rangle, \end{aligned} \tag{7.2}$$

and $0 \leq \theta \leq \frac{\pi}{4}$. The most general discrimination strategy is depicted in Fig. 7.1(b). A two-qubit entangled state $|\Psi\rangle_{\mathrm{I,II}}$ is employed. The measurement that should be identified is performed on qubit I, and the measurement outcome (0 or 1) specifies which measurement is then performed on qubit II.

In what follows, we assume equal a-priori probabilities of these two measurements. In such a case, as it is shown in [4], it is optimal to employ a maximally entangled singlet Bell state $|\Psi^-\rangle = (|01\rangle - |10\rangle)/\sqrt{2}$. If we observe measurement outcome 0 on qubit I, then qubit II is prepared in state $|\phi^\perp\rangle$ or $|\psi^\perp\rangle$. Similarly, outcome 1 heralds that qubit II is prepared in state $|\phi\rangle$ or $|\psi\rangle$. Since

$$|\phi\rangle = -\sigma_Y|\phi^\perp\rangle, \quad |\psi\rangle = \sigma_Y|\psi^\perp\rangle, \tag{7.3}$$

we can apply the unitary operation $\sigma_Y = |0\rangle\langle 1| - |1\rangle\langle 0|$ to qubit II when the measurement outcome on qubit I reads 0. Thus in this way the discrimination task of two quantum measurements is converted to discrimination of two fixed non-orthogonal quantum states $|\phi\rangle$ and $|\psi\rangle$.

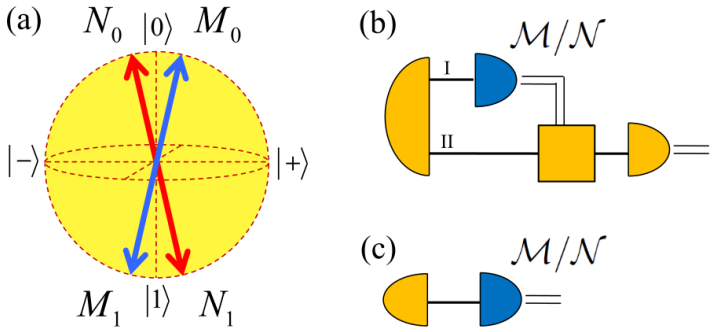

Figure 7.1: (a) Single-qubit measurements $\mathcal{M}$ and $\mathcal{N}$ on a Bloch sphere. (b) General measurement discrimination scheme involving entangled probe state. (c) Simple discrimination scheme with single-qubit probe. [32]

[32] These schemes were originally plotted by M. Sedlák.

As shown by Ivanovic, Dieks, and Peres (IDP) [76–78], perfect error-free ($P_E = 0$) discrimination between $|\phi\rangle$ and $|\psi\rangle$ is possible if we allow for a certain probability of inconclusive outcomes $P_I = |\langle\psi|\phi\rangle|$. Explicitly, we have

$$P_I = P_I^{\text{unambig}} = \cos(2\theta). \tag{7.4}$$

Unambiguous discrimination requires a generalized 3-component POVM which can be interpreted as a quantum filtering followed by a projective measurement on the filtered state. The required filter has the form $F = \tan\theta|0\rangle\langle 0| + |1\rangle\langle 1|$ and the filtered states become orthogonal, $F|\phi\rangle = \sqrt{2}\sin\theta|+\rangle$, and $F|\psi\rangle = \sqrt{2}\sin\theta|-\rangle$, where $|\pm\rangle = (|0\rangle \pm |1\rangle)/\sqrt{2}$. The square of the norm of the filtered states is equal to the success probability of unambiguous discrimination,

$$P_S = P_S^{\text{unambig}} = 2\sin^2\theta, \tag{7.5}$$

and $P_S + P_I = 1$. Due to various experimental imperfections, we will in practice encounter also the erroneous conclusive results occurring with probability P_E. This motivates us to consider a general discrimination scheme where we maximize P_S, hence minimize P_E, for a fixed fraction of inconclusive outcomes P_I. The optimal filter then reads $F = f|0\rangle\langle 0| + |1\rangle\langle 1|$, where $f = \sqrt{1 - P_I/\cos^2\theta}$, and a projective measurement in basis $|\pm\rangle$ should be performed after successful filtration similarly as before. This intermediate strategy optimally interpolates between IDP [76–78] and Helstrom [75] schemes, and we get [80, 81]

$$P_S = \frac{1}{2}\left(1 - P_I + \sin(2\theta)\sqrt{1 - \frac{P_I}{\cos^2\theta}}\right). \tag{7.6}$$

It is convenient to consider also a relative probability of successful discrimination for the subset of conclusive outcomes,

$$\tilde{P}_S = P_S/(1 - P_I). \tag{7.7}$$

The probability $\tilde{P}_S$ increases with P_I and $\tilde{P}_S = 1$ when $P_I = \cos(2\theta)$.

The optimality of the above protocol is proved in [4] with the help of the formalism of process POVM [108,198]. There it is shown that the optimization of discrimination of two projective qubit measurements becomes equivalent to optimization of the discrimination of two quantum states $|\phi\rangle$ and $|\psi\rangle$ by a 3-component POVM.

Optimal discrimination with single-qubit probes

To elucidate the importance of the entanglement state in the task of discrimination measurement, we provide a benchmark for the realized experiment. We determine the optimal discrimination strategy with unentangled single-qubit probes, see Fig. 7.1(c). In this case one has to guess $\mathcal{M}$ or $\mathcal{N}$ solely based on the measurement outcome on the probe qubit. For more details about the optimal single-qubit discrimination strategy, see [4]. Here we show only the result, which is used as the "classical" bound in Fig. 7.7. There, it is depicted by dashed lines for 7 different angles θ determining 7 different pairs of the measurement basis $\mathcal{M}$ and $\mathcal{N}$.

The optimal discrimination strategy is different for $P_I < P_{I,T}$ and $P_I \geq P_{I,T}$. The transition point $P_{I,T}$ is obtained as a result of optimization procedure. Then the overall success probability reads:

If $P_I \geq P_{I,T}$, the success probability is:

$$P_S = \frac{1}{2}(1 - P_I) + \frac{1}{4}\sin(2\theta)\sqrt{1 - \frac{(1-2P_I)^2}{\cos^2(2\theta)}}. \tag{7.8}$$

If $P_I < P_{I,T}$, then the success probability is:

$$P_S = \left(1 - \frac{P_I}{P_{I,T}}\right) P_{S,0} + \frac{P_I}{P_{I,T}} P_{S,T}. \tag{7.9}$$

Where:

$P_{I,T} = [1 + 3\cos^2(2\theta) + 2\cos^2(2\theta)\sqrt{1 + 3\cos^2(2\theta)}]/[2(1 + 4\cos^2(2\theta))]$,

$P_{S,0} = [1 + \sin(2\theta)]/2$,

$P_{S,T}$ is given by equation 7.8 where P_I is replaced with $P_{I,T}$, thus

$P_{S,T} = (1 - P_{I,T})/2 + \sin(2\theta)\sqrt{1 - (1 - 2P_{I,T})^2/\cos^2(2\theta)}/4$.

To compare it with the previous case of optimal entanglement-assisted discrimination, we consider also the relative probability of successful discrimination for the subset of conclusive outcomes $\tilde{P}_S$, given by equation (7.7).

For unambiguous discrimination ($P_E = 0$) with a single-qubit probe the success probability is given as $P_S^{\text{unambig}} = [1 - \cos^2(2\theta)]/2$, and $P_I^{\text{unambig}} = [1 + \cos^2(2\theta)]/2$.

7.3 Experiment

Our experimental demonstration of entanglement-assisted discrimination of quantum measurements is based on linear optics and qubits encoded into states of single photons. The scheme of our experimental setup is shown in Fig 7.2. First we describe general blocks of the experimental setup, then stabilization procedure and alignment routines.

Source: We use a spontaneous parametric down conversion (SPDC) type II, collinear and degenerated to create time-correlated orthogonally polarized photon pairs. Nonlinear crystal BBO, 2 mm thick, is pumped by a laser beam with central wavelength 405 nm and power 60 mW. The obtained signal and idler photons go through the same interference filter (Semrock MITC 4#) FWHM 2.7 nm. Subsequently, the photons are separated from each other by a polarizing beam splitter (PBS). The signal and idler photons are properly coupled into slow axis of polarization maintaining fibres (PM780-HP) and let directly to an entanglement state preparation (not shown in Figs 7.2 and 7.3).

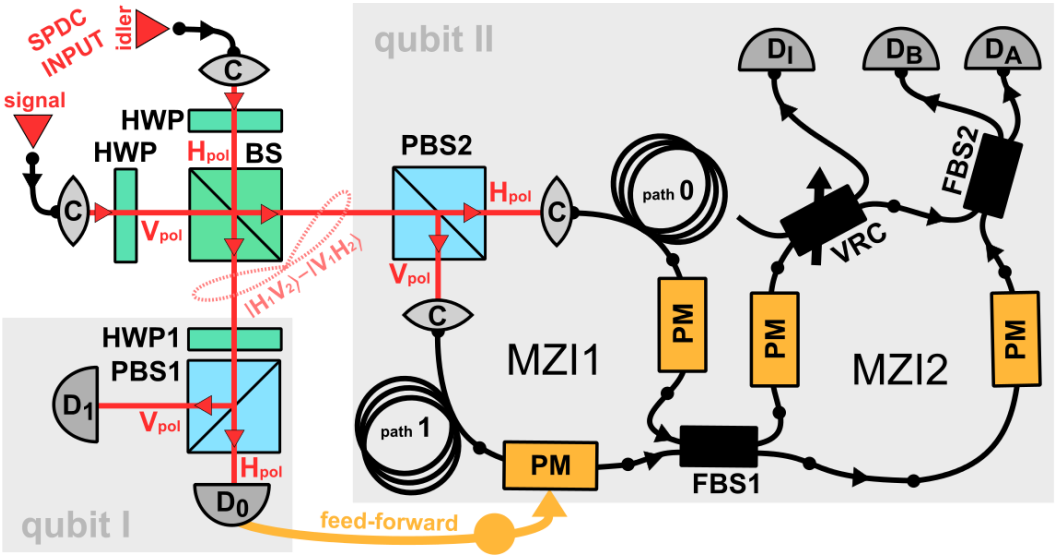

Figure 7.2: Scheme of the experimental setup for optimal entanglement-assisted discrimination of quantum measurements; BS – bulk beam splitter 50:50, FBS – fibre beam splitter 50:50, PBS – polarizing beam splitter, HWP – half-wave plate, C – collimating lens, PM – phase modulator, D – single-photon detector, VRC – variable ratio coupler which determines the amount of inconclusive results, SPDC – source of the photon pairs. Setup photo is shown at the end of this chapter in Fig. 7.10.

Then the signal and idler photons are outcoupled from the fibres. They are sent through linear polarizers (PBS) to increase their degree of polarization. Subsequently the polarization state of the signal (idler) photon is set by a half-wave plate (HWP) and a quarter-wave plate (QWP), respectively. This is shown in the orange block of Fig 7.3.

The signal photons enter a non-polarizing balanced beam splitter (BS) through the first input port, while the idler photons enter the BS through the second one. Behind this BS the post-selected two-photon polarization singlet Bell state $|\Psi^-\rangle$ is prepared by interfering the vertically polarized signal photon and the horizontally polarized idler photon. Unfortunately, the BS is not the ideal one. Its imperfections influence the resulting state, therefore additional corrections are needed. Unwanted phase shift between $|H,V\rangle$ and $|V,H\rangle$ is compensated by tilted HWP rotated at 0°, added into the appropriate output port of BS (port 2). The imbalanced splitting ratio of the BS, different from 50:50 and different for both its eigenmodes, causes that amplitudes of $|H,V\rangle$ and $|V,H\rangle$ are different. It is compensated by a tilted not-coated thin glass-plate inserted also into output port 2. Finally, HWPs rotated by 22.5° are added into both output ports of the BS. They have no influence to the entangled state itself. They are just necessary for later alignment purposes. They convert the horizontal (H) and vertical (V) linear polarization states to diagonal (D) and antidiagonal (A) ones (the purpose of these wave plates will be obvious later). The preparation of the post-selected two-photon polarization singlet Bell state is shown in the red middle block in Fig 7.3.

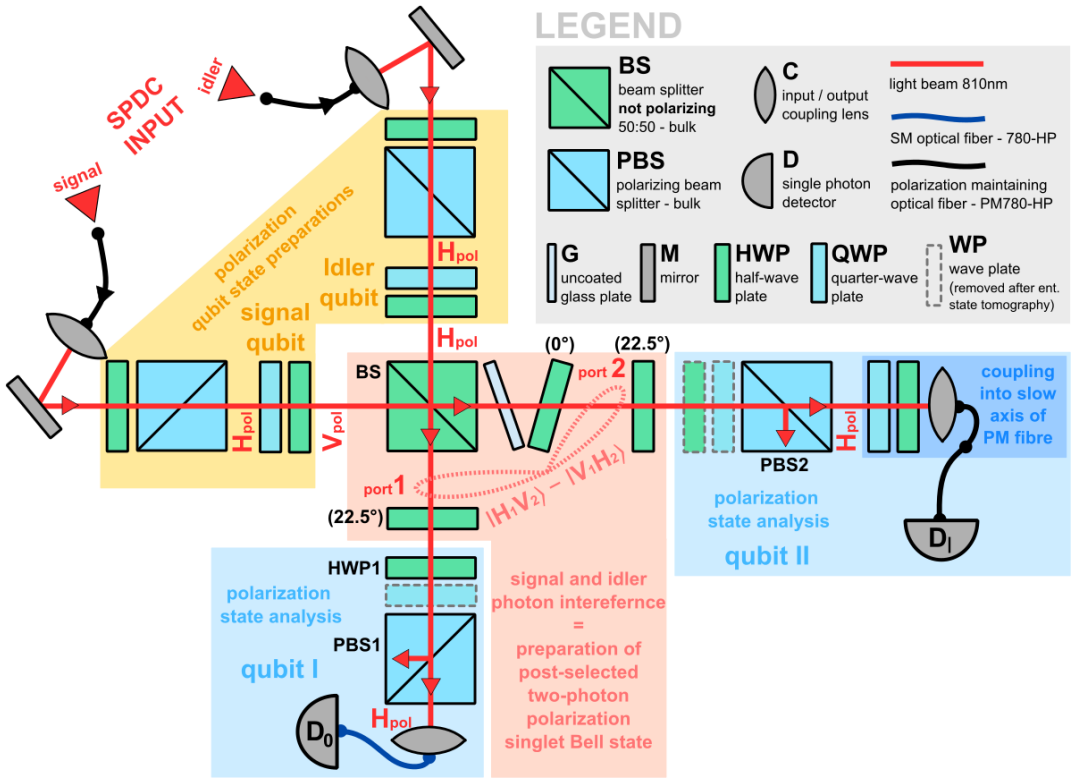

Figure 7.3: Experimental preparation and characterization of post-selected two-photon polarization singlet Bell state $|\Psi^-\rangle$. SPDC – source of the photon pairs, rest of the components is described in the legend in right upper corner. Photo of the state preparation is included almost at the end of this chapter in Fig. 7.9.

To characterize the prepared post-selected entanglement state, quantum state tomography is used. Polarization state analysis consisting of HWP, QWP in motorized rotation stages and PBS are placed into both output ports of the BS. This is shown in the blue blocks in Fig 7.3. After the state characterization, some of the wave-plates are removed (in Fig 7.3 depicted by dashed grey frame).

Qubits I and II are step-by-step projected onto 6 polarization states (H, V, D, A, R, L). 36 combinations of polarization projections are measured and coincidence rates between detectors are stored. From the measurement results a density matrix of the true output state is reconstructed. It is shown together with the ideal matrix in Fig 7.4. The observed purity of the state is better than 0.98, fidelity is higher than 0.99, and imaginary components are not higher than 0.01.

Before the state characterization, the temporal indistinguishability of idler and signal photon at the BS is maximized. The paths of the signal and idler photons are adjusted according to the minimum of Hong-Ou-Mandel (HOM) dip. HOM dips are measured for signal and idler photons both in the same polarization state. First, both photons are set to horizontal polarization states, then both to vertical. Visibilities of both dips are better than 0.97. Subsequently, the polarization states of signal and idler photons are set back to horizontal and vertical, respectively, to be perpendicular to each other and to create the singlet Bell state.

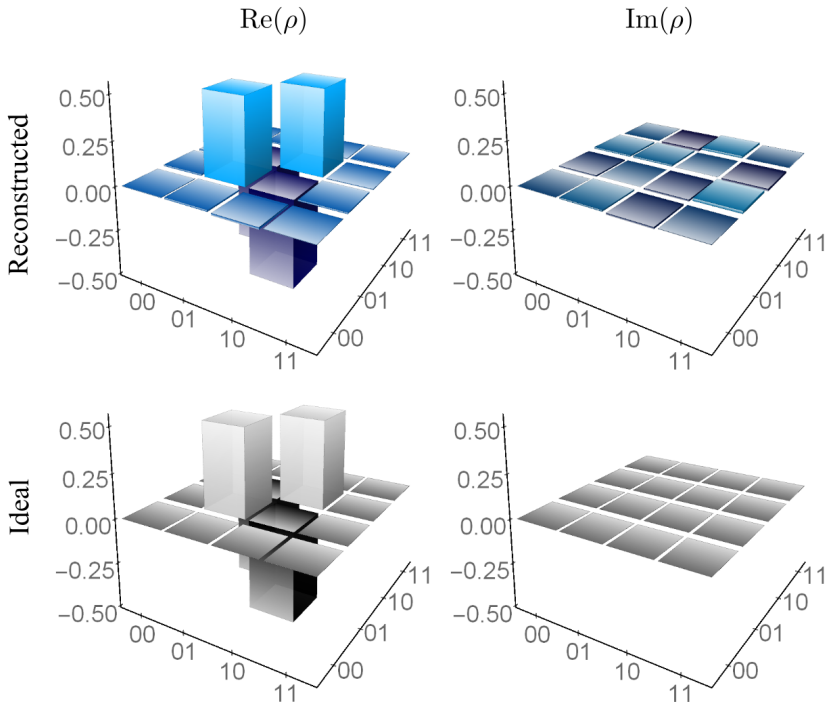

Figure 7.4: upper row – reconstructed Choi matrix ρ of the post-selected two-photon polarization singlet Bell state $|\Psi^-\rangle$ with purity > 0.98 and fidelity > 0.99; bottom row – ideal Choi matrix of $|\Psi^-\rangle$; left (right) column – real (imaginary) parts of the matrices.

Black box ($\mathcal{M}$ or $\mathcal{N}$) – qubit I: The measurement $\mathcal{M}$ or $\mathcal{N}$ that should be identified is performed on the first qubit of the entangled state $|\Psi^-\rangle$. Therefore, a combination of HWP1 and PBS1 is placed into the BS output port 1. It enables us to apply a projective measurement on qubit I in an arbitrary linearly polarized basis determined by the rotation of HWP1 (note: in general, arbitrary two polarization states can be transferred by unitary operations to the plane of linear polarizations). Basis states $|0\rangle$ and $|1\rangle$ are associated with diagonal $|D\rangle$ and anti-diagonal $|A\rangle$ linear polarizations states, respectively. Namely, $|\phi\rangle = \cos\theta|D\rangle + \sin\theta|A\rangle$ and similarly for other measurement-basis states, given by Eq. (7.2). Measurement outcomes 0 and 1 are indicated by clicks of single-photon detectors D_0 and D_1, respectively. This part of the setup is called *black box* – the device which *randomly* sets one of two measurement bases $\mathcal{M}$ or $\mathcal{N}$ with the same prior probability and applies it on the qubit I. It is depicted in Fig 7.2 in lower left corner, denoted by the gray frame *qubit I*. As a consequence of the projection of qubit I the state of qubit II is influenced. Thus information about the applied measurement on qubit I is encoded into its state. Then, the state of the second photon is analyzed, it is shown in Fig 7.2 in the middle-right part, denoted by the gray frame *qubit II*.

Photon analysis – qubit II: After the measurement on the first photon the second photon can be find in one of four possible polarization states, which corresponds to bases $\mathcal{M}$ and $\mathcal{N}$. Let us call the possible states of the second photon $M0, M1$ and $N0, N1$. Thus second photon state $M1$ is given by applied measurement $\mathcal{M}$ on qubit I followed by photon detection by detector D_1, analogically for the other states. $M1 = |\phi\rangle, M0 = |\phi^\perp\rangle, N1 = |\psi\rangle, N0 = |\psi^\perp\rangle$. The states $M0, M1(N0, N1)$ are perpendicular to each other and create basis $\mathcal{M}$ ($\mathcal{N}$).

Here we just remind, that polarization states $M1$ and $N1$ lie in the plane of linear polarization states H, V, D, A on the Bloch sphere. They are symmetrical around the diagonal states axis $|D\rangle/|A\rangle$ (in extreme cases, $M1$ and $N1$ could be $|H\rangle$ and $|V\rangle$ states or both of them could be in $|D\rangle$ state).

The second photon analysis consists of two serially connected fibre-based Mach-Zehnder interferometers (MZI1, MZI2) made of polarization maintaining fibres. The analyzed photon enters MZI1 through PBS2. PBS2 transforms quantum state of the second photon from polarization encoding to spatial (path) encoding. The spatially separated linearly horizontally and vertically polarized signals behind the PBS2 are coupled into slow axis of polarization maintaining fibres, which suppress unwanted changes of a polarization state during its propagation. The spatial modes of light $|0\rangle_{\mathrm{MZI1}}$ and $|1\rangle_{\mathrm{MZI1}}$ are represented by a photon propagating in lower and upper arm of MZI1, respectively and correspond to $|D\rangle$ and $|A\rangle$ polarization states.

A **feed-forward loop** is connected to MZI1 to conditionally change the state of the second photon. It is an electro-optical loop consisting of a single photon detector, a voltage divider and a phase modulator (PM). It conditionally applies a phase shift of π between arms of MZI1. The phase shift application is triggered by detector D_0. We employ the passive version of the feed-forward loop. It is in detail described in *Chapter 3, Methods and Tools* in the section *Real time electro-optical feed-forward loop*. Thus, when the first photon is detected by D_1, nothing happened. However, when the first photon is registered by detector D_0, the phase shift of π is applied into the lower arm of MZI1. It conditionally changes the state of the second photon. Then the second photon could be find only in two possible states. State $N0$ is mapped on $M1$ and $M0$ is mapped on $N1$ ($|\psi^{\perp}\rangle \rightarrow |\phi\rangle$ and $|\phi^{\perp}\rangle \rightarrow |\psi\rangle$, which is similar to the conditional application of unitary operation σ_Y in Eq. (7.3) up to an exchange of the role of $|\phi\rangle$ and $|\psi\rangle$). The discrimination problem of two measurement bases $\mathcal{M}$ and $\mathcal{N}$ (four possible states) is reformulated to discrimination problem of two single-qubit states $M1$ and $N1$ ($|\phi\rangle$ and $|\psi\rangle$).

At the end of MZI1, the photon interferes at the balanced fibre beam splitter (FBS1, the real component has the splitting ratio 48:52). By FBS1, the states are rotated in the plane of linear states about $\pi/2$. Than the arms of MZI2 create new basis states $|0\rangle_{\mathrm{MZI2}}$ and $|1\rangle_{\mathrm{MZI2}}$. These basis states correspond to $|H\rangle$ and $|V\rangle$ polarization modes. A variable ratio coupler (VRC) is placed into an upper arm of MZI2. It serves as a variable attenuator of the amplitude of the basis state $|0\rangle_{\mathrm{MZI2}}$, hence it implements the filter F. It is possible to set the VRC splitting ratio in such way, that the $|0\rangle_{\mathrm{MZI2}}$ component of the state is attenuated and the states $M1$ and $N1$ become perpendicular each other ($M1 \rightarrow |+\rangle \approx |D\rangle$ and $N1 \rightarrow |-\rangle \approx |A\rangle$). It is followed by projection onto the states superposition $|\pm\rangle$ (in polarization modes $|D\rangle/|A\rangle$). It is done via a balanced fibre beam splitter (FBS2, the real component has the splitting ratio 48:52) placed at the end of MZI2 and detectors D_A and D_B.

We are able to unambiguously distinguish between these two states M1 and N1. Thus, we are able to unambiguously distinguish between the bases $\mathcal{M}$ and $\mathcal{N}$ carrying out coincidence measurement with detectors D_0 and D_1. To determine the probability of inconclusive events, an additional detector D_I is used to monitor the VRC output port.

This experiment is not focused only to the unambiguous discrimination, where the states M1 and N1 are made perpendicular. Moreover, the intermediate strategies are studied.

Stabilization of MZIs: During the measurement, both interferometers MZI1 and MZI2 are thermally isolated and actively stabilized to reduce phase drifts caused by air flux and temperature fluctuations, as described in *Chapter 3, Methods and Tools*, in the section *Stabilization of experimental setup*. Resulting passive phase stability of each interferometer is approximately the same, better than 1 deg per second.

Sequential active stabilization of serially connected MZIs: each MZI contains one phase modulator (PM) used for its active phase stabilization. The stabilization routine of each MZI is based on intensity measurements at the end of the interferometer at least at one of its output ports.

An attenuated laser diode is used as a probe beam for the active stabilization procedure. It has the central wavelength 810 nm and the light went though the same interference filter as the photon pairs from SPDC. The polarization of the probe beam is set to horizontal, thus the beam is coupled just into the signal photon arm of the source. At the BS the beam is split. One part of the beam goes to the black box and it is blocked. The second part goes to MZIs. The polarization state of this part of the beam is changed from horizontal to diagonal by the HWP rotated at 22.5°. Then PBS1 behaves as balanced beam splitter. Thus, for active stabilization procedure MZI1 is always a balanced interferometer with high visibility. Because for the probe beam, both beam splitters (PBS1, FBS1) have a splitting ratio close to 50:50 and arms have balanced insertion losses.

During the stabilization of MZI1, the optical path between VRC and FBS2 is interrupt to prevent interference in MZI2. Then the output signal of MZI1 is detected by detectors D_I and D_A (D_B contains the same signal as D_A). Detector D_I is used only when the VRC splitting ratio is different from 0:100. For stabilization of MZI2, one arm of MZI1 is interrupted, thus the interference in MZI1 is stopped. Signals from both detectors D_A and D_B are used. When the VRC splitting ratio is 100:0, there is no interferometer MZI2 and just MZI1 has to be stabilized.

The MZIs are stabilized as follows: First, interference fringes of MZI1 and then MZI2 are scanned to obtain input parameters for the stabilization procedure. Subsequently, the stabilization procedure is applied to the interferometers in the same order. When MZI1 is stable, then stabilization of MZI2 starts. The overall time spend on stabilization of MZI2 is measured. When the time is longer than 1 s, the stabilization procedure, consisting of stabilization of MZI1 followed by stabilization of MZI2, starts again. At the end, the time is checked again. When both MZIs are stable within time limit, appropriate phase shifts are set. Then the signal from probe laser-diode is blocked, photon pairs are injected into the setup and the main measurement is performed for 1.5 s. After that, the stabilization procedure starts again.

The overall phase drift inside each MZI during the time period including stabilization and measurement is smaller than $\pi/100$.

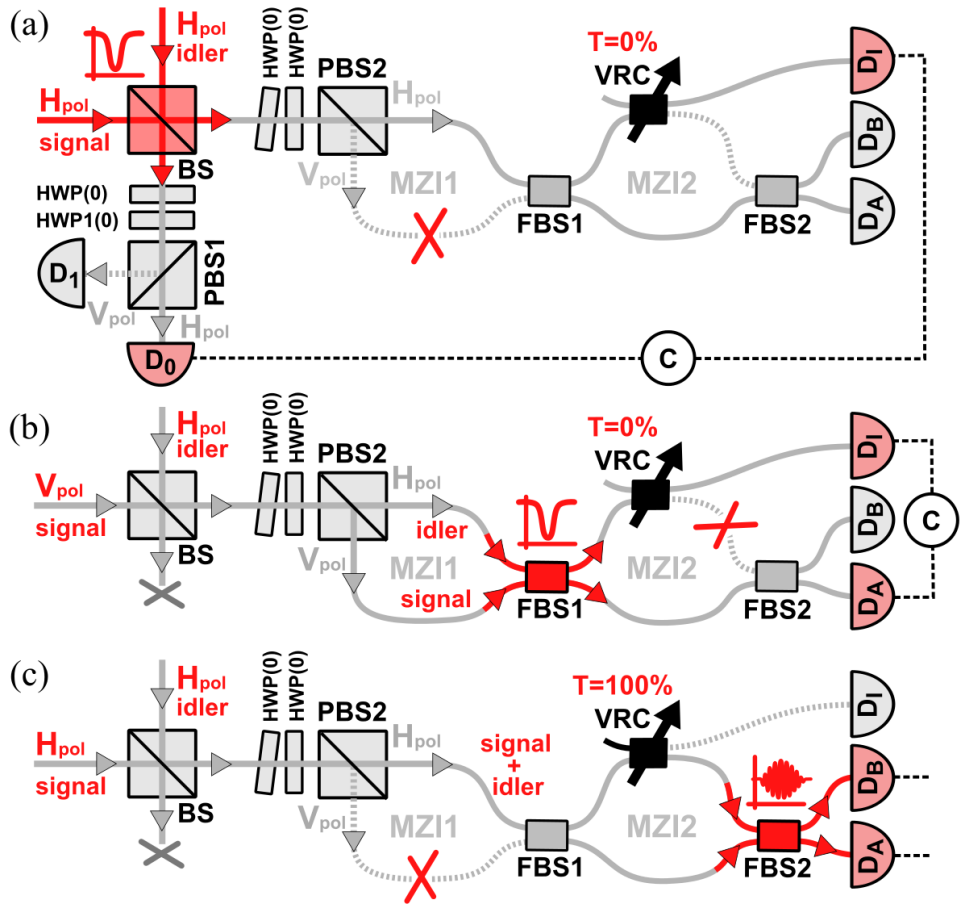

Figure 7.5: Schema of the three-step alignment procedure of experiment paths lengths according to HOM dip minimum or autocorrelation function maximum, for details see text.

Alignment procedure: Before the main measurement, it is necessary to precisely set lengths of the interferometers arms. It is done in three steps using the photon pairs from SPCD.

Firstly, paths between the SPDC source and the BS are aligned. It is schematically shown in Fig. 7.5(a). The polarization state of the idler photon is set to a horizontal linear polarization, thus signal and idler photons are in the same polarization state. The HWPs in front of PBS1 and PBS2 are rotated from 22.5° to 0°, to obtain the maximal photon count rate in horizontal-polarization outputs of PBSs. In MZI1 the arm corresponding to the vertical polarization is blocked to avoid any residual interference. In MZI2, the VRC splitting ratio is set to 100:0 to have the maximum count rate at detector D_I. Then the HOM dip is scanned with help of coincidence measurement between detectors D_0 & D_I. Its visibility is calculated and compared with maximum achieved value. Subsequently, the linear motorized stage is set to the position corresponding to the HOM dip minimum. If the visibility is repeatedly substantially lower (several percent) than the expected value, the spatial overlap of the photons at the BS is verified and eventually re-aligned, as well as the photons polarization states. When such alignment does not help to improve the dip visibility, it is necessary to re-align the source of photon pairs. Another warning that the source needs re-alignment is decreasing coincidence rate.

Secondly, the lengths of MZI1 arms are aligned. It is schematically shown in Fig. 7.5(b). The polarization of the idler photon is set back to the vertical linear polarization, thus the polarization states of signal and idler photon are perpendicular to each other. The HWP in front of the PBS2 is still set to 0° to not influence the polarization state. Everything is arranged in such way that horizontally polarized signal photons are in the upper arm and vertically polarized idler photons are in the lower arm of MZI1. Both signal and idler photons are led by a slow axis of polarization maintaining fibres to the first fibre beam splitter (FBS1) where they interfere. Just whole photon pair, which enters the MZI1[33], contributes to the HOM dip. The splitting ratio of VRC in MZI2 is set still to 100:0 to have no interference in MZI2. Then the HOM dip is scanned using the motorized stage of the air gap inside MZI1 and the coincidence measurement between detectors D_A & D_I is performed. Subsequently, the air gap position is set to HOM-dip minimum.

Thirdly, the lengths of MZI2 arms are aligned. It is schematically shown in Fig. 7.5(c). We utilize a phase sensitive measurement and we measure single-photon rate by detector D_A or D_B, no coincidence rate. To obtain higher rate, polarization of idler photon is set again to the horizontal linear polarization, thus signal and idler photons are in the same polarization state. The HWP in front of MZI1 is still set to 0°. Then, each photon that enters MZI1 is in the upper arm corresponding to horizontal linear polarization. As a result, all single photons and photon pairs enter FBS1 (MZI2) through a single input port. The VRC splitting ratio is set to 0:100 to balance MZI2 without additional losses (at detector D_I is no signal). The scan is performed by a linear motorized stage in air gap of MZI2. The envelope of the autocorrelation function of single photons and photons pairs are measured at the same time. Thus, the MZI2 arms lengths are balanced according to the maximum of the autocorrelation pattern envelope.

After this three-step alignment procedure, HWPs in front of PBS1 and PBS2 are rotated back to 22.5°. The polarization state of idler photon is set back to the vertical linear polarization to create the singlet Bell state.

VRC splitting ratio: When the whole setup is aligned, the appropriate splitting ratio of VRC is set. The probe beam is injected to the setup and only the upper arm of MZI1 is opened. We start with the VRC splitting ratio 0:100 to have no signal at detector D_I. The sum of count rates detected by D_A and D_B is measured for both arms of MZI2 separately. The balancing of insertion losses between arms of MZI2 is verified by comparing these measured values. Then the lower arm of MZI2 is interrupted. Subsequently, we tune the VRC splitting ratio till we reach required value. The VRC splitting ratio $R:T$ corresponds directly to single-photon count rates ratio $N_I : (N_A+N_B)$ from detectors D_I, D_A, D_B, respectively. All count rates N_k are corrected with respect to relative detection efficiencies η_k of single photon detectors D_k, where $k = I, A, B$. The count rate of detector D_I is also corrected with respect to different path transmittances from the VRC to detector D_I and from the VRC to detectors D_A and D_B. The value of this correction factor is 1/1.13.

[33]When the idler (signal) photon from the pair is reflected (transmitted) by the BS.

7.4 Measurement

Data acquisition: When the whole setup is aligned and the required VRC splitting ratio is set, then the main measurement begin. Interference fringes of MZI1 and MZI2 are scanned and their visibilities are compared with expected values. Then the stabilization procedure followed by the 1.5-s-long measurement period immediately starts and it is repeatedly applied. To accumulate enough data, it is repeated 70 times for each setting of the HWP1, which determines the measurement basis of the first qubit ($\mathcal{M}$, $\mathcal{N}$). When all data for all HWP1 settings are measured, the interference fringes of each MZI are scanned again and the splitting ration of VRC is verified. When the visibilities of these fringes are significantly lower than the expected values or the splitting ratio is different from the set one, all datasets are discarded and the setup is re-aligned. When obtained visibilities are high enough, another required splitting ratio of VRC is set and whole procedure starts again.

Note: Data in Fig.7.7 are measured in groups for different VRC splitting ratios (corresponding to different values of P_I). The reason is, that setting of VRC compared to setting of HWP is time consuming, more sensitive, less repeatable, and not under automatic computer control.

Data processing: For each basis $X = M, N$ we measure 6 two-photon coincidences C_{ik}^X represented by simultaneous clicks of pairs of detectors D_i & D_k, where $i = 0, 1$, and $k = A, B, I$. We measure the relative detection efficiencies η_i, η_k of the detectors, and their influence is compensated by rescaling of measured coincidence rates as $C_{ik}^X \rightarrow C_{ik}^X/(\eta_i\eta_k)$, (the efficiencies are listed in table 7.1, placed in the last section of this chapter). The measurement time is the same for both bases, it corresponds to equal a-priori probabilities of $\mathcal{M}$ and $\mathcal{N}$. Probabilities P_S, P_E, and P_I are determined as follow:

successful conclusive results $P_S = (C_{0A}^M + C_{1B}^M + C_{1A}^N + C_{0B}^N)/C_{\text{tot}}$,

erroneous conclusive results $P_E = (C_{0B}^M + C_{1A}^M + C_{1B}^N + C_{0A}^N)/C_{\text{tot}}$,

inconclusive results $P_I = (C_{0I}^M + C_{1I}^M + C_{0I}^N + C_{1I}^N)/C_{\text{tot}}$,

where C_{tot} denotes the sum of all 12 measured coincidence rates.

Measurement of entanglement based intermediate strategy: We perform measurements for 7 values of $\theta = j\pi/30$, $j = 1, 2, 3, 4, 5, 6, 7$ ($\theta = 6°, 12°, 18°, 24°, 30°, 36°, 42°$). These angles determine the basis $\mathcal{M}$ and $\mathcal{N}$. For each angle θ two positions of HWP1 are used: $(22.5° - \theta/4)$ and $(22.5° - \theta/4)$. The first one corresponds to basis $\mathcal{M}$ and the other one to $\mathcal{N}$. So, HWP1 angles in groups determining basis ($\mathcal{M}$, $\mathcal{N}$) are: $(12.0°, 33.0°)$, $(13.5°, 31.5°)$, $(15.0°, 30.0°)$, $(16.5°, 28.5°)$, $(18.0°, 27.0°)$, $(19.5°, 25.5°)$, $(21.0°, 24.0°)$. For each θ, the transmittance of VRC is varied from 1 to 0.1 with the step of 0.1, i.e. $T = 0.1, 0.2, 0.3, \ldots, 1.0$. For each splitting ratio of VRC and each setting of HWP1 in the black box, 70 repetitions of 1.5-s-long measurements (interlaced by active stabilization) is performed. The measurement is schematically shown in Fig. 7.6.

Measurement of entanglement based unambiguous discrimination: We have carried a separate test for 11 different $\theta_u = \arctan(\sqrt{T_u})$ corresponding to transmittances of the VRC, T_u varied from 1 to 0 with a step of 0.1, i.e. $T_u = 0.0, 0.1, 0.2, \ldots, 1.0$. The angles are listed in the table 7.2, placed in the last section of this chapter, *Tables & Additional material*. The measurement is schematically shown in Fig. 7.6.

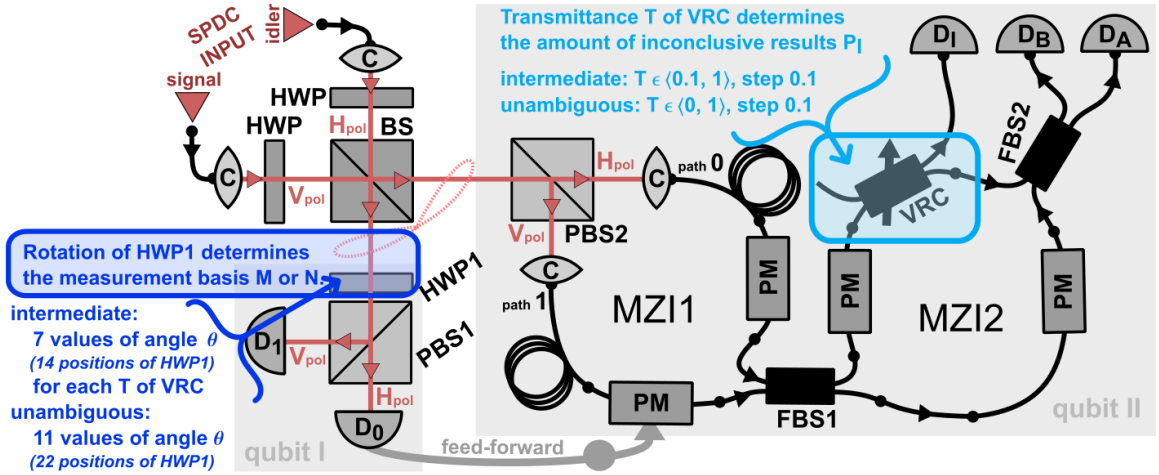

Figure 7.6: The scheme of the optimal entanglement-assisted discrimination of quantum measurements – for the intermediate and unambiguous strategies; SPDC – source of photon pairs, HWP – half-wave plate, (F)BS – (fibre) beam splitter 50:50, PBS – polarizing beam splitter, C – collimating lens, PM – phase modulator, D – single-photon detector, VRC – variable ratio coupler (It determines the amount of the inconclusive results.)

7.5 Results

Resulting dependences of $\tilde{P}_S$ on P_I for general **intermediate strategies** are plotted in Fig. 7.7. Obtained data are plotted by circles together with the theoretical curves representing the maximum $\tilde{P}_S$ achievable by the optimal entanglement-assisted protocol (solid lines) and by using the single-qubit probes (dashed lines). Statistical errors of the results are smaller than the size of symbols. We can see that for certain θ and P_I the experimental entanglement-based discrimination indeed outperforms the best strategy without entanglement. The slight reduction of the experimentally observed $\tilde{P}_S$ with respect to the theoretical prediction could be attributed to various experimental imperfections such as phase fluctuations inside MZIs, imbalance of MZIs arms lengths, small deviations in phase and polarization settings, slightly unbalanced splitting ratios of beam splitters, and small imperfections in the input singlet state. As indicated by the theoretical curves, the entanglement-based protocol theoretically outperforms the single-qubit scheme for all $P_I > 0$. The entanglement thus does not help only in the regime of minimum error discrimination ($P_I = 0$) where the optimal success probability $[1+\sin(2\theta)]/2$ can be achieved by a single-qubit probe prepared in state $|+\rangle$.

Unambiguous discrimination with a single-qubit probe is possible only if the probe is prepared in a state orthogonal to one of the projectors (7.1), say $|\vartheta\rangle = |\psi^{\perp}\rangle$. The resulting probability of inconclusive outcomes $P_I^{\text{unambig}} = [1 + \cos^2(2\theta)]/2$ is larger than the probability $\cos(2\theta)$ achieved by the entanglement-based scheme and the difference increases with θ. The experimental results of entanglement based unambiguous discrimination for 11 different θ_u are plotted in Fig. 7.8. They are in good agreement with the theory. The probability of errors P_E (which should theoretically be zero) does not exceed 3.2%. It is caused by experimental imperfections. The statistical errors of the results are smaller than the size of symbols.

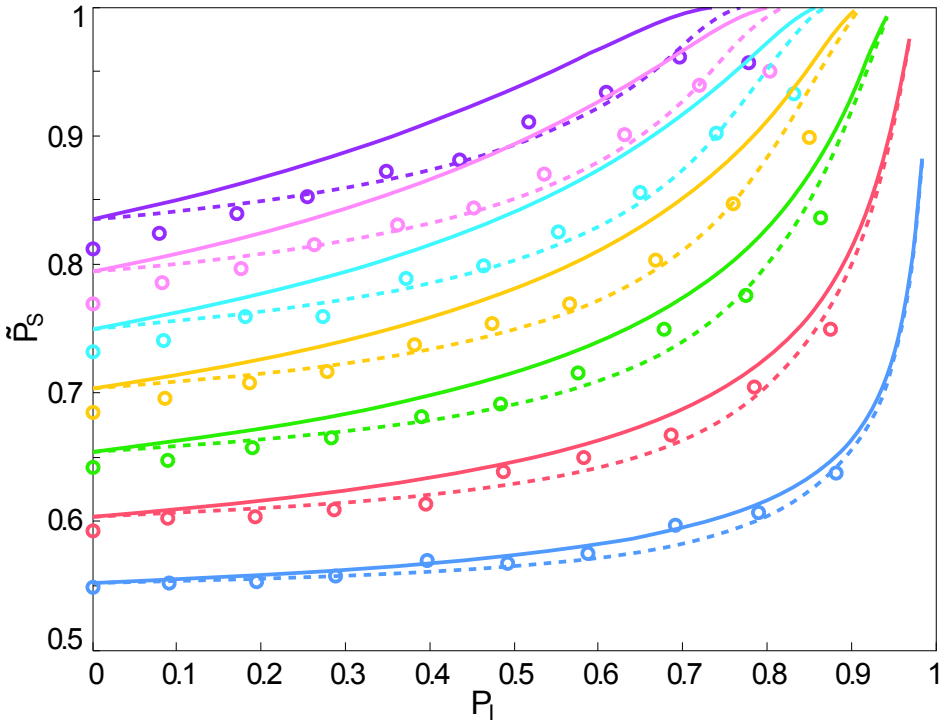

Figure 7.7: Optimal entanglement-assisted discrimination of measurement bases $\mathcal{M}$ and $\mathcal{N}$. Dependence of relative success probability $\tilde{P}_S$ on probability of inconclusive results P_I is plotted for 7 values of $\theta_j = j\pi/30$, $j = 1, 2, 3, 4, 5, 6, 7$ (values for each θ are depicted by one colour). The value of j increases from bottom to top. Shown are the experimental data (circles) as well as the maximum $\tilde{P}_S$ achievable by the optimal scheme using entangled state (solid lines), and using single-qubit probes only (dashed lines).

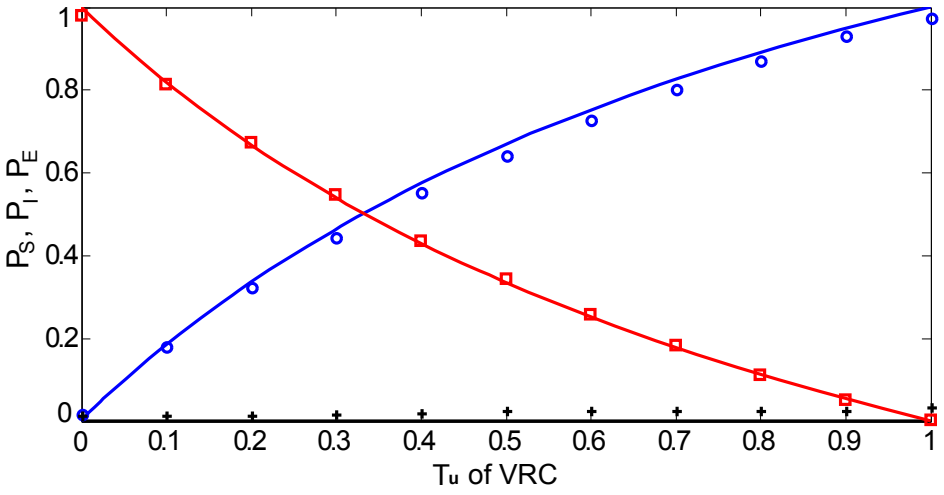

Figure 7.8: Entanglement based unambiguous discrimination of quantum measurements $\mathcal{M}$ and $\mathcal{N}$. Probabilities P_S (∘), P_I (□), and P_E (+) are plotted as functions of the VRC splitting ratio T_u. Lines represent theoretical predictions.

7.5.1 Tables & Additional material

Table 7.1: Measured relative detection efficiencies of single photon detectors.

detector	D_0	D_1	D_A	D_B	D_I
rel. efficiency	0.789	0.938	0.982	1.000	0.973/1.13* = 0.861

* Denotes the correction factor of paths transmittances.

Table 7.2: Entanglement based unambiguous discrimination: angles of rotation of HWP1 in the black box for basis $\mathcal{M}$ and $\mathcal{N}$ for transmissivity T_u of the VRC.

T_u of VRC	angle of rotation HWP1 [°]	
	basis $\mathcal{M}$	basis $\mathcal{N}$
1.0	0.000	45.000
0.9	0.754	44.246
0.8	1.595	43.405
0.7	2.541	42.459
0.6	3.619	41.381
0.5	4.868	40.132
0.4	6.344	38.656
0.3	8.145	36.855
0.2	10.453	34.547
0.1	13.726	31.274
0.0	22.500	22.500

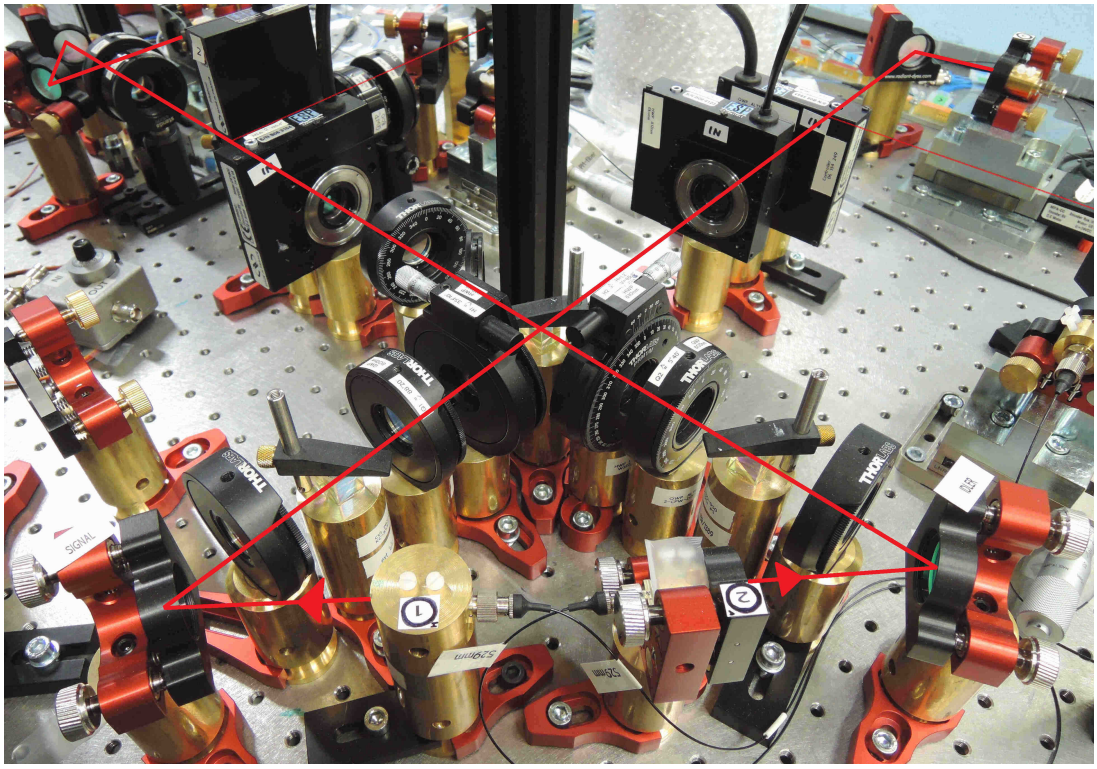

Figure 7.9: Photo of the post-selection entanglement state preparation with motorized wave plates serving for its characterization. Photons paths are shown by red lines.

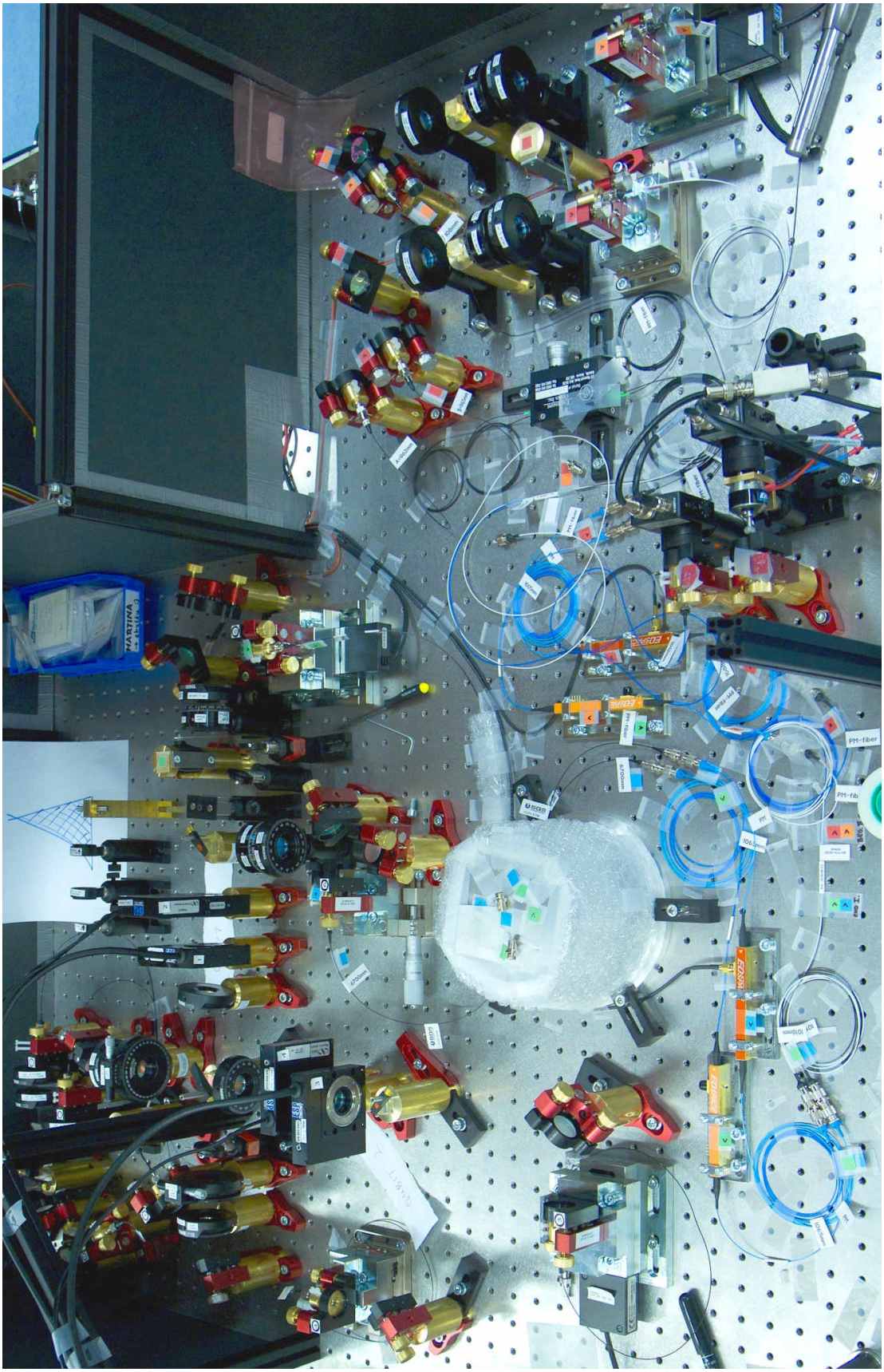

Figure 7.10: Photo of the experimental layout of the optimal entanglement-assisted discrimination of quantum measurements.

Chapter 8

Faithful conditional quantum state transfer between weakly coupled qubits

This chapter is based on the following publication:

[5] Martina Miková, Ivo Straka, Michal Mičuda, Vojtěch Krčmarský, Miloslav Dušek, Miroslav Ježek, Jaromír Fiurášek, and Radim Filip. *Faithful conditional quantum state transfer between weakly coupled qubits.* Scientific Reports **6**, 32125 (2016).

8.1 Basic idea

This last described experiment is devoted to demonstration of faithful conditional quantum state transfer between weakly coupled qubits. We use a linear optical setup with qubits encoded into polarization states of single photons. This platform serves as a suitable testbed for proof-of-principle verification of our protocol, whose applicability is, nevertheless, universal and by no means limited to photonic qubits.

Our scheme enables a probabilistic yet perfect unidirectional transfer of an arbitrary unknown state of a source qubit onto a target qubit prepared initially in a known state. The transfer is achieved by a combination of a suitable measurement on the source qubit and quantum filtering on the target qubit. The quantum filtering depends on the outcome of the measurement on the source qubit, initial state of target qubit and on mutual interaction of qubis.

In this way, quantum state can be transferred between various physical platforms or one can create a hybrid entangled state.

8.2 Theory

The theoretical part of [5] is done by my colleagues. Here, we mention only a part of the theory necessary for understanding of the protocol and its experimental realization.

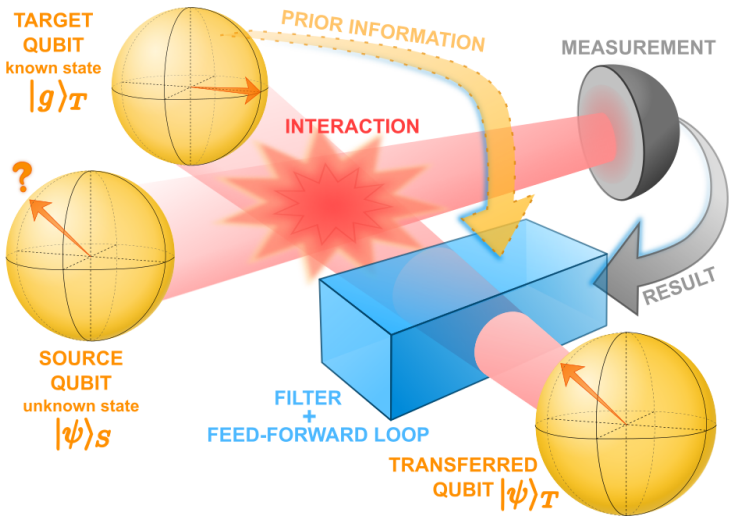

Figure 8.1: Quantum state transfer protocol. The initial state $|\psi\rangle_S$ of the source qubit S can be arbitrary and unknown. The goal is to transfer any state of source S to target T, initially in a known fixed state $|g\rangle_T$. The state transfer requires some interaction (unitary or probabilistic) between the source S and target T qubits. The transfer is performed by optimal measurement and feed-forward loop with optimal filter controlled by the measurement result and prior information about the initial target state $|g\rangle_T$.

Single qubit transfer: The goal of the universal quantum state transfer protocol is to faithfully map any quantum state $|\psi\rangle_S = \alpha|0\rangle_S + \beta|1\rangle_S$ of a source qubit S onto the target qubit T that is initially prepared in a known fixed state $|g\rangle_T$, as illustrated in Fig. 8.1. The source qubit could even be initially entangled with some ancillary qubit. For clarity of subsequent presentation, we shall consider a generic pure initial state of the source qubit $|\psi\rangle_S$. To make our treatment sufficiently general, we allow for both deterministic and probabilistic interactions $\hat{V}$ between the source and target qubits, hence $\hat{V}$ can be either a unitary operation or a non-unitary quantum filter satisfying $\hat{V}^\dagger\hat{V} \leq \hat{I}$. We thus consider the most general class of noiseless quantum interactions. The interaction $\hat{V}$ creates an entangled state of source and target qubits,

$$\hat{V}|\psi\rangle_S|g\rangle_T = \alpha|\Phi_0\rangle_{ST} + \beta|\Phi_1\rangle_{ST}, \tag{8.1}$$

where $|\Phi_j\rangle_{ST} = \hat{V}|j\rangle_S|g\rangle_T$. In the next step of the protocol we erase the correlations between source and target qubits by a projective measurement on the source qubit. If we project the source qubit onto a pure state $|\pi\rangle_S$, we prepare the target qubit in the following pure state,

$$|\varphi\rangle_T = \alpha|\phi_0\rangle_T + \beta|\phi_1\rangle_T, \tag{8.2}$$

where $|\phi_j\rangle_T = {}_S\langle\pi|\Phi_j\rangle_{ST}$. Note that states $|\phi_0\rangle$ and $|\phi_1\rangle$ are generally non-orthogonal, $\langle\phi_0|\phi_1\rangle \neq 0$, and they are not normalized and their norms can differ, $\langle\phi_0|\phi_0\rangle \neq \langle\phi_1|\phi_1\rangle$.

To complete the quantum state transfer we need to transform the two non-orthogonal states $|\phi_0\rangle$ and $|\phi_1\rangle$ onto normalized orthogonal basis states $|0\rangle$ and $|1\rangle$, respectively. Provided that $|\phi_0\rangle$ and $|\phi_1\rangle$ are linearly independent, this can be accomplished by a suitable quantum filter $\hat{G}$ applied to the target qubit,

$$\hat{G} = \frac{1}{N}\left(\frac{1}{\langle\phi_1^\perp|\phi_0\rangle}|0\rangle\langle\phi_1^\perp| + \frac{1}{\langle\phi_0^\perp|\phi_1\rangle}|1\rangle\langle\phi_0^\perp|\right). \tag{8.3}$$

Here $|\phi_j^\perp\rangle$ denotes a qubit state orthogonal to $|\phi_j\rangle$, $\langle\phi_j^\perp|\phi_j\rangle = 0$, and N is a normalization factor. We emphasize that the filter $\hat{G}$ does not depend on the input state $|\psi\rangle_S$ of the source qubit, it depends only on the initial state of the target qubit $|g\rangle_T$, the interaction $\hat{V}$, and the state $|\pi\rangle_S$ onto which the source qubit is projected. After filtering, the state of the target qubit becomes equal to the input state of the source qubit,

$$\hat{G}|\varphi\rangle_T = (\alpha|0\rangle + \beta|1\rangle)_T/N, \tag{8.4}$$

and the probability p of success of the transfer protocol reads $1/|N|^2$. To reach maximal probability of success, N has to be set such that the maximum singular value of $\hat{G}$ is equal to 1 and $\hat{G}^\dagger\hat{G} \leq \hat{I}$ is satisfied. The probability of success can be also maximized by optimization of the measurement strategy and enhanced by the feed-forward loop, which allows us to exploit both outcomes of projective measurement on the source qubit. The overall success probability of the protocol is discussed later.

Example of the interaction: To illustrate our method, we consider as an instructive example a class of symmetric probabilistic two-qubit interactions described by an operator $\hat{V}$ diagonal in the computational basis,

$$\hat{V} = |00\rangle\langle 00| + t_1|01\rangle\langle 01| + t_1|10\rangle\langle 10| + t_{11}|11\rangle\langle 11|, \tag{8.5}$$

where $t_1, t_{11} \in [-1, 1]$. It turns out that in this case it is advantageous to measure the source qubit in the balanced superposition basis $|\pm\rangle = \frac{1}{\sqrt{2}}(|0\rangle \pm |1\rangle)$. After some algebra we find that the conditional states of the target qubit corresponding to these two outcomes differ only by a sign in the superposition,

$$|\varphi_\pm\rangle_T = (\alpha|\phi_0\rangle \pm \beta|\phi_1\rangle)_T/\sqrt{2}. \tag{8.6}$$

It implies that the quantum filters $\hat{G}_+$ and $\hat{G}_-$ associated with the measurement outcomes $+$ and $-$ differ only by a fixed unitary transformation, $\hat{G}_- = \hat{U}_\pi\hat{G}_+$, where $\hat{U}_\pi = |0\rangle\langle 0| - |1\rangle\langle 1|$. The whole protocol can be therefore implemented using a *fixed* quantum filter $\hat{G}_+$ followed by a feed-forward-controlled unitary phase shift. This greatly simplifies the experimental implementation of the protocol.

Linear-optical emulation of the interaction: For the proof-of-principle demonstration of the state transfer protocol we use linear optics and qubits encoded into polarization states of single photons.

We thought about the suitable non-trivial interaction between single photons. Finally, we decided to make our study generic and test our procedure in the regime of weakly coupled qubits. Thus for the interaction between single photons, we utilize interference on a partially polarizing beam splitter (PPBS) that fully transmits horizontally polarized photons and only partially reflects vertically polarized photons, with corresponding amplitude transmittance t_V. We post-select on presence of a single photon in each output port of PPBS [199], then the interference results in the two-qubit transformation (8.5) with parameters $t_1 = t_V$ and $t_{11} = 2t_V^2 - 1$.

8.3 Experiment

First, we briefly describe the experiment, then we explain in detail general blocks of the experimental setup. Finally alignment routines and stabilization procedure are discussed. The simplified scheme of the experimental setup is shown in Fig 8.2.

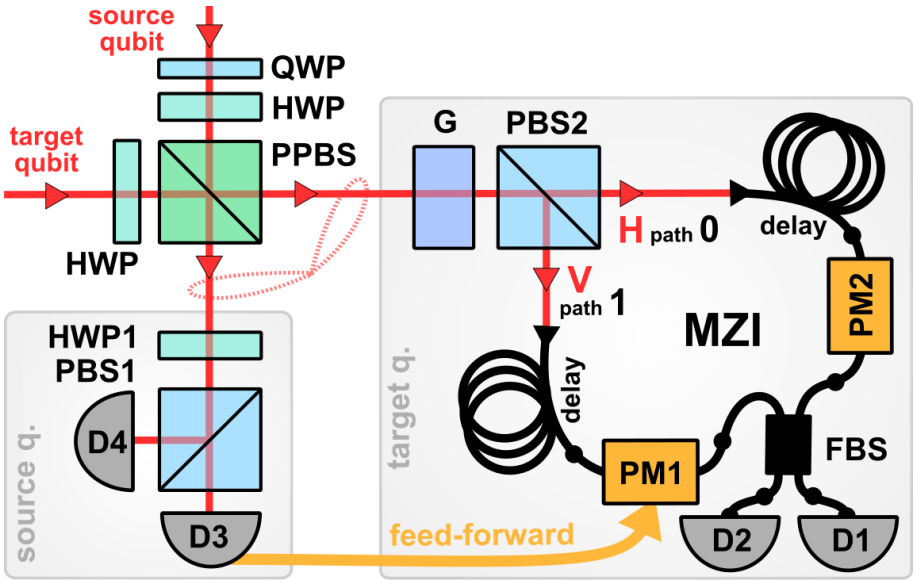

Figure 8.2: Simplified scheme of the experimental setup for the faithful conditional quantum state transfer between weakly coupled qubits. PPBS – partially polarizing bulk beam splitter ($T_H = 0.983, T_V = 0.334$); FBS – fibre beam splitter (47.6:52.4); G – adaptive state filtration $\hat{G}_+$; PBS – polarizing beam splitter; HWP – half-wave plate; QWP – quarter-wave plate; PM – phase modulator; D – single-photon detector; thinner red line – free space beam; thicker black line – single mode polarization maintaining optical fibre PM-780HP; thick yellow line – feed-forward loop with coaxial cables. The adaptive polarization state filter G is in detail shown in Fig.8.4. The complex scheme of the experiment and its photo are shown at the end of this chapter in Fig. 8.11 and Fig. 8.13, respectively.

Time correlated photon pairs are generated by frequency degenerate parametric down-conversion process. Arbitrary input states of the source and target qubit can be prepared by a combination of quarter-wave plates (QWPs) and half-wave plates (HWPs). The qubits interfere at the PPBS. Subsequently, the source qubit is measured in the basis of diagonal linear polarizations using a single-photon polarization detection block consisting of a half-wave plate HWP1, a polarizing beam splitter PBS1 and two single photon detectors D3 and D4. The polarization filter $\hat{G}_+$ on the target photon is implemented with the help of calcite beam displacers (BD) and HWPs, as described below and shown in Fig. 8.4.

The conditional π phase shift on the target qubit, which changes the filter $\hat{G}_+$ to $\hat{G}_-$, is applied by means of the feed-forward loop [1, 2, 30, 43]. To facilitate its experimental realization, we couple the target photon into a fibre-based Mach-Zehnder interferometer (MZI), thus the polarization qubit is converted into the spatially encoded qubit. The single photon detector D3, whose click indicates projection of the source qubit onto state $|-\rangle$. It triggers the feed-forward action. The signal from the detector is amplified and led to an integrated lithium-niobate phase modulator PM1 inserted in one arm of the fibre MZI, thereby applying the conditional π phase shift to state $|1\rangle_T$.

The setup stability is reached thorough passive isolation from environment. Simultaneously, MZI is actively phase stabilized every 1.5 s to reduce remaining phase drifts caused by temperature fluctuations and air flux below 2° during measurement periods.

Qubit state preparation: The source of correlated photon pairs is in detail described in *Chapter 3, Methods and Tools*. Current power of pump CW laser is 100 mW. The photons separated by a PBS are coupled into the slow axis of polarization maintaining fibres (PM-780HP) and proceeded directly to qubit state preparations.

The initial states of source and target qubits are encoded into the polarization degrees of freedom of signal and idler photons, respectively, by means of HWPs and QWPs, as shown in scheme of the experimental setup in Fig. 8.2. Computational basis states $|0\rangle$ and $|1\rangle$ correspond to horizontal and vertical linear polarization, respectively. The arbitrary states of unknown transferred source qubit can be written as: $|\psi\rangle_S = \alpha|H\rangle_2 + \beta|V\rangle_2$ and the known linearly polarized state of target qubit is: $|g\rangle_T = \gamma|H\rangle_1 + \delta|V\rangle_1$, where $\gamma = \cos(\omega)$, $\delta = \sin(\omega)$. The overall state in font of the PPBS in Fig. 8.3 reads:

$$|\mathrm{in}_{\mathrm{PPBS}}\rangle_{12} = |g\rangle_T \otimes |\psi\rangle_S = (\gamma|H\rangle_1 + \delta|V\rangle_1) \otimes (\alpha|H\rangle_2 + \beta|V\rangle_2). \tag{8.7}$$

Implementation of the interaction $\hat{V}$: To emulate the regime of weakly coupled qubits, the photons are mixed together at the PPBS. The ideal PPBS should be fully transmitting for horizontally polarized photons $T_H = 1$ and only partially transmitting for vertical polarization, for instance $T_V = 0.334$, where $T_x + R_x = 1, x = H, V$ and amplitude transmittance and reflectance are $t_x = \sqrt{T_x}, r_x = \sqrt{R_x}$. According to the two-qubit transformation described in Eq. (8.5) with parameters $t_1 = t_V$ and $t_{11} = 2t_V^2 - 1$, the resulting state behind the PPBS is (the mode notation is depicted in Fig. 8.3):

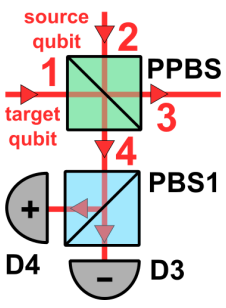

Figure 8.3: Scheme clarifying mode notation.

$$|\text{out}_{\text{PPBS}}\rangle_{34} = \hat{V}|\text{in}_{\text{PPBS}}\rangle_{12} = \alpha(\gamma|H_3H_4\rangle + \delta t_V|V_3H_4\rangle) + \beta(\gamma t_V|H_3V_4\rangle + \delta(2T_V - 1)|V_3V_4\rangle). \tag{8.8}$$

Projective measurement applied on the source qubit: Subsequently, the source qubit at the output port 4 of the PPBS is measured in the balance superposition of basis $|\pm\rangle$. The block of projective measurement on the source qubit consists of a half-wave plate HWP1, a polarizing beam splitter PBS1 and two single photon detectors D3 and D4. The rotation of the HWP1 in front of the PBS1 determines the measurement basis. Thus the measurement in $|\pm\rangle$ basis matches in polarizations the projection onto diagonal or anti-diagonal (D/A) linear polarization state, which corresponds to the click of single-photon detector D4 or D3, respectively. It is schematically shown in Fig.8.3. Numerical calculations indicate that for any t_V and ω it is optimal to measure the source qubit in the balanced superposition basis $|\pm\rangle_S$ (for detail see paper [5]),

$$\langle\pm|_4 = (\langle H|_4 \pm \langle V|_4)/\sqrt{2}. \tag{8.9}$$

After the source qubit projection, the resulting target-qubit state can be written as[34]:

$${}_4\langle\pm|\text{out}_{\text{PPBS}}\rangle_{34} = |\varphi_\pm\rangle_T = -(\alpha|\phi_0\rangle \pm \beta|\phi_1\rangle)/\sqrt{2}, \tag{8.10}$$

where the sign $\pm$ comes from the projection of the source qubit into D/A polarization state and $|\phi_0\rangle = \gamma|H\rangle + \delta t_V|V\rangle$, $|\phi_1\rangle = \gamma t_V|H\rangle + \delta(2T_V - 1)|V\rangle$. States $|\phi_0\rangle, |\phi_1\rangle$ are in general non-orthogonal and non-normalized. They depend on the known parameters: splitting ratio t_V of PPBS, initial target-qubit state parametrized by angle ω, and projective measurement on the source qubit.

Target-qubit state filtration: It is a task of the qubit state filtration to make filtered states $|\phi_0'\rangle, |\phi_1'\rangle$ orthogonal $\langle\phi_0'|\phi_1'\rangle = 0$, and of the same size $\langle\phi_0'|\phi_0'\rangle = \langle\phi_1'|\phi_1'\rangle$. The filter $\hat{G}_+$ acts as follows: $\hat{G}_+|\phi_0\rangle = |\phi_0'\rangle \propto |H\rangle$ and $\hat{G}_+|\phi_1\rangle = |\phi_1'\rangle \propto |V\rangle$. Thus the resulting state of the target qubit after successful filtration reads:

$$\hat{G}_+|\varphi_\pm\rangle_T = |\varphi_\pm'\rangle_T = -(\alpha|H\rangle \pm \beta|V\rangle)/N. \tag{8.11}$$

Any quantum filter $\hat{G}_+$ can be decomposed into a sequence $\hat{G}_+ = \hat{U}_2\hat{D}\hat{U}_1$, where $\hat{U}_{1,2}$ are unitary operations and the operator $\hat{D}$ is diagonal in the computational basis, $\hat{D} = |0\rangle\langle 0| + \lambda|1\rangle\langle 1|$, where $\lambda \in (0, 1]$ is an attenuation factor. Such decomposition enables physical implementation of the filter.

The realization of the filter $\hat{G}_+$ is shown in Fig. 8.4. It consists of HWPs and two calcite beam displacers (BDs), which form an interferometric device. The beam displacer BD_{IN} introduces a transversal spatial offset between V and H polarized beams. These two polarization components become spatially separated and can be individually addressed. The HWP(45°), which is placed in both paths, mutually exchange polarizations V and H. Then the BD_{OUT} puts the two spatial modes coherently together [200–202].

[34]The remaining index of PPBS output port is 3, we will not keep this notation in further text.

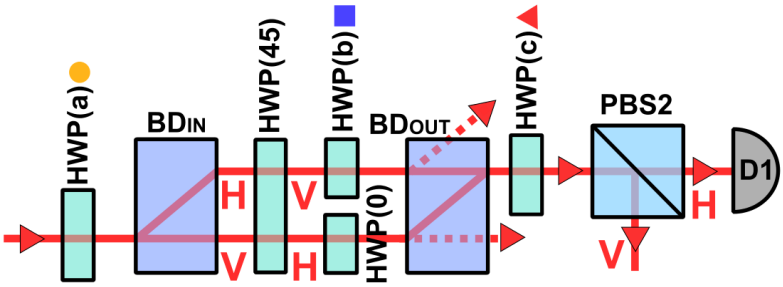

Figure 8.4: State filter G_+ consists of calcite MZI. BD – calcite beam displacer, BPS – polarizing beam-splitter, D – single-photon detector, HWP(x) – half-wave plate, where x is an angle of rotation from 0°. The angles a, b, c, which varied with initial target-qubit state, are shown in Fig. 8.5 by symbols ●, ■, ▲, respectively.

The half-wave plates WHP(a), HWP(c) at the input and output of the calcite MZI implement the unitary operations $\hat{U}_1$ and $\hat{U}_2$. HWP(a) appropriately rotates the states into the basis of calcite interferometer. Selective attenuation $\hat{D}$ of single basis mode is implemented by a suitable rotation of HWP(b) inserted inside the calcite MZI. HWP(b) influences just single spatial mode, which in combination with $\mathrm{BD}_{\mathrm{out}}$ attenuates the mode. The remaining HWP(0°) placed in the second arm of the MZI has no influence to polarization state, however, it compensates the optical length and dispersion of the arm. Finally, HWP(c) rotates the filtered states into the basis of PBS2.

As mentioned before, the proper filter $\hat{G}_+$ depends on the interaction $\hat{V}$, on the projective measurement applied on the source qubit, and on the initial target-qubit state $|g\rangle_T$, which is parametrized by angle ω. Interaction and measurement are fixed for our experiment. Thus we calculate the angles a, b, c of HWPs rotation for several values of ω, as visible in Fig. 8.5. These angles could be determined by standard matrix optics calculations or by singular value decomposition of the filter $\hat{G}_+$.

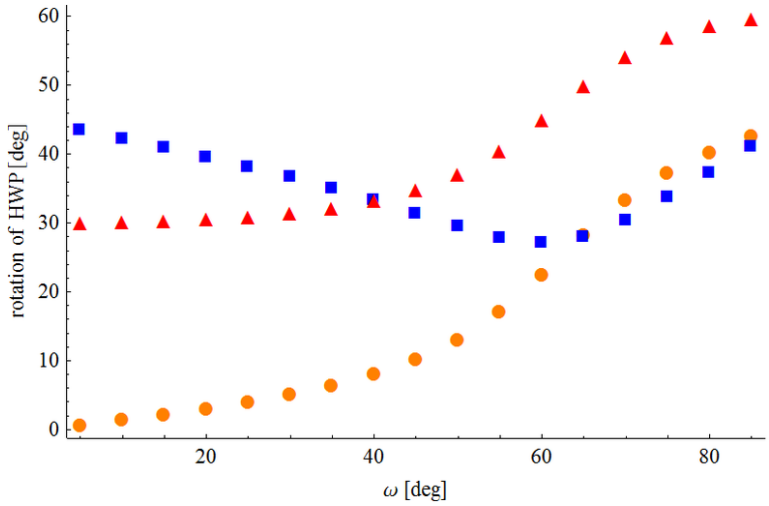

Figure 8.5: Settings of HWPs angles a, b, c in the state filter G_+ for certain angles ω, determining initial target-qubit state $|g\rangle_T$. (●) yellow circle – angle a, (■) blue square – angle b, (▲) red triangle – angle c.

Fibre-based Mach-Zehnder interferometer: The PBS2 creates an entrance into the fibre-based MZI. The qubit state is re-encoded from polarization degree of freedom into spatial one $|H\rangle = |0\rangle$ and $|V\rangle = |1\rangle$. The photon is coupled into the slow axis of polarization maintaining fibres (PM-780HP), then passes through the short delay lines (4.5 m) and enters integrated electro-optical phase modulators (PM), placed in each MZI arm. The total arm length is roughly 7.5 m in optical fibre. Subsequently, the photon interferes at the output fibre beam-splitter (FBS), with measured splitting ratio 47.6 : 52.4. Subsequently, it passes several meters of a polarizing fibre (HB830Z(5/80)) placed in both FBS output ports leading to detectors $D1$ and $D2$. This fibre acts as a post-selective polarization filter. It selects optical signal in a slow fibre axis, while the signal in a fast axis, which is not under our control, is attenuated. The photon interferes with measured visibility ∼95%.

Real-time feed-forward control: When the source qubit is detected by D4 corresponding to projection onto $|+\rangle$, then filter $\hat{G}_+$ is applied and no other action is needed. Thus the phase inside MZI is set to 0° and the qubit state remains unchanged. The output target qubit is in the same state as the input source qubit.

However, it is not the case, when the source qubit is detected by D3 corresponding to projection onto $|-\rangle$. Then, the correct quantum filter $\hat{G}_-$ has to be applied to change the target-qubit state. The quantum filter $\hat{G}_-$ differs from quantum filter $\hat{G}_+$ only about fixed unitary operation $\hat{U}_\pi$. This conditional application of the unitary operation, triggered by the click of detector D3, requires a real-time feed-forward loop. PM1 in the fibre-based MZI is a part of the loop. Via it a conditional π-phase shift is applied between MZI arms, see Fig. 8.2. After the successful application of $\hat{G}_-$ [35], the output target-qubit state is $|\varphi'\rangle_T = -(\alpha|0\rangle+\beta|1\rangle)/\sqrt{2}$. Again, it is in the same state as the input source qubit.

The total success probability of state transfer is given by a sum of two contributions,

$$p = \frac{1}{|N|^2} + \frac{1}{|N_-|^2}, \tag{8.12}$$

where N_- is the normalization factor of $\hat{G}_-$. The success probability of the result with a sign + and − is included in the normalization factor $1/|N|^2$ and $1/|N_-|^2$, respectively, because the filter $\hat{G}$, determined by Eq. (8.3), employs not normalized states.

The probabilistic nature of the quantum state transfer protocol is the price to pay for a faithful transfer of all states with unit fidelity. The quantum filter $\hat{G}$ is an essential part of the protocol. The average fidelity of states (8.2) obtained without filtering may even drop below the limit of 2/3, which is achievable by a purely classical measure-and-prepare strategy.

[35] It includes application of the quantum filter $\hat{G}_+$ followed by the feed-forward action applying phase shift of π, $\hat{G}_- = \hat{U}_\pi \hat{G}_+$.

Optical path alignment: First, optical paths of the signal and idler photons at the PPBS are adjusted according to the minimum of Hong-Ou-Mandel (HOM) dip, when both photons are in vertical polarization state. All wave-plates behind the PPBS are set in such way, that the measured count rate is maximized. One photon of the pair is detected by detector D4 and the second one by detector D1 or D2. In each MZI, just one arm corresponding to vertical polarization is opened, it prohibits any residual interference. The photons are detected only as coincidence rate C_{41}, respective C_{42}. Theoretical dip visibility is 66.9% and a measured dip visibility is 66.4%. Delay between photons at PPBS can be changed by motorized stage placed in the source of photon pairs. We scan the HOM dip and then we set the stage to the position of the dip minimum. During the final data accumulation, the coincidence rate in HOM dip minimum is checked in a several-hours period. If the rate is changed, we re-align the motorize stage to the current position of the HOM dip minimum.

Then, the optical paths in filter $\hat{G}_+$ (the calcite MZI) are adjusted by means of interference of a probe beam to the maximum of its autocorrelation function. The probe beam is an attenuated CW laser diode (LD) with central wavelength 810 nm, which goes through the same interference filter as photon pairs. Its polarization is set to horizontal, then the beam is coupled only to a target qubit path. Subsequently, the probe beam goes through the PPBS and HWP(a), where its polarization state is changed to diagonal. The beam enters the calcite MZI through $\mathrm{BD_{IN}}$. HWP(b) is set into a position without any filtration ($b = 0$). Thus the calcite MZI has balanced insertion losses of its arms. The arms correspond to H and V polarization as shown in Fig.8.4. The polarisation analysis is in diagonal and anti-diagonal basis created by HWP(c) and PBS2. A lower arm of fibre-based MZI is interrupted to see the interference pattern of calcite MZI at detector D1 respective D2. Then the phase in the MZI is set according to global intensity minimum. The phase is tuned by tilting $\mathrm{BD_{OUT}}$. The theoretical visibility of calcite MZI could be 100%, we reach 99.6%. Such device is phase stable within 2° for a several hours under our laboratory conditions.

Finally, optical paths in fibre-based MZI are adjusted according to the minimum of HOM dip at the FBS (47.6:52.4). The source and target qubits are set to the V and H polarization, respectively, to have the best possible coincidence rate C_{12} at the end of the MZI. The HWPs in the experiment are set according to the Fig. 8.6(a), thus signal and idler photon have different paths to the FBS, where they interfere. Path difference between MZI arms can be changed by a motorized stage placed in one of its air gaps. Via it, we scan the HOM dip. Maximal expected dip visibility is 99.1%, however, we reache maximally 94.4%, probably due to photons distinguishability at the FBS.

We assume that the optical paths for signal and idler photon are already balanced up to PBS2. Subsequently, we verify this assumption by scanning HOM dip at the end of the fibre MZI again according to Fig.8.6(b). When the minimum positions of HOM dips are the same, we know, that all setup is aligned properly. Then we set the stage to the position of the HOM dip minimum. Otherwise, it is necessary to check the HOM dip at PPBS and eventually the alignment of calcite MZI.

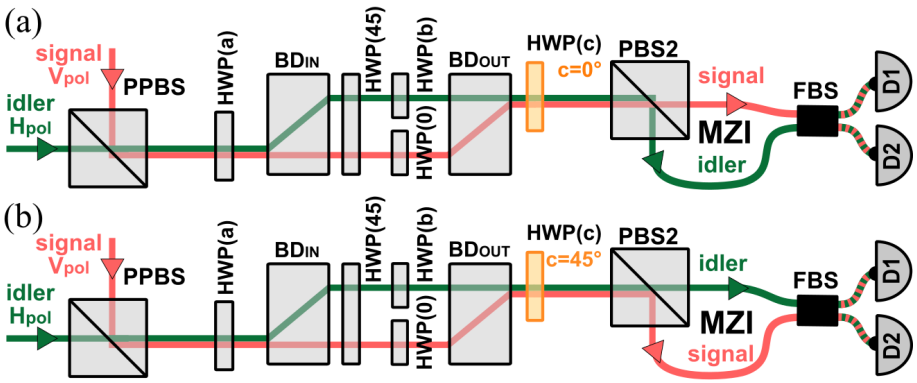

Figure 8.6: Scheme of HOM dip measurement at the end of the fibre-based MZI. Red path – signal photon, green path – idler photon. Two schemes in sub-figures (a) and (b) differ in a setting of HWP(c), where $c = 0°$ and $c = 45°$, respectively.

Note: For the first setup alignment we used this method iteratively for proper alignment of calcite MZI. When we were sure in PPBS HOM dip minimum, the calcite MZI was set to the maximum of its autocorrelation function (which we suppose to be the global maximum). Then, according to settings depicted in Fig. 8.6(a) and (b) positions of HOM dip minimum at the FBS were measured. The half of the difference between the dips positions should correspond to the path difference between calcite MZI arms. Thus we move to the adjacent minimum of calcite MZI and we repeat the alignment procedure.

Active stabilization procedure The passive phase stability of isolated fibre MZI is better than 1° per second. To reduce phase drifts caused by temperature gradients and air flux fluctuations in time, the active stabilization is implemented through PM2.

To obtain stabilization procedure as autonomous as possible, we decided to inject probe beam, serving for stabilization purposes, into the MZI through the second input port of PBS2. The beam polarization is set to diagonal, then PBS2 behaves for it as a balanced beam splitter. During the whole main measurement, input parameters of the stabilization procedure (probe beam intensity and interferometer visibility) are constant. If we chose the path of the probe beam through the calcite filter, the stabilization input parameters would be different for each setting of the filter. For each new setting, it would require measurements of these input parameters, otherwise the stabilization would not work properly. It would be also time consuming.

However, behind PBS2, optical signals from SPDC and probe beam are orthogonally polarized. Because of it, additional HWP and PBS are placed in each MZI arm. They are set in such way, that just 3 % of a probe beam or 97 % of single photons from SPDC is coupled into the slow axis of polarization maintaining fibres. It is shown in Fig. 8.7.

The slightly different phase for photons from SPDC and a probe beam at PBS2 is included as a phase offset in the stabilization procedure. This stabilization procedure interrupts the main measurement each 1.5 s. The optical signals are swapped and the automatic procedure verifies the probe beam intensity. In ideal case, it corresponds to intensity in the centre of the interference fringe. If it does not, the proper phase correction is applied via PM2. It is in detail described in *Chapter 3, Methods and Tools.*

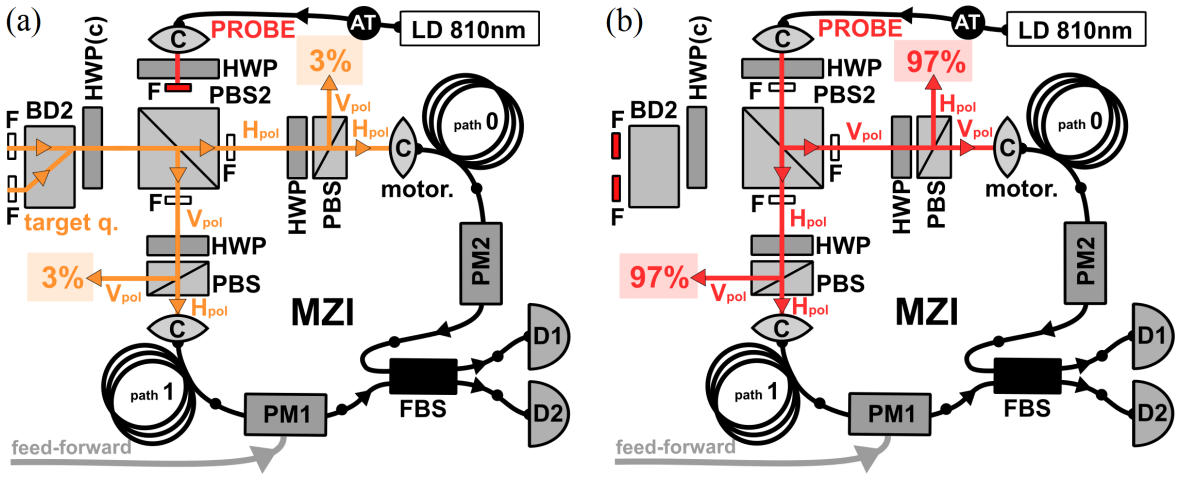

Figure 8.7: Schematically shown paths of photons: (a) – photon from SPDC – target qubit; (b) – probe beam – using for stabilization procedure of fibre MZI. Both these signals are coupled into slow axis of polarization maintaining optical fibres (PM-780HP) which creates MZI arms. LD – probe laser diode; F – flip beam-stop; PBS – polarizing beam splitter; C – coupling lens; HWP – half-wave plate; FBS – fibre beam splitter; BD – calcite beam displacers; PM – phase modulator; D – single-photon detector; orange line – target qubit; red line – probe beam, black line – optical fibre PM-780HP.

8.4 Measurement

It is important to verify the experimental feasibility, robustness and reliability of the quantum state transfer protocol and probe its potential limitations caused by various practical imperfections. Therefore, we experimentally test the quantum state transfer protocol for 17 different initial states of target photon, $|g\rangle_T = \cos\omega|0\rangle + \sin\omega|1\rangle$, with $\omega \in \{5°, 10°, 15°, ..., 85°\}$. For each choice of $|g\rangle_T$ we perform a full quantum process tomography of the resulting single-qubit quantum channel $\mathcal{L}$ describing the state transfer from source qubit to target qubit. The measurement process is schematically depicted in Fig. 8.8 and data acquisition is described below.

Data acquisition: For each of 17 initial target-qubit states, we realize 36 combinations of 6 input source-qubit states and 6 output projective measurements on target qubit. In all cases, we measure coincidence rate C_{ij} of two detectors Di & Dj normalized to their relative detection efficiencies, where $i \in \{3, 4\}$ and $j \in \{1, 2\}$.

The input set of the source-qubit state consists of polarization states $\{H, V, D, A, R, L\}$, it corresponds to set $\{0, 1, +, -, +i, -i\}$ in spatial encoding. For each state of source qubit the resulting target-qubit state is analyzed. The analysis is realized as projections onto the 6 states $\{0, 1, +, -, +i, -i\}$ via fibre-based MZI in 4 measurements. Projections onto $|\pm\rangle$ are done in single measurement by proper phase setting inside MZI to 0. Coincidences $C_{31} + C_{41}$ ($C_{32} + C_{42}$) correspond to the projection onto $|+\rangle$ ($|-\rangle$). Projections onto $|\pm i\rangle$ are measured in a similar way with phase inside MZI set to $\pi/2$. Then, projections onto $|0\rangle$ and $|1\rangle$ are measured separately. The projection onto $|0\rangle$ ($|1\rangle$) is reached by blocking of a lower (upper) arm of MZI. Then, the sum of all coincidences $C_{31} + C_{32} + C_{41} + C_{42}$ is measured.

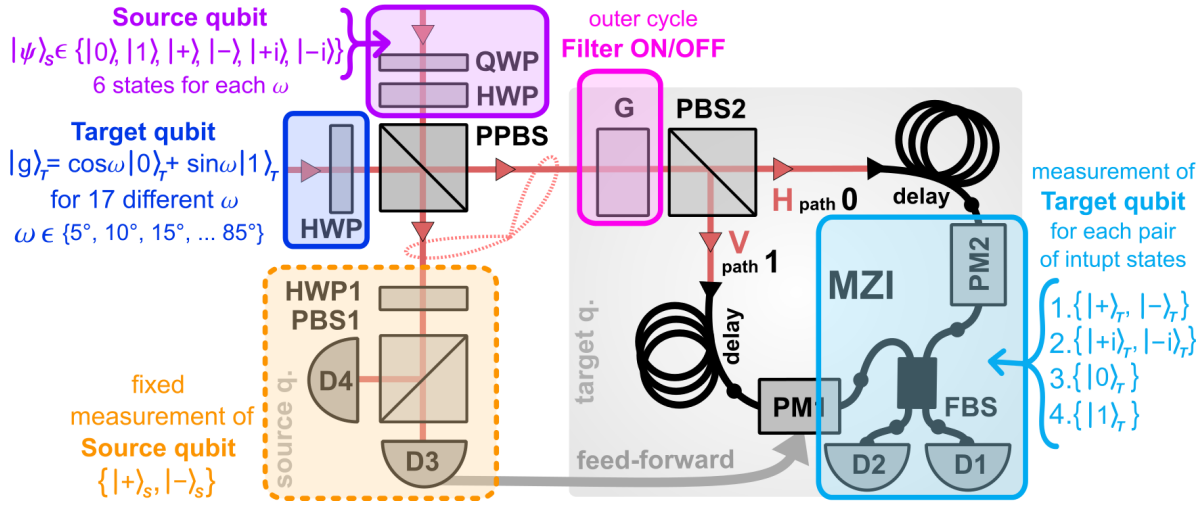

Figure 8.8: Scheme of data acquisition of quantum state transfer between weakly coupled qubits. Colour boxes show settings during measurement cycles. PPBS – partially polarizing beam splitter; FBS – fibre beam splitter 50:50; PBS – polarizing beam splitter; HWP – half-wave plate; PM – phase modulator; D – single-photon detector. G – quantum filter $\hat{G}_+$

To show the importance of the state filtration after the weak interaction, we characterize the protocol both with the filter $\hat{G}_+$ active and switched off (HWPs in $\hat{G}_+$ are set to $0° = a = b = c$, thus the HWPs do not influence the H and V polarization states).

For each of 17 angles ω, the process tomography of the qubit state transfer is performed. It consists of 24 measurements. Each measurement consists from 40 pcs of 1.5 -s-long data accumulation. The rate of coincidence events depends on ω and whether the filter $\hat{G}_+$ is active or switched off as shown further in Fig.8.10(b). Therefore the whole measurement is repeated several times to accumulate sufficient amount of data, see table 8.1. Just notice, that coincidence rates are not influenced by the feed-forward action.

Table 8.1: Number of measurement sets for angle ω (determining the target-qubit state) – *with* and *without* active filter G_+, in Fig. 8.10 it corresponds to ■ and ▼, respectively.

ω [*deg*]	5	10	15	20	25	30	35	40	45	50	55	60	65	70	75	80	85
with	16	13	11	11	10	10	8	5	8	5	4	4	4	6	8	10	12
without	4	4	4	4	4	2	2	2	2	2	2	2	2	2	4	4	4

8.5 Results & Discussion

Data processing: We characterize the resulting single-qubit quantum channel $\mathcal{L}$ describing the state transfer from the source qubit to the target qubit. This quantum channel can be conveniently represented by a matrix χ, which is a positive semidefinite operator on Hilbert space of two qubits. Physically, the quantum process matrix of a quantum channel $\mathcal{L}$ can be obtained by taking a pure maximally entangled Bell state $|\Phi^+\rangle = \frac{1}{\sqrt{2}}(|00\rangle + |11\rangle)$ and sending one of the qubits through the channel $\mathcal{L}$. A perfect state transfer corresponds to the identity channel whose matrix χ is equal to a projector onto Bell state $|\Phi^+\rangle$.

From measured data sets Choi process matrices χ are estimated for each initial target-qubit state $|g\rangle_T$, using the maximum-likelihood algorithm. In Fig. 8.9, we plot the reconstructed process matrices for $\omega = 55°$ with the calculated values of process fidelity $\mathcal{F}$, purity $\mathcal{P}$, and concurrence $\mathcal{C}$. To show the importance of the state filtration and the feed-forward in our protocol, we first switch off both of these operations, while accepting all coincidences. This emulates the situation when we have information that the interaction $\hat{V}$ between the source and the target qubit took place, but we do not perform any measurement on the source qubit (which can be inaccessible) and do not apply any operation to the target qubit. The resulting noisy quantum channel is shown in Fig. 8.9(a). If we switch on the fixed quantum filter $\hat{G}_+$ but keep the feed-forward switched off, we obtain the quantum channel plotted in Fig. 8.9(b). The theory predicts that the fixed filtering should yield a dephasing channel represented by a diagonal operator $\chi_{DC} = |00\rangle\langle 00| + |11\rangle\langle 11|$, and our data are in very good agreement with this theoretical expectation. Note that the dephasing channel is the best we can get without having access to measurement results on the source qubit, because the correlations present in the entangled state of source and target qubits destroy any phase coherence in the reduced density matrix of the target qubit. Finally, if we switch on also the feed-forward, we achieve faithful state transfer, with the resulting channel being close to the identity channel, see Fig. 8.9(c). In particular, compared to Fig. 8.9(b), the off-diagonal elements of the channel matrix are recovered, as the feed-forward ensures preservation of quantum coherence between the computational basis states.

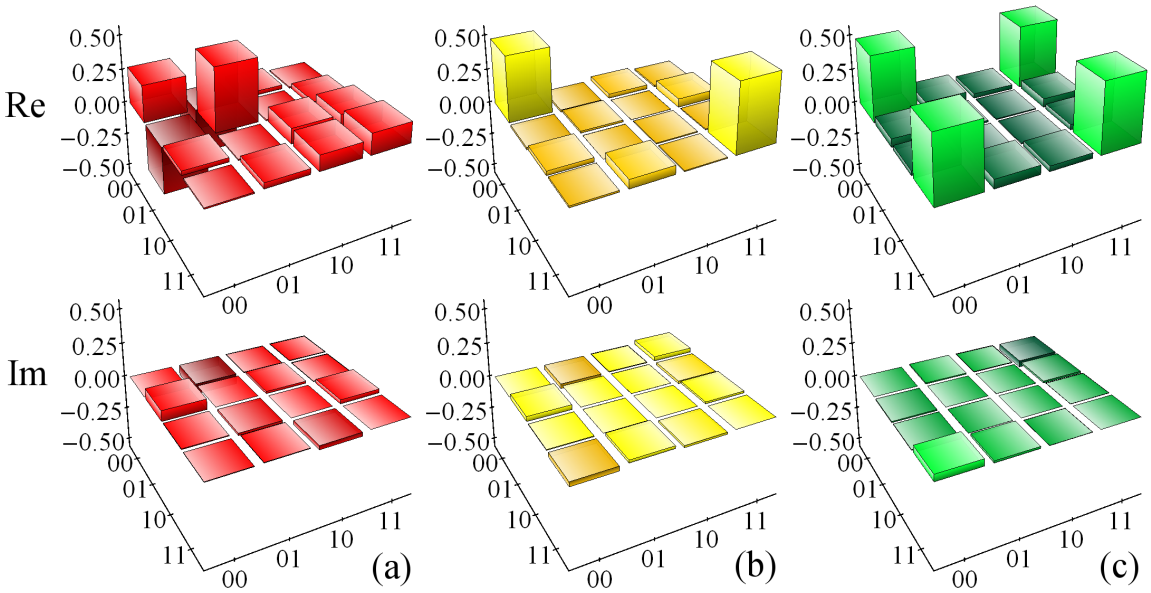

Figure 8.9: The reconstructed channel matrices χ for $\omega = 55°$. The first and the second row show real and imaginary parts of the reconstructed matrix, respectively. For ease of comparison, all matrices are normalized such that $\mathrm{Tr}(\chi) = 1$. The matrices are plotted for three scenarios: (a) - red - both filtering and feed-forward are switched off, $\mathcal{F} = 22.0$ %, $\mathcal{P} = 59.8$ %, $\mathcal{C} = 0.3$ %; (b) - yellow - filter is set on but feed-forward is switched off, $\mathcal{F} = 48.5$ %, $\mathcal{P} = 49.6$ %, $\mathcal{C} = 6.6$ %; (c) - green- full implementation with both quantum filter and feed-forward switched on, $\mathcal{F} = 95.7$ %, $\mathcal{P} = 94.6$ %, $\mathcal{C} = 92.3$ %; where $\mathcal{F}$ – fidelity, $\mathcal{P}$ – purity, and $\mathcal{C}$ – concurrence of the process matrix.

Subsequently, we provide the quantitative characterization of the quantum state transfer protocol performance in dependence on initial target-qubit state specified by angle ω. For each Choi matrix, we determine quantum process fidelity $\mathcal{F}$, which is defined as a normalized overlap of the channel matrix χ and the Bell state $|\Phi^+\rangle$. These results are summarized in Fig. 8.10(a). We achieve high fidelity with maximum $\mathcal{F} = 95.8$ % at $\omega = 50°$. Figure 8.10(b) simultaneously illustrates dependence of the success rate of the protocol on the initial target-qubit state. For each ω we plot the sum of all measured two-photon coincidences which is proportional to the success probability p. Since the same measurements are carried out for each ω and the measurement time is kept constant, the data for various ω are directly comparable. For reference, we plot also total coincidences recorded without active filtering $\hat{G}_+$. Thus we can see, how heavy is the quantum filtering. The success rate of the protocol is maximized at $\omega = 55°$. It is also confirmed by numerical optimization of the success probability (8.12) for the ideal protocol, where p is maximized at $\omega = 55.2°$, which is in excellent agreement with our experimental observations.

Experimental imperfections which reduce process fidelity below 1 include deviations of the interaction from ideal one (8.5), imperfection and decoherence of the source and target qubits. In our case, main imperfections are caused by partially distinguishable photons, imperfect retardation of wave plates, interference visibilities lower than one, and imperfection of the partially polarizing beam splitter (PPBS).

Let us mainly discuss the last mentioned imperfection. Our real PPBS is not perfectly transmitting horizontally polarized photons $T_H \neq 1$. The measured PPBS parameters are $T_H = 0.983, T_V = 0.334$. In such situation the true resulting state of target qubit $|\varphi_\pm^{\text{real}}\rangle_T$ cannot be written as the ideal one in Eqs. (8.6, 8.10) $|\varphi_\pm\rangle_T = (\alpha|\phi_0\rangle \pm \beta|\phi_1\rangle)/\sqrt{2}$ [36], but its reads:

$$\begin{aligned} |\varphi_\pm^{\text{real}}\rangle_T = & -\{\alpha[\gamma(R_H - T_H)|H\rangle \pm \delta r_H r_V|H\rangle - \delta t_H t_V|V\rangle] + \\ & + \beta[\gamma r_H r_V|V\rangle \pm \delta(R_V - T_V)|V\rangle \mp \gamma t_H t_V|H\rangle]\}/\sqrt{2}. \end{aligned} \tag{8.13}$$

This complicates the feed-forward action and the optimal state filtration. Because in such situation the optimal state filtration depends not only on the initial target-qubit state, but also on the unknown initial source-qubit state. Consequently, we decided not to consider this PPBS imperfect splitting ratio in the calculation of HWPs settings in filter $\hat{G}_+$, to keep it as simple as possible. Thus filter $\hat{G}_+$ is set for ideal PPBS with $T_H = 1$.

The effect caused by the PPBS imperfections plays a dominant role. The 1.7 % of horizontal polarization of unknown source qubit creates a parasitic signal, which is only partially attenuated by filter $\hat{G}_+$. When the initial state of the target photon becomes close to H or V polarized one, then the heavy quantum filtering is required. The filter transparency rapidly decreases out of the region $\omega \in [25°, 80°]$, as is visible in Fig. 8.10(b). It makes the protocol more sensitive to even small deviations as the parasitic coupling of the unknown source signal in H polarization. With the heavy filtration the part of parasitic signal starts to be comparable to the real signal, which substantially influences the output target-qubit state.

[36] Where $|\phi_0\rangle = \gamma|H\rangle + \delta t_V|V\rangle$, $|\phi_1\rangle = \gamma t_V|H\rangle + \delta(2T_V - 1)|V\rangle$ depend only on T_V, because $T_H = 1$.

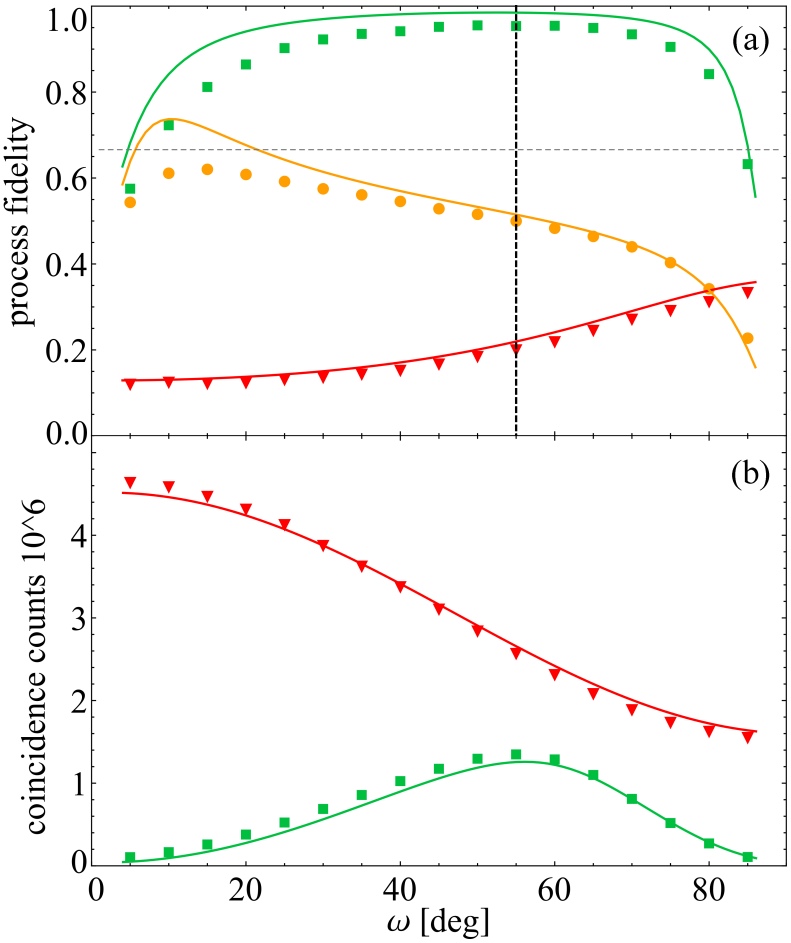

Figure 8.10: (a) dependence of quantum channel fidelity $\mathcal{F}$ and (b) two-photon coincidence counts on the initial target-qubit state determined by angle ω. The results are shown for three versions of the protocol: full implementation with both quantum filter and feed-forward switched on(■); quantum filter set on but feed-forward switched off (●), and both filtering and feed-forward switched off (▼). The horizontal dashed line shows the classical measure-and-prepare bound $\mathcal{F} = 2/3$. The vertical dashed line indicates the setting $\omega = 55°$ for which the channel matrices are plotted in Fig. 8.9. Solid lines indicate predictions of a theoretical model that accounts for imperfections of the PPBS where the source and target photons interfere. The data-sets with active feed-forward are measured directly, while the data-sets without the feed-forward are acquired by exchanging of coincidences C_{31} and C_{32} from previous data, it corresponds to feed-forward disconnection.

We include this PPBS imperfect splitting ratio ($T_H \neq 1$) into our theoretical model of process fidelity, which is shown by solid curves in Fig. 8.10(a). It indicates the influence of the imperfect qubits interaction at the PPBS in otherwise ideal protocol. As visible, the major fidelity decrease is caused right by the PPBS imperfections. As a good example can serve the green curve in Fig. 8.10(a) representing measurements with active state filtration $\hat{G}_+$ and with active feed-forward loop. If the whole experiment was ideal, the process fidelity would be $\mathcal{F} = 1$ for any initial state of a target qubit. But, the reconstructed process fidelity rapidly decreases, $\mathcal{F} < 0.9$, out of the region $\omega \in [25°, 75°]$, as it is indicated right by the model.

8.5.1 Additional material

In Fig. 8.11 a complex scheme of the experiment is shown. A photo of a forepart of fibre-based MZI is shown in Fig. 8.12. A photo of the whole experiment is in Fig. 8.13.

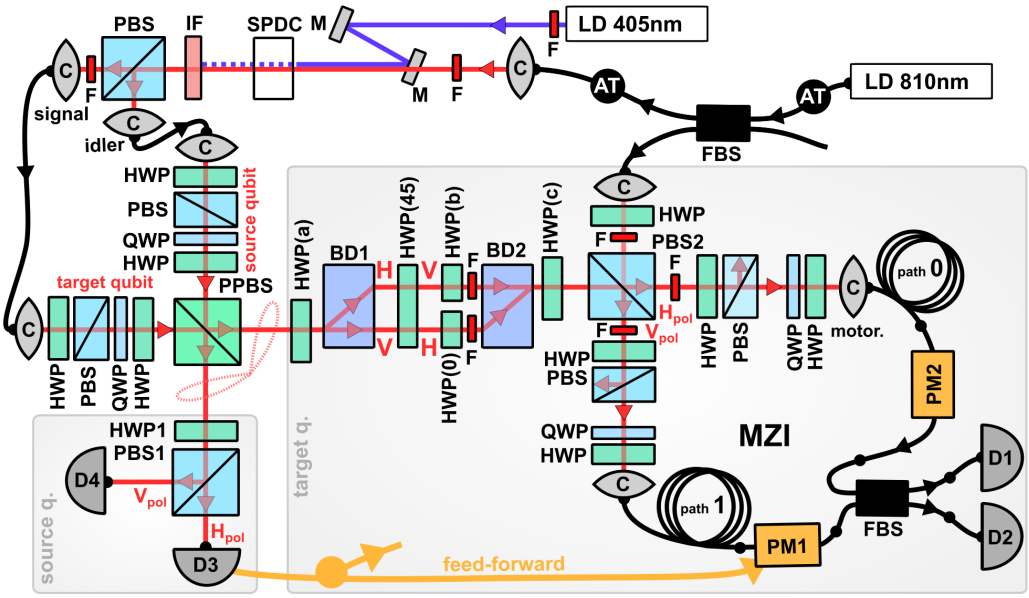

Figure 8.11: The complex scheme of the experimental setup for the faithful conditional quantum state transfer between weakly coupled qubits. It depicts how the probe beam is coupled into the setup and how the particular parts are connected together. LD - laser diode; F – flip beam-stop; SPDC – spontaneous parametric down conversion - source of photon pairs; IF – interference filter; PBS – polarizing beam splitter; C – coupling lens; HWP – half-wave plate; QWP – quarter-wave plate; PPBS – partially polarizing beam splitter; FBS – fibre beam splitter; BD – calcite beam displacers; PM – phase modulator; D – single-photon detector; AT – attenuation; red line – free space beam; black line – polarization maintaining optical fibre PM-780HP; thick yellow line – feed-forward loop with coaxial cables.

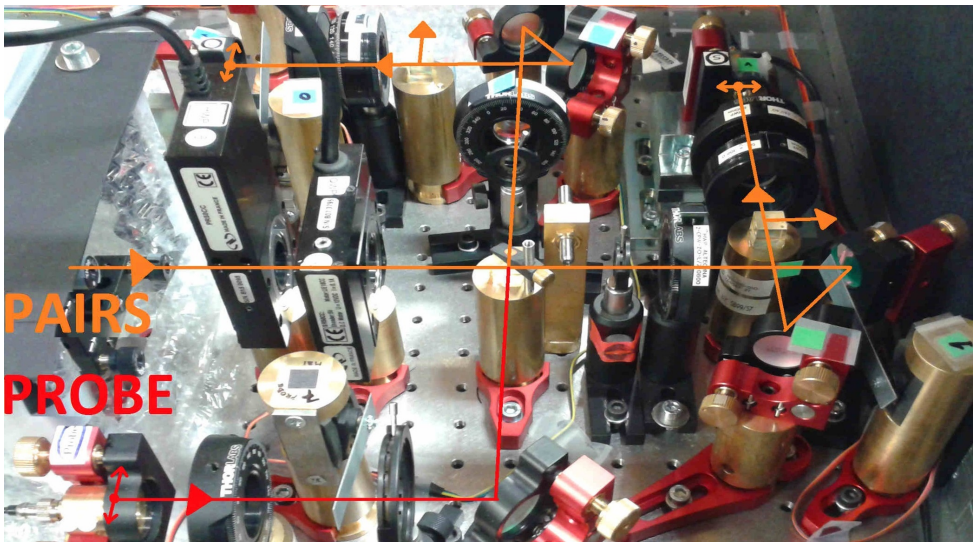

Figure 8.12: Photo of the forepart of the fibre-based MZI. There the target-qubit state (orange) is re-encoded from polarization encoding to spatial one and probe beam (red) is incoupled to the MZI via the second input port of the PBS2, as shown in Fig. 8.7.

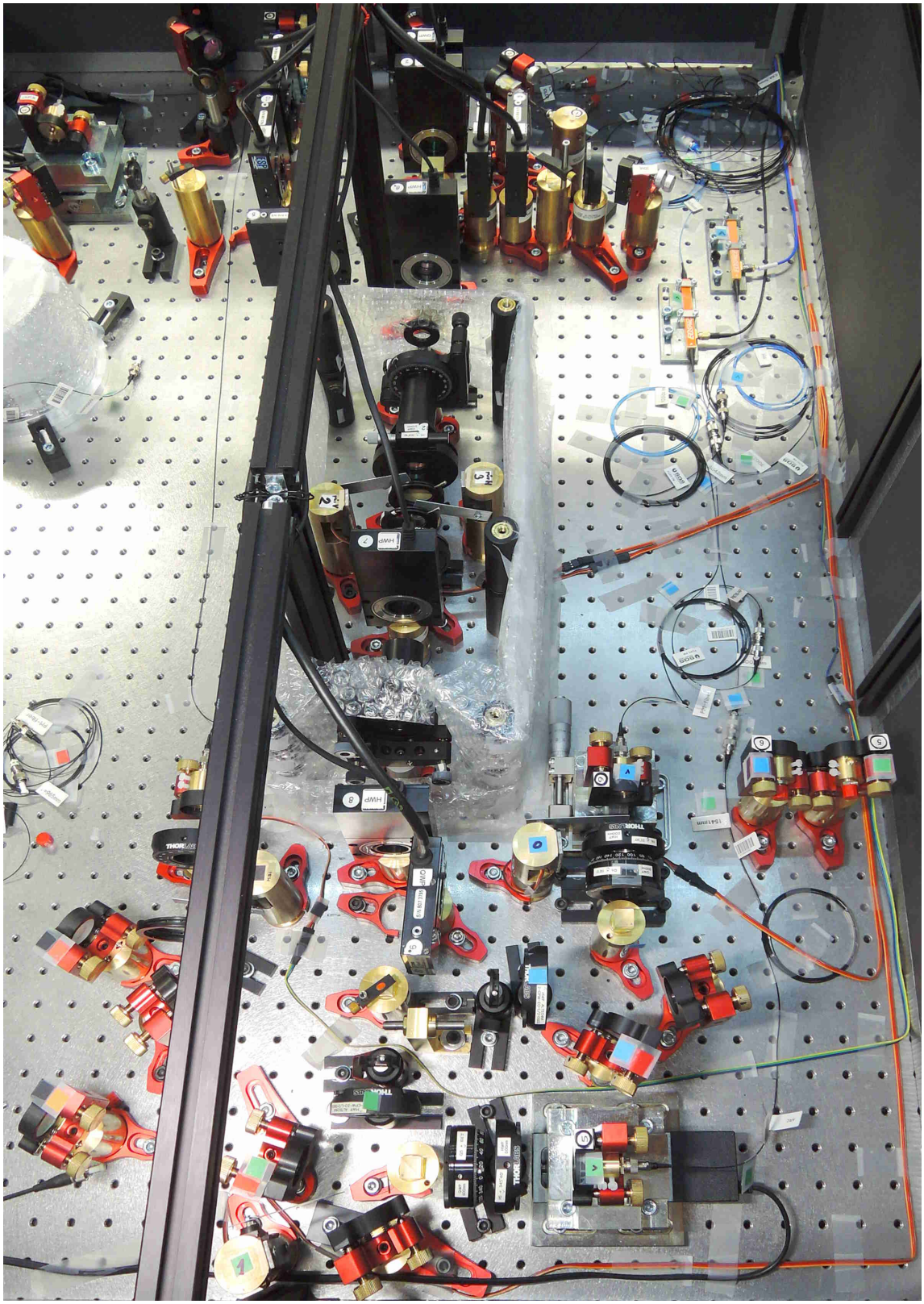

Figure 8.13: Photo of the experimental layout of the quantum state transfer between weakly coupled qubits.

Chapter 9

Conclusions

This Thesis is based on five original publications [1–5] and summarizes my main experimental results, in the area of experimental linear quantum information processing and quantum optics, produced during my Ph.D. studies.

As indicated, the experiments had a lot in common from the experimentalist's point of view. All of them utilized the platform of linear optics, employed the correlated photon pairs generated by SPDC, used coincidence measurement with single-photon detectors, and consisted of at least one fibre-based Mach-Zehnder interferometer, operating at single-photon level, which was actively phase stabilized. Most of the experiments utilized the feed-forward loop. We have realized a reliable and fast real-time electro-optical feed-forward loop, which does not require high voltage and operates at single-photon level. It conditionally applies a unitary operation onto one qubit that depends on measurement outcome realized on the second qubit. The feed-forward experimental implementation is based mainly on single-photon detector and integrated electro-optical phase modulator included in fibre-based Mach-Zehnder interferometer. We implemented both the passive and the active, i.e. electronically amplified, versions of the feed-forward loop. The fastest implementation applied the unitary operation in approximately 25 ns from the photon detection, as it was in detail described in *Chapter 3 Methods and Tools*. In our experiments, the feed-forward loop was utilized for different tasks: to increase the success probability of linear optical quantum gate [1], *Chapter 4*; to fully harness benefits of entanglement state in discrimination strategy of quantum measurements [4], *Chapter 5*; as a part of qubit state transfer protocol [2], *Chapter 7*; and as a part of quantum filter in quantum state transfer protocol between weakly coupled qubits [5], *Chapter 8*.

The other important technique, which we have implemented, was sequential active phase stabilization of complex interferometric layouts. The stabilization procedure was briefly described in *Chapter 3, Methods and Tools*, however, the specifics of the particular implementations were described in related chapters.

Chapter 4, based on publication [1], dealt with increasing efficiency of a linear-optical quantum gate using the electro-optical feed-forward loop. We employed feed-forward technique to double the success probability of a programmable linear-optical quantum phase gate in its fibre-based implementation. We showed that its application does not substantially affect either the process fidelity or the output-state fidelities.

In *Chapter 5*, based on publication [2], we experimentally investigated the properties of particles, which are used as qubit carriers, but whose noninformational degrees of freedom are nonfactorable. We can conclude that effective quantum indistinguishability, as a key resource for quantum information processing, can be quantified by a directly measurable parameter. We have experimentally demonstrated that this parameter represents a bound on the quality of quantum state transfer. We demonstrated it in a simple linear-optical fibre-based implementation of the qubit state transfer protocol. From the experimental results, it was confirmed that even if some degrees of freedom of two particles are entangled, the particles can still serve as good carriers of qubits.

In *Chapter 6*, based on publication [3], we experimentally implemented perfect quantum reading. We realized the fibre-based optical setup for perfect discrimination of two optical "devices", e.g. two memory records, which were represented by two beam splitters with different splitting ratios. A superposition of a single photon and vacuum was entering the beam splitter during the measurement. Thus the discriminated device was exposed in average just to a fraction of single-photon energy.

Subsequently, in *Chapter 7*, based on publication [4], we have experimentally implemented optimal strategies for discrimination between two known projective single-qubit quantum measurements. The experimental results clearly confirmed the advantage of the entanglement-assisted discrimination scheme compared to a single-qubit probe scheme. This experiment also demonstrates that the quantum optical technology is mature enough to harness the benefits of entanglement in quantum device discrimination, although the entanglement-based scheme is much more demanding than the single-qubit probe scheme. It requires entanglement and real-time feed-forward. Our experimental findings provide fundamental insight into the structure of optimal probabilistic discrimination schemes of quantum measurements.

Chapter 8, based on publication [5], refers about the experimental realization of faithful conditional quantum state transfer between weakly coupled photonics qubits. We have experimentally verified the probabilistic yet perfect unidirectional transfer of unknown single qubit source state through weak trace-decreasing interaction using optimal measurement and irreducible quantum filtering on the target qubit. The suitable filtering depends on the known initial target-qubit state, qubit-qubit interaction, and outcome of the measurement on the source qubit. Dependence of the filter on this measurement result is implemented by means of feed-forward. We experimentally proved that the method of qubit state transfer is feasible and robust. It is universally applicable because the protocol is not restricted to the photonic platform only. Therefore our proof-of-principle experimental results could serve as a cornerstone for a broad class of qubit state transfers in hybrid information processing, including atomic, solid state and optical qubits.

The main scientific contribution of this Thesis lies in the experimental implementation of newly suggested linear optical quantum information protocols [1–5]. The presented photonic experiments verify their experimental feasibility, robustness, and validate the theoretical predictions. Achieved results also show, that experimental linear quantum optics still serves as a suitable testbed for simulation of complicated processes.

Stručné shrnutí v češtině

Tato disertační práce je založena na pěti originálních publikacích [1–5], které shrnují mé hlavní experimentální výsledky základního výzkumu, které vznikly v průběhu mého doktorského studia. Hlavním cílem mého doktorského studia byla experimentální realizace nových lineárně optických kvantových protokolů pro kvantové zpracování informace či realizace samotných fotonických kvantových hradel.

Jednotlivé realizované experimenty mají z experimentálního hlediska mnoho společného. Využívaly lineárních optických prvků objemové a vláknové optiky, korelovaných párů fotonů z degenerované spontánní parametrické sestupné konverze a aktivní elektrooptické dopředné vazby. Kvantové bity byly v experimentech kódovány do polarizačních nebo prostorových stupňů volnosti jednotlivých fotonů. Jejich interakce byla zprostředkována pomocí jednofotonové nebo dvoufotonové interference a následné detekce pomocí jednofotonových detektorů. Každý z experimentů obsahoval alespoň jeden aktivně fázově stabilizovaný vláknový Machův-Zehnderův interferometr pracující na jednofotonové úrovni. Pro složitější interferometrická uspořádání byly vyvinuty komplexní metody aktivní stabilizace. Součástí vláknového interferometru byly vždy integrované elektrooptické vláknové fázové modulátory, které byly použity k zakódování fáze do stavu kvantového bitu, pro aktivní stabilizaci interferometru, nebo jako součást aktivní elektrooptické dopředné vazby. Tato aktivní vazba podmíněně zavádí unitární operaci na jeden kvantový bit, kde toto podmínění je určeno výsledkem měření na druhém kvantovém bitu. Nejrychlejší experimentální realizace této dopředné vazby zvládla zavést unitární operaci na druhý kvantový bit za 25 ns od detekce prvního fotonu detektorem.

Všechny realizované experimenty byly post-selekčního typu, a tedy výsledná měření byla realizována za současné detekce obou fotonů jako koincidenčních měření. Výstupem experimentu tedy byla pravděpodobnost určitého výsledku měření. Případně byl stav výstupního kvantového bitu zjišťován pomocí kvantové tomografie stavu nebo byl celý experiment plně charakterizován pomocí kvantové tomografie procesu. Tyto metody a nástroje sloužící pro realizaci jednotlivých experimentů jsou stručně popsány v kapitole *Chapter 3, Methods and Tools*.

Prvním řešeným projektem, popsaném v kapitole 4 a vycházejícím z publikace [1], byla experimentální implementace lineárně-optického programovatelného kvantového fázového hradla, na němž bylo demonstrováno zvýšení pravděpodobnosti úspěchu hradla právě pomocí aplikace elektrooptické dopředné vazby. Hradlo bylo kompletně charakterizováno pomocí kvantové tomografie procesu. Experimentální výsledky ukázaly, že použitím dopředné vazby byla zdvojnásobena pravděpodobnost úspěchu hradla a zároveň nebyla ovlivněna fidelita výstupního stavu ani fidelita procesu.

Navazujícím projektem, popsaném v kapitole 5 a v publikaci [2], byl experimentální výzkum vlivu nerozlišitelnosti částic nesoucích kvantovou informaci na přenos této informace. Byla navržena nová míra efektivní nerozlišitelnosti částic, která může být použita i pro kvantově provázané částice v dalších stupních volnosti, tedy pro částice, které nejsou ve faktorizovaném stavu. Pro experimentální testování této nové míry byl realizován experiment přenosu stavu kvantového bitu. Výsledky ukázaly, že tato nová přímo měřitelná míra efektivní nerozlišitelnosti částic reprezentuje reálnou hranici kvality protokolů pro přenos kvantové informace.

Dále, jak je popsáno v kapitole 6, založené na publikaci [3], byla realizována experimentální implementace jednoznačného čtení paměťového záznamu s využitím co nejmenší energie. Informace byla uložena jako odrazivosti paměťových buněk reprezentovaných dvěma děliči svazku s navzájem různými odrazivostmi. Cílem realizovaného experimentu bylo jednoznačně rozlišit tato dvě různá zařízení, děliče svazku. V průběhu měření do zařízení vstupovala superpozice jednoho fotonu a vakua. Neznámé zařízení tedy bylo v průměru vystaveno pouze zlomku energie jednoho fotonu. Výsledky prokázaly, že kvantové čtení je experimentálně realizovatelné tímto způsobem.

Dalším projektem, který je popsán v kapitole 7, vycházející z publikace [4], byla experimentální realizace optimálního rozlišení projektivních kvantových měření pomocí kvantově provázaného stavu. Cílem bylo optimálně rozlišit dvě známá projektivní měření na polarizačních módech fotonu. Byla zkoumána závislost rozlišovací strategie na pravděpodobnosti nejednoznačných výsledků, kdy sice nedocházelo k jednoznačnému rozlišení měřících bází, ale vždy tato strategie byla optimální. Výsledná experimentální data jasně demonstrovala výhodu strategie využívající kvantově provázané částice pro rozlišení dvou projektivních měření v porovnání se strategií využívající pouze jeden kvantový bit.

Cílem posledního popsaného experimentu v kapitole 8, založené na publikaci [5], bylo přenést neznámý kvantový stav jedné částice na druhou, cílovou, částici ve známém kvantovém stavu, i když jejich vzájemná interakce je pouze slabá. Pro dokončení úspěšného přenosu stavu kvantového bitu musela být použita aktivní filtrace stavu, která závisela na původním stavu cílového kvantového bitu, na vzájemné interakci částic a rovněž na výsledku měření neznámého kvantového bitu. Výsledek tohoto měření byl do kvantového filtru zahrnut pomocí elektrooptické dopředné vazby. Experimentálně jsme potvrdili, že tato metoda přenosu stavu kvantového bitu mezi slabě interagujícími částicemi přenese kvantový stav bitu s vysokou věrohodností. Vzhledem k tomu, že tento protokol není omezen na fotonické kvantové bity, dosažené experimentální výsledky mohou pomoci při realizaci přenosu stavu například v hybridních kvantových systémech.

Hlavním vědeckým přínosem mé disertační práce byla experimentální implementace nově navržených lineárně optických kvantových protokolů pro kvantové zpracování informace [1–5]. Tyto práce experimentálně ověřily základní principy a uskutečnitelnost navržených teoretických protokolů v reálných experimentálních podmínkách. Dosažené výsledky ukazují, že lineární kvantová optika stále slouží i jako vhodné testovací zařízení na simulaci složitějších procesů.

Publications of the author and a list of citations

The Thesis is based on the following publications:

■ Martina Miková, Helena Fikerová, Ivo Straka, Michal Mičuda, Jaromír Fiurášek, Miroslav Ježek, and Miloslav Dušek. *Increasing effciency of a linear-optical quantum gate using electronic feed-forward.* Physical Review A **85**, 012305 (2012).

■ Michele Dall'Arno, Alessandro Bisio, Giacomo Mauro D'Ariano, Martina Miková, Miroslav Ježek, and Miloslav Dušek. *Experimental implementation of unambiguous quantum reading.* Physical Review A **85**, 012308 (2012).

■ Martina Miková, Helena Fikerová, Ivo Straka, Michal Mičuda, Miroslav Ježek, Miloslav Dušek, and Radim Filip. *Carrying qubits with particles whose noninformational degrees of freedom are nonfactorable.* Physical Review A **87**, 042327 (2013).

■ Martina Miková, Michal Sedlák, Ivo Straka, Michal Mičuda, Mário Ziman, Miroslav Ježek, Miloslav Dušek, and Jaromír Fiurášek. *Optimal entanglement-assisted discrimination of quantum measurements.* Physical Review A **90**, 022317 (2014).

■ Martina Miková, Ivo Straka, Michal Mičuda, Vojtěch Krčmarský, Miloslav Dušek, Miroslav Ježek, Jaromír Fiurášek, and Radim Filip. *Faithful conditional quantum state transfer between weakly coupled qubits.* Scientific Reports **6**, 32125 (2016).

Other co-author publications:

■ Michal Mičuda, Ivo Straka, Martina Miková, Miloslav Dušek, Niclosla Jean Cerf, Jaromír Fiurášek, and Miroslav Ježek. *Noiseless loss suppression in quantum optical communication.* Physical Review Letters **109**, 180503 (2012).

■ Michal Mičuda, Michal Sedlák, Ivo Straka, Martina Miková, Miloslav Dušek, Miroslav Ježek, and Jaromír Fiurášek. *Efficient experimental estimation of fidelity of linear optical quantum toffoli gate.* Physical Review Letters **111**, 160407 (2013).

■ Ivo Straka, Ana Predojevic, Tobias Huber, Lukáš Lachman, Lorenz Butschek, Martina Miková, Michal Mičuda, Glenn S. Solomon, Gregor Weihs, Miroslav Ježek, and Radim Filip. *Quantum non-gaussian depth of single-photon states.* Physical Review Letters **113**, 223603 (2014).

■ Michal Mičuda, Ester Doláková, Ivo Straka, Martina Miková, Miloslav Dušek, Jaromír Fiurášek, and Miroslav Ježek. *Highly stable polarization independent Mach-Zehnder interferometer.* Review of Scientific Instruments **85**, 083103 (2014).

■ Miroslav Ježek, Michal Mičuda, Ivo Straka, Martina Miková, Miloslav Dušek, and Jarimír Fiurášek. *Orthogonalization of partly unknown quantum states.* Physical Review A **89**, 042316 (2014).

■ Michal Mičuda, Michal Sedlák, Ivo Straka, Martina Miková, Miloslav Dušek, Miroslav Ježek, and Jaromír Fiurášek. *Process-fidelity estimation of a linear optical quantum-controlled-Z gate: A comparative study.* Physical Review A **89**, 042304 (2014).

■ Ivo Straka, Martina Miková, Michal Mičuda, Miloslav Dušek, Miroslav Ježek, and Radim Filip. *Conditional cooling limit for a quantum channel going through an incoherent environment.* Scientofic Reports **5**, 16721 (2015).

■ Michal Mičuda, Martina Miková, Ivo Straka, Michal Sedlák, Miloslav Dušek, Miroslav Ježek, and Jaromír Fiurášek. *Tomographic characterization of a linear optical quantum Toffoli gate.* Physical Review A **92**, 032312 (2015).

■ Michal Mičuda, Robert Stárek, Ivo Straka, Martina Miková, Miloslav Dušek, Miroslav Ježek, Radim Filip, and Jaromír Fiurášek. *Quantum controlled-Z gate for weakly interacting qubits.* Physical Review A **92**, 022341 (2015).

■ Michal Mičuda, Ivo Straka, Martina Miková, Miloslav Dušek, Miroslav Ježek, Jaromír Fiurášek, and Radim Filip. *Experimental test of robust quantum detection and restoration of a qubit.* Physical Review A **92**, 012324 (2015).

■ Robert Stárek, Michal Mičuda, Ivo Straka, Martina Miková, Miroslav Ježek, Radim Filip, and Jaromír Fiurášek. *Control and enhancement of interferometric coupling between two photonic qubits.* Physical Review A **93**, 042321 (2016).

■ Michal Mičuda, Robert Stárek, Ivo Straka, Martina Miková, Michal Sedlák, Miroslav Ježek, and Jaromír Fiurášek. *Experimental replication of single-qubit quantum phase gates.* Physical Review A **93**, 052318 (2016).

■ Robert Stárek, Michal Mičuda, Martina Miková, Ivo Straka, Miloslav Dušek, Miroslav Ježek, and Jaromír Fiurášek. *Experimental investigation of a four-qubit linear-optical quantum logic circuit.* Scientific Reports **6**, 33475 (2016).

■ Michal Mičuda, Dominik Koutný, Martina Miková, Ivo Straka, Miroslav Ježek, and Ladislav Mišta. *Experimental demonstration of a fully inseparable quantum state with nonlocalizable entanglement.* Scientific Reports **7**, 45045 (2017).

■ Michal Mičuda, Robert Stárek, Petr Marek, Martina Miková, Ivo Straka, Miroslav Ježek, Toshiyuki Tashima, Şahin K. Özdemir, and Mark Tame. *Experimental characterization of a non-local convertor for quantum photonic networks.* Optics Express **25** (7), 7839-7848 (2017).

List of citations:

citations (without self-citations) of the publications relevant for this Thesis

■ Martina Miková, Helena Fikerová, Ivo Straka, Michal Mičuda, Jaromír Fiurášek, Miroslav Ježek, and Miloslav Dušek. *Increasing effciency of a linear-optical quantum gate using electronic feed-forward.* Physical Review A **85**, 012305 (2012).

1. M. Bula, K. Bartkiewicz, A. Černoch, and K. Lemr. *Entanglement-assisted scheme for nondemolition detection of the presence of a single photon.* Physical Review A **87**, 033826 (2013)

2. M. Suda, C. Pacher, M. Peev, M. Dušek, and F. Hipp *Quantum interference of photons in simple networks.* Quantum Information Processing **12**, 1915–1945 (2013).

3. K. Lemr, K. Bartkiewicz, A. Černoch, and J. Soubusta. *Resource-efficient linear-optical quantum router.* Physical Review A **87**, 062333 (2013).

4. K. Lemr, A. Černoch. *Linear-optical programmable quantum router.* Optics Communications **300**, 282-285 (2013).

5. M. Gajdacz , T. Opatrný, K. K. Das. *An atomtronics transistor for quantum gates.* Physics Letters A **378**, 1919–1924 (2014).

6. C.-C. Qu, L. Zhou, Y.-B. Sheng. *Cascaded Multi-Level Linear-Optical Quantum Router.* International Journal of Theoretical Physics **54**, 3004–3017 (2015).

7. K. Lemr, K. Bartkiewicz, A. Černoch. *Scheme for a linear-optical controlled-phase gate with programmable phase shift.* Journal of Optics **17**, 125202 (2015).

8. J. Fiurášek. *Interconversion between single-rail and dual-rail photonic qubits.* Physical Review A **95**, 033802 (2017).

■ Michele Dall'Arno, Alessandro Bisio, Giacomo Mauro D'Ariano, Martina Miková, Miroslav Ježek, and Miloslav Dušek. *Experimental implementation of unambiguous quantum reading.* Physical Review A **85**, 012308 (2012).

1. C. Weedbrook, S. Pirandola, R. García-Patrón, N. J. Cerf, T. C. Ralph, J. H. Shapiro, and S. Lloyd *Gaussian quantum information.* Reviews of Modern Physics **84**, 621 (2012).

2. C. Lupo, V. Giovannetti, S. Pirandola, S. Mancini, and S. Lloyd. *Capacities of linear quantum optical systems.* Physical Review A **85**, 062314 (2012).

3. G. Spedalieri, C. Lupo, S. Mancini, S. L. Braunstein, and S. Pirandola. *Quantum reading under a local energy constraint.* Physical Review A **86**, 012315 (2012).

4. R. Nair, B. J. Yen, S. Guha, J. H. Shapiro, and S. Pirandola. *Symmetric M-ary phase discrimination using quantum-optical probe states.* Physical Review A **86**, 022306 (2012).

5. M. Dall'Arno, A. Bisio, and G. M. D'Ariano. *Ideal quantum reading of optical memories.* International Journal of Quantum Information **10**, 1241010 (2012).

6. M. Dall'Arno, A. Bisio, and G. M. D'Ariano. *Ideal quantum reading of optical memories.* 21st International Laser Physics Workshop, Journal of Physics: Conference Series **414**, 012038 (2013).

7. G. Spedalieri, C. Weedbrook, and S. Pirandola. *A limit formula for the quantum fidelity.* Journal of Physics A: Mathematical and Theoretical **46**, 025304 (2013).

8. J. P. Tej, A. R. Usha Devi, and A. K. Rajagopal. *Quantum reading of digital memory with non-Gaussian entangled light.* Physical Review A **87**, 052308 (2013).

9. S. Guha and J. H. Shapiro. *Reading boundless error-free bits using a single photon.* Physical Review A **87**, 062306 (2013).

10. C. Lupo, S. Pirandola, V. Giovannetti, and S. Mancini. *Quantum reading capacity under thermal and correlated noise.* Physical Review A **87**, 062310 (2013).

11. M. Gavenda, L. Čelechovská, M. Dušek, and R. Filip. *Quantum noise eater for a single photonic qubit.* New Journal of Physics **15**, 083050 (2013).

12. M. Dall'Arno, A. Bisio, and G. Mauro D'Ariano. *Quantum Reading of Unitary Optical Devices.* 11th International Conference on Quantum Communication, Measurement and Computing (QCMC) Book Series: AIP Conference Proceedings **1633**, 219-221 (2014).

13. M. Dall'Arno. *Quantum reading for the practical man.* International Journal of Quantum Information **12**, 1560018 (2014).

14. W. Roga, D. Buono, and F. Illuminati. *Device-independent quantum reading and noise-assisted quantum transmitters.* New Journal of Physics **17**, 013031 (2015).

15. G. Spedalieri. *Cryptographic Aspects of Quantum Reading.* Entropy **17**, 2218-2227 (2015).

16. L. Banchi, S. L. Braunstein, and S. Pirandola. *Quantum Fidelity for Arbitrary Gaussian States.* Physical Review Letters **115**, 260501 (2015).

17. S. Pirandola and C. Lupo. *Ultimate Precision of Adaptive Noise Estimation.* Physical Review Letters **118**, 100502 (2017).

18. C. Lupo and S. Pirandola. *Super-Additivity and Entanglement Assistance in Quantum Reading.* Quantum Information & Computation **17**, 611-622 (2017).

■ Martina Miková, Helena Fikerová, Ivo Straka, Michal Mičuda, Miroslav Ježek, Miloslav Dušek, and Radim Filip. *Carrying qubits with particles whose noninformational degrees of freedom are nonfactorable.* Physical Review A **87**, 042327 (2013).

1. V. S. Shchesnovich. *Universality of Generalized Bunching and Efficient Assessment of Boson Sampling.* Physical Review Letters **116**, 123601 (2016).

■ Martina Miková, Michal Sedlák, Ivo Straka, Michal Mičuda, Mário Ziman, Miroslav Ježek, Miloslav Dušek, and Jaromír Fiurášek. *Optimal entanglement-assisted discrimination of quantum measurements.* Physical Review A **90**, 022317 (2014).

1. M. Sedlák and M. Ziman. *Optimal single-shot strategies for discrimination of quantum measurements.* Physical Review A **90**, 052312 (2014).

2. T.-Q. Cao, F. Gao, Z.-C. Zhang, Y.-H. Yang, and Q.-Y. Wen. *Perfect discrimination of projective measurements with the rank of all projectors being one.* Quantum Information Processing **14**, 2645-2656 (2015).

3. T.-Q. Cao, F. Gao, Y.-H. Yang, Z.-C. Zhang, and Q.-Y. Wen *Determination of locally perfect discrimination for two-qubit unitary operations.* Quantum Information Processing **15**, 529-549 (2016).

4. T.-Q. Cao, Y.-H. Yang, Z.-C. Zhang, G.-J. Tian, F. Gao, and Q.-Y. Wen. *Minimal number of runs and the sequential scheme for local discrimination between special unitary operations.* Scientific Reports **6**, 26696 (2016).

5. T.-Q. Cao, F. Gao, G.-J. Tian, S.-C. Xie, and Q.-Y. Wen. *Local discrimination scheme for some unitary operations.* Science China Physics, Mechanics & Astronomy **59**, 690311 (2016).

■ Martina Miková, Ivo Straka, Michal Mičuda, Vojtěch Krčmarský, Miloslav Dušek, Miroslav Ježek, Jaromír Fiurášek, and Radim Filip. *Faithful conditional quantum state transfer between weakly coupled qubits.* Scientific Reports **6**, 32125 (2016).

1. J. Fiurášek. *Interconversion between single-rail and dual-rail photonic qubits.* Physical Review A **95**, 033802 (2017).

Bibliography

[1] M. Miková, H. Fikerová, I. Straka, M. Mičuda, J. Fiurášek, M. Ježek, and M. Dušek. Increasing efficiency of a linear-optical quantum gate using electronic feed-forward. *Phys. Rev. A*, 85:012305, 2012.

[2] M. Miková, H. Fikerová, I. Straka, M. Mičuda, M. Ježek, M. Dušek, and R. Filip. Carrying qubits with particles whose noninformational degrees of freedom are nonfactorable. *Phys. Rev. A*, 87:042327, 2013.

[3] M. Dall'Arno, A. Bisio, G. M. D'Ariano, M. Miková, M. Ježek, and M. Dušek. Experimental implementation of unambiguous quantum reading. *Phys. Rev. A*, 85:012308, 2012.

[4] M. Miková, M. Sedlák, I. Straka, M. Mičuda, M. Ziman, M. Ježek, M. Dušek, and J. Fiurášek. Optimal entanglement-assisted discrimination of quantum measurements. *Phys. Rev. A*, 90:022317, 2014.

[5] M. Miková, I. Straka, M. Mičuda, V. Krčmarský, M. Dušek, M. Ježek, J. Fiurášek, and R. Filip. Faithful conditional quantum state transfer between weakly coupled qubits. *Sci. Rep.*, 6:32125, 2016.

[6] G. Vidal, L. Masanes, and J. I. Cirac. Storing quantum dynamics in quantum states: A stochastic programmable gate. *Phys. Rev. Lett.*, 88:047905, 2002.

[7] M. Mičuda, M. Ježek, M. Dušek, and J. Fiurášek. Experimental realization of a programmable quantum gate. *Phys. Rev. A*, 78:062311, 2008.

[8] E. Knill, R. Laflamme, and G. J. Milburn. A scheme for efficient quantum computation with linear optics. *Nature*, 409:46–52, 2001.

[9] D. Gottesman and I. L. Chuang. Demonstrating the viability of universal quantum computation using teleportation and single-qubit operations. *Nature*, 402:390–393, 1999.

[10] P. Kok, W. J. Munro, K. Nemoto, T. C. Ralph, J. P. Dowling, and G. J. Milburn. Linear optical quantum computing with photonic qubits. *Rev. Mod. Phys.*, 79:135–174, 2007.

[11] M. A. Nielsen and I. L. Chuang. *Quantum Computation and Quantum Information.* Cambridge University Press, Cambridge, 2000.

[12] E. Knill. Bounds on the probability of success of postselected nonlinear sign shifts implemented with linear optics. *Phys. Rev. A*, 68:064303, 2003.

[13] M. A. Nielsen and I. L. Chuang. Programmable quantum gate arrays. *Phys. Rev. Lett.*, 79:321–324, 1997.

[14] M. Hillery, V. Bužek, and M. Ziman. Probabilistic implementation of universal quantum processors. *Phys. Rev. A*, 65:022301, 2002.

[15] M. Hillery, M.and Ziman and V. Bužek. Improving the performance of probabilistic programmable quantum processors. *Phys. Rev. A*, 69:042311, 2004.

[16] M. Hillery, M. Ziman, and V. Bøužek. Approximate programmable quantum processors. *Phys. Rev. A*, 73:022345, 2006.

[17] G. Björk and Y. Yamamoto. Generation of nonclassical photon states using correlated photon pairs and linear feedforward. *Phys. Rev. A*, 37:4229–4239, 1988.

[18] K. Watanabe and Y. Yamamoto. Quantum correlation and state reduction of photon twins produced by a parametric amplifier. *Phys. Rev. A*, 38:3556–3565, 1988.

[19] J. Mertz, A. Heidmann, C. Fabre, E. Giacobino, and S. Reynaud. Observation of high-intensity sub-poissonian light using an optical parametric oscillator. *Phys. Rev. Lett.*, 64:2897–2900, 1990.

[20] J. Mertz, A. Heidmann, and C. Fabre. Generation of sub-poissonian light using active control with twin beams. *Phys. Rev. A*, 44:3229–3238, 1991.

[21] C. H. Bennett, G. Brassard, C. Crépeau, R. Jozsa, A. Peres, and W. K. Wootters. Teleporting an unknown quantum state via dual classical and einstein-podolsky-rosen channels. *Phys. Rev. Lett.*, 70:1895–1899, 1993.

[22] A. Furusawa, J. L. Sørensen, S. L. Braunstein, C. A. Fuchs, H. J. Kimble, and E. S. Polzik. Unconditional quantum teleportation. *Science*, 282:706–709, 1998.

[23] W. Pfaff, B. J. Hensen, H. Bernien, S. B. van Dam, M. S. Blok, T. H. Taminiau, M. J. Tiggelman, R. N. Schouten, M. Markham, D. J. Twitchen, and R. Hanson. Unconditional quantum teleportation between distant solid-state quantum bits. *Science*, 345:532–535, 2014.

[24] L. Steffen, Y. Salathe, M. Oppliger, P. Kurpiers, M. Baur, C. Lang, C. Eichler, G. Puebla-Hellmann, A. Fedorov, and A. Wallraff. Deterministic quantum teleportation with feed-forward in a solid state system. *Nature*, 500:319–322, 2013.

[25] M. Riebe, H. Häffner, C. F. Roos, W. Hänsel, J. Benhelm, G. P. T. Lancaster, T. W. Körber, C. Becher, F. Schmidt-Kaler, D. F. V. James, and R. Blatt. Deterministic quantum teleportation with atoms. *Nature*, 429:734–737, 2004.

[26] M. D. Barrett, J. Chiaverini, T. Schaetz, J. Britton, W. M. Itano, J. D. Jost, E. Knill, C. Langer, D. Leibfried, R. Ozeri, and D. J. Wineland. Deterministic quantum teleportation of atomic qubits. *Nature*, 429:737–739, 2004.

[27] M. A. Nielsen, E. Knill, and R. Laflamme. Complete quantum teleportation using nuclear magnetic resonance. *Nature*, 396:52–55, 1998.

[28] X.-S. Ma, T. Herbst, T. Scheidl, D. Wang, S. Kropatschek, W. Naylor, B. Wittmann, A. Mech, J. Kofler, E. Anisimova, V. Makarov, T. Jennewein, R. Ursin, and A. Zeilinger. Quantum teleportation over 143 kilometres using active feed-forward. *Nature*, 489:269–273, 2012.

[29] R. Ursin, T. Jennewein, M. Aspelmeyer, R. Kaltenbaek, M. Lindenthal, P. Walther, and A. Zeilinger. Communications: Quantum teleportation across the danube. *Nature*, 430:849–849, 2004.

[30] S. Giacomini, F. Sciarrino, E. Lombardi, and F. De Martini. Active teleportation of a quantum bit. *Phys. Rev. A*, 66:030302, 2002.

[31] I. L. Chuang and Y. Yamamoto. Simple quantum computer. *Phys. Rev. A*, 52:3489–3496, 1995.

[32] T. C. Ralph. Robust transmission and reconstruction of fragile optical states. *Phys. Rev. A*, 56:4187–4192, 1997.

[33] J.-W. Pan, C. Simon, Č. Brukner, and A. Zeilinger. Entanglement purification for quantum communication. *Nature*, 410:1067–1070, 2001.

[34] D. Bouwmeester. Bit-flip-error rejection in optical quantum communication. *Phys. Rev. A*, 63:040301, 2001.

[35] S. Borisenok and Saifullah. Linear feedforward control of two-level quantum system by modulated external field. *Optics Communications*, 284:3562–3567, 2011.

[36] T. Satoh, Y. Matsuzaki, K. Kakuyanagi, W. J. Munro, K. Semba, H. Yamaguchi, and S. Saito. Scalable quantum computation architecture using always-on ising interactions via quantum feedforward. *Phys. Rev. A*, 91:052329, 2015.

[37] A. A. Rakhubovsky, N. Vostrosablin, and R. Filip. Squeezer-based pulsed optomechanical interface. *Phys. Rev. A*, 93:033813, 2016.

[38] J. Fiurášek. Interconversion between single-rail and dual-rail photonic qubits. *Phys. Rev. A*, 95:033802, 2017.

[39] T. B. Pittman, B. C. Jacobs, and J. D. Franson. Demonstration of feed-forward control for linear optics quantum computation. *Phys. Rev. A*, 66:052305, 2002.

[40] G. Brida, M. V. Chekhova, M. Genovese, M. Gramegna, L. A. Krivitsky, and S. P. Kulik. Conditional unitary transformation on biphotons. *Phys. Rev. A*, 70:032332, 2004.

[41] T. B. Pittman, B. C. Jacobs, and J. D. Franson. Demonstration of quantum error correction using linear optics. *Phys. Rev. A*, 71:052332, 2005.

[42] F. Sciarrino, M. Ricci, F. De Martini, R. Filip, and L. Mišta. Realization of a minimal disturbance quantum measurement. *Phys. Rev. Lett.*, 96:020408, 2006.

[43] R. Prevedel, P. Walther, F. Tiefenbacher, P. Böhi, R. Kaltenbaek, T. Jennewein, and A. Zeilinger. High-speed linear optics quantum computing using active feed-forward. *Nature*, 445:65–69, 2007.

[44] G. Vallone, E. Pomarico, F. De Martini, and P. Mataloni. Active one-way quantum computation with two-photon four-qubit cluster states. *Phys. Rev. Lett.*, 100:160502, 2008.

[45] T.-M. Zhao, H. Zhang, J. Yang, Z.-R. Sang, X. Jiang, X.-H. Bao, and J.-W. Pan. Entangling different-color photons via time-resolved measurement and active feed forward. *Phys. Rev. Lett.*, 112, 2014.

[46] X.-F. Xu, X.-H. Bao, and J.-W. Pan. Demonstration of active feedforward one-way quantum computing with photon-matter hyperentanglement. *Phys. Rev. A*, 86:050304, 2012.

[47] P. K. Lam, T. C. Ralph, E. H. Huntington, and H.-A. Bachor. Noiseless signal amplification using positive electro-optic feedforward. *Phys. Rev. Lett.*, 79:1471–1474, 1997.

[48] B. C. Buchler, E. H. Huntington, and T. C. Ralph. Noiseless phase quadrature amplification via an electro-optic feed-forward technique. *Phys. Rev. A*, 60:529–533, 1999.

[49] O. Glöckl, U. L. Andersen, R. Filip, W. P. Bowen, and G. Leuchs. Squeezed-state purification with linear optics and feedforward. *Phys. Rev. Lett.*, 97:053601, 2006.

[50] U. L. Andersen, M. Sabuncu, R. Filip, and G. Leuchs. Experimental demonstration of coherent state estimation with minimal disturbance. *Phys. Rev. Lett.*, 96:020409, 2006.

[51] U. L. Andersen and R. Filip. Chapter 6 quantum feed-forward control of light. In *Progress in Optics*, pages 365–414. Elsevier BV, 2009.

[52] S. L. Braunstein and P. van Loock. Quantum information with continuous variables. *Rev. Mod. Phys.*, 77:513–577, 2005.

[53] A. Yariv and P. Yeh. *Optical Waves in Crystal, Propagation and Control of Laser Radiation*. John Wiley & Sons, Inc., 1984.

[54] E. L. Wooten, K. M. Kissa, A. Yi-Yan, E. J. Murphy, D. A. Lafaw, P. F. Hallemeier, D. Maack, D. V. Attanasio, D. J. Fritz, G. J. McBrien, and D. E. Bossi. A review of lithium niobate modulators for fiber-optic communications systems. *IEEE J. Sel. Top. Quantum Electron.*, 6:69–82, 2000.

[55] W. S. C. Chang, editor. *RF Photonic Technology in Optical Fiber Links*. Cambridge University Press (CUP), 2002.

[56] A. Chen and E. Murphy. *Broadband Optical Modulators: Science, Technology, and Applications*. CRC Press, 2011.

[57] A. Migdall, S. Polyakov, J. Fan, and J. Bienfang. *Single-Photon Generation and Detection Physics and Applications*, volume 45. Academic Press, 2013.

[58] P. Böhi, R. Prevedel, T. Jennewein, A. Stefanov, F. Tiefenbacher, and A. Zeilinger. Implementation and characterization of active feed-forward for deterministic linear optics quantum computing. *Applied Physics B*, 89:499–505, 2007.

[59] R. Prevedel. Ph.d. thesis: Experimental all-optical one-way quantum computing. *supervisor: A. Zeilinger*, 2009.

[60] X.-S. Ma, S. Zotter, N. Tetik, A. Qarry, T. Jennewein, and A. Zeilinger. A high-speed tunable beam splitter for feed-forward photonic quantum information processing. *Optics Express*, 19:22723, 2011.

[61] L. Mach. Ueber einen interferenzrefraktor. *Zeitschrift für Instrumentenkunde*, 12:89–93, 1891.

[62] L. Zehnder. Ein neuer interferenzrefraktor. *Zeitschrift für Instrumentenkunde*, 11:275–285, 1891.

[63] M. Suda, C. Pacher, M. Peev, M. Dušek, and F. Hipp. Quantum interference of photons in simple networks. *Quant. Inf. Proc.*, 12:1915–1945, 2012.

[64] M. Mičuda, E. Doláková, I. Straka, M. Miková, M. Dušek, J. Fiurášek, and M. Ježek. Highly stable polarization independent mach-zehnder interferometer. *Rev. Sci. Instrum.*, 85:083103, 2014.

[65] I. Marcikic, H. de Riedmatten, W. Tittel, H. Zbinden, M. Legré, and N. Gisin. Distribution of time-bin entangled qubits over 50 km of optical fiber. *Phys. Rev. Lett.*, 93:180502, 2004.

[66] V. Makarov, A. Brylevski, and D. R. Hjelme. Real-time phase tracking in single-photon interferometers. *Applied Optics*, 43:4385, 2004.

[67] L. Bartůšková, A. Černoch, R. Filip, J. Fiurášek, J. Soubusta, and M. Dušek. Optical implementation of the encoding of two qubits to a single qutrit. *Phys. Rev. A*, 74:022325, 2006.

[68] L. Bartůšková, M. Dušek, A. Černoch, J. Soubusta, and J. Fiurášek. Fiber-optics implementation of an asymmetric phase-covariant quantum cloner. *Phys. Rev. Lett.*, 99:120505, 2007.

[69] C. H. Bennett and G. Brassard. Quantum cryptography: Public key distribution and coin tossing. *Proceedings of IEEE International Conference on Computers, Systems and Signal Processing*, pages 175–179, 1984.

[70] W. K. Wootters and W. H. Zurek. A single quantum cannot be cloned. *Nature*, 299:802–803, 1982.

[71] M. Dušek, M. Jahma, and N. Lütkenhaus. Unambiguous state discrimination in quantum cryptography with weak coherent states. *Phys. Rev. A*, 62:022306, 2000.

[72] J. von Neumann. *Mathematical Foundations of Quantum Mechanics*. An English translation by Robert T. Beyer, Princeton University Press, 1955.

[73] A. S. Holevo. Statistical decision theory for quantum systems. *J. Multivar. Anal.*, 3:337–394, 1973.

[74] C. W. Helstrom. Quantum detection and estimation theory. *J. Stat. Phys.*, 1:231–252, 1969.

[75] C. W. Helstrom. *Quantum Detection and Estimation Theory.* Academic Press, New York, 1976.

[76] I. D. Ivanovic. How to differentiate between non-orthogonal states. *Phys. Lett. A*, 123:257–259, 1987.

[77] D. Dieks. Overlap and distinguishability of quantum states. *Phys. Lett. A*, 126:303–306, 1988.

[78] A. Peres. How to differentiate between non-orthogonal states. *Phys. Lett. A*, 128:19, 1988.

[79] G. Jaeger and A. Shimony. Optimal distinction between two non-orthogonal quantum states. *Phys. Lett. A*, 197:83–87, 1995.

[80] A. Chefles and S. M. Barnett. Strategies for discriminating between non-orthogonal quantum states. *J. Mod. Opt.*, 45:1295–1302, 1998.

[81] C.-W. Zhang, C.-F. Li, and G.-C. Guo. General strategies for discrimination of quantum states. *Phys. Lett. A*, 261:25 – 29, 1999.

[82] M. Ježek J. Fiurášek. Optimal discrimination of mixed quantum states involving inconclusive results. *Phys. Rev. A*, 67:012321, 2003.

[83] A. Hayashi, T. Hashimoto, and M. Horibe. State discrimination with error margin and its locality. *Phys. Rev. A*, 78:012333, 2008.

[84] H. Sugimoto, T. Hashimoto, M. Horibe, and A. Hayashi. Discrimination with error margin between two states: Case of general occurrence probabilities. *Phys. Rev. A*, 80:052322, 2009.

[85] E. Bagan, R. Muñoz Tapia, G. A. Olivares-Rentería, and J. A. Bergou. Optimal discrimination of quantum states with a fixed rate of inconclusive outcomes. *Phys. Rev. A*, 86:040303, 2012.

[86] M. Dušek and V. Bužek. Quantum-controlled measurement device for quantum-state discrimination. *Phys. Rev. A*, 66:022112, 2002.

[87] Q. Zhuang, Z. Zhang, and J. H. Shapiro. Optimum mixed-state discrimination for noisy entanglement-enhanced sensing. *Phys. Rev. Lett.*, 118:040801, 2017.

[88] B. Huttner, A. Muller, J. D. Gautier, H. Zbinden, and N. Gisin. Unambiguous quantum measurement of nonorthogonal states. *Phys. Rev. A*, 54:3783–3789, 1996.

[89] S. M. Barnett and E. Riis. Experimental demonstration of polarization discrimination at the helstrom bound. *J. Mod. Opt.*, 44:1061, 1997.

[90] R. B. M. Clarke, A. Chefles, S. M. Barnett, and E. Riis. Experimental demonstration of optimal unambiguous state discrimination. *Phys. Rev. A*, 63:040305, 2001.

[91] M. Mohseni, A. M. Steinberg, and J. A. Bergou. Optical realization of optimal unambiguous discrimination for pure and mixed quantum states. *Phys. Rev. Lett.*, 93:200403, 2004.

[92] L. Bartůšková, A. Černoch, J. Soubusta, and M. Dušek. Programmable discriminator of coherent states: Experimental realization. *Phys. Rev. A*, 77:034306, 2008.

[93] J. Soubusta, A. Černoch, J. Fiurášek, and M. Dušek. Experimental realization of a programmable quantum-state discriminator and a phase-covariant quantum multimeter. *Phys. Rev. A*, 69:052321, 2004.

[94] M. A. Solís-Prosser, M. F. Fernandes, O. Jiménez, A. Delgado, and L. Neves. Experimental minimum-error quantum-state discrimination in high dimensions. *Phys. Rev. Lett.*, 118:100501, 2017.

[95] J. Bae and L.-C. Kwek. Quantum state discrimination and its applications. *J. Phys. A*, 48:083001, 2015.

[96] S. M. Barnett and S. Croke. Quantum state discrimination. *Adv. Opt. Photon.*, 1:238–278, 2009.

[97] S. M. Barnett, R. B. M. Clarke, V. M. Kendon, E. Riis, A. Chefles, and M. Sasaki. *Experimental Quantum State Discrimination*, pages 59–67. Springer US, Boston, MA, 2002.

[98] A. Chefles. Quantum state discrimination. *Contemporary Physics*, 41:401–424, 2000.

[99] A. Acín. Statistical distinguishability between unitary operations. *Phys. Rev. Lett.*, 87:177901, 2001.

[100] G. M. D'Ariano, P. Lo Presti, and M. G. A. Paris. Using entanglement improves the precision of quantum measurements. *Phys. Rev. Lett.*, 87:270404, 2001.

[101] M. F. Sacchi. Optimal discrimination of quantum operations. *Phys. Rev. A*, 71:062340, 2005.

[102] G. Wang and M. Ying. Unambiguous discrimination among quantum operations. *Phys. Rev. A*, 73:042301, 2006.

[103] R. Duan, Y. Feng, and M. Ying. Perfect distinguishability of quantum operations. *Phys. Rev. Lett.*, 103:210501, 2009.

[104] M. Piani and J. Watrous. All entangled states are useful for channel discrimination. *Phys. Rev. Lett.*, 102:250501, 2009.

[105] A. W. Harrow, A. Hassidim, D. W. Leung, and J. Watrous. Adaptive versus nonadaptive strategies for quantum channel discrimination. *Phys. Rev. A*, 81:032339, 2010.

[106] M. Ziman and M. Sedlák. Single-shot discrimination of quantum unitary processes. *J. Mod. Opt.*, 57:253–259, 2010.

[107] T. Hashimoto, A. Hayashi, M. Hayashi, and M. Horibe. Unitary-process discrimination with error margin. *Phys. Rev. A*, 81:062327, 2010.

[108] G. Chiribella, G. M. D'Ariano, and P. Perinotti. Memory effects in quantum channel discrimination. *Phys. Rev. Lett.*, 101:180501, 2008.

[109] P. Zhang, L. Peng, Z.-W. Wang, X.-F. Ren, B.-H. Liu, Y.-F. Huang, and G.-C. Guo. Linear optical implementation of perfect discrimination between single-bit unitary operations. *J. Phys. B*, 41:195501, 2008.

[110] A. Laing, T. Rudolph, and J. L. O'Brien. Experimental quantum process discrimination. *Phys. Rev. Lett.*, 102:160502, 2009.

[111] J. Trapani and M. G. A. Paris. Entanglement as a resource for discrimination of classical environments. *Physics Letters A*, 381:245 – 251, 2017.

[112] M. Sedlák and M. Ziman. Optimal single-shot strategies for discrimination of quantum measurements. *Phys. Rev. A*, 90:052312, 2014.

[113] M. Ziman and T. Heinosaari. Discrimination of quantum observables using limited resources. *Phys. Rev. A*, 77:042321, 2008.

[114] Z. Ji, Y. Feng, R. Duan, and M. Ying. Identification and distance measures of measurement apparatus. *Phys. Rev. Lett.*, 96:200401, 2006.

[115] J. Fiurášek and M. Mičuda. Optimal two-copy discrimination of quantum measurements. *Phys. Rev. A*, 80:042312, 2009.

[116] S. Pirandola. Quantum reading of a classical digital memory. *Phys. Rev. Lett.*, 106:090504, 2011.

[117] A. Bisio, M. Dall'Arno, and G. M. D'Ariano. Tradeoff between energy and error in the discrimination of quantum-optical devices. *Phys. Rev. A*, 84:012310, 2011.

[118] R. Nair. Discriminating quantum-optical beam-splitter channels with number-diagonal signal states: Applications to quantum reading and target detection. *Phys. Rev. A*, 84:032312, 2011.

[119] S. Pirandola, C. Lupo, V. Giovannetti, S. Mancini, and S. L. Braunstein. Quantum reading capacity. *New J. Phys.*, 13:113012, 2011.

[120] O. Hirota. Error free quantum reading by quasi bell state of entangled coherent states. *arXiv:1108.4163v2*, 2011.

[121] G. M. D'Ariano, P. Lo Presti, and M. G. A. Paris. Improved discrimination of unitary transformations by entangled probes. *J. Opt. B*, 4:273, 2002.

[122] R. Duan, Y. Feng, and M. Ying. Entanglement is not necessary for perfect discrimination between unitary operations. *Phys. Rev. Lett.*, 98:100503, 2007.

[123] M. Sedlák. Quantum theory of unambiguous measurements. *Acta Physica Slovac*, 59:653–792, 2009.

[124] Z. Hradil. Quantum-state estimation. *Phys. Rev. A*, 55:R1561–R1564, 1997.

[125] Z. Hradil, J. Řeháček, J. Fiurášek, and M. Ježek. Maximum-likelihood methods in quantum mechanics. In M. G. A. Paris and J. Řeháček, editors, *Quantum State Estimation, Lect. Notes Phys. 649*, chapter 3, page 59. Springer-Verlag, Berlin Heidelberg, 2004.

[126] A. K. Ekert, C. M. Alves, D. K. L. Oi, M. Horodecki, P. Horodecki, and L. C. Kwek. Direct estimations of linear and nonlinear functionals of a quantum state. *Phys. Rev. Lett.*, 88:217901, 2002.

[127] R. Filip. Overlap and entanglement-witness measurements. *Phys. Rev. A*, 65:062320, 2002.

[128] M. Hendrych, M. Dušek, R. Filip, and J. Fiurášek. Simple optical measurement of the overlap and fidelity of quantum states. *Phys. Lett. A*, 310:95–100, 2003.

[129] C. K. Hong, Z. Y. Ou, and L. Mandel. Measurement of subpicosecond time intervals between two photons by interference. *Phys. Rev. Lett.*, 59:2044–2046, 1987.

[130] L. Mandel and E. Wolf. *Optical coherence and quantum optics*. Cambridge University Press (CUP), 1995.

[131] A. Peres. *Quantum Theory: Concepts and Methods*. Kluwer Academic Publishers, Dordrecht, 1995.

[132] C. Santori, D. Fattal, J. Vuckovic, G. S. Solomon, and Y. Yamamoto. Indistinguishable photons from a single-photon device. *Nature*, 419:594–597, 2002.

[133] W. H. Zurek. Decoherence, einselection, and the quantum origins of the classical. *Rev. Mod. Phys.*, 75:715–775, 2003.

[134] M. Halder, A. Beveratos, N. Gisin, V. Scarani, C. Simon, and H. Zbinden. Entangling independent photons by time measurement. *Nat. Phys.*, 3:692–695, 2007.

[135] H. Defienne, M. Barbieri, I. A. Walmsley, B. J. Smith, and S. Gigan. Two-photon quantum walk in a multimode fiber. *Sci. Adv.*, 2:1501054, 2016.

[136] D. N. Biggerstaff, R. Heilmann, A. A. Zecevik, M. Gräfe, M. A. Broome, A. Fedrizzi, S. Nolte, A. Szameit, A. G. White, and I. Kassal. Enhancing coherent transport in a photonic network using controllable decoherence. 7:11282, 2016.

[137] C. Macchiavello, G. M. Palma, and A. Zeilinger. *Quantum Computation and Quantum Information Theory*. World Scientific Publishing, Singapore, 2000.

[138] N. Gisin and R. Thew. Quantum communication. *Nat. Photon.*, 1:165–171, 2007.

[139] H. Häfner, C.F. Roos, and R. Blatt. Quantum computing with trapped ions. *Phys. Rep.*, 469:155 – 203, 2008.

[140] H. J. Kimble. The quantum internet. *Nature*, 453:1023–1030, 2008.

[141] M. Saffman, T. G. Walker, and K. Mølmer. Quantum information with rydberg atoms. *Rev. Mod. Phys.*, 82:2313–2363, 2010.

[142] J. H. Plantenberg, P. C. de Groot, C. J. P. M. Harmans, and J. E. Mooij. Demonstration of controlled-not quantum gates on a pair of superconducting quantum bits. *Nature*, 447:836–839, 2007.

[143] A. Kuzmich, W. P. Bowen, A. D. Boozer, A. Boca, C. W. Chou, L.-M. Duan, and H. J. Kimble. Generation of nonclassical photon pairs for scalable quantum communication with atomic ensembles. *Nature*, 423:731–734, 2003.

[144] C. H. van der Wal, M. D. Eisaman, A. André, R. L. Walsworth, D. F. Phillips, A. S. Zibrov, and M. D. Lukin. Atomic memory for correlated photon states. *Science*, 301:196–200, 2003.

[145] T. Wilk, S. C. Webster, A. Kuhn, and G. Rempe. Single-atom single-photon quantum interface. *Science*, 317:488–490, 2007.

[146] S. T. Yılmaz, P. Fallahi, and A. Imamoğlu. Quantum-dot-spin single-photon interface. *Phys. Rev. Lett.*, 105:033601, 2010.

[147] A. Stute, B. Casabone, B. Brandstätter, K. Friebe, T.E. Northup, and R. Blatt. Quantum-state transfer from an ion to a photon. *Nat. Photon.*, 7:219–222, 2013.

[148] H. Bernien, B. Hensen, W. Pfaff, G. Koolstra, M. S. Blok, L. Robledo, T. H. Taminiau, M. Markham, D. J. Twitchen, L. Childress, and R. Hanson. Heralded entanglement between solid-state qubits separated by three metres. *Nature*, 497:86–90, 2013.

[149] J.-M. Pirkkalainen, S. U. Cho, Jian Li, G. S. Paraoanu, P. J. Hakonen, and M. A. Sillanpaa. Hybrid circuit cavity quantum electrodynamics with a micromechanical resonator. *Nature*, 494:211–215, 2013.

[150] T. G. Tiecke, J. D. Thompson, N. P. de Leon, L. R. Liu, V. Vuletic, and M. D. Lukin. Nanophotonic quantum phase switch with a single atom. *Nature*, 508:241–244, 2014.

[151] T. R. Tan, J. P. Gaebler, Y. Lin, Y. Wan, R. Bowler, D. Leibfried, and D. J. Wineland. Multi-element logic gates for trapped-ion qubits. *Nature*, 528:380–383, 2015.

[152] C. J. Ballance, V. M. Schäfer, J. P. Home, D. J. Szwer, S. C. Webster, D. T. C. Allcock, N. M. Linke, T. P. Harty, D. P. L. Aude Craik, D. N. Stacey, A. M. Steane, and D. M. Lucas. Hybrid quantum logic and a test of bell's inequality using two different atomic isotopes. *Nature*, 528:384–386, 2015.

[153] R. Riedinger, S. Hong, R. A. Norte, J. A. Slater, J. Shang, A. G. Krause, V. Anant, M. Aspelmeyer, and S. Gröblacher. Non-classical correlations between single photons and phonons from a mechanical oscillator. *Nature*, 530:313–316, 2016.

[154] K. Hammerer, Anders S. Sørensen, and Eugene S. Polzik. Quantum interface between light and atomic ensembles. *Rev. Mod. Phys.*, 82:1041–1093, 2010.

[155] N. Daniilidis and H. Häffner. Quantum interfaces between atomic and solid-state systems. *Annu. Rev. Condens. Matter Phys.*, 4:83–112, 2013.

[156] J. Majer, J. M. Chow, J. M. Gambetta, Jens Koch, B. R. Johnson, J. A. Schreier, L. Frunzio, D. I. Schuster, A. A. Houck, A. Wallraff, A. Blais, M. H. Devoret, S. M. Girvin, and R. J. Schoelkopf. Coupling superconducting qubits via a cavity bus. *Nature*, 449:443–447, 2007.

[157] A. Reiserer, N. Kalb, G. Rempe, and S. Ritter. A quantum gate between a flying optical photon and a single trapped atom. *Nature*, 508:237–240, 2014.

[158] D. N. Matsukevich. Quantum state transfer between matter and light. *Science*, 306:663–666, 2004.

[159] M. Wallquist, K. Hammerer, P. Rabl, M. Lukin, and P. Zoller. Hybrid quantum devices and quantum engineering. *Physica Scripta*, 2009:014001, 2009.

[160] Z.-Liang Xiang, S. Ashhab, J. Q. You, and F. Nori. Hybrid quantum circuits: Superconducting circuits interacting with other quantum systems. *Rev. Mod. Phys.*, 85:623–653, 2013.

[161] G. Kurizki, P. Bertet, Y. Kubo, K. Mølmer, D. Petrosyan, P. Rabl, and J. Schmiedmayer. Quantum technologies with hybrid systems. *Proceedings of the National Academy of Sciences*, 112:3866–3873, 2015.

[162] L. You and M. S. Chapman. Quantum entanglement using trapped atomic spins. *Phys. Rev. A*, 62:052302, 2000.

[163] F. Verstraete, J. Dehaene, and B. DeMoor. Local filtering operations on two qubits. *Phys. Rev. A*, 64:010101, 2001.

[164] J. J. Sakurai. *Modern Quantum Mechanics*. Addison-Wesley Publ. Comp., revised ed. 1994.

[165] M. Dušek. *Koncepční otázky kvantové teorie*. Palacký University Olomouc, 2002.

[166] R. C. Jones. A new calculus for the treatment of optical systems I. description and discussion of the calculus. *J. Opt. Soc. Am.*, 31(7):488–493, 1941.

[167] B. E. A. Saleh and M. C. Teich. *Fundamentals of Photonics*. Wiley interscience - 2. edition, New Jersey, 2007.

[168] F. Mitschke. *Fiber Optics, Physics and Tehcnology*. Springer Nature, 2009.

[169] M. Miková. *Optical implementation of quantum operations for quantum information processing using entangled photons: application of electronics feed-forward*. Master's thesis, Department of Optics, Faculty of Science, Palacký University Olomouc, 2011. supervisor: M. Dušek.

[170] Publik labbook of our laboratory – Quantum Optics Laboratory Olomouc (QOLO), http://quantum.opticsolomouc.org/archives/1177. 2017.

[171] Single photon counting modules from Excelitas, http://www.excelitas.com/pages/product/single-photon-counting-modules-spcm.aspx. 2017.

[172] M. Miková. Textbook for laboratory classes OPT/EFO and EFOX : Charakterizace integrovaného elektro-optoického fázového modulátoru. 2014–2016.

[173] M. Dušek. *Měření půlvlnného napětí fázových modulátorů*. Protocol, Department of Optics, Faculty of Science, Palacký University Olomouc, 1997.

[174] H. Fikerová. *Optical setup for quantum information processing*. Bachelor's thesis, Department of Optics, Faculty of Science, Palacký University Olomouc, 2010. supervisor: M. Dušek.

[175] G. G. Stokes. *Cambridge & Dublin Mathematical Journal*, 4:1, 1849.

[176] R. A. Campos, B. E. A. Saleh, and M. C. Teich. Quantum-mechanical lossless beam splitter: SU(2) symmetry and photon statistics. *Phys. Rev. A*, 40:1371–1384, 1989.

[177] I. Straka. *Optical frequency conversion and non-classical light generation*. Master's thesis, Department of Optics, Faculty of Science, Palacký University Olomouc, 2012. supervisor: M. Ježek.

[178] H. Fikerová. *Quantum optics-based experiments in quantum information processing*. Master's thesis, Department of Optics, Faculty of Science, Palacký University Olomouc, 2014. supervisor: M. Dušek.

[179] J.P Goure and I. Verrier. *Optical Fibre Devices*. IOP Publishing Ltd, 2002.

[180] Special thanks for J. Běhal who plotted the graphs and measured the VRC splitting ratio with his colleagues (V. Krčmarský, J. Hloušek, J. Bílek) during practice OPT/EFO 2014/2015 under my and M. Ježek's supervision.

[181] L. Čelechovská (Bartůšková). *Kvantové optické experimenty v kvantové teorii informace*. PhD thesis, Department of Optics, Faculty of Science, Palacký University Olomouc, 2011. supervisor: M. Dušek.

[182] J. Peřina. *Coherence of Light*. Kluwer Academic Publisher, 1985.

[183] M. Hendrych, M. Dušek, and O. Haderka. The effect of beam-splitter imperfections and losses on fringe visibility in a mach-zehnder interferometer. *Acta Physica Slovaka*, 46:393–398, 1996.

[184] R. Stárek. *Characterization of polarization-maintaining fibers*. Bachelor's thesis, Department of Optics, Faculty of Science, Palacký University Olomouc, 2013. supervisor: M. Mičuda.

[185] M. Ježek, I. Straka, M. Mičuda, M. Dušek, J. Fiurášek, and R. Filip. Experimental test of the quantum non-gaussian character of a heralded single-photon state. *Phys. Rev. Lett.*, 107:213602, 2011.

[186] R. W. Boyd. *Nonlinear Optics*. Academic Press, 3rd Edition, 2007.

[187] V. G. Dmitriev, G. G. Gurzadyan, and D. N. Nikogosyan. *Handbook of Nonlinear Optical Crystals*. Springer Series in Optical Sciences, 1999.

[188] V. Švarc. Aktivní fázová stabilizace interferometru pomocí zpětnovazební PID regulace, 2016. supervisor: M. Miková.

[189] M. Dušek. *Aktivní stabilizace interference*. Protocol, Department of Optics, Faculty of Science, Palacký University Olomouc, 1997.

[190] M. Hendrych. *Experimental Quantum Cryptography*. PhD thesis, Department of Optics, Faculty of Science, Palacký University Olomouc, 2002. supervisor: Jan Peřina.

[191] M. Ježek, J. Fiurášek, and Z. Hradil. Quantum inference of states and processes. *Phys. Rev. A*, 68:012305, 2003.

[192] R. Jozsa. Fidelity for mixed quantum states. *J. Mod. Opt.*, 41:2315–2323, 1994.

[193] A. Jamiołkowski. Linear transformations which preserve trace and positive semidefiniteness of operators. *Rep. Math. Phys.*, 3:275–278, 1972.

[194] M.-D. Choi. Completely positive linear maps on complex matrices. *Linear Algebra and its Applications*, 10:285–290, 1975.

[195] N. Gisin, G. Ribordy, W. Tittel, and H. Zbinden. Quantum cryptography. *Rev. Mod. Phys.*, 74:145–195, 2002.

[196] J.-W. Pan, Z.-B. Chen, C.-Y. Lu, H. Weinfurter, A. Zeilinger, and M. Żukowski. Multiphoton entanglement and interferometry. *Rev. Mod. Phys.*, 84:777–838, 2012.

[197] J. P. Torres, K. Banaszek, and I.A. Walmsley. Engineering nonlinear optic sources of photonic entanglement. *Progress in Optics*, 56:227 – 331, 2011.

[198] M. Ziman. Process positive-operator-valued measure: A mathematical framework for the description of process tomography experiments. *Phys. Rev. A*, 77:062112, 2008.

[199] R. Stárek, M. Mičuda, I. Straka, M. Miková, M. Ježek, R. Filip, and J. Fiurášek. Control and enhancement of interferometric coupling between two photonic qubits. *Phys. Rev. A*, 93:042321, 2016.

[200] E. Jeffrey, N. A. Peters, and P. G. Kwiat. Towards a periodic deterministic source of arbitrary single-photon states. *New J. Phys.*, 6:100, 2004.

[201] N. A. Peters, J. T. Barreiro, M. E. Goggin, T.-C. Wei, and P. G. Kwiat. Remote state preparation: Arbitrary remote control of photon polarization. *Phys. Rev. Lett.*, 94:150502, 2005.

[202] M. Ježek, M. Mičuda, I. Straka, M. Miková, M. Dušek, and J. Fiurášek. Orthogonalization of partly unknown quantum states. *Phys. Rev. A*, 89:042316, 2014.

UNIVERZITA PALACKÉHO V OLOMOUCI
PŘÍRODOVĚDECKÁ FAKULTA

Katedra optiky

Kvantově optické experimenty zaměřené na kvantové zpracování informace

Martina Miková

AUTOREFERÁT DISERTAČNÍ PRÁCE

Olomouc 2017

PALACKY UNIVERSITY OLOMOUC
FACULTY OF SCIENCE
Department of Optics

Quantum optical experiments focused on quantum information processing

Martina Miková

SUMMARY OF DOCTORAL THESIS

Olomouc 2017

Výsledky prezentované v disertační práci byly získány v rámci prezenčního doktorského studia studijního oboru Optika a optoelektronika (1701V029), ve studijním programu Fyzika (P1701) na Přírodovědecké fakultě Univerzity Palackého v Olomouci.

Doktorandka:	**Mgr. Martina Miková**
Školitel:	**prof. RNDr. Miloslav Dušek, Dr.** Katedra optiky Přírodovědecká fakulta Univerzita Palackého v Olomouc, ČR
Konzultant:	**RNDr. Miroslav Ježek, Ph.D.** Katedra optiky Přírodovědecká fakulta Univerzita Palackého v Olomouc, ČR
Oponenti:	**prof. RNDr. Petr Malý DrSc.** Katedra chemické fyziky a optiky Matematicko-fyzikální fakulta Univerzita Karlova, Praha, ČR
	prof. Andreas Poppe Ph.D. Optická a kvantová laboratoř Německé výzkumné centrum Evropský výzkumný institut, Mnichov, Německo
Předseda komise:	**prof. RNDr. Zdeněk Hradil, CSc.** Katedra optiky Přírodovědecká fakulta Univerzita Palackého v Olomouc, ČR

Autoreferát byl rozeslán dne ..... 2017.

Obhajoba se koná dne ..... 2017 v ..... hodin před komisí pro obhajobu disertační práce vědního oboru Fyzika, studijního oboru Optika a optoelektronika na katedře optiky Přírodovědecké fakulty Univerzity Palackého v Olomouci, na adrese 17. listopadu 12, 771 46, Olomouc.

S disertační prací je možné se seznámit na studijním oddělení Přírodovědecké fakulty Univerzity Palackého v Olomouci, sídlícím na stejné adrese.

Results presented in the Ph.D. thesis were obtained during full-time doctoral study in study field Optics and optoelectronics (1701V029), study program Physics (P1701), of Faculty of Science, Palacký University in Olomouc.

Ph.D. candidate:	**Mgr. Martina Miková**
Supervisor:	**Prof. RNDr. Miloslav Dušek, Dr.** Department of Optics Faculty of Science Palacký University Olomouc, CZ
Co-Supervisor:	**RNDr. Miroslav Ježek, Ph.D.** Department of Optics Faculty of Science Palacký University Olomouc, CZ
Reviewers:	**Prof. RNDr. Petr Malý DrSc.** Department of Chemical Physics and Optics Faculty of Mathematics and Physics Charles University, Prague, CZ
	Prof. Andreas Poppe Ph.D. Optical and Quantum Laboratory German Research Center European Research Institute, Munich, DE
Chairman of the committee:	**Prof. RNDr. Zdeněk Hradil, CSc.** Department of Optics Faculty of Science Palacký University Olomouc, CZ

The summary was sent on ..... 2017.

The defence will take a place on ..... 2017 at ..... o'clock in front of the committee for doctoral study program Optics and optoelectronics at the Department of optics, Faculty of Science, Palacký University Olomouc, residing at 17. listopadu 12, 771 46 Olomouc, Czech Republic.

The Ph.D. thesis is available at the study department of Faculty of Science of Palacký University Olomouc, residing at the same address.

Declaration

The thesis is based on five original publications [1–5]. My contribution to these publications consists of the experimental implementations of newly suggested proof-of-principle quantum information protocols to validate the theoretical predictions and experimentally verify their feasibility and robustness. The theory is work of my colleagues (co-authors of the publications).

I declare that I wrote this Ph.D. Thesis "Quantum optical experiments focused on quantum information processing" on my own under the guidance of my supervisor prof. RNDr. Miloslav Dušek, Dr. and my co-supervisor RNDr. Miroslav Ježek, Ph.D. by using the resources which are referred in the Bibliography.

I agree with the further usage of this Thesis according to the requirements of Palacký University and the Department of Optics.

In Olomouc, ... 2017

.....
Martina Miková

Abstrakt

Tato disertační práce je založena na pěti originálních publikacích [1–5] a shrnuje hlavní experimentální výsledky, které vznikly během mého doktorského studia.

První realizovaný experiment testoval využití elektro-optické dopředné vazby pro zvýšení pravděpodobnosti úspěchu lineárně optických hradel [1]. Experimentální výsledky ukázaly, že dopředná vazba zdvojnásobila pravděpodobnost úspěchu lineárně-optického programovatelného kvantového fázového hradla aniž by ovlivnila kvalitu dosažených výsledků. Koncept zavedení podmíněné operace pomocí dopředné vazby byl úspěšně aplikován i v dalších realizovaných experimentech.

Následující experimenty se zabývaly přenosem kvantového stavu a rozlišovacími strategiemi. Bylo sestrojeno experimentální zařízení pro bezchybné rozlišení dvou optických paměťových záznamů reprezentovaných dvěma děliči svazku s navzájem různými odrazivostmi [3]. Realizované zařízení využívalo nejmenší možné energie, v průběhu měření byl paměťový záznam vystaven v průměru pouze zlomku energie jednoho fotonu. Následným projektem byla experimentální realizace optimálního rozlišení dvou známých projektivních kvantových měření pomocí kvantově provázaného stavu [4]. Výsledná experimentální data jasně demonstrovala výhodu rozlišovací strategie využívající dvě kvantově provázané částice v porovnání se strategií využívající pouze jeden kvantový bit.

Dále byl realizován experiment pro přenos stavu kvantového bitu. Experiment byl využit k ověření nově navržené, přímo měřitelné míry efektivní nerozlišitelnosti částic, která určuje reálnou hranici kvality přenosu kvantového stavu [2]. Zároveň jsme tuto míru porovnali s běžně užívaným překryvem stavů, i když překryv stavů lze použít pouze tehdy, jsou-li tyto částice ve faktorizovaném stavu. Výsledky experimentu potvrdily, že částice mohou sloužit pro přenos kvantové informace, i když jsou jejich další stupně volnosti provázané. Posledním realizovaným experimentem byl přenos neznámého kvantového stavu mezi dvěma vzájemně slabě interagujícími částicemi [5]. Přenosu kvantového stavu bylo dosaženo vhodným měřením fotonu, který nesl neznámý kvantový stav, v kombinaci s aplikací filtrace na stav cílového fotonu. Optimální filtrace závisí na vzájemné interakci částic, na výsledku měření a na původním stavu částice, na niž je neznámý stav přenášen.

Výsledky těchto experimentů přispěly k rozvoji základního výzkumu v oblasti experimentální lineární kvantové optiky a kvantového zpracování informace.

Klíčová slova

Experimentální kvantová optika, lineární optika, vláknová optika, kvantové zpracování informace, elektro-optická dopředná vazba, integrovaný elektro-optický fázový modulátor, fotony, Machův-Zehnderův interferometr, sekvenční aktivní fázová stabilizace.

Abstract

This Thesis is based on five original publications [1–5] and concludes my main experimental results reached during the years of my Ph.D. studies.

Firstly, we experimentally verify the possibility of increasing success probability of linear optical quantum gates utilizing an electro-optical feed-forward loop [1]. We find out that the loop doubles the success probability of linear-optical programmable quantum phase gate. Moreover, any gate parameters like a fidelity, purity etc. are not influenced. The concept of a conditionally applied operation via the feed-forward loop is successfully implemented into other experiments.

Further publications deal with quantum state transfer and discrimination tasks. We experimentally implement a device for perfect discrimination of two optical memory records which are represented by two beam splitters with different splitting ratios [3]. For discrimination, this device utilizes in average less than fraction of a single photon energy. Further, we experimentally implement the device for optimal discrimination of two known projective single-qubit quantum measurements [4]. The experimental results clearly confirm the advantage of the proposed more demanding entanglement-assisted discrimination scheme compared to a single-qubit probe scheme.

A quantum state transfer is experimentally realized to examine particle properties. A new measure of particles' effective indistinguishability directly determines the fidelity of the transferred state [2]. We compare it with commonly used overlap of quantum states of particles, which is defined only for factorable states. The experimental results confirm that even if some noninformational degrees of freedom of two particles are entangled, the particles can still serve as good carriers of qubits. Finally, we experimentally realize a faithful unidirectional qubit state transfer between two weakly interacting photonic qubits [5]. The qubit state transfer is achieved by a combination of a suitable measurement on the unknown qubit and a quantum filtering on the target qubit. The filtering depends on the initial target-qubit state and on the outcome of the measurement applied on the unknown qubit.

The results of these proof-of-principle experiments support scientific research in the area of experimental linear-optical quantum information processing and quantum optics.

Key words

Quantum optics experiments, linear optics, fibre optics, quantum information processing, electro-optical feed-forward loop, integrated electro-optical phase modulator, photons, Mach-Zehnder interferometer, sequential active phase stabilization.

Contents

Abstrakt (CZ) viii

Abstract ix

1 Goals of the Thesis and a brief introduction 1

2 Increasing efficiency of a linear-optical quantum gate using electronic feed-forward loop 3

3 Carrying qubits with particles whose noninformational degrees of freedom are nonfactorable 11

4 Experimental implementation of perfect quantum reading of beam splitters 17

5 Optimal entanglement-assisted discrimination of quantum measurements 23

6 Faithful conditional quantum state transfer between weakly coupled qubits 31

7 Conclusions 41

Stručné shrnutí v češtině (CZ) 43

Publications of the author and a list of citations 45

Bibliography 51

Chapter 1

Goals of the Thesis and a brief introduction

The aim of the Thesis is to comprehensively present experiments which were realized during my Ph.D. studies. The goal of these proof-of-principle linear-optics quantum information processing experiments is to implement the suggested theoretical protocols, verify their feasibility, robustness, and sensitivity to real conditions. Below, chapters describing the individual experiments are briefly introduced:

Chapter 2 describes the increase of success probability of a linear optical programmable phase gate via successful implementation of the fast electro-optical feed-forward loop. The probabilistic programmable phase gate itself was proposed by *Vidal, Masanes, and Cirac in 2002* [6]. For the first time, the gate was experimentally implemented using only bulk linear-optical elements and reached only 25 % success probability [7]. We reached the theoretical limit of 50 % in the fibre-optics gate implementation via the fast electro-optical feed-forward loop. We verified the increase of the success probability and characterized the gate operation by means of quantum process tomography. We demonstrated that the use of feed-forward loop affects neither the process fidelity nor the output state fidelities. The *Chapter 2* is based on a publication [1]: Martina Miková, Helena Fikerová, Ivo Straka, Michal Mičuda, Jaromír Fiurášek, Miroslav Ježek, and Miloslav Dušek. *Increasing efficiency of a linear-optical quantum gate using electronic feed-forward.* Physical Review A **85**, 012305 (2012).

In *Chapter 3*, we have experimentally tested and verified the relevance of *effective indistinguishability* of particles carrying qubits to quantum information transfer and processing. In contrast to commonly used overlap of quantum states of particles, defined only for factorable states, this measure can be generally applied to any joint state of the particles. We test the new measure of *effective indistinguishability* on photons produced by parametric down-conversion employed in a simple linear-optical quantum state transfer protocol. There the measure directly determines the fidelity of the transferred state. The experimental results confirmed that even if other degrees of freedom of two particles are entangled, the particles can still serve as good carriers of qubits. *Chapter 3* is

based on publication [2]: Martina Miková, Helena Fikerová, Ivo Straka, Michal Mičuda, Miroslav Ježek, Miloslav Dušek, and Radim Filip. *Carrying qubits with particles whose noninformational degrees of freedom are nonfactorable.* Physical Review A **87**, 042327 (2013).

In *Chapter 4*, there is described the experimental implementation of perfect quantum reading of optical memory records utilizing the smallest possible energy amount. We built the suggested device for perfect and unambiguous distinguishing between two different memory records represented by two mutually different beam-splitters. During the measurement, a superposition of a single photon and vacuum state entered into the beam-splitter. The experimental results of the quantum reading showed that the memory records can be perfectly distinguished even if they are in average exposed to a fraction of photon energy and confirmed the theoretical predictions. *Chapter 4* is based on publication [3]: Michele Dall'Arno, Alessandro Bisio, Giacomo Mauro D'Ariano, Martina Miková, Miroslav Ježek, and Miloslav Dušek. *Experimental implementation of unambiguous quantum reading.* Physical Review A **85**, 012308 (2012).

In *Chapter 5*, we experimentally investigated optimal discrimination between two projective single-qubit measurements on polarization states of a single photon in a scenario where the measurement can be performed only once. We investigated the discrimination strategy in dependence on the amount of inconclusive outcomes. The experimental results demonstrate the advantage of discrimination strategy utilizing entanglement probe state in comparison with unentangled single-qubit probes, for any nonzero rate of inconclusive outcomes. *Chapter 5* is based on publication [4]: Martina Miková, Michal Sedlák, Ivo Straka, Michal Mičuda, Mário Ziman, Miroslav Ježek, Miloslav Dušek, and Jaromír Fiurášek. *Optimal entanglement-assisted discrimination of quantum measurements.* Physical Review A **90**, 022317 (2014).

In *Chapter 6*, there is described the experimental demonstration of a procedure for faithful quantum state transfer between two weakly interacting qubits. The scheme enables a probabilistic yet perfect unidirectional transfer of an arbitrary unknown state of a source qubit onto a target qubit prepared initially in a known state. The transfer is achieved by a combination of a suitable measurement on the source qubit and a quantum filtering on the target qubit. The filtering depends on the outcome of the measurement on the source qubit, initial state of the target qubit, and qubits' mutual interaction. We experimentally verify feasibility and robustness of the transfer using a linear optical setup with qubits encoded into polarization states of single photons. However, the theoretical suggestion of the transfer itself is not restricted to a particular experimental platform. *Chapter 6* is based on publication [5]: Martina Miková, Ivo Straka, Michal Mičuda, Vojtěch Krčmarský, Miloslav Dušek, Miroslav Ježek, Jaromír Fiurášek, and Radim Filip. *Faithful conditional quantum state transfer between weakly coupled qubits.* Scientific Reports **6**, 32125 (2016).

Chapter 2

Increasing efficiency of a linear-optical quantum gate using electronic feed-forward loop

This chapter is based on the following publication:

[1] Martina Miková, Helena Fikerová, Ivo Straka, Michal Mičuda, Jaromír Fiurášek, Miroslav Ježek, and Miloslav Dušek. *Increasing efficiency of a linear-optical quantum gate using electronic feed-forward.* Physical Review A **85**, 012305 (2012).

Basic idea

As already mentioned, the probabilistic programmable phase gate is proposed by Vidal, Masanes, and Cirac [6]. The gate rotates a single-qubit state along the z-axis of the Bloch sphere. In other words, the arbitrary input state $\alpha|0\rangle + \beta|1\rangle$ is at the output of the gate rotated in following way $\alpha|0\rangle + e^{i\varphi}\beta|1\rangle$. In the simplest case, the angle of rotation, the phase shift φ, is programmed into the state of a single qubit. Thus according to [6] the overall gate success probability is limited by 50 %. Let us stress, that this programmable quantum phase gate has no classical analogy. An exact specification of the angle of rotation φ would require infinitely many classical bits.

For the first time, the gate was experimentally implemented in 2008 [7]. It was based on linear optics using bulk elements. Its success probability reached only 25 %. Later in 2012, we showed how to increase the success probability of the gate to its quantum mechanical limit of 50 %[1] by means of electronic feed forward loop [1].

I started to work on this experiment during my Master's studies. I have finished it at the beginning of my Ph.D. studies. Therefore particular details about the experimental layout are described in my Master's thesis [8]. Here we focus mainly on the full characterization of the gate by means of quantum process tomography.

[1] The success probabilities discussed here do not include signal attenuation due to technological losses.

Theory

Here I would like to stress, that the theoretical part of [1] is not my work. A part of the theory directly related to the experiment is described below. For more details see also [6].

The programmable phase gate is a two-qubit gate, consisting of a data and a program qubit. The gate can be experimentally implemented by the linear optical setup shown in Fig. 2.1. The qubits are encoded into the states of single photons using spatial encoding. It means, each qubit is represented by a single photon which may propagate into two optical fibres. Basis states $|0\rangle$ and $|1\rangle$ correspond to the presence of the photon in the first or the second fibre, respectively.

The gate performs a unitary evolution of the data qubit (D) which depends on the state of the program qubit (P).

$$U(\varphi) = |0\rangle_D\langle 0| + e^{i\varphi}|1\rangle_D\langle 1|. \tag{2.1}$$

The program qubit contains information about the phase shift φ encoded in following way $|\psi\rangle_P = (|0\rangle_P + e^{i\varphi}|1\rangle_P)/\sqrt{2}$.

Without loss of generality, we can consider only pure input states of the data qubit $|\psi_{\text{in}}\rangle_D = \alpha|0\rangle_D + \beta|1\rangle_D$, where $|\alpha|^2 + |\beta|^2 = 1$. Then the initial state of the gate is:

$$|\psi\rangle_P \otimes |\psi_{\text{in}}\rangle_D = (\alpha|0\rangle_P \otimes |0\rangle_D + \beta|0\rangle_P \otimes |1\rangle_D + \alpha e^{i\varphi}|1\rangle_P \otimes |0\rangle_D + \beta e^{i\varphi}|1\rangle_P \otimes |1\rangle_D)/\sqrt{2}. \tag{2.2}$$

The gate operation can be described as follows[2] $|0\rangle_P \to |0\rangle_P, |1\rangle_P \to |1\rangle_D, |1\rangle_D \to |1\rangle_P$, $|0\rangle_D \to |0\rangle_D$, modes corresponding to $|1\rangle_D$ and $|1\rangle_P$ are swapped. After passing though the gate the overall state reads:

$$(\alpha|0\rangle_P \otimes |0\rangle_D + \beta|0\rangle_P \otimes |1\rangle_P + \alpha e^{i\varphi}|1\rangle_D \otimes |0\rangle_D + \beta e^{i\varphi}|1\rangle_D \otimes |1\rangle_P)/\sqrt{2}. \tag{2.3}$$

If we consider only cases when a single photon emerges in each output port of the gate (it corresponds to the coincidence measurement), the conditional two-photon output state is:

$$(\alpha|0\rangle_D \otimes |0\rangle_P + \beta e^{i\phi}|1\rangle_D \otimes |1\rangle_P)/\sqrt{2}, \tag{2.4}$$

(the normalization reflects the fact that the probability of this situation is 1/2). We can rewrite this state as:

$$\big[(\alpha|0\rangle_D + \beta e^{i\varphi}|1\rangle_D) \otimes |+\rangle_P + (\alpha|0\rangle_D - \beta e^{i\varphi}|1\rangle_D) \otimes |-\rangle_P\big]/2, \tag{2.5}$$

where $|\pm\rangle_P = (|0\rangle_P \pm |1\rangle_P)/\sqrt{2}$. If we realize a measurement on the program qubit in the basis $\{|\pm\rangle_P\}$, then the output state of the data qubit collapses into one of the two following states according to the result of the measurement:

$$|\psi_{\text{out}\pm}\rangle_D = \alpha|0\rangle_D \pm \beta e^{i\varphi}|1\rangle_D. \tag{2.6}$$

[2] Notice, that each of these kets represents a single photon in one of four modes (fibres).

If the measurement outcome is $|+\rangle_P$, then the unitary transformation $U(\varphi)$ is applied to the data qubit. If the outcome is $|-\rangle_P$, then $U(\varphi + \pi)$ is executed. Than the data-qubit state acquire an extra π phase shift. The corrective phase shift of $-\pi$ is applied via the food-forward loop PM. (However, in practice we apply a phase shift of π which is equivalent.) Subsequently, the final output state of the data qubit reads:

$$|\psi_{\text{out}}\rangle_D = \alpha|0\rangle_D + e^{i\varphi}\beta|1\rangle_D. \tag{2.7}$$

Experiment

Scheme of the experimental setup is shown in Fig. 2.1.

Photon pair: Pairs of photons are created by type-II collinear frequency-degenerate spontaneous parametric down conversion (SPDC) in a two-millimetre long BBO crystal pumped by a diode laser (Coherent Cube) at 405 nm [9,10] (it is not shown in the figure). Photons of each pair are separated by a polarizing beam splitter and coupled into single-mode fibres (780-HP). The same polarization states are set on both photons via fibre polarization controllers (PCs).

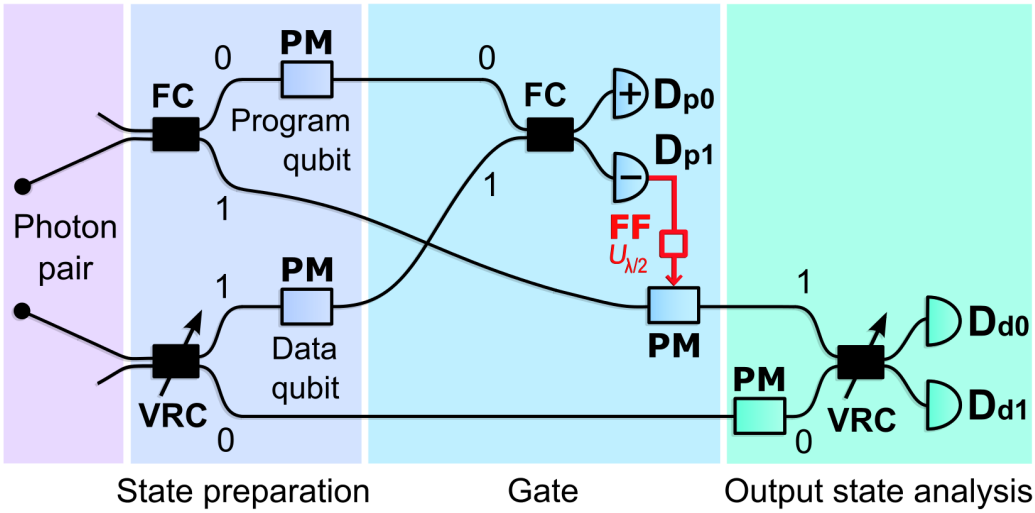

Figure 2.1: Scheme of the experimental implementation of the programmable quantum phase gate. FC – fibre coupler, VRC – variable ratio coupler, PM – phase modulator, FF – electro-optical feed-forward loop, D – detector.

State preparation: By means of fibre beam splitters and phase modulators (PMs), required input states of the program and data qubits are prepared. To prepare a program-qubit state $|\psi\rangle_P = (|0\rangle_P + e^{i\varphi}|1\rangle_P)/\sqrt{2}$ the balanced beam splitter with fixed splitting ratio 50:50 (FC) is used. An arbitrary state of the data qubit $|\psi_{\text{in}}\rangle_D = \alpha|0\rangle_D + \beta|1\rangle_D$ is prepared via the variable ratio coupler (VRC). All employed PMs are based on the linear electro-optic effect in lithium niobate. Their half-wave voltages are roughly 1.5 V. These PMs exhibit relatively high dispersion. Therefore, one PM is placed in each interferometer arm in order to compensate dispersion effects. The overall phase of a quantum state is irrelevant. It is equivalent to apply either a phase shift φ to $|1\rangle$ or $-\varphi$ to $|0\rangle$.

Gate: The gate itself consists of exchange of basis states of input qubits $|1\rangle_D$ and $|1\rangle_P$

(swap of two rails) and of the auxiliary measurement on the data qubit (see Fig. 2.1). The measurement in basis $\{|\pm\rangle_P\}$ is accomplished by a fibre coupler with fixed splitting ratio 50:50 and two single-photon detectors. Detectors D_{p0}, D_{d0}, and D_{d1} belong to a quad module SPCM-AQ4C (from PerkinElmer, with total efficiencies 50–60 %, dark counts 370–440 s^{-1}, response time 33–40 ns). A single module SPCM AQR-14FC is used as D_{p1}. It serves for the feed-forward operation, because of its faster response time (from PerkinElmer, total efficiency about 50 %, dark counts 180 s^{-1}, response time 17 ns, the output electric pulse FWHM = 30 ns, height approximately 2.5 V).

To implement the feed forward, the signal from detector D_{p1} is led to a passive voltage divider, in order to change the voltage level to the half-wave voltage level ($\sim$1.5 V). Then it is directly led to the PM to change the phase shift by π. Coaxial cables are as short as possible. The total delay is 33 ns, it includes a response time of the detector and feed-forward loop setting. To compensate this delay, photon wave-packets representing data qubits are retarded by additional fibre delay lines (6,6-m-long fibre in each interferometer arm). The timing of the feed-forward electric pulse and the photon arrivals to the PM are precisely tuned. The coherence time of photons created by our SPDC source is $\gtrsim 2$ ps.

Output state analysis: The right-most block in Fig. 2.1 enables us to measure the data qubit at the output of the gate in an arbitrary basis. These measurements are necessary for the gate performance evaluation.

The experimental setup is formed by two interconnected Mach-Zehnder interferometers (MZI). Total lengths of shorter MZI arms are $\sim$10.5 m (the upper interferometer in Fig. 2.1). The arms lengths of the longer MZI are $\sim$21.5 m (the lower interferometer in Fig. 2.1). To balance the arm lengths we use motorized air gaps with adjustable lengths. In MZI arms equipped with PMs without integrated polarizers we use air gaps also for placing bulk polarizers and wave plates. They select the proper polarization mode of PMs. To obtain high interference visibilities, the polarization states at the end of both interferometer arms must be the same. It is ensured by the PCs.

To reduce the effect of the phase drift caused by fluctuations of temperature and temperature gradients, we apply both passive and active stabilization. The experimental setup is covered by a shield minimizing air flux around components and both fibre delay-lines are coiled on an aluminium cylinder which is thermally isolated. Besides, an active stabilization[3] is performed after each three seconds of measurement. It is based on intensity measurements for phase shifts 0 and $\pi/2$. If necessary it calculates the phase compensation and applies corresponding corrective voltage to the phase modulator. This guarantees a precision of the phase setting during the measurement period better than $\pi/200$. For the stabilization purposes, we use the probe laser diode at 810 nm. To ensure the same spectral range, both the probe beam and SPDC generated photons pass through the same band-pass interference filter (spectral FWHM 2 nm, Andover). During active stabilization, the source is automatically switched from SPDC to the probe beam.

[3]This stabilization procedure is implemented into the MATLAB code by H. Fikerová.

Measurement

To fully characterize the programmable quantum phase gate, we perform the quantum process tomography [11]. To see the influence of the feed-forward loop, we performed the process tomography for both disconnected loop and active loop. We set various combinations of input states and output measurements. From the measured data, we reconstruct the process matrix χ.

For a fixed state of the program qubit, we used six different input states of the data qubit, namely $|0\rangle, |1\rangle, |\pm\rangle = (|0\rangle \pm |1\rangle)/\sqrt{2}$, and $|\pm i\rangle = (|0\rangle \pm i|1\rangle)/\sqrt{2}$. For each of these input states, the output state of the data qubit is measured in three different measurement basis, $\{|0\rangle, |1\rangle\}, \{|\pm\rangle\}$, and $\{|\pm i\rangle\}$. Each time we simultaneously measure two-photon coincidence count rates between detectors D_{p0} & D_{d0}, D_{p0} & D_{d1}, D_{p1} & D_{d0}, D_{p1} & D_{d1} in 12 three-second intervals. Unequal detector efficiencies are compensated by proper rescaling of measured coincidence counts. This procedure is repeated for 7 phase shifts encoded into the program qubit, $\varphi \in \{0, \pi/6, \pi/3, \pi/2, \pi 2/3, \pi 5/6, \pi\} = \{0°, 30°, 60°, 90°, 120°, 150°, 180°\}$. It is schematically shown in Fig 2.2.

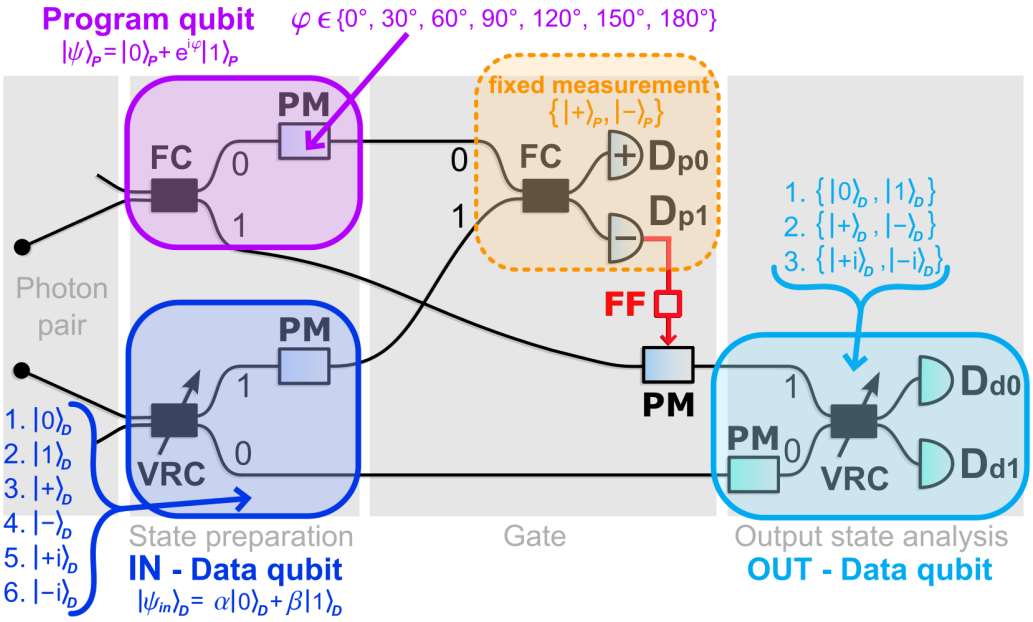

Figure 2.2: Block scheme of the tomographic measurement of the programmable phase gate with the feed-forward loop. FC – fibre coupler, VRC – variable ratio coupler, PM – phase modulator, FF – electro-optical feed-forward loop, D – detector.

Results

From the measured data, we reconstruct Choi matrices χ describing the function of the gate for several different phase shifts φ. We utilize the maximum likelihood estimation technique [12, 13]. In the upper part of Fig. 2.3 there are examples of reconstructed Choi matrices of the programmable phase gate for $\varphi = 0$, $\varphi = \pi/2$ and $\varphi = \pi$, respectively. For comparison, in the lower part of Fig. 2.3, there are examples of ideal Choi matrices of the gate for the same phases φ of the program qubit.

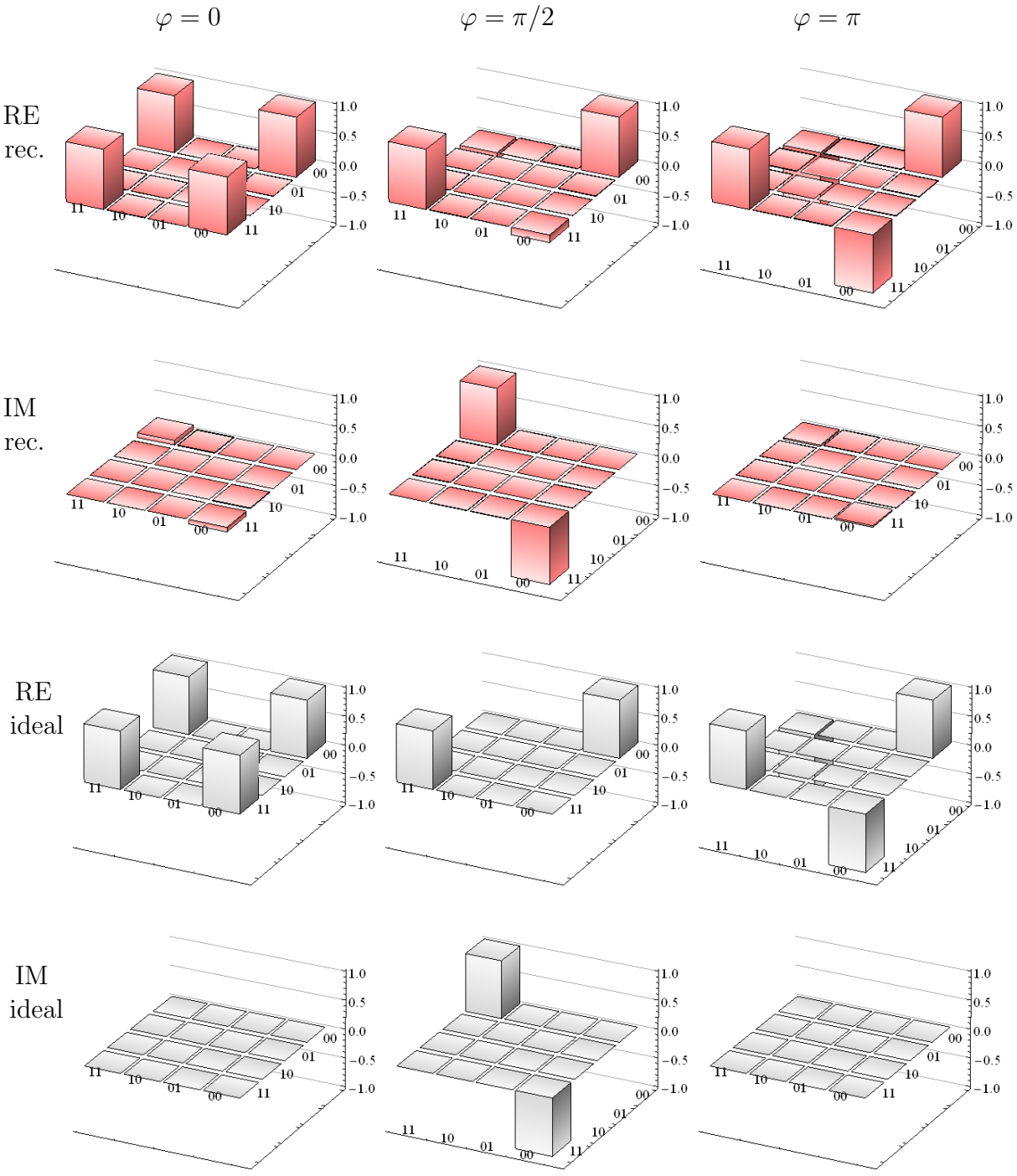

Figure 2.3: Choi matrices of the gate with active feed-forward loop. Upper Pink part – reconstructed process matrices, they real (imaginary) parts are displayed in the first (second) row. Lower Gray part – ideal process matrices, they real (imaginary) parts are displayed in the third (fourth) row. The left, middle and right columns display process matrices for $\varphi = 0$, $\varphi = \pi/2$ and $\varphi = \pi$ encoded into the program qubit, respectively.

To quantify the quality of gate operation we calculate the process fidelity. If χ_{id} is a one-dimensional projector, then the common definition of the process fidelity is

$$\mathcal{F}_\chi = \mathrm{Tr}[\chi\chi_{\mathrm{id}}]/(\mathrm{Tr}[\chi]\mathrm{Tr}[\chi_{\mathrm{id}}]). \tag{2.8}$$

Here, χ_{id} represents the ideal transformation of our gate. In particular,

$$\chi_{\mathrm{id}} = \sum_{i,j=0,1} |i\rangle\langle j| \otimes U|i\rangle\langle j|U^\dagger, \tag{2.9}$$

where U is the unitary operation (2.1) applied by the gate.

We have also reconstructed density matrices of data qubit output states corresponding to all input states. We calculate their fidelities and purities. The fidelity of output state ρ_{out} is defined as $\mathcal{F} = \langle\psi_{\mathrm{out}}|\rho_{\mathrm{out}}|\psi_{\mathrm{out}}\rangle$, where $|\psi_{\mathrm{out}}\rangle = U|\psi_{\mathrm{in}}\rangle$ with $|\psi_{\mathrm{in}}\rangle$ being the (pure) input state and $\rho_{\mathrm{out}} = \mathrm{Tr}_{\mathrm{in}}[\chi(\rho_{\mathrm{in}}^T \otimes I_{\mathrm{out}})]$ [4]. The purity of the output state is given as $\mathcal{P} = \mathrm{Tr}[\rho_{\mathrm{out}}^2]$. If the input state is pure, the output state is expected to be pure as well.

The left part of the Table 2.1 shows process fidelities for seven different phase shifts with active feed-forward loop. It also shows the average and minimal values of output state fidelities and average and minimal purities of output states. Fidelities and purities are averaged over six output states corresponding to six input states described above. Also minimum values are related to these sets of states. Statistical errors are estimated to be lower than 0.005 for process fidelities and lower than 0.01 for output-state fidelities and purities. Deviations of the experimental values from the ideal ones are mainly due to imperfections in splitting-ratio settings, phase fluctuations, polarization misalignment, and partial distinguishability of the photons in a pair.

To evaluate how the feed-forward affects the performance of the gate, we have also calculated process fidelities, output state fidelities and output state purities for the cases when the feed-forward is not active. It means, that we select only the situations when detector D_{p0} (corresponding to $|+\rangle_P$) clicked and no corrective action is needed (like in Ref. [7]). Coincidences are measured between detectors D_{p0} & D_{d0} and D_{p0} & D_{d1} only. The total coincidence rate (44 coincidences per second in average) is half in comparison with the sum of all conclusive-result rates in the case with active feed-forward (88 coincidences per second in average). Values of fidelities and purities are displayed in the right part of the Table 2.1. One can see that there is no substantial difference between the operation *with* feed-forward (success probability 50 %) and *without* feed-forward (success probability 25 %). In particular, the process fidelity in the case *with* feed forward, averaged over all 7 phases, $\mathcal{F}_\chi^{\mathrm{with}} = 0.976 \pm 0.003$ and the average process fidelity in the case *without* feed-forward $\mathcal{F}_\chi^{\mathrm{without}} = 0.979 \pm 0.005$. The process fidelity remains unchanged and moreover the gate success probability is doubled by the feed-forward loop.

[4] The input state is $\rho_{\mathrm{in}} = |\psi_{\mathrm{in}}\rangle\langle\psi_{\mathrm{in}}|$. $\mathrm{Tr}_{\mathrm{in}}$ is trace over input Hilbert space. T denotes transposition of matrix and I denotes identity operation.

	WITH feed-forward, $p_{\text{succ}} = 50\,\%$					WITHOUT feed-forward, $p_{\text{succ}} = 25\,\%$				
φ	$\mathcal{F}_\chi$	$\mathcal{F}_{\text{av}}$	$\mathcal{F}_{\text{min}}$	$\mathcal{P}_{\text{av}}$	$\mathcal{P}_{\text{min}}$	$\mathcal{F}_\chi$	$\mathcal{F}_{\text{av}}$	$\mathcal{F}_{\text{min}}$	$\mathcal{P}_{\text{av}}$	$\mathcal{P}_{\text{min}}$
0	0.976	0.985	0.970	0.974	0.947	0.977	0.985	0.973	0.975	0.953
$\pi/6$	0.977	0.986	0.972	0.975	0.951	0.975	0.985	0.972	0.973	0.949
$\pi/3$	0.977	0.985	0.970	0.975	0.943	0.988	0.989	0.971	0.980	0.946
$\pi/2$	0.974	0.983	0.973	0.975	0.953	0.979	0.986	0.976	0.976	0.957
$2\pi/3$	0.978	0.987	0.962	0.988	0.961	0.981	0.989	0.966	0.982	0.935
$5\pi/6$	0.972	0.981	0.953	0.974	0.944	0.974	0.984	0.961	0.976	0.947
π	0.980	0.987	0.975	0.977	0.961	0.979	0.986	0.977	0.978	0.960

Table 2.1: Process fidelities ($\mathcal{F}_\chi$), average ($\mathcal{F}_{\text{av}}$) and minimal ($\mathcal{F}_{\text{min}}$) output-state fidelities, average ($\mathcal{P}_{\text{av}}$) and minimal ($\mathcal{P}_{\text{min}}$) output-state purities for different phases (φ). The left part of the table shows the results *with* feed forward ($p_{\text{succ}} = 50\,\%$), while the right part of the table shows the results *without* feed forward ($p_{\text{succ}} = 25\,\%$).

Chapter 3

Carrying qubits with particles whose noninformational degrees of freedom are nonfactorable

This chapter is based on the following publication:

[2] Martina Miková, Helena Fikerová, Ivo Straka, Michal Mičuda, Miroslav Ježek, Miloslav Dušek, and Radim Filip. *Carrying qubits with particles whose noninformational degrees of freedom are nonfactorable.* Physical Review A **87**, 042327 (2013).

Basic idea

Here we experimentally investigate directly measurable parameter, D, quantifying effective indistinguishability of particles. This new measure can be used for an arbitrary quantum state of particles, in contrast to the commonly used overlap of quantum states, which is defined only for factorable states, for details see [2]. To show how distinguishability of particles used as information carriers affects quantum information processing we design a relatively simple linear-optical quantum-state-transfer protocol. It depends only on indistinguishability of particles, so we can exclude influence of other imperfections of resources. We consider the transfer of a state of a source qubit (S) to a target qubit (T). The qubits are represented by single-photons. The transfer is performed by a partial exchange of photons, optimal measurement on S, and conditional feed-forward correction on T. We show that fidelity of the transferred state depends directly on D. The parameter D not only quantifies the effective indistinguishability of particles but also determines an upper bound of quantum state transfer quality. We show that particles can serve as good carriers of qubits even if their internal degrees of freedom are entangled.

The suggested experimental layout follows the setup employed in previous publication [1]. This work [2], focused on the effective indistinguishability of particles quantifying by the measurable parameter, is also summarized by my colleague Helena in her Master's thesis [14].

Theory

Here we show only a few parts of theoretical results of [2], which are directly related to the experiment. The theory is work of my colleagues.

Let us have two particles, source S and target T, carrying the same qubit states (only certain degrees of freedom are used for encoding qubit states). Subsequently, let $\rho_{E,ST}$ denotes the state, not necessarily separable, of all other (inaccessible) degrees of freedom. Internal *environmental* E degrees of freedom can even be entangled with external environment. Clearly, these environmental degrees of freedom are responsible for distinguishability of particles. The theory of quantum information processing requires all resources to be in the same states which are decoupled from each other, in our notation $\rho_{E,ST} = \rho_{E,S} \otimes \rho_{E,T}$ (their total state must be factorable) and $\rho_{E,S} = \rho_{E,T}$ (environmental states of two spatially separated particles are indistinguishable). But these strict conditions are not always fulfilled in practice.

Let us define a measure $|D|$ quantifying a level of the effective indistinguishability of particles carrying qubits as a mean value of a flip operator:

$$D = \mathrm{Tr}\left[F\,\rho_{E,ST}\right], \tag{3.1}$$

where F is the flip operator acting on the joint environment of both particles, which exchange their basis states. The flip operator has two eigenvalues ± 1, thus $-1 \leq Tr[F\rho] \leq 1$, subsequently $0 \leq |D| \leq 1$.

To demonstrate the relevance of effective indistinguishability $|D|$, we have proposed and experimentally tested the simplest example of a quantum information transfer, where $|D|$ directly determines the quantum fidelity of the transferred state. It manifests a clear operational meaning of the above defined effective indistinguishability.

We consider only equatorial states of the source qubit S

$$|\Psi\rangle_S = (|0\rangle_S + e^{i\varphi}|1\rangle_S)/\sqrt{2}, \tag{3.2}$$

where phase φ may be unknown during the transfer. This state should be transferred to target qubit T represented by another single photon, which is in state

$$|\Phi\rangle_T = (|0\rangle_T + |1\rangle_T)/\sqrt{2} \tag{3.3}$$

at the beginning. In our case, basis states $|0\rangle$ and $|1\rangle$ correspond to the presence of the photon in the first or the second fibre, respectively. All other degrees of freedom, all physical differences between the particles, are described by a density matrix of the environmental state $\rho_{E,ST}$. So the overall initial state reads:

$$\rho_{\mathrm{ini}} = |\Psi\rangle_S\langle\Psi| \otimes |\Phi\rangle_T\langle\Phi| \otimes \rho_{E,ST}. \tag{3.4}$$

To avoid, an imperfect interaction between qubits (which can also limit the quality of the transfer) we consider implementation without any direct interaction. The transfer of the quantum state is performed by a partial exchange of the photons. Thus we swap two

rails between S and T see Fig. 3.1 and it swaps some of basis states. Then the optimal measurement on qubit S is performed, in the basis $\{|\pm\rangle_S\}$, where $|\pm\rangle_S = (|0\rangle_S \pm |1\rangle_S)/\sqrt{2}$. It is followed by conditional feed-forward correction on T, which corrects the phase shift of π (similarly like in previous *Chapter 2*). So we obtain the same output states of the target qubit for both outcomes $|+\rangle_S$ or $|-\rangle_S$ of the measurement on the source qubit.

The resulting output state of the target qubit is:

$$\rho_T = \frac{1+D}{2}|\Psi\rangle_S\langle\Psi| + \frac{1-D}{2}|\Psi^\perp\rangle_S\langle\Psi^\perp|, \tag{3.5}$$

where $|\Psi^\perp\rangle_S = (|0\rangle_S - e^{i\varphi}|1\rangle_S)/\sqrt{2}$ is the orthogonal complement to $|\Psi\rangle_S$. The output state ρ_T (3.5) corresponds to the original qubit state, $|\Psi\rangle_S$, disturbed by decoherence, with its off-diagonal elements (in the computation basis) reduced by factor D.

In the case when $|D| = 1$, resources behave in the same way as if they are factorable even if they actually are not. It means, they can be used for encoding of qubits even if some of their degrees of freedom are e.g. entangled. Thus the output target qubit is the same state as the source qubit.

$$|\Theta\rangle_T = (|0\rangle_T + e^{i\varphi}|1\rangle_T)/\sqrt{2} \equiv |\Psi\rangle_S. \tag{3.6}$$

Experimental quantum information processing and transfer often use photonic qubits [15,16] encoded into photons generated by spontaneous parametric down-conversion (SPDC). These photons represent a typical example of qubit carriers with internal degrees of freedom which may exhibit complex behaviour [17, 18]. The information is usually encoded into polarization or spatial degrees of freedom but frequency degrees of freedom are entangled. Thus parameter $|D|$ quantifies effective indistinguishability of resources for quantum information processing.

It can be shown by calculations [2] that the measured coincidence rate is:

$$R(\Delta t) \propto 1 - D \tag{3.7}$$

The parameter D is obtained as:

$$D = 1 - R_{\text{rel}}, \tag{3.8}$$

where R_{rel} is normalized coincidence rate with respect to coincidence rate R_{out} measured far from the HOM dip position, where the particles are completely distinguishable,

$$R_{\text{rel}} = R(\Delta t)/R_{\text{out}}. \tag{3.9}$$

In this experiment qubits are encoded into spatial modes. Thus the role of the "environment" is played by frequency degrees of freedom. Parameter D can be really measured only by means of a beam splitter and coincidence detection. It can be varied by changing delay Δt between the two photons. Its negative values correspond to partially entangled states containing vectors from anti-symmetric subspace.

If generated photons have a frequency spectrum with rectangular shape, with FWHM=v and central frequency $\omega_0/2$ then $D = \text{sinc}(\Delta t\, v)$.

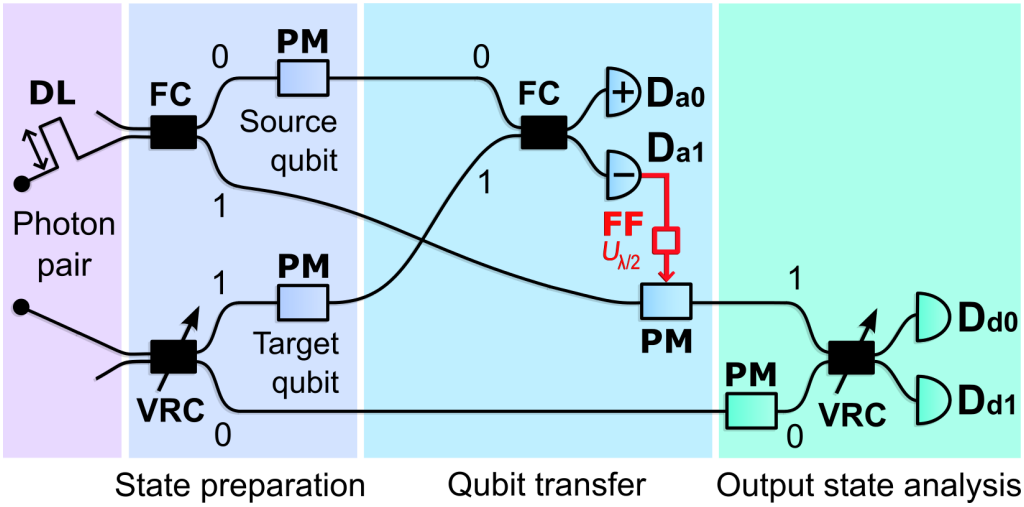

Figure 3.1: Scheme of the experiment implementation of the qubit state transfer protocol. DL – delay line, FC – fibre couplers, VRC – variable ratio couplers, PM – phase modulators, FF – feed-forward loop, D – detectors. The couplers and PMs in the *State preparation* stage enable us to prepare required qubit states (each qubit is represented by a single photon which may propagate in two optical fibres). In *Qubit transfer* stage, the two rails are swapped and the auxiliary measurement on the source qubit is performed. The middle PM applies conditional phase shift depending on the measurement result. The PM is a part of the feed-forward loop and also the part of the protocol. *Output state analysis* stage consists of PM and VRC, which serve for output state tomography.

Experiment

Our setup is depicted in Fig. 3.1. Photon pairs are created by collinear frequency-degenerate type-II SPDC in a BBO crystal pumped at 405 nm. Both photons pass through the same band-pass interference filter of *approximately* rectangular shape with central frequency 810 m and spectral width (FWHM) 2.7 nm. Then they are separated by a polarizing beam splitter and coupled into single-mode fibres. One of the photons is retarded by Δt in a delay line (DL) with adjustable length. By means of polarization controllers both photons are set to have the same polarization states. Qubit states are encoded into spatial modes of individual photons. Each basis state corresponds to a single photon in one, $|0\rangle$, or in another, $|1\rangle$, of two optical fibres. Initial equatorial states of both qubits are prepared using fibre couplers (FC and VRC) with splitting ratio 50:50 and integrated electro-optical phase modulators (PMs). The source qubit is in the "unknown" equatorial state (3.2) and the target qubit is in initial state (3.3).

The key part of our device is the swap of two rails between source qubits and target qubit followed by measurement on the source qubit. This measurement is performed in basis $(|0\rangle \pm |1\rangle)/\sqrt{2}$ using a FC with fixed splitting ratio 50:50 and two single photon detectors. When detector D_{a1} clicks, phase correction π is applied on the target qubit by means of feed-forward loop. The feed-forward uses a direct electric signal from detector D_{a1}. The electric signal is modified by a passive voltage divider to circa 1.5 V and then it is led to the PM (1.5 V corresponds to the phase shift of π). Output states of target qubit are characterized by quantum tomography. Different measurement bases are set by a PM

and VRC. Photons are counted by detectors D_{d0} and D_{d1}. Small differences in detector efficiencies are corrected numerically in data sets.

The whole experimental setup consists of two interconnected Mach-Zehnder interferometers. Lengths of their arms are balanced by motorized air gaps (not shown in the figure). To reduce a phase drift caused by environmental influences, like air convection and temperature fluctuations, the whole setup is covered and actively stabilized. After each 3 s period of measurement the phase drifts are determined and compensated by adding a proper correcting voltage on the PMs. The HOM dip [19], which we use for characterization of input photons properties, is measured at the output VRC.

Measurements

The target qubit is prepared in state (3.3) and the source qubit is prepared in state (3.2) with phase $\varphi = 0°, 30°, 60°, 90°, 120°, 150°, 180°$, in sequence. On the output we perform measurement on the target qubit in three different bases: $\{|0\rangle, |1\rangle\}$, $\{(|0\rangle \pm |1\rangle)/\sqrt{2}\}$, and $\{(|0\rangle \pm i|1\rangle)/\sqrt{2}\}$, for each setting of input states. Each measurement consists of 15 three-second measurement intervals interlaced by active stabilization. During the measurement, the coincidences between detectors D_{a0} & D_{d0}, D_{a0} & D_{d1}, D_{a1} & D_{d0}, and D_{a1} & D_{d1} are accumulated. Each such measurement set is repeated 16 times with different delays Δt between the input photons. It corresponds to 16 different positions in HOM dip. The measurement is depicted in block scheme in Fig. 3.2.

To evaluate the parameter D, we measure the coincidence rate $R(\Delta t)$ between detectors D_{d0} & D_{d1}, in each of these 16 positions in the HOM dip. Once, we measure separately this coincidences in position far from the dip to obtain R_{out}.

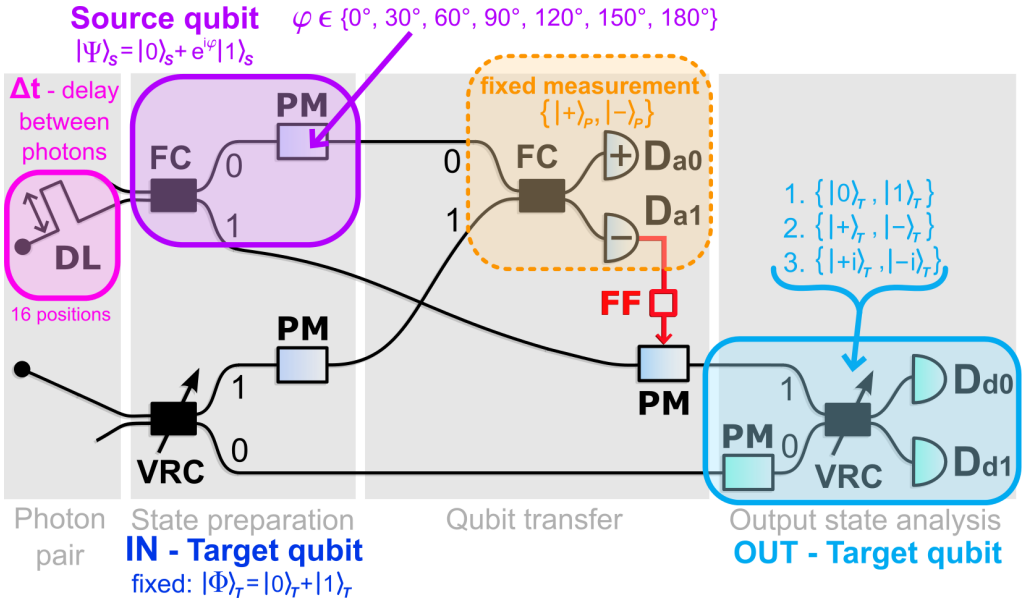

Figure 3.2: Block scheme of the final measurement of the qubit state transfer protocol. FC – fire coupler, VRC – variable ratio coupler, PM – phase modulator, FF – electro-optical feed-forward loop, D – detector, DL – delay line.

Results

The measured results are used to reconstruct output density matrices, ρ_T^{rec}, by means of maximum-likelihood quantum tomography [12,13,20]. Reconstruction of density matrices enable us to calculate various quantities including purity and overlap with corresponding input states.

For each position in HOM dip, corresponding to certain delay Δt, we evaluate parameter $D = 1 - R_{\mathrm{rel}}$. R_{rel} is the normalized coincidence rate $R(\Delta t)$ between detectors D_{d0} & D_{d1} with respect to the coincidence rate measured far from the dip, R_{out} It is obtained as $R_{\mathrm{rel}} = R(\Delta t)/R_{\mathrm{out}}$.

Negative values of D correspond to the positions in the raised "shoulders" of the HOM dip, as it is shown in the inset in the bottom right corner in Fig. 3.3. They reveal that "environments" of our photons are entangled. The values of $\langle\Psi|_S\,\rho_T|\Psi\rangle_S$ lower than 0.5 mean that roles of states $|\Psi\rangle_S$ and $|\Psi^{\perp}\rangle_S$ are swapped (see Eq. 3.5).

According to the theory, overlap $\langle\Psi|_S\,\rho_T|\Psi\rangle_S = \frac{1+D}{2}$ and eigenvalues of ρ_T are $\frac{1+D}{2}$ and $\frac{1-D}{2}$, see Eq. (3.5). Fig. 3.3 shows the overlap and the maximal eigenvalue as functions of parameter D. Each point represents an average over all seven phases φ. Vertical error bars visualize standard deviations obtained from ensembles of measurements with different phases. Due to various experimental imperfections (phase fluctuations, drift of splitting ratios, etc.) they are greater than standard deviations calculated purely from Poissonian photo-count distribution. But on the graph they are mostly smaller than the size of symbols. Horizontal error bars reflect (Poissonian) statistical fluctuations of coincidence rates $R(\Delta t)$ and R_{out}. Average output state fidelity, $[\mathrm{Tr}(\sqrt{\sqrt{\rho_T}\rho_T^{\mathrm{rec}}\sqrt{\rho_T}})]^2$, (averaged over all phases and all delays) was 99.2 ± 0.8 %. The measured HOM dip is shown in the lower right inset of Fig. 3.3. Relative measurement error is less than 6 % in its minimum and less than 2 % for maximal values. Dip visibility is 96.4 ± 0.4 %.

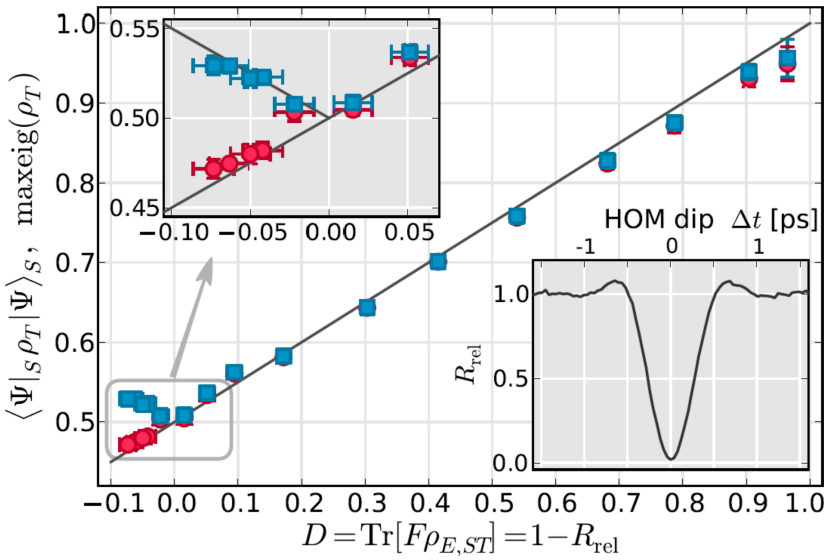

Figure 3.3: Dependence of the quality of qubit-state transfer on the parameter D. Red circles denote the overlap of output and input states, $\langle\Psi|_S\,\rho_T\,|\Psi\rangle_S$. Blue squares denote maximal eigenvalues of output states ρ_T. Straight lines are theoretical predictions. The upper left inset magnifies the area where D is close to zero. The lower right inset shows the measured Hong-Ou-Mandel dip, R_{rel} denotes relative (normalized) coincidence rate.[5]

[5]This graph is originally plotted by M. Dušek.

Chapter 4

Experimental implementation of perfect quantum reading of beam splitters

This chapter is based on the following publication:

[3] Michele Dall'Arno, Alessandro Bisio, Giacomo Mauro D'Ariano, Martina Miková, Miroslav Ježek, and Miloslav Dušek. *Experimental implementation of unambiguous quantum reading.* Physical Review A **85**, 012308 (2012).

Basic idea

The next experiment implements unambiguous reading of optical memories using the smallest possible amount of energy. The information is stored as a reflectivity of the memory cell. The experimentalist challenge is to built theoretically suggested device [3] which can perfectly and unambiguously distinguish two different memory records.

In the experiment, the memory cell is represented by a beam splitter. Two different reflectivities of the beam splitter determine two memory records represented by two devices, I and U. Our aim is to discriminate between these two devices. It corresponds to reading of the memory record.

During the measurement process, a superposition of a single photon and vacuum enters the unknown device (I or U). Thus the unknown device is in average exposed just to the fraction of single-photon energy. The experimental results confirm the feasibility of quantum reading.

Theory

The comprehensive theoretical background of ambiguous, unambiguous, and perfect quantum reading is described in [3]. The theoretical part of this paper is work of our Italian colleagues. Here we show only a part of the theory, directly related to our experiment.

One can be interested in discrimination between two unitary operations described by unitary matrices U_1 and U_2, where $U_1 \neq U_2$. These matrices can be written as $U_1 = W^\dagger I W$ and $U_2 = W^\dagger U W$, where I represents identity operation and W is a unitary matrix. Thus discrimination between two general operations U_1 and U_2 is unitary-equivalent to discrimination between I and U. The special case of such unitary operation U is the action of a beam splitter. Reflectivity of such beam splitter may convincingly represent an optical memory record.

Let us call our two devices I and U according to the performed unitary operations. Our aim is to discriminate between these two devices.

Device U is depicted in scheme (4.1). It is realized by a beam splitter V, with reflectivity R_V, and phase shifters acting on each input and output mode. But, in our experimental realization, two $-\pi/2$ phase shifters on mode 1 are irrelevant and they can be discarded. It is because the input mode 1 acts on a vacuum state and the output mode 1 is immediately followed by a photo-detector. Without loss of generality, we can also apply a cumulative phase shift of π on input mode 2 in front of beam splitter V. So we can redefine device U as follows:

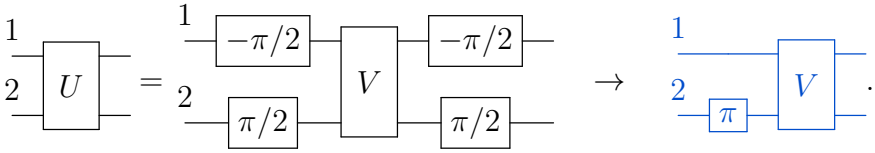

(4.1)

Device I makes the identity operation. It is represented by a beam splitter with unit reflectivity without any additional phase shifts:

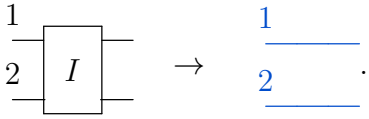

(4.2)

The theoretical scheme for perfect quantum reading is experimentally feasible with present quantum optical technology. The general setup consists of an MZI with beam splitters B and $B^\dagger$, acting on modes 2 and 3, see scheme (4.3). An additional beam splitter, representing the unknown device, is inserted in the MZI arm corresponding to mode 2. During the measurement procedure the unknown device is randomly chosen from the set $\{I, U\}$ with equal prior probabilities. The optimal strategy for quantum reading i.e., the optimal discrimination between these two devices (beam splitters with different reflectivities) is described by the following scheme where $\Pi_U, \Pi_{U'}$ and Π_I denote photo-counters:

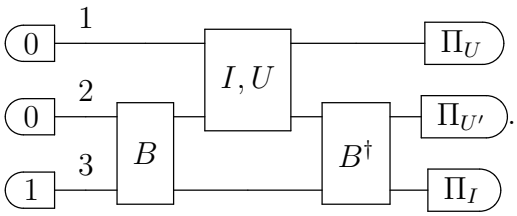

(4.3)

In our experimental setup, the unknown device is realized by a fibre beam splitter with a variable splitting ratio, VRC-mid. The device U is represented by $R_V \neq 1$ plus a cumulative phase of π.

To provide optimal discrimination the reflectivity and transmissivity of beam splitters B must be given as:

$$R_B = \frac{\sqrt{R_V}}{1+\sqrt{R_V}}, \qquad T_B = \frac{1}{1+\sqrt{R_V}}. \tag{4.4}$$

The optimal measurement for perfect discrimination is implemented by three photocounters Π_U, $\Pi_{U'}$, and Π_I. The conditional probabilities $p_{X|Y}$ of photon detection by the detector Π_X $(X = U, U', I)$ given that the unknown device is Y $(Y = U, I)$ read:

$$p_{U|U} = 1 - \sqrt{R_V}, \qquad p_{U'|U} = \sqrt{R_V}, \qquad p_{I|I} = 1, \qquad p_{I|U} = p_{U|I} = p_{U'|I} = 0 \tag{4.5}$$

Detecting a photon by the detector Π_U or $\Pi_{U'}$ implies that the unknown device is U. While a photon detection by the detector Π_I implies that the unknown device is I.

Experiment & Measurement

To demonstrate experimental feasibility of quantum reading we have built a laboratory setup, shown in Fig. 4.1, for perfect discrimination of two beam splitters according to scheme (4.3). It consists of a Mach-Zehnder interferometer (MZI) with an additional beam splitter VRC-mid in its upper arm. The beam splitter has a variable splitting ratio and it serves as the unknown device which has to be discriminated.

We use a heralded single photon source based on spontaneous parametric down conversion (SPDC). Namely, we employ a collinear frequency-degenerate SPDC process with type-II phase matching in a 2 mm-long BBO crystal pumped by a cw laser diode (Coherent Cube) at 405 nm. In this process pairs of photons at 810 nm are created. Photons from each pair are separated by a polarizing beam splitter and coupled into single-mode optical fibres. One of them is led directly to a trigger single-photon detector D_T (PerkinElmer SPCM AQR-14FC) which heralds the creation of a pair. The second photon enters MZI through a variable ratio coupler VRC-in.

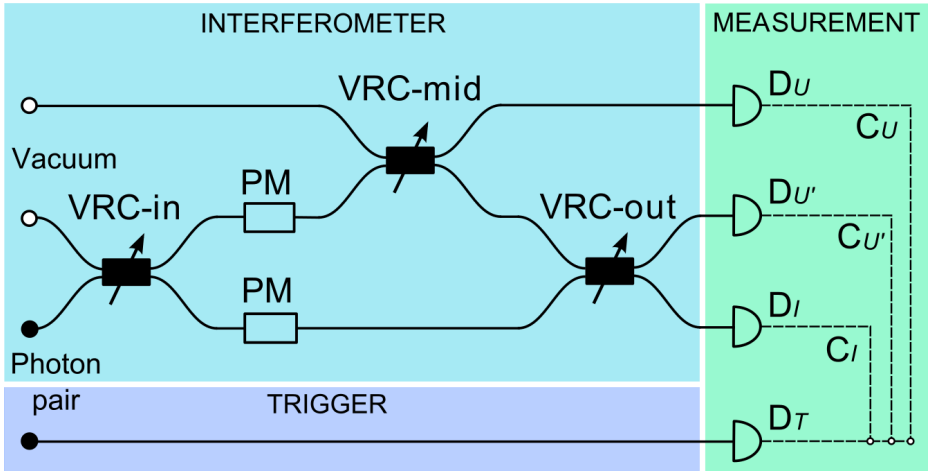

Figure 4.1: Scheme of the experimental implementation of perfect quantum reading. VRC – variable ratio coupler, PM – phase modulator, D – detector, C – coincidence rate.

An additional variable ratio coupler, VRC-mid, represents the unknown device. When its reflectivity equals one, $R_V = 1$, it corresponds to device I. To switch to device U one has to set a required splitting ratio, $R_V \neq 1$, and apply additional phase shift of π, see scheme (4.1). In the experiment phase shifts are introduced by electro-optical phase modulators (PMs). Their half-wave voltages are ∼1.5 V. These phase modulators exhibit relatively high dispersion. Therefore one PM is placed in each interferometer arm in order to compensate dispersion effects. In case of a device U we use the PM in the upper interferometer arm to apply the additional phase shift of π.

Output fibres from the interferometer and from the unknown device are connected to single-photon detectors D_U, $\mathrm{D}_{U'}$, and D_I. These detectors are parts of Perkin-Elmer quad module SPCM-AQ4C.

To reduce the effect of the phase drift caused by air convection, fluctuations of temperature, and temperature gradients, we apply both passive and active stabilization. The experimental setup is covered by a shield minimizing air flux around the components. Besides, after each three seconds of measurement an active phase stabilization of MZI is performed. The stabilization procedure[6] measures intensity for a phase shift of $\pi/2$ and if necessary it calculates phase compensation and applies corrective voltage to the phase modulator in the lower interferometer arm. These results are in the precision of the phase setting during the measurement period better than $\pi/200$.

For each pair of devices U and I the proper splitting ratio of fibre couplers VRC-in and VRC-out must be set to discriminate these devices optimally. Thus the MZI beam splitters B, VRC-in and VRC-out, are set for relevant R_V according to eq. (4.4). We perform measurement for 11 different devices U with intensity reflectivities $0, 0.1, 0.2, \ldots, 1$. For each pair of devices U and I the counts at detectors D_U, $\mathrm{D}_{U'}$, and D_I are cumulated

[6]The stabilization procedure employed in this experiment is implemented into the MATLAB code by H. Fikerová, within her Bachelor's [21] and Master's [14] thesis.

during 30 three-second measurement intervals interlaced by stabilization procedures. All measurements are done in coincidence with the trigger detector D_T. It means we measure coincidence counts $C_U, C_{U'}, C_I$ between detectors $D_T \,\&\, D_U$, $D_T \,\&\, D_{U'}$, and $D_T \,\&\, D_I$, respectively, using 3 ns coincidence time window. These results are normalized to obtain relative frequencies, $f_j = C_j/(C_U + C_{U'} + C_I)$, where $j = U, U', I$. Because, relative frequencies can be directly compared with theoretical probabilities of photon detection.

Results

The final experimental results provided for the perfect quantum reading of devices U and I are depicted below. Measured relative frequencies and theoretical probabilities are listed in Table 4.1 and shown in Figure 4.2. The left parts of the table 4.1 and Fig. 4.2 summarize the results for devices U, while the right parts of the table 4.1 and Fig. 4.2 show the results obtained with device I inserted. Each row in the table corresponds to one pair of U and I with R_V being the reflectivity of a device U. It corresponds to different MZI settings and alignments.

One can observe very good agreement between the theory and the experiment. Small discrepancies appear mainly due to imperfections in splitting-ratio settings, phase fluctuations, and polarization misalignment. In coincidence measurements the contribution of detector noise is completely negligible and error bars are smaller than symbols in the figure 4.2.

The advantage of the implemented setup is that in an ideal case there is one photon in the output ports. It makes detection relatively easy. Nevertheless, it is still a superposition of a single photon and vacuum what is entering the unknown device. So the unknown device is exposed just to a fraction of energy of a single photon in average. Even if the overall success probability of the setup is relatively low because of technological losses, we were able to measure precisely the relative probabilities of all outputs and our experiment convincingly validate the theoretical predictions.

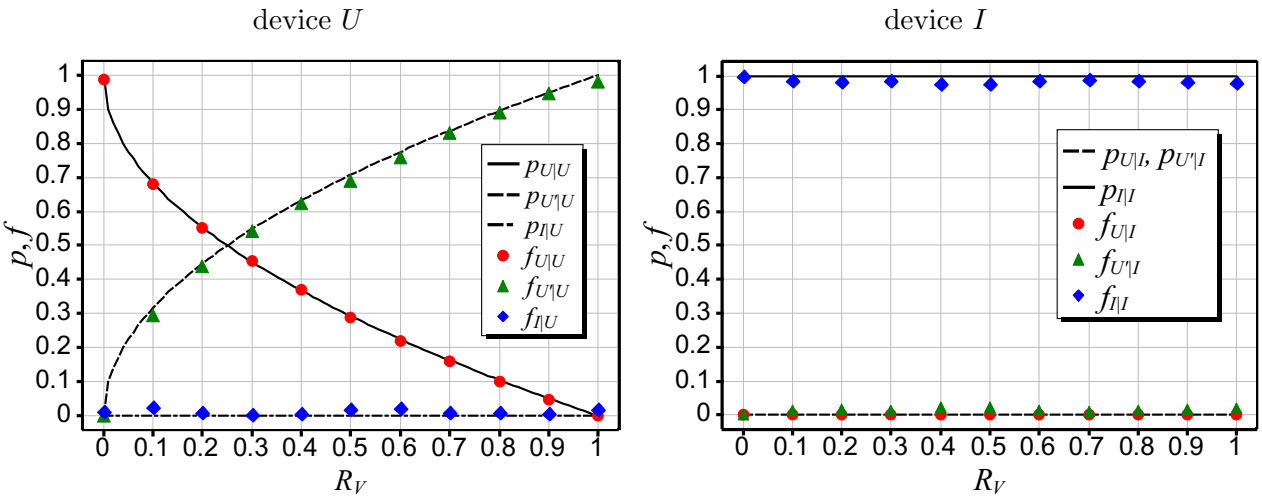

Figure 4.2: Results for devices U and I are shown in left and right graph, respectively. Detection probabilities and measured relative frequencies are plotted as a functions of the reflectivity R_V of VRC-mid. Where different reflectivities R_V of VRC-mid correspond to different devices U and to appropriate settings of MZI. [7]

	device U						device I					
	theory			experiment			theory			experiment		
R_V	$p_{U\|U}$	$p_{U'\|U}$	$p_{I\|U}$	$f_{U\|U}$	$f_{U'\|U}$	$f_{I\|U}$	$p_{U\|I}$	$p_{U'\|I}$	$p_{I\|I}$	$f_{U\|I}$	$f_{U'\|I}$	$f_{I\|I}$
0.0	1.000	0.000	0	0.986	0.000	0.014	0	0	1	0.000	0.002	0.998
0.1	0.684	0.316	0	0.680	0.295	0.025	0	0	1	0.000	0.012	0.988
0.2	0.553	0.447	0	0.551	0.440	0.009	0	0	1	0.000	0.018	0.982
0.3	0.452	0.548	0	0.455	0.542	0.003	0	0	1	0.000	0.012	0.988
0.4	0.368	0.633	0	0.369	0.623	0.008	0	0	1	0.000	0.023	0.977
0.5	0.293	0.707	0	0.288	0.691	0.021	0	0	1	0.000	0.022	0.978
0.6	0.225	0.775	0	0.219	0.758	0.022	0	0	1	0.000	0.014	0.986
0.7	0.163	0.837	0	0.160	0.830	0.010	0	0	1	0.000	0.011	0.989
0.8	0.106	0.894	0	0.100	0.891	0.009	0	0	1	0.000	0.013	0.987
0.9	0.051	0.949	0	0.046	0.946	0.007	0	0	1	0.000	0.018	0.982
1.0	0.000	1.000	0	0.000	0.980	0.020	0	0	1	0.000	0.021	0.979

Table 4.1: Results for devices U and I are summarized in left and right part of the table, respectively. R_V – reflectivity of VRC-mid in device U. **Device** U inserted in the MZI: $p_{U|U}, p_{U'|U}, p_{I|U}$ – theoretical probabilities of photon detection at detectors D_U, $\mathrm{D}_{U'}$, D_I, respectively, $f_{U|U}, f_{U'|U}, f_{I|U}$ – relative frequencies measured at detectors D_U, $\mathrm{D}_{U'}$, D_I, respectively (measured in coincidence with D_T). **Device** I inserted inside the MZI: $p_{U|I}, p_{U'|I}, p_{I|I}$ – theoretical probabilities of photon detection at detectors D_U, $\mathrm{D}_{U'}$, D_I, respectively, $f_{U|I}, f_{U'|I}, f_{I|I}$ – relative frequencies measured at detectors D_U, $\mathrm{D}_{U'}$, D_I, respectively (measured in coincidence with D_T).

[7] These graphs were originally plotted by M. Dušek.

Chapter 5

Optimal entanglement-assisted discrimination of quantum measurements

This chapter is based on the following publication:

[4] Martina Miková, Michal Sedlák, Ivo Straka, Michal Mičuda, Mário Ziman, Miroslav Ježek, Miloslav Dušek, and Jaromír Fiurášek. *Optimal entanglement-assisted discrimination of quantum measurements.* Physical Review A **90**, 022317 (2014).

Basic idea

In this chapter we experimentally investigate optimal discrimination between two projective single-qubit measurements $\mathcal{M}$ and $\mathcal{N}$ in a scenario where the measurement can be performed only once [4]. We consider general discrimination strategies[8] involving a certain fraction of inconclusive outcomes, P_I. It is shown that the optimal discrimination procedure requires entangled probe state for any nonzero rate of inconclusive outcomes $P_I > 0$. Due to various experimental imperfections, it is necessary to include also additional erroneous conclusive results. Therefore we consider general discrimination scheme where we maximize success probability P_S, hence minimize P_E, for a fixed fraction of P_I; $P_S + P_I + P_E = 1$. We experimentally implement this optimal discrimination strategy for projective measurements on polarization states of single photons. Our setup is based on linear optics, polarization maintaining fibre interferometers, and single-photon detectors. The setup involves the real-time electro-optical feed-forward loop which allows us to fully harness the benefits of entanglement in discrimination of quantum measurements. The experimental data unequivocally confirm the advantage of entanglement-based discrimination strategy as compared to our benchmark, provide by optimal discrimination schemes using single-qubit probes without any entanglement.

[8] Where inconclusive results P_I and conclusive erroneous results P_E are in general nonzero.

Theory

The theory in [4] is a work of my colleagues. Therefore, below is described only the part of the theory directly related to the experiment. For more details regarding for example the protocol optimality, please see the paper.

Optimal entanglement-assisted discrimination

The measurement bases $\mathcal{M}$ and $\mathcal{N}$ are illustrated in Fig. 5.1(a). Without loss of generality, the projectors specifying the measurements can be parametrized by a single angle θ,

$$\begin{aligned} M_0 &= |\phi\rangle\langle\phi|, & M_1 &= |\phi^\perp\rangle\langle\phi^\perp|, \\ N_0 &= |\psi\rangle\langle\psi|, & N_1 &= |\psi^\perp\rangle\langle\psi^\perp|, \end{aligned} \tag{5.1}$$

where

$$\begin{aligned} |\phi\rangle &= \cos\theta|0\rangle + \sin\theta|1\rangle, & |\phi^\perp\rangle &= \sin\theta|0\rangle - \cos\theta|1\rangle, \\ |\psi\rangle &= \cos\theta|0\rangle - \sin\theta|1\rangle, & |\psi^\perp\rangle &= \sin\theta|0\rangle + \cos\theta|1\rangle, \end{aligned} \tag{5.2}$$

and $0 \leq \theta \leq \frac{\pi}{4}$. The most general discrimination strategy is depicted in Fig. 5.1(b). A two-qubit entangled state $|\Psi\rangle_{\mathrm{I,II}}$ is employed. The measurement that should be identified is performed on qubit I, and the measurement outcome (0 or 1) specifies which measurement is then performed on qubit II.

In what follows, we assume equal a-priori probabilities of these two measurements. In such a case, as it is shown in [4], it is optimal to employ a maximally entangled singlet Bell state $|\Psi^-\rangle = (|01\rangle - |10\rangle)/\sqrt{2}$. If we observe measurement outcome 0 on qubit I, then qubit II is prepared in state $|\phi^\perp\rangle$ or $|\psi^\perp\rangle$. Similarly, outcome 1 heralds that qubit II is prepared in state $|\phi\rangle$ or $|\psi\rangle$. Since

$$|\phi\rangle = -\sigma_Y|\phi^\perp\rangle, \quad |\psi\rangle = \sigma_Y|\psi^\perp\rangle, \tag{5.3}$$

we can apply the unitary operation $\sigma_Y = |0\rangle\langle 1| - |1\rangle\langle 0|$ to qubit II when the measurement outcome on qubit I reads 0. Thus in this way the discrimination task of two quantum measurements is converted to discrimination of two fixed non-orthogonal quantum states $|\phi\rangle$ and $|\psi\rangle$.

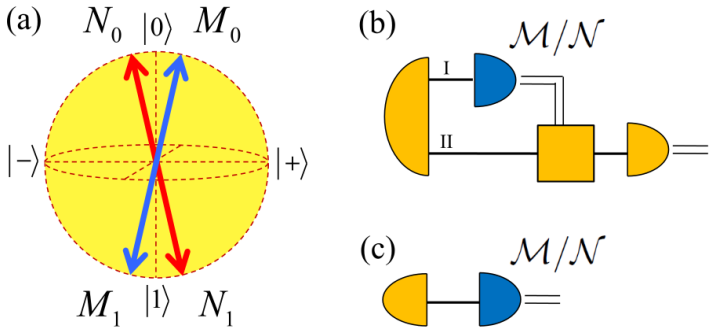

Figure 5.1: (a) Single-qubit measurements $\mathcal{M}$ and $\mathcal{N}$ on a Bloch sphere. (b) General measurement discrimination scheme involving entangled probe state. (c) Simple discrimination scheme with single-qubit probe. [9]

[9] These schemes were originally plotted by M. Sedlák.

As shown by Ivanovic, Dieks, and Peres (IDP) [22–24], perfect error-free ($P_E = 0$) discrimination between $|\phi\rangle$ and $|\psi\rangle$ is possible if we allow for a certain probability of inconclusive outcomes $P_I = |\langle\psi|\phi\rangle|$. Explicitly, we have

$$P_I = P_I^{\text{unambig}} = \cos(2\theta). \tag{5.4}$$

Unambiguous discrimination requires a generalized 3-component POVM which can be interpreted as a quantum filtering followed by a projective measurement on the filtered state. The required filter has the form $F = \tan\theta|0\rangle\langle 0| + |1\rangle\langle 1|$ and the filtered states become orthogonal, $F|\phi\rangle = \sqrt{2}\sin\theta|+\rangle$, and $F|\psi\rangle = \sqrt{2}\sin\theta|-\rangle$, where $|\pm\rangle = (|0\rangle \pm |1\rangle)/\sqrt{2}$. The square of the norm of the filtered states is equal to the success probability of unambiguous discrimination,

$$P_S = P_S^{\text{unambig}} = 2\sin^2\theta, \tag{5.5}$$

and $P_S + P_I = 1$. Due to various experimental imperfections, we will in practice encounter also the erroneous conclusive results occurring with probability P_E. This motivates us to consider a general discrimination scheme where we maximize P_S, hence minimize P_E, for a fixed fraction of inconclusive outcomes P_I. The optimal filter then reads $F = f|0\rangle\langle 0| + |1\rangle\langle 1|$, where $f = \sqrt{1 - P_I/\cos^2\theta}$, and a projective measurement in basis $|\pm\rangle$ should be performed after successful filtration similarly as before. This intermediate strategy optimally interpolates between IDP [22–24] and Helstrom [25] schemes, and we get [26, 27]

$$P_S = \frac{1}{2}\left(1 - P_I + \sin(2\theta)\sqrt{1 - \frac{P_I}{\cos^2\theta}}\right). \tag{5.6}$$

It is convenient to consider also a relative probability of successful discrimination for the subset of conclusive outcomes,

$$\tilde{P}_S = P_S/(1 - P_I). \tag{5.7}$$

The probability $\tilde{P}_S$ increases with P_I and $\tilde{P}_S = 1$ when $P_I = \cos(2\theta)$.

The optimality of the above protocol is proved by my colleagues in [4] with the help of the formalism of process POVM [28, 29]. They show that the optimization of discrimination of two projective qubit measurements becomes equivalent to optimization of the discrimination of two quantum states $|\phi\rangle$ and $|\psi\rangle$ by a 3-component POVM.

Optimal discrimination with single-qubit probes

To elucidate the importance of the entanglement state in the task of discrimination measurement, we provide a benchmark for the realized experiment. We determine the optimal discrimination strategy with unentangled single-qubit probes, see Fig. 5.1(c). In this case one has to guess $\mathcal{M}$ or $\mathcal{N}$ solely based on the measurement outcome on the probe qubit. For more details about the optimal single-qubit discrimination strategy, see [4]. Here we show only the result, which is used as the "classical" bound in Fig. 5.4. There, it is depicted by dashed lines for 7 different angles θ determining 7 different pairs of the measurement basis $\mathcal{M}$ and $\mathcal{N}$.

The optimal discrimination strategy is different for $P_I < P_{I,T}$ and $P_I \geq P_{I,T}$. The transition point $P_{I,T}$ is obtained as a result of optimization procedure. Then the overall success probability reads:

If $P_I \geq P_{I,T}$, the success probability is:

$$P_S = \frac{1}{2}(1 - P_I) + \frac{1}{4}\sin(2\theta)\sqrt{1 - \frac{(1-2P_I)^2}{\cos^2(2\theta)}}. \tag{5.8}$$

If $P_I < P_{I,T}$, then the success probability is:

$$P_S = \left(1 - \frac{P_I}{P_{I,T}}\right) P_{S,0} + \frac{P_I}{P_{I,T}} P_{S,T}. \tag{5.9}$$

Where:
$P_{I,T} = [1 + 3\cos^2(2\theta) + 2\cos^2(2\theta)\sqrt{1 + 3\cos^2(2\theta)}]/[2(1 + 4\cos^2(2\theta))]$,
$P_{S,0} = [1 + \sin(2\theta)]/2$,
$P_{S,T}$ is given by equation 5.8 where P_I is replaced with $P_{I,T}$, thus
$P_{S,T} = (1 - P_{I,T})/2 + \sin(2\theta)\sqrt{1 - (1 - 2P_{I,T})^2/\cos^2(2\theta)}/4$.

To compare it with the previous case of optimal entanglement-assisted discrimination, we consider also the relative probability of successful discrimination for the subset of conclusive outcomes $\tilde{P}_S$, given by equation (5.7).

For unambiguous discrimination ($P_E = 0$) with a single-qubit probe the success probability is given as $P_S^{\text{unambig}} = [1 - \cos^2(2\theta)]/2$, and $P_I^{\text{unambig}} = [1 + \cos^2(2\theta)]/2$.

Experiment

Our experimental demonstration of entanglement-assisted discrimination of quantum measurements is based on linear optics and qubits encoded into states of single photons. The scheme of our experimental setup is shown in Fig. 5.2. Time-correlated orthogonally polarized photon pairs are generated by the process of collinear frequency-degenerate type-II spontaneous parametric down-conversion in a 2 mm thick BBO crystal pumped by a CW laser diode at 405 nm. A post-selected two-photon polarization singlet Bell state $|\Psi^-\rangle$ is prepared by interfering the vertically polarized signal photon and horizontally polarized idler photon at a balanced beam splitter (BS). The state is characterized by quantum state tomography and we observed purity $> 98\%$ and fidelity $> 99\%$.

In the main experiment, the measurement that should be identified is performed on the first photon of the entangled pair $|\Psi^-\rangle$. The measurement basis ($\mathcal{M}$ or $\mathcal{N}$) is set by rotating a half-wave plate HWP1 in front of the polarizing beam splitter PBS1. We associated the basis states $|0\rangle$ and $|1\rangle$ with diagonal $|D\rangle$ and anti-diagonal $|A\rangle$ linear polarizations, respectively. Namely, $|\phi\rangle = \cos\theta|D\rangle + \sin\theta|A\rangle$ and similarly for other measurement-basis states. Measurement outcomes 0 and 1 are indicated by clicks of

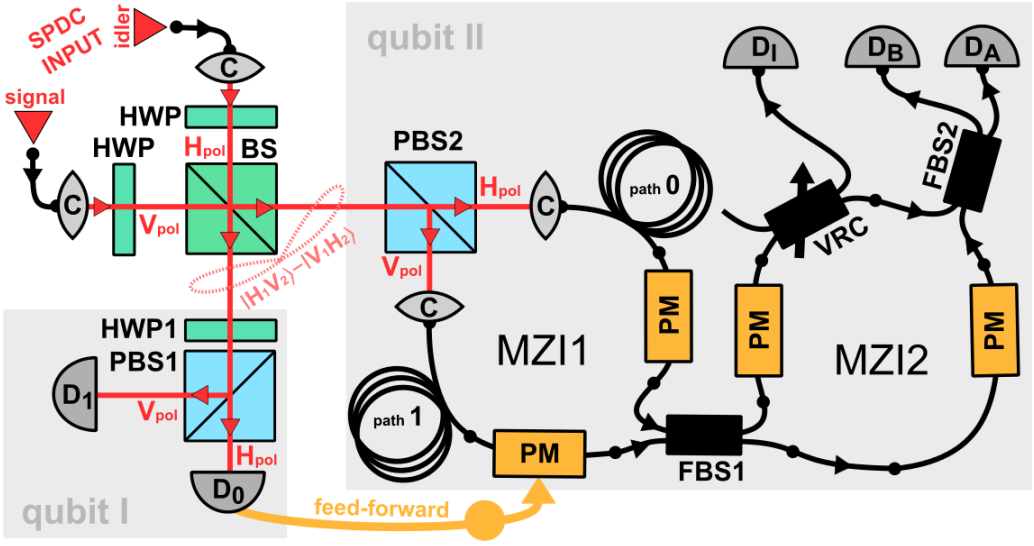

Figure 5.2: Scheme of the experimental setup for optimal entanglement-assisted discrimination of quantum measurements; BS – bulk beam splitter 50:50, FBS – fibre beam splitter 50:50, PBS – polarizing beam splitter, HWP – half-wave plate, C – collimating lens, PM – phase modulator, D – single-photon detector, VRC – variable ratio coupler which determines the amount of inconclusive results, SPDC – source of the photon pairs.

detectors D_0 and D_1, respectively. Polarization state of the second photon is transformed to path encoding with the help of PBS2 and the photon is coupled into the first of two serially connected fibre-based Mach-Zehnder interferometers (MZI1). Thus, polarization states $|V\rangle = (|D\rangle + |A\rangle)/\sqrt{2} \equiv |+\rangle$ and $|H\rangle = (|D\rangle - |A\rangle)/\sqrt{2} \equiv |-\rangle$ are then represented by a photon propagating in the lower and upper interferometer arm, respectively. We employ polarization maintaining fibres which suppressed unwanted changes of photon's polarization state during its propagation in the fibres. Both interferometers MZI1 and MZI2 are thermally isolated and actively stabilized to reduce phase drifts caused by temperature fluctuations and air flux. If detector D_0 registers a photon then an electronic feed-forward loop [1] conditionally changes the state of the second photon in MZI1 by applying a π-phase shift in the lower interferometer arm. This results in transformation $|\phi^{\perp}\rangle \to |\psi\rangle$ and $|\psi^{\perp}\rangle \to |\phi\rangle$ which is equivalent to the conditional application of unitary operation σ_Y in Eq. (5.3) up to an exchange of the role of $|\phi\rangle$ and $|\psi\rangle$.

The discrimination problem is thus reduced to a discrimination between two single-qubit states $|\phi\rangle$ and $|\psi\rangle$. Behind the balanced fibrecoupler FBS1 propagation of a photon through the upper (lower) arm corresponds to the state $|0\rangle$ ($|1\rangle$). A variable-ratio coupler (VRC) placed in the upper arm of MZI2 is used as a variable attenuator of the amplitude of the basis state $|0\rangle$, hence it implements the filter F. Projection onto the superposition states $|\pm\rangle$ is achieved using the final balanced fibre coupler FBS2 and detectors D_A and D_B. To determine the probability of inconclusive events, additional detector D_I is used to monitor the output of the tunable fibre coupler VRC.

Measurement

For each basis $X = M, N$ we measure 6 two-photon coincidences C_{ik}^X represented by simultaneous clicks of pairs of detectors D_i & D_k, where $i = 0, 1$, and $k = A, B, I$. We measured the relative detection efficiencies η_i, η_k of the detectors, and their influence is compensated by rescaling the measured coincidence rates as $C_{ik}^X \to C_{ik}^X/(\eta_i\eta_k)$. The measurement time is the same for both bases which corresponds to equal a-priori probabilities of $\mathcal{M}$ and $\mathcal{N}$. The probabilities P_S and P_I are then determined as $P_S = (C_{0A}^M + C_{1B}^M + C_{1A}^N + C_{0B}^N)/C_{\text{tot}}$ and $P_I = (C_{0I}^M + C_{1I}^M + C_{0I}^N + C_{1I}^N)/C_{\text{tot}}$, where C_{tot} denotes the sum of all 12 measured coincidence rates.

Measurement of entanglement based intermediate strategy: We perform measurements for 7 values of $\theta = j\pi/30$, $j = 1, 2, 3, 4, 5, 6, 7$ ($\theta = 6°, 12°, 18°, 24°, 30°, 36°, 42°$). For each θ, the transmittance of VRC is varied from 1 to 0.1 with the step of 0.1, i.e. $T = 0.1, 0.2, 0.3, \ldots, 1.0$. For each splitting ratio of VRC and each setting of HWP1, 70 repetitions of 1.5-s-long measurements (interlaced by active stabilization) is performed. The measurement is schematically shown in Fig. 5.3.

Measurement of entanglement based unambiguous discrimination: We have carried a separate test for 11 different $\theta_u = \arctan(\sqrt{T_u})$ corresponding to transmittances of the VRC, T_u varied from 1 to 0 with a step of 0.1, i.e. $T_u = 0.0, 0.1, 0.2, \ldots, 1.0$. The measurement is also schematically shown in Fig. 5.3.

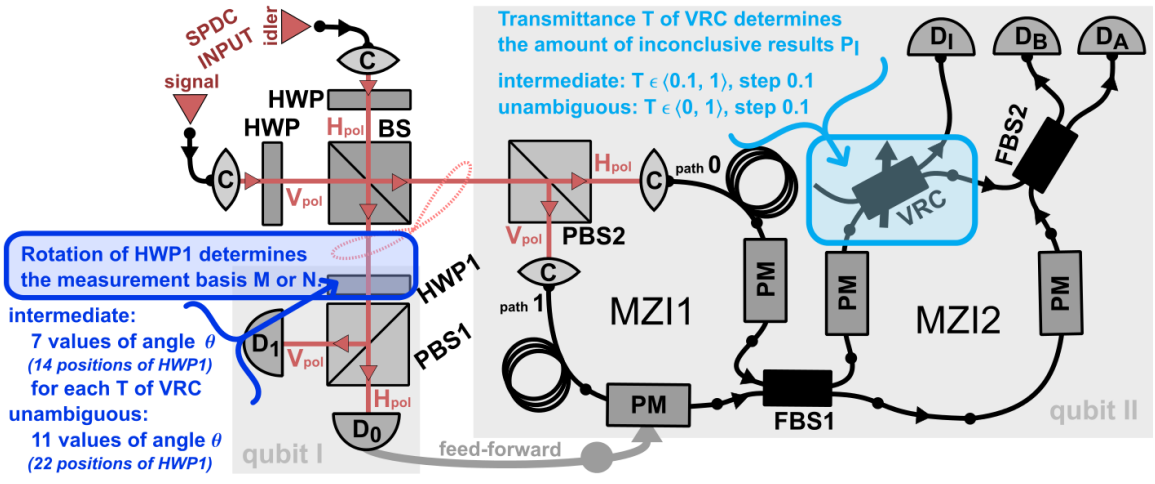

Figure 5.3: The scheme of the optimal entanglement-assisted discrimination of quantum measurements – for the intermediate and unambiguous strategies; SPDC – source of photon pairs, HWP – half-wave plate, (F)BS – (fibre) beam splitter 50:50, PBS – polarizing beam splitter, C – collimating lens, PM – phase modulator, D – single-photon detector, VRC – variable ratio coupler (It determines the amount of the inconclusive results.)

Results

Resulting dependences of $\tilde{P}_S$ on P_I for general **intermediate strategies** are plotted in Fig. 5.4. Obtained data are plotted by circles together with the theoretical curves representing the maximum $\tilde{P}_S$ achievable by the optimal entanglement-assisted protocol (solid lines) and by using the single-qubit probes (dashed lines). Statistical errors of the results are smaller than the size of symbols. We can see that for certain θ and P_I the experimental entanglement-based discrimination indeed outperforms the best strategy without entanglement. The slight reduction of the experimentally observed $\tilde{P}_S$ with respect to the theoretical prediction could be attributed to various experimental imperfections such as phase fluctuations inside MZIs, imbalance of MZIs arms lengths, small deviations in phase and polarization settings, slightly unbalanced splitting ratios of beam splitters, and small imperfections in the input singlet state. As indicated by the theoretical curves, the entanglement-based protocol theoretically outperforms the single-qubit scheme for all $P_I > 0$. The entanglement thus does not help only in the regime of minimum error discrimination ($P_I = 0$) where the optimal success probability $[1+\sin(2\theta)]/2$ can be achieved by a single-qubit probe prepared in state $|+\rangle$.

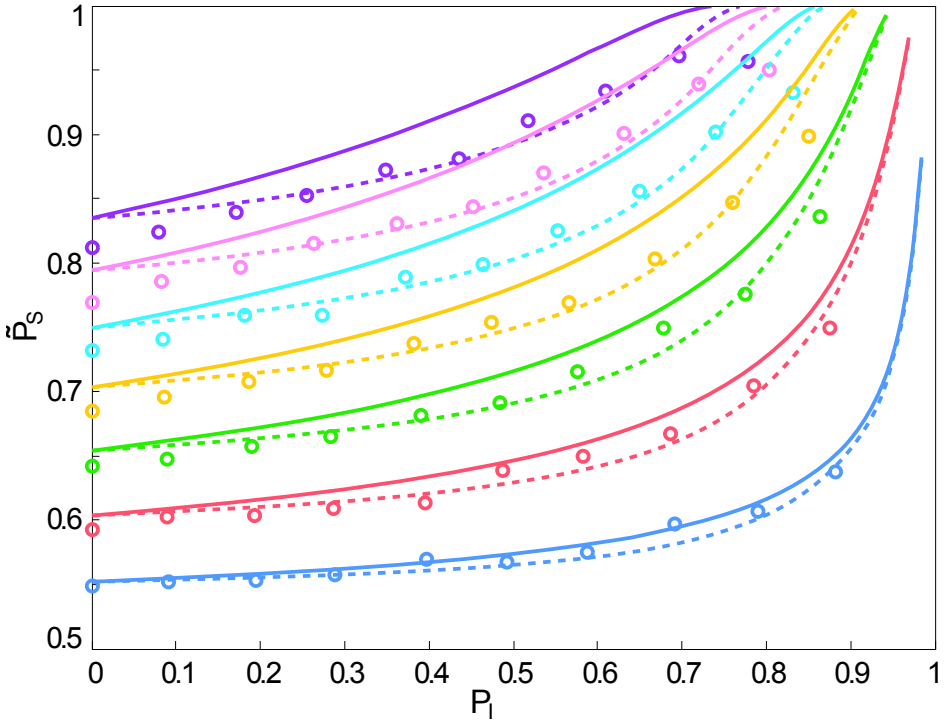

Figure 5.4: Optimal entanglement-assisted discrimination of measurement bases $\mathcal{M}$ and $\mathcal{N}$. Dependence of relative success probability $\tilde{P}_S$ on probability of inconclusive results P_I is plotted for 7 values of $\theta_j = j\pi/30$, $j = 1, 2, 3, 4, 5, 6, 7$ (values for each θ are depicted by one colour). The value of j increases from bottom to top. Shown are the experimental data (circles) as well as the maximum $\tilde{P}_S$ achievable by the optimal scheme using entangled state (solid lines), and using single-qubit probes only (dashed lines).

Unambiguous discrimination with a single-qubit probe is possible only if the probe is prepared in a state orthogonal to one of the projectors (5.1), say $|\vartheta\rangle = |\psi^{\perp}\rangle$. The resulting probability of inconclusive outcomes $P_I^{\text{unambig}} = [1 + \cos^2(2\theta)]/2$ is larger than the probability $\cos(2\theta)$ achieved by the entanglement-based scheme and the difference increases with θ. The experimental results of entanglement based unambiguous discrimination for 11 different θ_u are plotted in Fig. 5.5. They are in good agreement with the theory. The probability of errors P_E (which should theoretically be zero) does not exceed 3.2%. It is caused by experimental imperfections. The statistical errors of the results are smaller than the size of symbols.

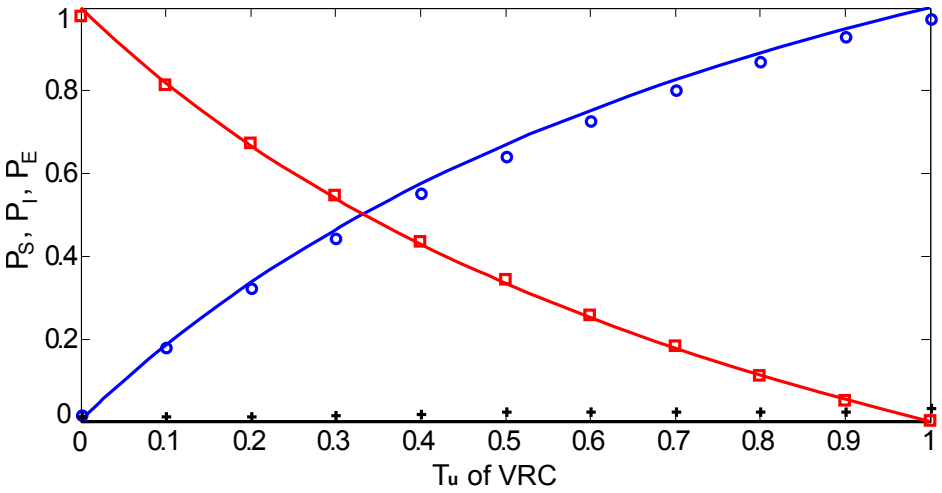

Figure 5.5: Entanglement based unambiguous discrimination of quantum measurements $\mathcal{M}$ and $\mathcal{N}$. Probabilities P_S (○), P_I (□), and P_E (+) are plotted as functions of the VRC splitting ratio T_u. Lines represent theoretical predictions.

Chapter 6

Faithful conditional quantum state transfer between weakly coupled qubits

This chapter is based on the following publication:

[5] Martina Miková, Ivo Straka, Michal Mičuda, Vojtěch Krčmarský, Miloslav Dušek, Miroslav Ježek, Jaromír Fiurášek, and Radim Filip. *Faithful conditional quantum state transfer between weakly coupled qubits.* Scientific Reports **6**, 32125 (2016).

Basic idea

This last described experiment is devoted to demonstration of faithful conditional quantum state transfer between weakly coupled qubits. We use a linear optical setup with qubits encoded into polarization states of single photons. This platform serves as a suitable testbed for proof-of-principle verification of our protocol, whose applicability is, nevertheless, universal and by no means limited to photonic qubits.

Our scheme enables a probabilistic yet perfect unidirectional transfer of an arbitrary unknown state of a source qubit onto a target qubit prepared initially in a known state. The transfer is achieved by a combination of a suitable measurement on the source qubit and quantum filtering on the target qubit. The quantum filtering depends on the outcome of the measurement on the source qubit, initial state of target qubit and on mutual interaction of qubis.

In this way, quantum state can be transferred between various physical platforms or one can create a hybrid entangled state.

Theory

The theoretical part of [5] is done by my colleagues. Here, we mention only a part of the theory necessary for good understanding of the protocol and its experimental realization.

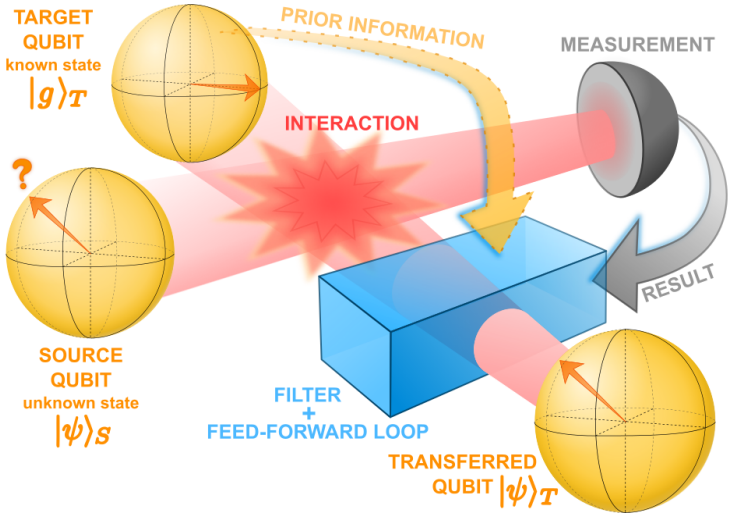

Figure 6.1: Quantum state transfer protocol. The initial state $|\psi\rangle_S$ of the source qubit S can be arbitrary and unknown. The goal is to transfer any state of source S to target T, initially in a known fixed state $|g\rangle_T$. The state transfer requires some interaction (unitary or probabilistic) between the source S and target T qubits. The transfer is performed by optimal measurement and feed-forward loop with optimal filter controlled by the measurement result and prior information about the initial target state $|g\rangle_T$.

Single qubit transfer: The goal of the universal quantum state transfer protocol is to faithfully map any quantum state $|\psi\rangle_S = \alpha|0\rangle_S + \beta|1\rangle_S$ of a source qubit S onto the target qubit T that is initially prepared in a known fixed state $|g\rangle_T$, as illustrated in Fig. 6.1. The source qubit could even be initially entangled with some ancillary qubit. For clarity of subsequent presentation, we shall consider a generic pure initial state of the source qubit $|\psi\rangle_S$. To make our treatment sufficiently general, we allow for both deterministic and probabilistic interactions $\hat{V}$ between the source and target qubits, hence $\hat{V}$ can be either a unitary operation or a non-unitary quantum filter satisfying $\hat{V}^\dagger\hat{V} \leq \hat{I}$. We thus consider the most general class of noiseless quantum interactions. The interaction $\hat{V}$ creates an entangled state of source and target qubits,

$$\hat{V}|\psi\rangle_S|g\rangle_T = \alpha|\Phi_0\rangle_{ST} + \beta|\Phi_1\rangle_{ST}, \tag{6.1}$$

where $|\Phi_j\rangle_{ST} = \hat{V}|j\rangle_S|g\rangle_T$. In the next step of the protocol we erase the correlations between source and target qubits by a projective measurement on the source qubit. If we project the source qubit onto a pure state $|\pi\rangle_S$, we prepare the target qubit in the following pure state,

$$|\varphi\rangle_T = \alpha|\phi_0\rangle_T + \beta|\phi_1\rangle_T, \tag{6.2}$$

where $|\phi_j\rangle_T = {}_S\langle\pi|\Phi_j\rangle_{ST}$. Note that states $|\phi_0\rangle$ and $|\phi_1\rangle$ are generally non-orthogonal, $\langle\phi_0|\phi_1\rangle \neq 0$, and they are not normalized and their norms can differ, $\langle\phi_0|\phi_0\rangle \neq \langle\phi_1|\phi_1\rangle$.

To complete the quantum state transfer we need to transform the two non-orthogonal states $|\phi_0\rangle$ and $|\phi_1\rangle$ onto normalized orthogonal basis states $|0\rangle$ and $|1\rangle$, respectively. Provided that $|\phi_0\rangle$ and $|\phi_1\rangle$ are linearly independent, this can be accomplished by a suitable quantum filter $\hat{G}$ applied to the target qubit,

$$\hat{G} = \frac{1}{N}\left(\frac{1}{\langle\phi_1^\perp|\phi_0\rangle}|0\rangle\langle\phi_1^\perp| + \frac{1}{\langle\phi_0^\perp|\phi_1\rangle}|1\rangle\langle\phi_0^\perp|\right). \tag{6.3}$$

Here $|\phi_j^\perp\rangle$ denotes a qubit state orthogonal to $|\phi_j\rangle$, $\langle\phi_j^\perp|\phi_j\rangle = 0$, and N is a normalization factor. We emphasize that the filter $\hat{G}$ does not depend on the input state $|\psi\rangle_S$ of the source qubit, it depends only on the initial state of the target qubit $|g\rangle_T$, the interaction $\hat{V}$, and the state $|\pi\rangle_S$ onto which the source qubit is projected. After filtering, the state of the target qubit becomes equal to the input state of the source,

$$\hat{G}|\varphi\rangle_T = (\alpha|0\rangle + \beta|1\rangle)_T/N, \tag{6.4}$$

and the probability p of success of the transfer protocol reads $1/|N|^2$. To reach maximal probability of success, N has to be set such that the maximum singular value of $\hat{G}$ is equal to 1 and $\hat{G}^\dagger\hat{G} \leq \hat{I}$ is satisfied. The probability of success can be also maximized by optimization of the measurement strategy and enhanced by the feed-forward loop, which allows us to exploit both outcomes of projective measurement on the source qubit. The overall success probability of the protocol is discussed later.

Example of the interaction: To illustrate our method, we consider as an instructive example a class of symmetric probabilistic two-qubit interactions described by an operator $\hat{V}$ diagonal in the computational basis,

$$\hat{V} = |00\rangle\langle 00| + t_1|01\rangle\langle 01| + t_1|10\rangle\langle 10| + t_{11}|11\rangle\langle 11|, \tag{6.5}$$

where $t_1, t_{11} \in [-1, 1]$. It turns out that in this case it is advantageous to measure the source qubit in the balanced superposition basis $|\pm\rangle = \frac{1}{\sqrt{2}}(|0\rangle \pm |1\rangle)$. After some algebra we find that the conditional states of the target qubit corresponding to these two outcomes differ only by a sign in the superposition,

$$|\varphi_\pm\rangle_T = (\alpha|\phi_0\rangle \pm \beta|\phi_1\rangle)_T/\sqrt{2}. \tag{6.6}$$

It implies that the quantum filters $\hat{G}_+$ and $\hat{G}_-$ associated with the measurement outcomes + and − differ only by a fixed unitary transformation, $\hat{G}_- = \hat{U}_\pi\hat{G}_+$, where $\hat{U}_\pi = |0\rangle\langle 0| - |1\rangle\langle 1|$. The whole protocol can be therefore implemented using a *fixed* quantum filter $\hat{G}_+$ followed by a feed-forward-controlled unitary phase shift. This greatly simplifies the experimental implementation of the protocol.

Linear-optical emulation of the interaction: For the proof-of-principle demonstration of the state transfer protocol we use linear optics and qubits encoded into polarization states of single photons.

We thought about the suitable non-trivial interaction between single photons. Finally, we decided to make our study generic and test our procedure in the regime of weakly coupled qubits. Thus for the interaction between single photons, we utilize interference on a partially polarizing beam splitter (PPBS) that is fully transmitting for horizontally polarized photons and only partially reflecting for vertically polarized photons, with corresponding amplitude transmittance t_V. We post-select on presence of a single photon in each output port of PPBS [30], then the interference results in the two-qubit transformation (6.5) with parameters $t_1 = t_V$ and $t_{11} = 2t_V^2 - 1$.

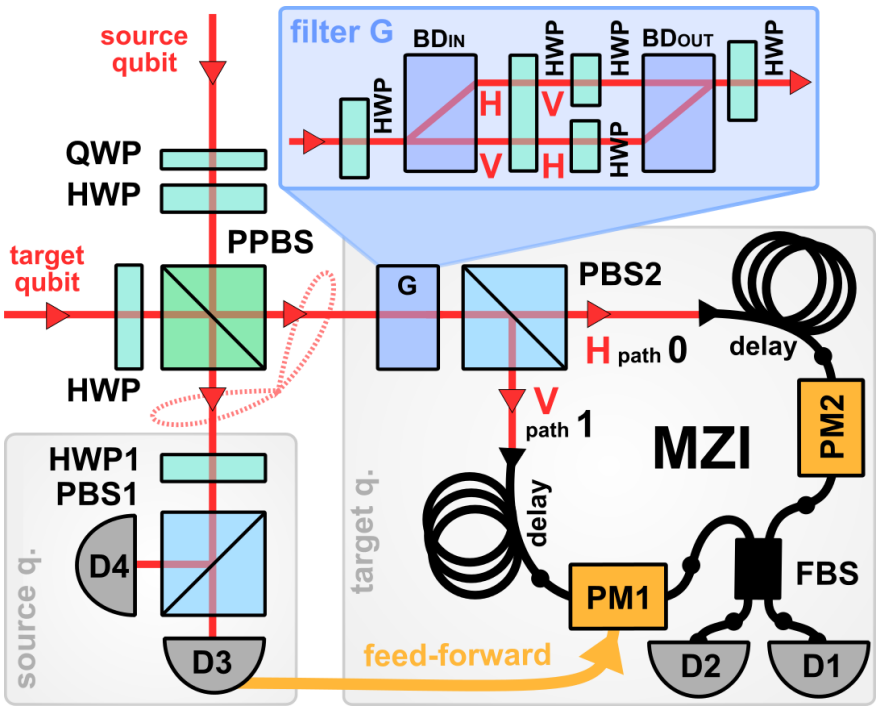

Figure 6.2: Simplified scheme of the experimental setup for the faithful conditional quantum state transfer between weakly coupled qubits. PPBS – partially polarizing bulk beam splitter ($T_H = 0.983, T_V = 0.334$); FBS – fibre beam splitter (47.6:52.4); G – adaptive state filtration $\hat{G}_+$; PBS – polarizing beam splitter; HWP – half-wave plate; QWP – quarter-wave plate; BD – calcite beam displacer; PM – phase modulator; D – single-photon detectors; thinner red line – free space beam; thicker black line – single mode polarization maintaining optical fibre PM-780HP; thick yellow line – feed-forward loop with coaxial cables.

Experiment

Time correlated photon pairs are generated in the process of frequency degenerate parametric down-conversion and fed to the input of the experimental setup shown in Fig. 6.2. Arbitrary input states of source and target qubit can be prepared by a combination of quarter-wave plate (QWP) and half-wave plate (HWP). The qubits interact at a partially polarizing beam splitter (PPBS) with transmittance $T_V = t_V^2 = 0.334$. Subsequently, the source qubit is measured in the basis of diagonal linear polarizations using a single-photon polarization detection block consisting of a half-wave plate HWP1, a polarizing beam splitter PBS1 and two single photon detectors D3 and D4. The polarization filter $\hat{G}_+ = \hat{U}_2\hat{D}\hat{U}_1$ on the target photon is implemented with the help of calcite beam displacers (BD) and half-wave plates, see the inset in the upper part of Fig. 6.2. The half-wave plates at the input and output of the filter implement the unitary operations $\hat{U}_1$ and $\hat{U}_2$. Selective attenuation of vertical or horizontal polarization is implemented by a suitable rotation of half-wave plates inserted inside an interferometer formed by the two calcite beam displacers. Since a beam displacer introduces a transversal spatial offset between vertically and horizontally polarized beams, these two polarization components become spatially separated inside the interferometer and can be individually addressed [31–33].

The conditional π phase shift on the target qubit is applied by means of an active electro-optical feed-forward loop [1, 34, 35]. To facilitate its experimental realization, we couple the target photon into fibre-based Mach-Zehnder interferometer (MZI), thus converting the polarization qubit into qubit encoded in which way information. A sufficiently long optical fibre delays the photon and provides time necessary for processing the electronic signal produced by the single photon detector D3 whose click indicates projection of source qubit onto state $|-\rangle$. This signal is amplified and fed to an integrated lithium-niobate phase modulator PM1 inserted in one arm of the fiber interferometer, thereby applying the conditional π phase shift to state $|1\rangle_T$. The required stability of the setup is reached by thorough isolation from the environment and, simultaneously, by active phase stabilization of MZI every 1.5 s to reduce phase drifts caused by remaining temperature and air-pressure fluctuations below 2° during the measurement.

The experimental imperfections which reduce the fidelity below 1 include partially distinguishable photons, imperfect retardation of wave plates, interference visibility lower than one, and imperfection of the partially polarizing beam splitter, which is not perfectly transmitting for horizontally polarized photons, and the experimentally determined horizontal transmittance is $T_H = 0.983$. This latter effect plays dominant role when the initial state of the target photon becomes close to horizontally or vertically polarized one. Heavy quantum filtering is required in such cases, as illustrated in Fig. 6.5(b), which makes the protocol more sensitive to parasitic coupling in horizontal polarization.

Real-time feed-forward control: When the source qubit is detected by D4 corresponding to projection onto $|+\rangle$, then filter $\hat{G}_+$ is applied and no other action is needed. Thus the phase inside MZI is set to 0° and the qubit state remains unchanged. The output target qubit is in the same state as the input source qubit.

However, it is not the case, when the source qubit is detected by D3 corresponding to projection onto $|-\rangle$. Then, the correct quantum filter $\hat{G}_-$ has to be applied to change the target-qubit state. The quantum filter $\hat{G}_-$ differs from quantum filter $\hat{G}_+$ only about fixed unitary operation $\hat{U}_\pi$. This conditional application of the unitary operation, triggered by the click of detector D3, requires a real-time feed-forward loop. PM1 in the fibre-based MZI is a part of the loop. Via it a conditional π-phase shift is applied between MZI arms, see Fig. 6.2. After the successful application of $\hat{G}_-$ [10], the output target-qubit state is $|\varphi'\rangle_T = -(\alpha|0\rangle+\beta|1\rangle)/\sqrt{2}$. Again, it is in the same state as the input source qubit.

The total success probability of state transfer is given by a sum of two contributions,

$$p = \frac{1}{|N|^2} + \frac{1}{|N_-|^2}, \tag{6.7}$$

where N_- is the normalization factor of $\hat{G}_-$. The success probability of the result with a sign + and − is included in the normalization factor $1/|N|^2$ and $1/|N_-|^2$, respectively, because the filter $\hat{G}$, determined by eq.(6.3), employs not normalized states.

The probabilistic nature of the quantum state transfer protocol is the price to pay for a faithful transfer of all states with unit fidelity. The quantum filter $\hat{G}$ is an essential part of the protocol. The average fidelity of states (6.2) obtained without filtering may even drop below the limit of 2/3, which is achievable by a purely classical measure-and-prepare strategy.

Measurement

It is important to verify the experimental feasibility, robustness and reliability of the quantum state transfer protocol and probe its potential limitations caused by various practical imperfections. Therefore, we experimentally test the quantum state transfer protocol for 17 different initial states of target photon, $|g\rangle_T = \cos\omega|0\rangle + \sin\omega|1\rangle$, with $\omega \in \{5°, 10°, 15°, ..., 85°\}$. For each choice of $|g\rangle_T$ we perform a full quantum process tomography of the resulting single-qubit quantum channel $\mathcal{L}$ describing the state transfer from source qubit to target qubit. The measurement process is schematically depicted in Fig. 6.3 and data acquisition is described below.

For each of 17 initial target-qubit states, we realize 36 combinations of 6 input source-qubit states and 6 output projective measurements on target qubit. In all cases, we measure coincidence rate C_{ij} of two detectors Di & Dj normalized to their relative detection efficiencies, where $i \in \{3, 4\}$ and $j \in \{1, 2\}$.

To show the importance of the state filtration after the weak interaction, we characterize the protocol both with the filter $\hat{G}_+$ active and switched off (HWPs in $\hat{G}_+$ are set to 0°, thus the HWPs do not influence the H and V polarization states). The rate of coincidence events depends on ω (initial target-qubit state) and whether the filter $\hat{G}_+$ is active or switched off as shown further in Fig.6.5(b). Therefore the whole measurement is repeated several times to accumulate sufficient amount of data.

[10] It includes application of the quantum filter $\hat{G}_+$ followed by the feed-forward action applying phase shift of π, $\hat{G}_- = \hat{U}_\pi \hat{G}_+$.

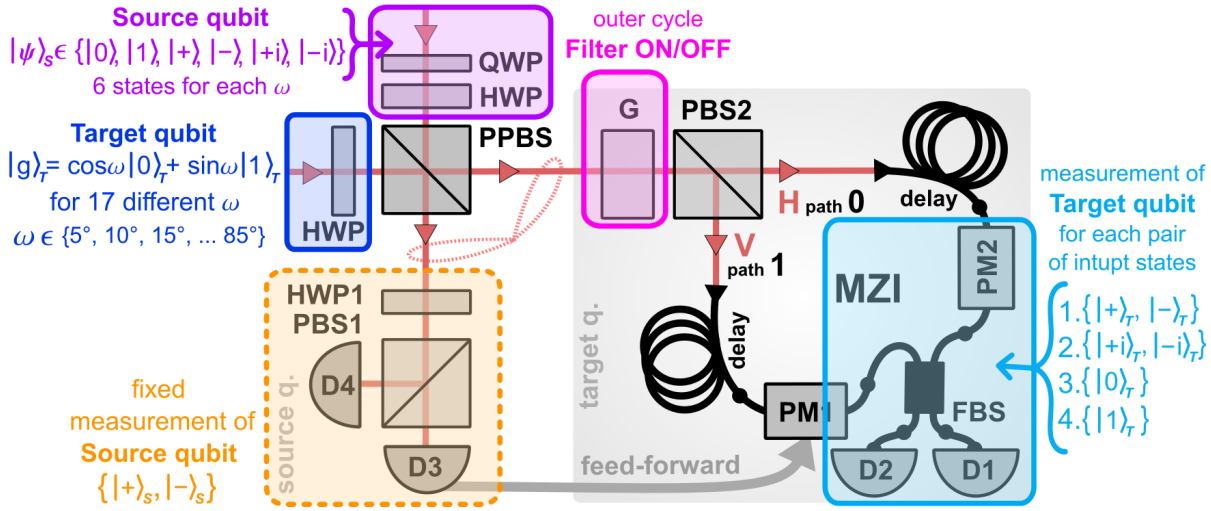

Figure 6.3: Scheme of data acquisition of quantum state transfer between weakly coupled qubits. Colour boxes show settings during measurement cycles. PPBS – partially polarizing beam splitter; FBS – fibre beam splitter 50:50; PBS – polarizing beam splitter; HWP – half-wave plate; PM – phase modulator; D – single-photon detector. G – quantum filter $\hat{G}_+$

Results

We characterize the resulting single-qubit quantum channel $\mathcal{L}$ describing the state transfer from the source qubit to the target qubit. This quantum channel can be conveniently represented by a matrix χ, which is a positive semidefinite operator on Hilbert space of two qubits. Physically, the quantum process matrix of a quantum channel $\mathcal{L}$ can be obtained by taking a pure maximally entangled Bell state $|\Phi^+\rangle = \frac{1}{\sqrt{2}}(|00\rangle + |11\rangle)$ and sending one of the qubits through the channel $\mathcal{L}$. A perfect state transfer corresponds to the identity channel whose matrix χ is equal to a projector onto Bell state $|\Phi^+\rangle$.

From measured data sets Choi process matrices χ are estimated for each initial target-qubit state $|g\rangle_T$, using the maximum-likelihood algorithm. In Fig. 6.4, we plot the reconstructed process matrices for $\omega = 55°$ with the calculated values of process fidelity $\mathcal{F}$, purity $\mathcal{P}$, and concurrence $\mathcal{C}$. To show the importance of the state filtration and the feed-forward in our protocol, we first switch off both of these operations, while accepting all coincidences. This emulates the situation when we have information that the interaction $\hat{V}$ between the source and the target qubit took place, but we do not perform any measurement on the source qubit (which can be inaccessible) and do not apply any operation to the target qubit. The resulting noisy quantum channel is shown in Fig. 6.4(a). If we switch on the fixed quantum filter $\hat{G}_+$ but keep the feed-forward switched off, we obtain the quantum channel plotted in Fig. 6.4(b). The theory predicts that the fixed filtering should yield a dephasing channel represented by a diagonal operator $\chi_{DC} = |00\rangle\langle 00| + |11\rangle\langle 11|$, and our data are in very good agreement with this theoretical expectation. Note that the dephasing channel is the best we can get without having access to measurement results on the source qubit, because the correlations present in the entangled state of source and target qubits destroy any phase coherence in the re-

duced density matrix of the target qubit. Finally, if we switch on also the feed-forward, we achieve faithful state transfer, with the resulting channel being close to the identity channel, see Fig. 6.4(c). In particular, compared to Fig. 6.4(b), the off-diagonal elements of the channel matrix are recovered, as the feed-forward ensures preservation of quantum coherence between the computational basis states.

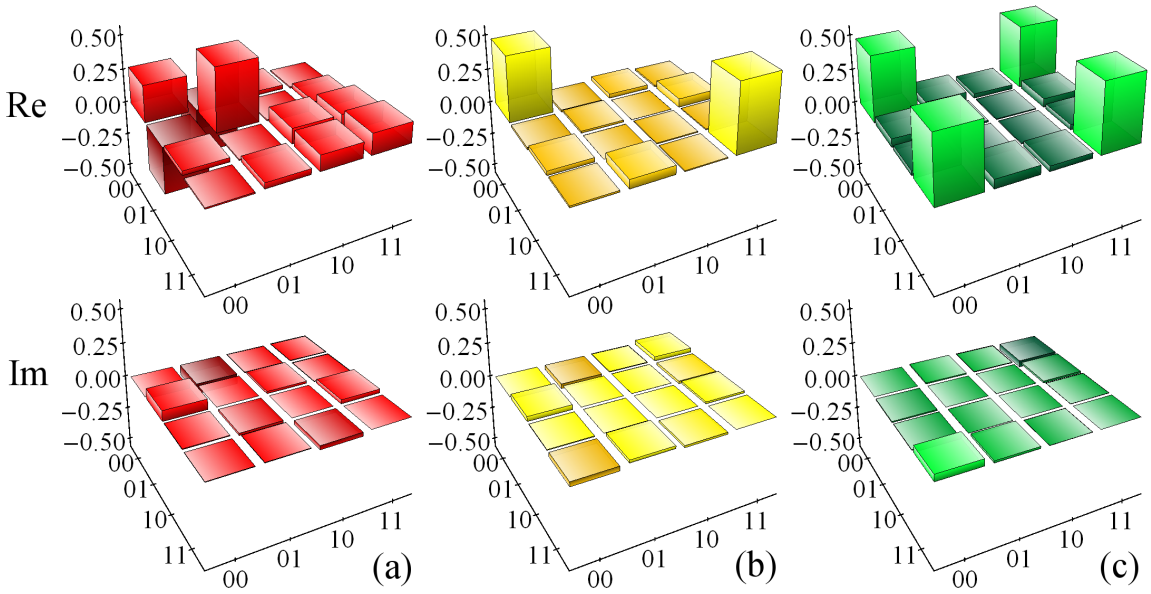

Figure 6.4: The reconstructed channel matrices χ for $\omega = 55°$. The first and the second row show real and imaginary parts of the reconstructed matrix, respectively. For ease of comparison, all matrices are normalized such that $\mathrm{Tr}(\chi) = 1$. The matrices are plotted for three scenarios: (a) - red - both filtering and feed-forward are switched off, $\mathcal{F} = 22.0$ %, $\mathcal{P} = 59.8$ %, $\mathcal{C} = 0.3$ %; (b) - yellow - filter is set on but feed-forward is switched off, $\mathcal{F} = 48.5$ %, $\mathcal{P} = 49.6$ %, $\mathcal{C} = 6.6$ %; (c) - green- full implementation with both quantum filter and feed-forward switched on, $\mathcal{F} = 95.7$ %, $\mathcal{P} = 94.6$ %, $\mathcal{C} = 92.3$ %; where $\mathcal{F}$ – fidelity, $\mathcal{P}$ – purity, and $\mathcal{C}$ – concurrence of the process matrix.

Subsequently, we provide the quantitative characterization of the quantum state transfer protocol performance in dependence on initial target-qubit state specified by angle ω. For each Choi matrix, we determine quantum process fidelity $\mathcal{F}$, which is defined as a normalized overlap of the channel matrix χ and the Bell state $|\Phi^+\rangle$. These results are summarized in Fig. 6.5(a). We achieve high fidelity with maximum $\mathcal{F} = 95.8$ % at $\omega = 50°$. Figure 6.5(b) simultaneously illustrates dependence of the success rate of the protocol on the initial target-qubit state. For each ω we plot the sum of all measured two-photon coincidences which is proportional to the success probability p. Since the same measurements are carried out for each ω and the measurement time is kept constant, the data for various ω are directly comparable. For reference, we plot also total coincidences recorded without active filtering $\hat{G}_+$. Thus we can see, how heavy is the quantum filtering. The success rate of the protocol is maximized at $\omega = 55°$. It is also confirmed by numerical optimization of the success probability (6.7) for the ideal protocol, where p is maximized at $\omega = 55.2°$, which is in excellent agreement with our experimental observations.

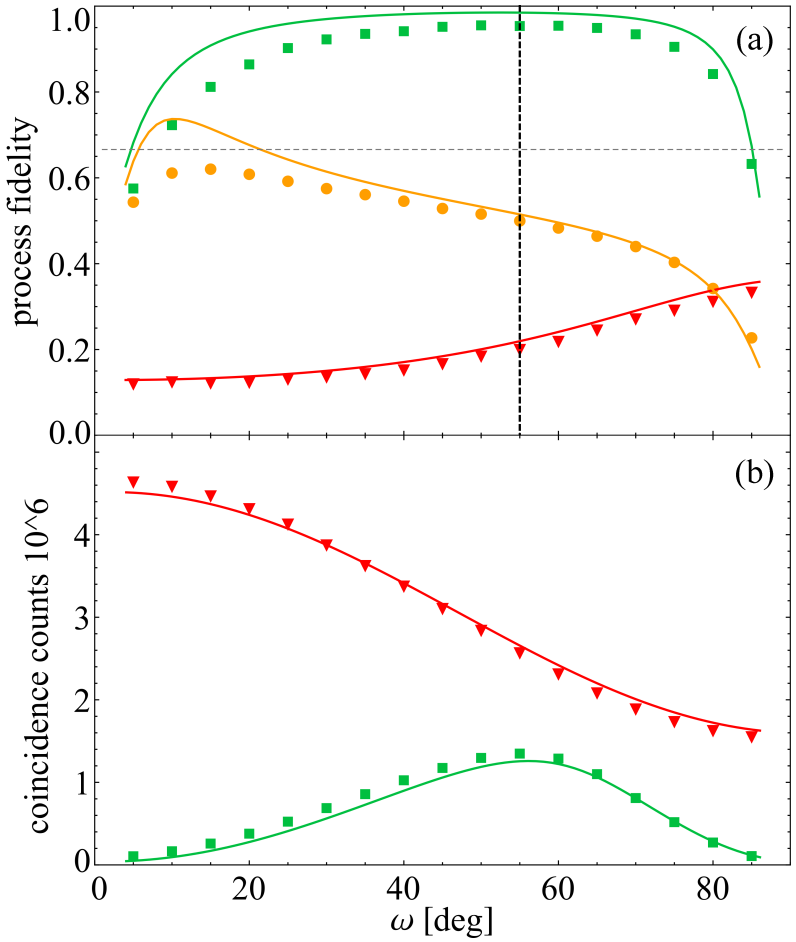

Figure 6.5: (a) dependence of quantum channel fidelity $\mathcal{F}$ and (b) two-photon coincidence counts on the initial target-qubit state determined by angle ω. The results are shown for three versions of the protocol: full implementation with both quantum filter and feed-forward switched on(■); quantum filter set on but feed-forward switched off (●), and both filtering and feed-forward switched off (▼). The horizontal dashed line shows the classical measure-and-prepare bound $\mathcal{F} = 2/3$. The vertical dashed line indicates the setting $\omega = 55°$ for which the channel matrices are plotted in Fig. 6.4. Solid lines indicate predictions of a theoretical model that accounts for imperfections of the PPBS where the source and target photons interfere. The data-sets with active feed-forward are measured directly, while the data-sets without the feed-forward are acquired by exchanging of coincidences C_{31} and C_{32} from previous data, it corresponds to feed-forward disconnection.

Chapter 7

Conclusions

This Thesis is based on five original publications [1–5] and summarizes my main experimental results, in the area of experimental linear quantum information processing and quantum optics, produced during my Ph.D. studies.

As indicated, the experiments had a lot in common from the experimentalist's point of view. All of them utilized the platform of linear optics, employed the correlated photon pairs generated by SPDC, used coincidence measurement with single-photon detectors, and consisted of at least one fibre-based Mach-Zehnder interferometer, operating at single-photon level, which was actively phase stabilized. Most of the experiments utilized the feed-forward loop. We have realized a reliable and fast real-time electro-optical feed-forward loop, which does not require high voltage and operates at single-photon level. It conditionally applies a unitary operation onto one qubit that depends on measurement outcome realized on the second qubit. The feed-forward experimental implementation is based mainly on single-photon detector and integrated electro-optical phase modulator included in fibre-based Mach-Zehnder interferometer. We implemented both the passive and the active, i.e. electronically amplified, versions of the feed-forward loop. The fastest implementation applied the unitary operation in approximately 25 ns from the photon detection. In our experiments, the feed-forward loop was utilized for different tasks: to increase the success probability of linear optical quantum gate [1], *Chapter 2*; to fully harness benefits of entanglement state in discrimination strategy of quantum measurements [4], *Chapter 3*; as a part of qubit state transfer protocol [2], *Chapter 5*; and as a part of quantum filter in quantum state transfer protocol between weakly coupled qubits [5], *Chapter 6*.

The other important technique, which we have implemented, was sequential active phase stabilization of complex interferometric layouts. The stabilization procedure was briefly described in chapter *Methods and Tools*, however, the specifics of the particular implementations were described in related chapters.

Chapter 2, based on publication [1], dealt with increasing efficiency of a linear-optical quantum gate using the electro-optical feed-forward loop. We employed feed-forward technique to double the success probability of a programmable linear-optical quantum phase gate in its fibre-based implementation. We showed that its application does not substantially affect either the process fidelity or the output-state fidelities.

In *Chapter 3*, based on publication [2], we experimentally investigated the properties of particles, which are used as qubit carriers, but whose noninformational degrees of freedom are nonfactorable. We can conclude that effective quantum indistinguishability, as a key resource for quantum information processing, can be quantified by a directly measurable parameter. We have experimentally demonstrated that this parameter represents a bound on the quality of quantum state transfer. We demonstrated it in a simple linear-optical fibre-based implementation of the qubit state transfer protocol. From the experimental results, it was confirmed that even if some degrees of freedom of two particles are entangled, the particles can still serve as good carriers of qubits.

In *Chapter 4*, based on publication [3], we experimentally implemented perfect quantum reading. We realized the fibre-based optical setup for perfect discrimination of two optical "devices", e.g. two memory records, which were represented by two beam splitters with different splitting ratios. A superposition of a single photon and vacuum was entering the beam splitter during the measurement. Thus the discriminated device was exposed in average just to a fraction of single-photon energy.

Subsequently, in *Chapter 5*, based on publication [4], we have experimentally implemented optimal strategies for discrimination between two known projective single-qubit quantum measurements. The experimental results clearly confirmed the advantage of the entanglement-assisted discrimination scheme compared to a single-qubit probe scheme. This experiment also demonstrates that the quantum optical technology is mature enough to harness the benefits of entanglement in quantum device discrimination, although the entanglement-based scheme is much more demanding than the single-qubit probe scheme. It requires entanglement and real-time feed-forward. Our experimental findings provide fundamental insight into the structure of optimal probabilistic discrimination schemes of quantum measurements.

Chapter 6, based on publication [5], refers about the experimental realization of faithful conditional quantum state transfer between weakly coupled photonics qubits. We have experimentally verified the probabilistic yet perfect unidirectional transfer of unknown single qubit source state through weak trace-decreasing interaction using optimal measurement and irreducible quantum filtering on the target qubit. The suitable filtering depends on the known initial target-qubit state, qubit-qubit interaction, and outcome of the measurement on the source qubit. Dependence of the filter on this measurement result is implemented by means of feed-forward. We experimentally proved that the method of qubit state transfer is feasible and robust. It is universally applicable because the protocol is not restricted to the photonic platform only. Therefore our proof-of-principle experimental results could serve as a cornerstone for a broad class of qubit state transfers in hybrid information processing, including atomic, solid state and optical qubits.

The main scientific contribution of this Thesis lies in the experimental implementation of newly suggested linear optical quantum information protocols [1–5]. The presented photonic experiments verify their experimental feasibility, robustness, and validate the theoretical predictions. Achieved results also show, that experimental linear quantum optics still serves as a suitable testbed for simulation of complicated processes.

Stručné shrnutí v češtině

Tato disertační práce je založena na pěti originálních publikacích [1–5], které shrnují mé hlavní experimentální výsledky základního výzkumu, které vznikly v průběhu mého doktorského studia. Hlavním cílem mého doktorského studia byla experimentální realizace nových lineárně optických kvantových protokolů pro kvantové zpracování informace či realizace samotných fotonických kvantových hradel.

Jednotlivé realizované experimenty mají z experimentálního hlediska mnoho společného. Využívaly lineárních optických prvků objemové a vláknové optiky, korelovaných párů fotonů z degenerované spontánní parametrické sestupné konverze a aktivní elektrooptické dopředné vazby. Kvantové bity byly v experimentech kódovány do polarizačních nebo prostorových stupňů volnosti jednotlivých fotonů. Jejich interakce byla zprostředkována pomocí jednofotonové nebo dvoufotonové interference a následné detekce pomocí jednofotonových detektorů. Každý z experimentů obsahoval alespoň jeden aktivně fázově stabilizovaný vláknový Machův-Zehnderův interferometr pracující na jednofotonové úrovni. Pro složitější interferometrická uspořádání byly vyvinuty komplexní metody aktivní stabilizace. Součástí vláknového interferometru byly vždy integrované elektrooptické vláknové fázové modulátory, které byly použity k zakódování fáze do stavu kvantového bitu, pro aktivní stabilizaci interferometru, nebo jako součást aktivní elektrooptické dopředné vazby. Tato aktivní vazba podmíněně zavádí unitární operaci na jeden kvantový bit, kde toto podmínění je určeno výsledkem měření na druhém kvantovém bitu. Nejrychlejší experimentální realizace této dopředné vazby zvládla zavést unitární operaci na druhý kvantový bit za 25 ns od detekce prvního fotonu detektorem.

Všechny realizované experimenty byly post-selekčního typu, a tedy výsledná měření byla realizována za současné detekce obou fotonů jako koincidenčních měření. Výstupem experimentu tedy byla pravděpodobnost určitého výsledku měření. Případně byl stav výstupního kvantového bitu zjišťován pomocí kvantové tomografie stavu nebo byl celý experiment plně charakterizován pomocí kvantové tomografie procesu. Tyto metody a nástroje sloužící pro realizaci jednotlivých experimentů jsou stručně popsány v práci, v kapitole *Methods and Tools*.

Prvním řešeným projektem, popsaném v kapitole 2 a vycházejícím z publikace [1], byla experimentální implementace lineárně-optického programovatelného kvantového fázového hradla, na němž bylo demonstrováno zvýšení pravděpodobnosti úspěchu hradla právě pomocí aplikace elektrooptické dopředné vazby. Hradlo bylo kompletně charakterizováno pomocí kvantové tomografie procesu. Experimentální výsledky ukázaly, že použitím dopředné vazby byla zdvojnásobena pravděpodobnost úspěchu hradla a zároveň nebyla ovlivněna fidelita výstupního stavu ani fidelita procesu.

Navazujícím projektem, popsaném v kapitole 3 a v publikaci [2], byl experimentální výzkum vlivu nerozlišitelnosti částic nesoucích kvantovou informaci na přenos této informace. Byla navržena nová míra efektivní nerozlišitelnosti částic, která může být použita i pro kvantově provázané částice v dalších stupních volnosti, tedy pro částice, které nejsou ve faktorizovaném stavu. Pro experimentální testování této nové míry byl realizován experiment přenosu stavu kvantového bitu. Výsledky ukázaly, že tato nová přímo měřitelná míra efektivní nerozlišitelnosti částic reprezentuje reálnou hranici kvality protokolů pro přenos kvantové informace.

Dále, jak je popsáno v kapitole 4, založené na publikaci [3], byla realizována experimentální implementace jednoznačného čtení paměťového záznamu s využitím co nejmenší energie. Informace byla uložena jako odrazivosti paměťových buněk reprezentovaných dvěma děliči svazku s navzájem různými odrazivostmi. Cílem realizovaného experimentu bylo jednoznačně rozlišit tato dvě různá zařízení, děliče svazku. V průběhu měření do zařízení vstupovala superpozice jednoho fotonu a vakua. Neznámé zařízení tedy bylo v průměru vystaveno pouze zlomku energie jednoho fotonu. Výsledky prokázaly, že kvantové čtení je experimentálně realizovatelné tímto způsobem.

Dalším projektem, který je popsán v kapitole 5, vycházející z publikace [4], byla experimentální realizace optimálního rozlišení projektivních kvantových měření pomocí kvantově provázaného stavu. Cílem bylo optimálně rozlišit dvě známá projektivní měření na polarizačních módech fotonu. Byla zkoumána závislost rozlišovací strategie na pravděpodobnosti nejednoznačných výsledků, kdy sice nedocházelo k jednoznačnému rozlišení měřících bází, ale vždy tato strategie byla optimální. Výsledná experimentální data jasně demonstrovala výhodu strategie využívající kvantově provázané částice pro rozlišení dvou projektivních měření v porovnání se strategií využívající pouze jeden kvantový bit.

Cílem posledního popsaného experimentu v kapitole 6, založené na publikaci [5], bylo přenést neznámý kvantový stav jedné částice na druhou, cílovou, částici ve známém kvantovém stavu, i když jejich vzájemná interakce je pouze slabá. Pro dokončení úspěšného přenosu stavu kvantového bitu musela být použita aktivní filtrace stavu, která závisela na původním stavu cílového kvantového bitu, na vzájemné interakci částic a rovněž na výsledku měření neznámého kvantového bitu. Výsledek tohoto měření byl do kvantového filtru zahrnut pomocí elektrooptické dopředné vazby. Experimentálně jsme potvrdili, že tato metoda přenosu stavu kvantového bitu mezi slabě interagujícími částicemi přenese kvantový stav bitu s vysokou věrohodností. Vzhledem k tomu, že tento protokol není omezen na fotonické kvantové bity, dosažené experimentální výsledky mohou pomoci při realizaci přenosu stavu například v hybridních kvantových systémech.

Hlavním vědeckým přínosem mé disertační práce byla experimentální implementace nově navržených lineárně optických kvantových protokolů pro kvantové zpracování informace [1–5]. Tyto práce experimentálně ověřily základní principy a uskutečnitelnost navržených teoretických protokolů v reálných experimentálních podmínkách. Dosažené výsledky ukazují, že lineární kvantová optika stále slouží i jako vhodné testovací zařízení na simulaci složitějších procesů.

Publications of the author and a list of citations

The thesis is based on these publications:

■ Martina Miková, Helena Fikerová, Ivo Straka, Michal Mičuda, Jaromír Fiurášek, Miroslav Ježek, and Miloslav Dušek. *Increasing effciency of a linear-optical quantum gate using electronic feed-forward.* Physical Review A **85**, 012305 (2012).

■ Michele Dall'Arno, Alessandro Bisio, Giacomo Mauro D'Ariano, Martina Miková, Miroslav Ježek, and Miloslav Dušek. *Experimental implementation of unambiguous quantum reading.* Physical Review A **85**, 012308 (2012).

■ Martina Miková, Helena Fikerová, Ivo Straka, Michal Mičuda, Miroslav Ježek, Miloslav Dušek, and Radim Filip. *Carrying qubits with particles whose noninformational degrees of freedom are nonfactorable.* Physical Review A **87**, 042327 (2013).

■ Martina Miková, Michal Sedlák, Ivo Straka, Michal Mičuda, Mário Ziman, Miroslav Ježek, Miloslav Dušek, and Jaromír Fiurášek. *Optimal entanglement-assisted discrimination of quantum measurements.* Physical Review A **90**, 022317 (2014).

■ Martina Miková, Ivo Straka, Michal Mičuda, Vojtěch Krčmarský, Miloslav Dušek, Miroslav Ježek, Jaromír Fiurášek, and Radim Filip. *Faithful conditional quantum state transfer between weakly coupled qubits.* Scientific Reports **6**, 32125 (2016).

Other co-author publications:

■ Michal Mičuda, Ivo Straka, Martina Miková, Miloslav Dušek, Niclosla Jean Cerf, Jaromír Fiurášek, and Miroslav Ježek. *Noiseless loss suppression in quantum optical communication.* Physical Review Letters **109**, 180503 (2012).

■ Michal Mičuda, Michal Sedlák, Ivo Straka, Martina Miková, Miloslav Dušek, Miroslav Ježek, and Jaromír Fiurášek. *Efficient experimental estimation of fidelity of linear optical quantum toffoli gate.* Physical Review Letters **111**, 160407 (2013).

■ Ivo Straka, Ana Predojevic, Tobias Huber, Lukáš Lachman, Lorenz Butschek, Martina Miková, Michal Mičuda, Glenn S. Solomon, Gregor Weihs, Miroslav Ježek, and Radim Filip. *Quantum non-gaussian depth of single-photon states.* Physical Review Letters **113**, 223603 (2014).

■ Michal Mičuda, Ester Doláková, Ivo Straka, Martina Miková, Miloslav Dušek, Jaromír Fiurášek, and Miroslav Ježek. *Highly stable polarization independent Mach-Zehnder interferometer.* Review of Scientific Instruments **85**, 083103 (2014).

■ Miroslav Ježek, Michal Mičuda, Ivo Straka, Martina Miková, Miloslav Dušek, and Jarimír Fiurášek. *Orthogonalization of partly unknown quantum states.* Physical Review A **89**, 042316 (2014).

■ Michal Mičuda, Michal Sedlák, Ivo Straka, Martina Miková, Miloslav Dušek, Miroslav Ježek, and Jaromír Fiurášek. *Process-fidelity estimation of a linear optical quantum-controlled-Z gate: A comparative study.* Physical Review A **89**, 042304 (2014).

■ Ivo Straka, Martina Miková, Michal Mičuda, Miloslav Dušek, Miroslav Ježek, and Radim Filip. *Conditional cooling limit for a quantum channel going through an incoherent environment.* Scientofic Reports **5**, 16721 (2015).

■ Michal Mičuda, Martina Miková, Ivo Straka, Michal Sedlák, Miloslav Dušek, Miroslav Ježek, and Jaromír Fiurášek. *Tomographic characterization of a linear optical quantum Toffoli gate.* Physical Review A **92**, 032312 (2015).

■ Michal Mičuda, Robert Stárek, Ivo Straka, Martina Miková, Miloslav Dušek, Miroslav Ježek, Radim Filip, and Jaromír Fiurášek. *Quantum controlled-Z gate for weakly interacting qubits.* Physical Review A **92**, 022341 (2015).

■ Michal Mičuda, Ivo Straka, Martina Miková, Miloslav Dušek, Miroslav Ježek, Jaromír Fiurášek, and Radim Filip. *Experimental test of robust quantum detection and restoration of a qubit.* Physical Review A **92**, 012324 (2015).

■ Robert Stárek, Michal Mičuda, Ivo Straka, Martina Miková, Miroslav Ježek, Radim Filip, and Jaromír Fiurášek. *Control and enhancement of interferometric coupling between two photonic qubits.* Physical Review A **93**, 042321 (2016).

■ Michal Mičuda, Robert Stárek, Ivo Straka, Martina Miková, Michal Sedlák, Miroslav Ježek, and Jaromír Fiurášek. *Experimental replication of single-qubit quantum phase gates.* Physical Review A **93**, 052318 (2016).

■ Robert Stárek, Michal Mičuda, Martina Miková, Ivo Straka, Miloslav Dušek, Miroslav Ježek, and Jaromír Fiurášek. *Experimental investigation of a four-qubit linear-optical quantum logic circuit.* Scientific Reports **6**, 33475 (2016).

■ Michal Mičuda, Dominik Koutný, Martina Miková, Ivo Straka, Miroslav Ježek, and Ladislav Mišta. *Experimental demonstration of a fully inseparable quantum state with nonlocalizable entanglement.* Scientific Reports **7**, 45045 (2017).

■ Michal Mičuda, Robert Stárek, Petr Marek, Martina Miková, Ivo Straka, Miroslav Ježek, Toshiyuki Tashima, Şahin K. Özdemir, and Mark Tame. *Experimental characterization of a non-local convertor for quantum photonic networks.* Optics Express **25** (7), 7839-7848 (2017).

List of citations:

citations of the publications relevant for this Thesis without self-citations

■ Martina Miková, Helena Fikerová, Ivo Straka, Michal Mičuda, Jaromír Fiurášek, Miroslav Ježek, and Miloslav Dušek. *Increasing effciency of a linear-optical quantum gate using electronic feed-forward.* Physical Review A **85**, 012305 (2012).

1. M. Bula, K. Bartkiewicz, A. Černoch, and K. Lemr. *Entanglement-assisted scheme for nondemolition detection of the presence of a single photon.* Physical Review A **87**, 033826 (2013)

2. M. Suda, C. Pacher, M. Peev, M. Dušek, and F. Hipp *Quantum interference of photons in simple networks.* Quantum Information Processing **12**, 1915–1945 (2013).

3. K. Lemr, K. Bartkiewicz, A. Černoch, and J. Soubusta. *Resource-efficient linear-optical quantum router.* Physical Review A **87**, 062333 (2013).

4. K. Lemr, A. Černoch. *Linear-optical programmable quantum router.* Optics Communications **300**, 282-285 (2013).

5. M. Gajdacz , T. Opatrný, K. K. Das. *An atomtronics transistor for quantum gates.* Physics Letters A **378**, 1919–1924 (2014).

6. C.-C. Qu, L. Zhou, Y.-B. Sheng. *Cascaded Multi-Level Linear-Optical Quantum Router.* International Journal of Theoretical Physics **54**, 3004–3017 (2015).

7. K. Lemr, K. Bartkiewicz, A. Černoch. *Scheme for a linear-optical controlled-phase gate with programmable phase shift.* Journal of Optics **17**, 125202 (2015).

8. J. Fiurášek. *Interconversion between single-rail and dual-rail photonic qubits.* Physical Review A **95**, 033802 (2017).

■ Michele Dall'Arno, Alessandro Bisio, Giacomo Mauro D'Ariano, Martina Miková, Miroslav Ježek, and Miloslav Dušek. *Experimental implementation of unambiguous quantum reading.* Physical Review A **85**, 012308 (2012).

1. C. Weedbrook, S. Pirandola, R. García-Patrón, N. J. Cerf, T. C. Ralph, J. H. Shapiro, and S. Lloyd *Gaussian quantum information.* Reviews of Modern Physics **84**, 621 (2012).

2. C. Lupo, V. Giovannetti, S. Pirandola, S. Mancini, and S. Lloyd. *Capacities of linear quantum optical systems.* Physical Review A **85**, 062314 (2012).

3. G. Spedalieri, C. Lupo, S. Mancini, S. L. Braunstein, and S. Pirandola. *Quantum reading under a local energy constraint.* Physical Review A **86**, 012315 (2012).

4. R. Nair, B. J. Yen, S. Guha, J. H. Shapiro, and S. Pirandola. *Symmetric M-ary phase discrimination using quantum-optical probe states.* Physical Review A **86**, 022306 (2012).

5. M. Dall'Arno, A. Bisio, and G. M. D'Ariano. *Ideal quantum reading of optical memories.* International Journal of Quantum Information **10**, 1241010 (2012).

6. M. Dall'Arno, A. Bisio, and G. M. D'Ariano. *Ideal quantum reading of optical memories.* 21st International Laser Physics Workshop, Journal of Physics: Conference Series **414**, 012038 (2013).

7. G. Spedalieri, C. Weedbrook, and S. Pirandola. *A limit formula for the quantum fidelity.* Journal of Physics A: Mathematical and Theoretical **46**, 025304 (2013).

8. J. P. Tej, A. R. Usha Devi, and A. K. Rajagopal. *Quantum reading of digital memory with non-Gaussian entangled light.* Physical Review A **87**, 052308 (2013).

9. S. Guha and J. H. Shapiro. *Reading boundless error-free bits using a single photon.* Physical Review A **87**, 062306 (2013).

10. C. Lupo, S. Pirandola, V. Giovannetti, and S. Mancini. *Quantum reading capacity under thermal and correlated noise.* Physical Review A **87**, 062310 (2013).

11. M. Gavenda, L. Čelechovská, M. Dušek, and R. Filip. *Quantum noise eater for a single photonic qubit.* New Journal of Physics **15**, 083050 (2013).

12. M. Dall'Arno, A. Bisio, and G. Mauro D'Ariano. *Quantum Reading of Unitary Optical Devices.* 11th International Conference on Quantum Communication, Measurement and Computing (QCMC) Book Series: AIP Conference Proceedings **1633**, 219-221 (2014).

13. M. Dall'Arno. *Quantum reading for the practical man.* International Journal of Quantum Information **12**, 1560018 (2014).

14. W. Roga, D. Buono, and F. Illuminati. *Device-independent quantum reading and noise-assisted quantum transmitters.* New Journal of Physics **17**, 013031 (2015).

15. G. Spedalieri. *Cryptographic Aspects of Quantum Reading.* Entropy **17**, 2218-2227 (2015).

16. L. Banchi, S. L. Braunstein, and S. Pirandola. *Quantum Fidelity for Arbitrary Gaussian States.* Physical Review Letters **115**, 260501 (2015).

17. S. Pirandola and C. Lupo. *Ultimate Precision of Adaptive Noise Estimation.* Physical Review Letters **118**, 100502 (2017).

18. C. Lupo and S. Pirandola. *Super-Additivity and Entanglement Assistance in Quantum Reading.* Quantum Information & Computation **17**, 611-622 (2017).

■ Martina Miková, Helena Fikerová, Ivo Straka, Michal Mičuda, Miroslav Ježek, Miloslav Dušek, and Radim Filip. *Carrying qubits with particles whose noninformational degrees of freedom are nonfactorable.* Physical Review A **87**, 042327 (2013).

1. V. S. Shchesnovich. *Universality of Generalized Bunching and Efficient Assessment of Boson Sampling.* Physical Review Letters **116**, 123601 (2016).

■ Martina Miková, Michal Sedlák, Ivo Straka, Michal Mičuda, Mário Ziman, Miroslav Ježek, Miloslav Dušek, and Jaromír Fiurášek. *Optimal entanglement-assisted discrimination of quantum measurements.* Physical Review A **90**, 022317 (2014).

1. M. Sedlák and M. Ziman. *Optimal single-shot strategies for discrimination of quantum measurements.* Physical Review A **90**, 052312 (2014).

2. T.-Q. Cao, F. Gao, Z.-C. Zhang, Y.-H. Yang, and Q.-Y. Wen. *Perfect discrimination of projective measurements with the rank of all projectors being one.* Quantum Information Processing **14**, 2645-2656 (2015).

3. T.-Q. Cao, F. Gao, Y.-H. Yang, Z.-C. Zhang, and Q.-Y. Wen *Determination of locally perfect discrimination for two-qubit unitary operations.* Quantum Information Processing **15**, 529-549 (2016).

4. T.-Q. Cao, Y.-H. Yang, Z.-C. Zhang, G.-J. Tian, F. Gao, and Q.-Y. Wen. *Minimal number of runs and the sequential scheme for local discrimination between special unitary operations.* Scientific Reports **6**, 26696 (2016).

5. T.-Q. Cao, F. Gao, G.-J. Tian, S.-C. Xie, and Q.-Y. Wen. *Local discrimination scheme for some unitary operations.* Science China Physics, Mechanics & Astronomy **59**, 690311 (2016).

■ Martina Miková, Ivo Straka, Michal Mičuda, Vojtěch Krčmarský, Miloslav Dušek, Miroslav Ježek, Jaromír Fiurášek, and Radim Filip. *Faithful conditional quantum state transfer between weakly coupled qubits.* Scientific Reports **6**, 32125 (2016).

1. J. Fiurášek. *Interconversion between single-rail and dual-rail photonic qubits.* Physical Review A **95**, 033802 (2017).

Bibliography

[1] M. Miková, H. Fikerová, I. Straka, M. Mičuda, J. Fiurášek, M. Ježek, and M. Dušek. Increasing efficiency of a linear-optical quantum gate using electronic feed-forward. *Phys. Rev. A*, 85:012305, 2012.

[2] M. Miková, H. Fikerová, I. Straka, M. Mičuda, M. Ježek, M. Dušek, and R. Filip. Carrying qubits with particles whose noninformational degrees of freedom are nonfactorable. *Phys. Rev. A*, 87:042327, 2013.

[3] M. Dall'Arno, A. Bisio, G. M. D'Ariano, M. Miková, M. Ježek, and M. Dušek. Experimental implementation of unambiguous quantum reading. *Phys. Rev. A*, 85:012308, 2012.

[4] M. Miková, M. Sedlák, I. Straka, M. Mičuda, M. Ziman, M. Ježek, M. Dušek, and J. Fiurášek. Optimal entanglement-assisted discrimination of quantum measurements. *Phys. Rev. A*, 90:022317, 2014.

[5] M. Miková, I. Straka, M. Mičuda, V. Krčmarský, M. Dušek, M. Ježek, J. Fiurášek, and R. Filip. Faithful conditional quantum state transfer between weakly coupled qubits. *Sci. Rep.*, 6:32125, 2016.

[6] G. Vidal, L. Masanes, and J. I. Cirac. Storing quantum dynamics in quantum states: A stochastic programmable gate. *Phys. Rev. Lett.*, 88:047905, 2002.

[7] M. Mičuda, M. Ježek, M. Dušek, and J. Fiurášek. Experimental realization of a programmable quantum gate. *Phys. Rev. A*, 78:062311, 2008.

[8] M. Miková. *Optical implementation of quantum operations for quantum information processing using entangled photons: application of electronics feed-forward.* Master's thesis, Department of Optics, Faculty of Science, Palacký University Olomouc, 2011. supervisor: M. Dušek.

[9] M. Ježek, I. Straka, M. Mičuda, M. Dušek, J. Fiurášek, and R. Filip. Experimental test of the quantum non-gaussian character of a heralded single-photon state. *Phys. Rev. Lett.*, 107:213602, 2011.

[10] I. Straka. *Optical frequency conversion and non-classical light generation.* Master's thesis, Department of Optics, Faculty of Science, Palacký University Olomouc, 2012. supervisor: M. Ježek.

[11] M. A. Nielsen and I. L. Chuang. *Quantum Computation and Quantum Information.* Cambridge University Press, Cambridge, 2000.

[12] M. Ježek, J. Fiurášek, and Z. Hradil. Quantum inference of states and processes. *Phys. Rev. A*, 68:012305, 2003.

[13] Z. Hradil, J. Řeháček, J. Fiurášek, and M. Ježek. Maximum-likelihood methods in quantum mechanics. In M. G. A. Paris and J. Řeháček, editors, *Quantum State Estimation, Lect. Notes Phys. 649*, chapter 3, page 59. Springer-Verlag, Berlin Heidelberg, 2004.

[14] H. Fikerová. *Quantum optics-based experiments in quantum information processing.* Master's thesis, Department of Optics, Faculty of Science, Palacký University Olomouc, 2014. supervisor: M. Dušek.

[15] P. Kok, W. J. Munro, K. Nemoto, T. C. Ralph, J. P. Dowling, and G. J. Milburn. Linear optical quantum computing with photonic qubits. *Rev. Mod. Phys.*, 79:135–174, 2007.

[16] N. Gisin, G. Ribordy, W. Tittel, and H. Zbinden. Quantum cryptography. *Rev. Mod. Phys.*, 74:145–195, 2002.

[17] J.-W. Pan, Z.-B. Chen, C.-Y. Lu, H. Weinfurter, A. Zeilinger, and M. Żukowski. Multiphoton entanglement and interferometry. *Rev. Mod. Phys.*, 84:777–838, 2012.

[18] J. P. Torres, K. Banaszek, and I.A. Walmsley. Engineering nonlinear optic sources of photonic entanglement. *Progress in Optics*, 56:227 – 331, 2011.

[19] C. K. Hong, Z. Y. Ou, and L. Mandel. Measurement of subpicosecond time intervals between two photons by interference. *Phys. Rev. Lett.*, 59:2044–2046, 1987.

[20] Z. Hradil. Quantum-state estimation. *Phys. Rev. A*, 55:R1561–R1564, 1997.

[21] H. Fikerová. *Optical setup for quantum information processing.* Bachelor's thesis, Department of Optics, Faculty of Science, Palacký University Olomouc, 2010. supervisor: M. Dušek.

[22] I. D. Ivanovic. How to differentiate between non-orthogonal states. *Phys. Lett. A*, 123:257–259, 1987.

[23] D. Dieks. Overlap and distinguishability of quantum states. *Phys. Lett. A*, 126:303–306, 1988.

[24] A. Peres. How to differentiate between non-orthogonal states. *Phys. Lett. A*, 128:19, 1988.

[25] C. W. Helstrom. *Quantum Detection and Estimation Theory.* Academic Press, New York, 1976.

[26] A. Chefles and S. M. Barnett. Strategies for discriminating between non-orthogonal quantum states. *J. Mod. Opt.*, 45:1295–1302, 1998.

[27] C.-W. Zhang, C.-F. Li, and G.-C. Guo. General strategies for discrimination of quantum states. *Phys. Lett. A*, 261:25 – 29, 1999.

[28] M. Ziman. Process positive-operator-valued measure: A mathematical framework for the description of process tomography experiments. *Phys. Rev. A*, 77:062112, 2008.

[29] G. Chiribella, G. M. D'Ariano, and P. Perinotti. Memory effects in quantum channel discrimination. *Phys. Rev. Lett.*, 101:180501, 2008.

[30] R. Stárek, M. Mičuda, I. Straka, M. Miková, M. Ježek, R. Filip, and J. Fiurášek. Control and enhancement of interferometric coupling between two photonic qubits. *Phys. Rev. A*, 93:042321, 2016.

[31] E. Jeffrey, N. A. Peters, and P. G. Kwiat. Towards a periodic deterministic source of arbitrary single-photon states. *New J. Phys.*, 6:100, 2004.

[32] N. A. Peters, J. T. Barreiro, M. E. Goggin, T.-C. Wei, and P. G. Kwiat. Remote state preparation: Arbitrary remote control of photon polarization. *Phys. Rev. Lett.*, 94:150502, 2005.

[33] M. Ježek, M. Mičuda, I. Straka, M. Miková, M. Dušek, and J. Fiurášek. Orthogonalization of partly unknown quantum states. *Phys. Rev. A*, 89:042316, 2014.

[34] S. Giacomini, F. Sciarrino, E. Lombardi, and F. De Martini. Active teleportation of a quantum bit. *Phys. Rev. A*, 66:030302, 2002.

[35] R. Prevedel, P. Walther, F. Tiefenbacher, P. Böhi, R. Kaltenbaek, T. Jennewein, and A. Zeilinger. High-speed linear optics quantum computing using active feed-forward. *Nature*, 445:65–69, 2007.